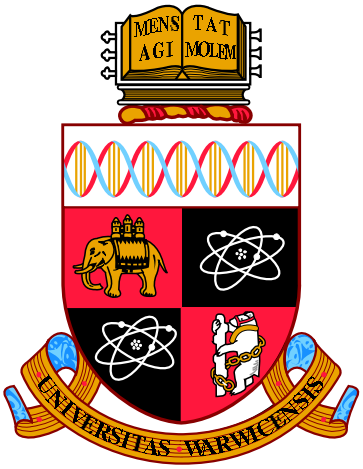

Phased electromagnetic acoustic transducer arrays for enhanced ultrasonic inspection

by

Lunci Xiang

Thesis

Submitted to the University of Warwick

for the degree of

Doctor of Philosophy

The Department of Physics

July 2021

Contents

List of Tables

List of Figures

Acknowledgments

'Learning, focus, discipline' and *'thinking, courage, diversity'*.

Firstly, I want to thank my country for offering a stable and prosperous society for my generation. I thank every chance that allowed me to get an education no matter if it was public-funded or self-funded. This is the foundation shaping me.

I want to thank my family for your unconditional support, love and education; my father, for your influence of responsibility and concentration; my mother, for your wise words of being humble and patient, and my lively, young sister, for the positive influence from your happiness.

Secondly, I want to thank my supervisor, Rachel Edwards. From the first meeting to the present, you have provided such a great amount of understanding, guidance and advice to me. It is your support that recreates my confidence. I appreciate your enthusiastic attitude towards work and the life because I was influenced in a way to look at this world from a different perspective. I learnt so much from you, and it was your company that made all the outcomes come true throughout this wonderful adventure.

I want to thank my second supervisor, Steve Dixon for your broad vision. The experience you shared completed my training, with absolute meaning on the foundation of the work. I want to thank the guidance from both you and Rachel Edwards, to make me think comprehensively and gain the real fun from physics! I also want to thank our group, Warwick Ultrasound in Physics, for the warm atmosphere here. I was well looked after during the years, not only in academic matters but also the lifestyle.

I want to thank my colleagues Dr. Lei Kang and Dr. Zhichao Li, for your help in transducer design and finite element model building. I also enjoyed chatting with you about being an ethnic minority in the UK and the worries or expectations about our shared culture.

Thirdly, I want to thank my friends, Leijia Luo, Luting Deng and Yangsi Shangguan (in alphabetic order); Leijia, for your continuous understanding, encouragement, and the motivation for a high pursuit of life over the decades; Luting, for our shared values and your lovely stories of the law and financial industries. I have to say 'forcing' me to go hiking really made me too tired to think and so got fully relaxed; Yangsi, for all of the things we have been through together when we were younger in college, the days when we first came to UK and the patience being my listener over the years.

Also, special thanks to my dog, Pipi. Thanks very much for your company when I was isolated at home due to the Covid pandemic over the past year. I felt much more calmed and peaceful as long as I touched fluffy you, even though it looked like I had bothered you too much that you didn't want to respond.

Finally, I want to thank myself. I am very proud to present my work, and I deserve this PhD degree. I wish I could stay pure, focused and enthusiastic no matter what situation it will become in the future.

Lunci Xiang

Dec. 2021

Declarations

I declare that the work presented in this thesis is my own except where stated otherwise, and was carried out entirely at the University of Warwick during the period between Aug 2017 and Jul 2021, under the supervision of Dr. Rachel Edwards (main supervisor) and Prof. Steve Dixon. The research reported here has not been submitted, either wholly or in part, in this or any other academic institution, for admission to a higher degree. Parts of this work have been published in the following peer-reviewed journal articles or conference proceeding:

1. L. Xiang, S. Dixon, et al., "Lift-off performance of electromagnetic acoustic transducers (EMATs) for surface acoustic wave generation", NDT & E Int., **126**: 102576, 2022.

2. L. Xiang, S. Dixon, et al., "Generation of Rayleigh waves using a phased electromagnetic acoustic transducer (EMAT) array", IEEE International Ultrasonics Symposium (IUS), 2020.

3. L. Xiang, D. Greenshields, et al., "Phased electromagnetic acoustic transducer array for Rayleigh wave surface defect detection", IEEE Trans Ultrason Ferroelectr Freq Control, **67**(7): 1403–1411, 2020.

4. L. Xiang and R. S. Edwards, "Multiple wavemode scanning for near and far-side defect characterisation", J Nondestruct Eval, **39** 9, 2020.

Abstract

Material defects such as surface breaking defects exist in engineering systems in all major industries, including railway, aerospace and nuclear power industries. Non-destructive testing (NDT) plays an important role for routine inspection of structures to identify issues. This work focuses on development of novel electromagnetic acoustic transducers (EMATs) for use in the field of NDT for enhanced surface crack characterisation. EMATs are an established non-contact ultrasonic technique [11], consisting typically of coil and magnet. They are safe for use in many environments and relatively inexpensive, and are gaining more attention nowadays in practical use.

In this work, firstly, a phased EMAT array system has been developed for enhanced characterisation of surface-breaking defects. Rayleigh surface waves were used as the tool for surface crack detection and characterisation. A new ultrasonic model of EMATs generating Rayleigh waves was described in detail, from considering a single linear coil used as the ultrasonic source element to the full model of the array consisting of multiple linear coils. The coil ultrasonic behaviour with/without lift-off (distance between the EMAT and the sample surface) is discussed. At zero lift-off (EMAT in contact with the sample), the single coil induced source spatial shape was studied, which was standardised to a rectangular function and extended to form the linear coil array. At a finite lift-off, the coil-induced current can exhibit a spatial distortion, and the generated ultrasound will suffer from a subsequent frequency shift. A single 1.5 mm wide linear coil showed a decrease in peak frequency for the wideband Rayleigh wave of the order of 100 kHz/mm with lift-off. Formation of the 1-D linear coil array is then presented. The array model was studied comprehensively for its Rayleigh wave frequency/wavelength behaviour without lift-off to give instruction for the phased operation, where a particular frequency is desired. When some lift-off was present, a similar phenomenon of frequency reduction to the case of the single linear coil was found and understood when using array EMATs.

An in-house built four-channel EMAT phased driver was used to control the array EMAT. An array of four linear coils that was individually controlled were developed for either narrowband or broadband Rayleigh wave generation. Controlling the delay between when the channels are activated makes it possible to change the Rayleigh wave wavelength without requiring the physical separation of the coils to be changed. The experimental results show that the four-coil phased system can

generate a wavelength range from 3 to 11.7 mm, with a significantly improved signal-to-noise ratio (SNR) compared to conventional single coil EMATs. The detection range of the surface crack has thereby been widened, showing proven sensitivity to surface cracks that were deeper than 1 mm. The lift-off behaviour comparison between physically spaced coils and those pulsed with time delays is given, showing them to be equivalent for all but the smallest separations which are required to give a high frequency/small wavelength signal.

Secondly, a dual-mode (Rayleigh wave and shear-vertical bulk wave) pitch-catch EMAT system was developed for faster inspection for surface cracks on both near- and opposite sides of a bar sample. The EMAT transmitter and receiver used the racetrack design, giving good SNRs for an incident Rayleigh wave propagating on the sample near-side surface for near-side surface crack characterisation, and an angled shear wave propagating into the bulk for far-side surface crack detection. Defects were indicated by a reduction in the transmitted Rayleigh wave amplitude, and by blocking of the shear wave. Used together, a full picture of both surfaces can be obtained, with the ability to identify the spurious crack signal that may be found when using only a single wavemode, and the ability to accurately measure the complex geometric information of the near-side surface crack.

Nomenclature

α	Ultrasound amplitude drop rate
α_a	Ultrasound amplitude drop rate (absorption)
α_s	Ultrasound amplitude drop rate (scattering)
$\bar{\mu}$	Relative permeability
$\bar{D}$	Average diameter of the scatterer
$\bar{F}_s^{(L)}$	Static Lorentz force (normalised)
$\bar{f}_s^{(L)}$	Static Lorentz force array (normalised)
δ	Electromagnetic skin depth
$\Delta\tau$	Time delay unit
δ_{ij}	Kronecker delta
ϵ	Permittivity
Γ_{ij}	Christoffel acoustic tensor
$\hat{\bar{f}}_s^{(L)}$	Static Lorentz force array (normalised) in Fourier domain
$\hat{S}$	Detected ultrasound (in Fourier domain) generated by an EMAT array
λ	Wavelength
λ_p	Wavelength to give peak amplitude
λ_R	Rayleigh wave wavelength
λ, μ	Lamé constant

μ	Permeability
μ_0	Permeability (free space)
$\nabla\cdot$	Divergence of a vector field
$\nabla\times$	Curl of a vector field
ν	Poisson's ratio
ω	Angular frequency
$\otimes$	Convolution operator
ρ	Density
ρ_f	Free charge density
σ	Conductivity
σ	Stress
σ_{ij}	Stress tensor
τ_j or $\tau_{0,j}$	Time delay for jth coil element
$\mathbf{A}$	Magnetic vector potential
$\mathbf{A}_r^V$	Magnetic vector potential in free space when considering EMAT receiving process
$\mathbf{B}$	Magnetic flux density
$\mathbf{B}_0$	Biasing field (static)
$\mathbf{D}$	Electric flux density
$\mathbf{E}$	Electric field
$\mathbf{E}_r^M$	Electric field in the material when considering EMAT receiving process
$\mathbf{F}^{(L)}$	Lorentz force
$\mathbf{F}^{(M)}$	Magnetisation force
$\mathbf{F}_{dynamic}^{(L)}$	Lorentz force (dynamic)

$\mathbf{F}_{static}^{(L)}$ or $\mathbf{F}_{s}^{(L)}$	Lorentz force (static)
$\mathbf{H}$	Magnetic field
$\mathbf{J}$	Current density
$\mathbf{J}_D$	Displacement current density
$\mathbf{J}_e$	Eddy- (mirror) current density
$\mathbf{J}_r^M$	Current density in the material when considering EMAT receiving process
$\mathbf{M}$	Magnetisation
$\mathbf{M}_0$	Magnetisation within biasing field
$\mathbf{P}$	Electric polarisation
$\mathbf{u}$	Displacement
$\mathbf{V}_r^V$	Potential difference in free space when considering EMAT receiving process
θ	Incident angle
θ_E	Surface crack inclined angle
$\tilde{E}_{z_0}$	Electric field at the sample surface
$\tilde{H}_{z_0}$	Magnetic field at the sample surface
$\tilde{J}_{e,y}$	y-component of eddy-current density from all depths
$\tilde{J}_{e,y}^{tot}$	Two-coil eddy-current density model
ε	Strain
ε_{ij}	Strain tensor
$\vec{i}$	Unit vector in Cartesian coordinates
$\vec{j}$	Unit vector in Cartesian coordinates
$\vec{k}$	Unit vector in Cartesian coordinates
a	EMAT linear coil width

$B_{0,z}$	z-component of biasing field (static)
C	Elastic constant
c	Ultrasound speed
c_L	Longitudinal wave speed
c_R	Rayleigh wave speed
c_T	Shear wave speed
C_{ijkl}	4th order elasticity tensor (81 components)
d_{eff} or D_{eff}	Linear coil spacing (phased) in the EMAT coil array
d_{ij}	Piezoelectric coefficient tensor
$d_{j,0}$	Physical separation between jth element and the reference element
d or D	Linear coil spacing in the EMAT coil array
e	Electron charge
f	Frequency
f_p^*	Upper limit of the frequency to give peak amplitude
f_p^D	Frequency to give peak amplitude in the coil width spatial function
f_p^H	Frequency to give peak amplitude in the coil spacing and number spatial function
f_p^T	Frequency to give peak amplitude in the full coil array spatial function
f_0	Centre frequency
f_p	Frequency to give peak amplitude
$F_{E_{IP}}$	Rayleigh wave signal enhancement factor
f_{fitted}	Gaussian fitted frequency
$f_s^{(L)}$	Static Lorentz force array

h	EMAT Lift-off
H_x^M	x-component of magnetic field in the material
H_z^M	z-component of magnetic field in the material
i	$\sqrt{-1}$
$J_{e,y}$	y-component of eddy-current density
k	Wavenumber
k_s	Ultrasound frequency shift rate
N	Number of the applied coil
N_{di}	Number of the applied coil dipole
p	Pressure wave
q	Electric charge
R_h	Mode converted Rayleigh wave
R_i	Incident Rayleigh wave
R_p	Pressure wave reflection coefficient
R_r	Reflected Rayleigh wave
R_t	Transmitted Rayleigh wave
$S(t)$	Detected ultrasound generated by an EMAT array
$s(t)$	Detected ultrasound
$S_{ph}(t)$	Detected ultrasound generated by a phased EMAT array
t	Time
T_0	Time period
t_E	Surface crack vertical depth
T_p	Pressure wave transmission coefficient
u^y	Ultrasonic displacement
u_0	Ultrasonic displacement at sample surface

v_{IP}	In-plane velocity
v_{OP}	Out-of-plane velocity
$y(t)$	Driving signal
Z	Acoustic impedance
4IR	Fourth Industrial Revolution
AC	Alternating current
CM	Composite meander-coil
cMUT	Capacitive micro-machined ultrasonic transducer
ECT	Eddy-current Testing
EM	Electromagnetic
emf	Electromotive force
FEM	Finite Element Method
FFT	Fast Fourier Transform
FMC	Full matrix capture
FWHM	Full width half maximum
GCC	Gauge corner cracking
GWT	Guided wave testing
IGSCC	Intergranular stress corrosion cracking
IOS	Intelligent Optical Systems
IP	In-plane
LPI	Liquid penetrant inspection
MEMS	Micro-electromechanical system
MOSFET	Metal-Oxide-Semiconductor Field-Effect Transistor
MPI	Magnetic particle inspection
MUT	Micro-machined ultrasonic transducer

NDE	Non-destructive evaluation
NdFeB	Neodymium-Iron-Boron
NDI	Non-destructive inspection
NDT	Non-destructive testing
OP	Out-of-plane
PA	Phased array
pMUT	Piezoelectric micro-machined ultrasonic transducer
PPM	Periodic permanent magnetic
PZT	Lead zirconate titanate
RCF	Rolling contact fatigue
ROI	Region of interest
RS	Rochelle salt
RT	Radiographic testing
SAM	Synthetic aperture method
SAW	Surface acoustic wave
SCC	Stress corrosion cracking
SH	Shear-horizontal
SM	Standard meander-coil
SNR	Signal-to-noise ratio
SV	Shear-vertical
TFM	Total focusing method
TGSCC	Transgranular stress corrosion cracking
TOFD	Time-of-flight diffraction
UT	Ultrasonic testing

Chapter 1

Background

This work focuses on novel electromagnetic acoustic transducer (EMAT) designs for applications in the field of industrial non-destructive evaluation (NDE). It utilises the phasing technique for near-side surface inspection (chapters 5 and 6) and develops multiple ultrasonic mode techniques for double-sided surface inspection (chapter 7). The novel designs of EMATs presented in this work are intended to be used for enhanced surface crack characterisation on metal surfaces.

This chapter first introduces the material defects that can exist in engineering components, structures and systems. Secondly, the concept and necessity of NDE with its unique advantages is outlined. An overview of conventional NDE techniques for material surface/subsurface characterisation is given in the following sections, with more weight given to ultrasonic testing (UT), including three established methods that are relevant to this work. The benefits of EMATs and the outline of this work are illustrated at the end of the chapter.

1.1 Defects in industrial applications

The technology explosion since the first industrial revolution has led to many different types of material being used in every aspect of human life in today's world [12]. From materials of natural origin that can be found everywhere, such as wood and cotton to composites that are man-made and specific to a purpose, materials exhibiting proper structural or functional properties are the central concern for choice as a component within an industrial application. Nevertheless, material integrity will degrade in various technical stages, from design and production to the component's lifetime during service. The interaction between engineered materials and the environment, for example, the mechanical loading they are subjected to, or the

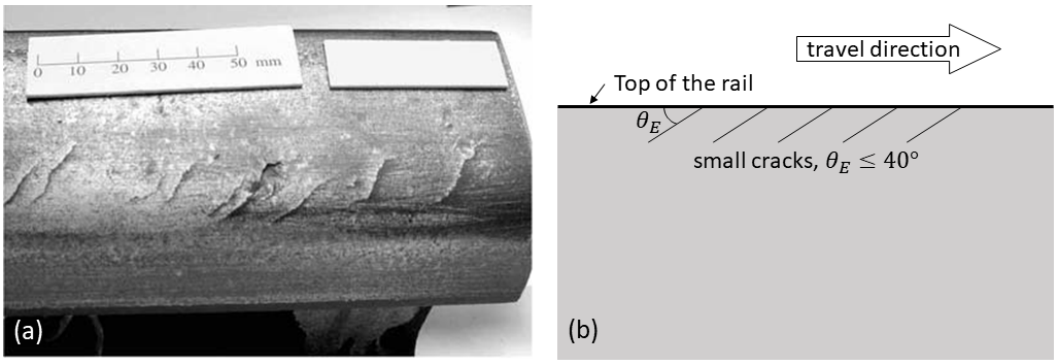

Figure 1.1: (a) Surface cracks in railways due to rolling contact fatigue. The cracks are located in the gauge corner (picture taken from [1]). (b). Cross-sectioned view of the cracks. The cracks are growing inclined with an angle of θ_E (less than 40°) into the rail track depth direction.

environmental influence such as chemical content or temperatures, may eventually lead to faults or failure of the components, structures and systems [2].

In this work, the defects of interest are surface-breaking defects. This type of defect can be formed by various mechanisms and can be found in many situations. There are two primary types of influence that are responsible for causing a surface-breaking defect; fatigue and corrosion. Fatigue is the phenomenon of the degradation of material property under dynamic loading. Permanent damage in the form of micro-cracks is initiated at the place where the stress is localised and they will progressively grow with the number of cyclic loads until final fracture occurs [13]. One typical surface cracking problem due to fatigue is rolling contact fatigue (RCF) in railway tracks [14]. When the train wheel rolls on the top of the rail head, a high pressure is produced onto the rail head surface by the intimate contact between the wheel and the rail. Surface flaws can arise after repeated passing of the wheel over the track. Note that, at the crown, where the rail is straight, the pressure is less likely to lead to a fracture, however, at the gauge corner (bends on the track), the pressure is over a smaller area and hence increases and cracking occurs. Figure 1.1(a) is a photograph showing the appearance of the fatigue cracking above the gauge corner, namely gauge corner cracking (GCC), in a steel rail [1]. Such cracks often grow in clusters with a shallow angle to the rail top surface [14], illustrated in figure 1.1(b).

Corrosion is when a material interaction with the surrounding environment leads to changes in its properties. The corrosive effect is attributable to chemical or electrochemical reactions between the metal and the environment, sometimes accompanied by other factors such as heat, mechanical stress or biological (micro-organisms) participants. The result of corrosion is harmful and can lead to material

loss and impairment of the technical system [2].

Another hazardous type of surface crack is stress-corrosion cracking (SCC) where cracks are initiated by the simultaneous action of stress and the corrosive environment. Alloys such as stainless steel and the family of aluminium alloys are susceptible to SCC, although the underlying mechanism is difficult to standardise and still under research [15]. SCC can start from the exposed material surface and propagate along a grain boundary, giving intergranular SCC (IGSCC). Branched features can be formed after the IGSCC grows into the bulk of the material, before a sudden fracture occurs. Another type of SCC, transgranular SCC (TGSCC), does not have a preference for propagation along grain boundaries, and can be even harder to predict [15]. Unlike other corrosive attack, SCC is often hidden as it is more difficult to characterise from the material surface condition as the defects can be closed. A careful diagnostics strategy is therefore needed to prevent any catastrophic failure of the item that can be caused by SCC.

1.2 Non-destructive evaluation (NDE)

Functionality and reliability is indispensable to all technical systems, but faults and failures may occur over time. Regular and stringent quality checks are therefore needed. Non-destructive evaluation (also known as non-destructive testing (NDT) or non-destructive inspection (NDI)) plays an important role in performance control and condition monitoring of industrial components. Many organisations concerned with NDE and quality control have been founded across the world, such as the American Society For Nondestructive Testing (ASNT), American Society for Testing and Materials (ASTM), European Organisation For Quality Control (EOQC), British Institute of Nondestructive Testing (BINDT), etc. International standards have been formed for NDE and NDE engineers [16].

NDE has been widely used for routine material inspection. It refers to the science and technology of assessing the object (product, machine, structures, etc) without impairing their current performance and future serviceability [2, 17, 18]. Unlike destructive testing, such as tensile testing to evaluate the material mechanical properties, a material which has undertaken NDE can retain its original functionality for future usage. NDE is well-used for defect localisation and characterisation, where the latter is the central concern of this thesis.

There are many advantages provided by NDE technology. For example, if a product can be properly examined by NDE techniques, the factor of ignorance of its state can be reduced and a higher reliability and safety level can be obtained. This

is beneficial for both customer and manufacturer as the chance of a faulty product can be minimised and the manpower of rework can be eliminated to reduce the cost. Components such as rails, turbines and nuclear power plants, are normally inspected during shut-downs; for example, using the conventional dye-penetrant method requires sample surface preparation so it is clean enough for appropriate penetrant use. Advanced NDE allows for on-line monitoring during operation, which can lead to significant savings in time and cost and an increase in system productivity [2]. Much research and development is now happening for on-line NDE inspection techniques. Future NDE techniques will be expected to be part of the Fourth Industrial Revolution (4IR), where digital and physical networks are fused organically to enable self-diagnosis and resource efficiency improvements for future society [19]. Intelligent and efficient inspection methods can play a key role in the transition of NDE to the 4IR. The EMAT technique is one of the potential methods for fast on-line ultrasonic inspection.

While NDE is capable of providing a wealth of information about an object, it is never comprehensive enough to give a diagnostic of a black box with absolute accuracy. Gaining knowledge from different NDE methods is the basis of integrity for testing by an NDE practitioner. An overview of conventional NDE methods is given in the next section. As a highly multi-disciplinary subject, advancement of NDE requires understanding of topics such as classical physics, material science, mechanical engineering, and chemistry.

1.3 Overview of conventional NDE methods

There have been a large number of NDE methods developed or used since the 1900s [16], among which the most widely accepted for surface or subsurface defect detection are, visual testing, liquid penetrant inspection (LPI), magnetic particle inspection (MPI), eddy-current testing (ECT) and UT. It should be noted that UT is available for both surface and volumetric detection, while the other techniques are primarily focused on surface inspection.

When launching a NDE process for a certain diagnostics purpose, a framework that is generally applicable can be summarised as [17, 18];

1. preparation of the testpiece material. For example, pre-clean of the inspection surface before using LPI.

2. Implementing the testing technique. For example, using ultrasound as a tool for sensing the voids/flaws/cracks in a material through sound reflection.

3. Understanding interaction between the testing probe and the test sample, which may lead to a modified testing signal that carries sample as well as defect information.

4. Detection of the testing signals sent in step 2.

5. Signal processing of the received signal.

6. Data interpretation.

7. Delivery of the examination results.

The system consists of three parts; the test sample, the probing instrumentation and the human inspector. Each part corresponds to one or more steps listed above; for example, the test sample is dominant in step 1 and 3, the probing instrumentation affects from step 2 to 5, and the human inspector skill determines steps 5,6 and 7. It can be seen that all three parts are indispensable and they are inter-dependent.

In the sections below, a brief introduction is given to each basic NDE method, from the physical principle to its limitations. Information is summarised from references [2, 16, 17, 18, 20].

1.3.1 Visual testing

Visual testing, as its name refers, indicates that the material examination is by human eyes (or, potentially, cameras with machine vision techniques applied). It includes the optical illumination of the object and the sensing of the reflected light. It is often accompanied by optical aids such as borescope, fibrescopes and videoscopes etc. [20]. Generally, visual testing is usable on all materials. A wealth of information about the surface condition of an opaque sample can be provided, including the colours and shapes of the surface cracks and the gloss of the surface finish, etc.

The principle of visual testing is the simplest, but it is still widely used. Evaluation of sophisticated structures usually combines multiple NDE methods and visual testing is always implemented in the first instance, where feasible. However, visual testing is highly subjective and is hard to document. An experienced inspector is required. Recently, development of visual testing has benefited from advances in optics, robotics and imaging processing [20].

1.3.2 Liquid Penetrant Inspection (LPI)

LPI is a method based on capillary action between a liquid applied to a sample surface and the surface-breaking defects, which makes the latter visible [2]. The basic

steps of implementing a LPI start from surface preparation, where any contaminants or surface finish that can prevent the penetrant from entering the flaws are removed. Then the liquid penetrant is applied onto the inspection area and remains there for a sufficient period of time to allow enough penetrant to seep into the surface flaw. Excess penetrant outside the flaw area is then carefully removed before a developer (either dry or wet) is used to draw out the penetrant that has been trapped by the flaw. A dwell time for the developer is allowed to permit a sufficient 'bleedout' of the trapped penetrant. It is the colour contrast between the visible dyes (or fluorescent dyes) of the penetrant and the developer that allow us to identify the cracks by shining light (or ultraviolet light) onto the sample.

LPI is an inexpensive technique with high sensitivity to open defects, that has been widely used. Examination by LPI relies on acuity of the operator, but training for an LPI inspector is easier than that of other methods such as ECT or UT. However, LPI is not suitable for inspecting a material with a rough or porous surface. Also, only those surface cracks with open mouths are detectable by LPI. The liquid and developer must be fully removed after each inspection.

1.3.3 Magnetic Particle Inspection (MPI)

MPI uses small magnetic particles to visualise the surface/subsurface cracks within a magnetised material. Figure 1.2 shows the magnetic flux distribution in a cracked material after being magnetised. The direction of the internal magnetic field is from right (south pole) to left (north pole). Due to the air gap created by the surface crack, the magnetic field experiences distortion, leading to magnetic leakage fields that can be indicated by a fine ferromagnetic powder applied to the sample. The solid arrows in figure 1.2 are used to indicate the magnetic flux. At the crack mouth, the material behaves like two separated magnets, and the flux is 'curved' due to the discontinuities of the magnetic properties between the air and the material. Ferromagnetic powders (either in dry or wet form) around such leakage fields indicate the presence of the crack.

The MPI method can also detect subsurface cracks, and it is widely recognised that, the stronger the magnetisation is, the deeper the effective detection thickness [16]. The general procedure of launching a MPI test includes surface preparation, magnetisation of the workpiece, application of the ferromagnetic powder, material illumination and inspection, and finally demagnetisation of the workpiece and removal of the magnetic particle [16].

Both LPI and MPI can be considered as enhanced visual methods. However, MPI offers better time savings than LPI as no extra dwell time is required. Also,

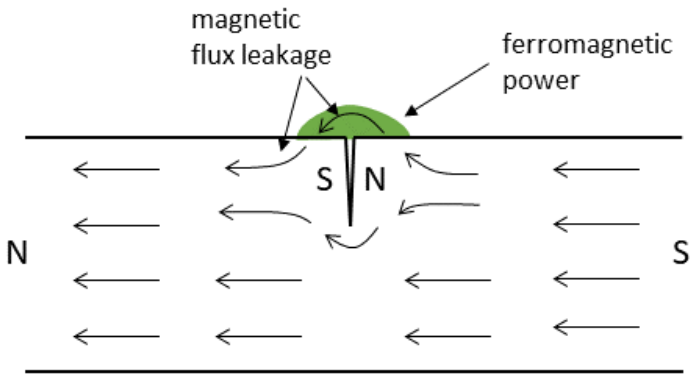

Figure 1.2: Principle of the MPI method. Magnetic leakage fields (curved arrows) are indicated by the accumulation of a fine ferromagnetic powder (area above the crack in green).

MPI allows for subsurface defect detection, which is not applicable for either visual testing or LPI. For deeper cracks, however, a strong magnetisation is required, which can lead to overheating of the material when the magnetisation is undertaken by a high-power encircling coil. The drawback of MPI compared to LPI is that it is only applicable on magnetic materials with the testing temperature below their Curie temperatures. The orientation of the crack can significantly affect the detection probability, for example, if a narrow crack is parallel to the direction of the internal magnetic field, no flux leakage arises, thus the crack is not observable. Multi-direction magnetisation is required to improve the detection accuracy, which increases inspection time. Both techniques require cleaning of the sample after inspection, which has an environmental impact.

1.3.4 Eddy-current Testing (ECT)

ECT is an electromagnetic NDE method that can evaluate the surface/subsurface discontinuities in a conductive material. Unlike MPI, where it is the magnetic field within the magnetised workpiece being used, ECT uses small external coils carrying alternating currents to deliver an electromagnetic field in the testing medium. Figure 1.3 shows the principle of ECT using a single solenoid coil to inspect a flat, cracked, conductor. The coil is driven by an alternating current, and a dynamic magnetic field, indicated by the solid arrow pointed into the sample, is generated. This electromagnetic field is the primary field in this scenario. Secondary fields that resist the primary field (i.e with an opposite direction with respect to the primary field) will be induced within a conductor when it is placed close to the inspection

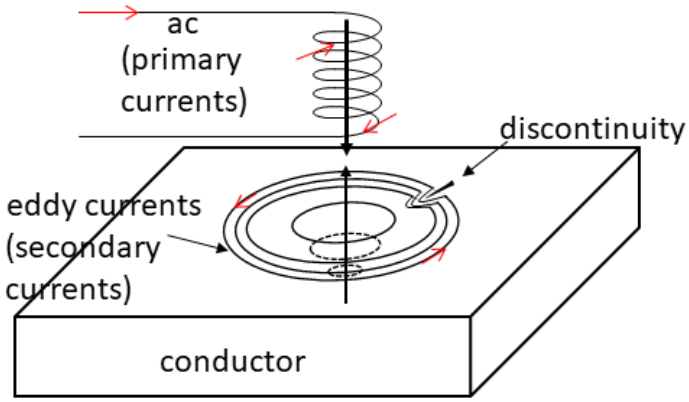

Figure 1.3: Principle of ECT method using a solenoid coil to detect a crack in a flat conductor. Eddy currents are induced within the conductor via the AC driven coil. At the surface crack, the eddy currents are disrupted and the changes in signals detected are the indication of crack presence.

coil. For a circular coil, the induced electrical currents flow in a circular path and attenuate exponentially over the conductor thickness direction; these are the eddy currents. The characteristics of the eddy current will be detailed in section 3.2.1 when discussing EMAT generation. A back electromotive force (emf) is induced in the inspection coil due to the existence of the eddy current. When encountering a surface discontinuity (shown in black, filled triangle), the eddy current is disrupted, and so the change in emf in the coil allows the detection of the discontinuity.

ECT is a method with high sensitivity. It is not only capable of flaw detection, but also material/coating thickness gauging and measurements of physical properties such as hardness, conductivity etc [16, 21, 22]. ECT is available for non-contact inspection, as it does not need direct contact between the coil probe and the sample surface. It can give results more quickly than LPI or MPI. However, ECT is only applicable on conducting materials and requires scanning of the sample. The eddy current is confined to a very thin region near the material surface (see section 3.2.1 for more details), leading to a small frequency-dependent effective depth for subsurface defect detection. The high sensitivity of ECT to many parameters means the testing condition needs to be strictly controlled so only one factor is varied during the measurement. A skilful ECT operator is required to interpret the ECT results.

1.3.5 Radiographic Testing (RT)

Radiographic testing (RT) is another NDE method that has been widely applied in industry. X-rays or gamma-rays are used as ionising ration that can penetrate through a testpiece material, to produce a photographic image (radiograph) [17]. A basic film radiograph can provide information about a cavity (such as a volumetric defect) two-dimensionally from the interpretation of the intensity of the X-rays (or gamma-rays) when they reach the film. For example, a small intensity is obtained in the absence of a cavity due to the higher degree of the material absorption, whereas intensity is larger when a cavity occurs and there is less absorption.

RT is a versatile technique that can be used for both metallic or non-metallic samples. It provides high sensitivity for material volumetric inspection in different engineering components [2, 17]. However, X-rays or gamma-rays are very hazardous and suitable precautions are always required. Conventional RT equipment is bulkier and more expensive than other NDE methods such as LPI or ECT. More details of RT technique are not included in this thesis as it is less used for surface crack detection.

1.3.6 Ultrasonic Testing (UT)

UT is a versatile method that has been extensively used in all major industries including nuclear, rail, aerospace and process industries [2]. It is also the technique of central concern in this work. UT is not limited to surface/subsurface applications, but is also available for bulk inspection.

In the UT method, an ultrasonic wave is used as the testing probe for object examination. An ultrasonic wave is a mechanical stress wave where the frequency of the vibration is more than 20 kHz [23]. The characteristics of ultrasound propagation is similar to that of optical waves, where reflection/transmission, refraction and scattering can occur when the wave encounters an obstacle. The beam directivity of ultrasound makes it an ideal technique for crack detection or material thickness gauging.

In a conventional UT system, an ultrasound wave is first sent by an ultrasonic emitter into the target medium. Such a wave can be transmitted, reflected and scattered at any discontinuities during the path of propagation. Then, a receiver (either the same transducer as the emitter or a separate one) is used to detect the reflected/transmitted signal, which carries information about any material discontinuities. Careful interpretation/data analysis is then performed on the received signal to give information about the material imperfections such as cracks, porosi-

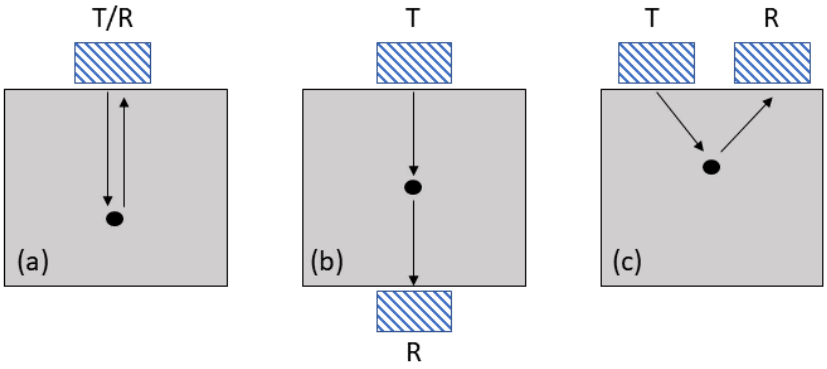

Figure 1.4: Generation arrangements of UT transducers. 'T' refers to ultrasound transmitter. 'R' refers to ultrasound receiver. (a) Pulse-echo mode. (b) Through-transmission method. (c) Reflection method.

ties, inclusions etc.

The arrangement of the sound emitter/receiver can be categorised into three types according to the locations and the number of ultrasound transducers being applied; pulse-echo method, through-transmission method and reflection method [16]. Figure 1.4 illustrates these. In pulse-echo mode (figure 1.4(a)), a single transducer is used to generate ultrasound and detect the reflected sound signal. This method has been widely applied since only a single side of the test sample is required to be accessible for a single transducer. One of the most popular applications based on this configuration is ultrasonic thickness gauging [24], where the sample thickness can be accurately measured by calculating the ultrasound time-of-flight (with knowledge of the sound speed). The degree of the metal thickness loss due to corrosion, erosion etc can be evaluated non-destructively. In figures 1.4(b) and (c), which correspond to through-transmission and reflection methods respectively, two separate transducers are needed, in which one is for ultrasound generation and the other is for detection. In the through-transmission method, access to both sides of the workpiece is required, so the transmitted bulk wave can be detected by the receiver. The reflection method is also called the pitch-catch method, where both transmitter and receiver are placed on the same side of the sample, using the reflected wave signal to evaluate the defect. The position of the defect can be understood from the ray path given in figure 1.4(c). Angle beam transducers are typically used for this arrangement.

The ultrasonic data obtained by UT transducers is normally displayed in three formats; A-scan (amplitude mode display), B-scan (brightness mode display) and C-scan (time-motion mode). Figure 1.5 gives a brief demonstration of each. An

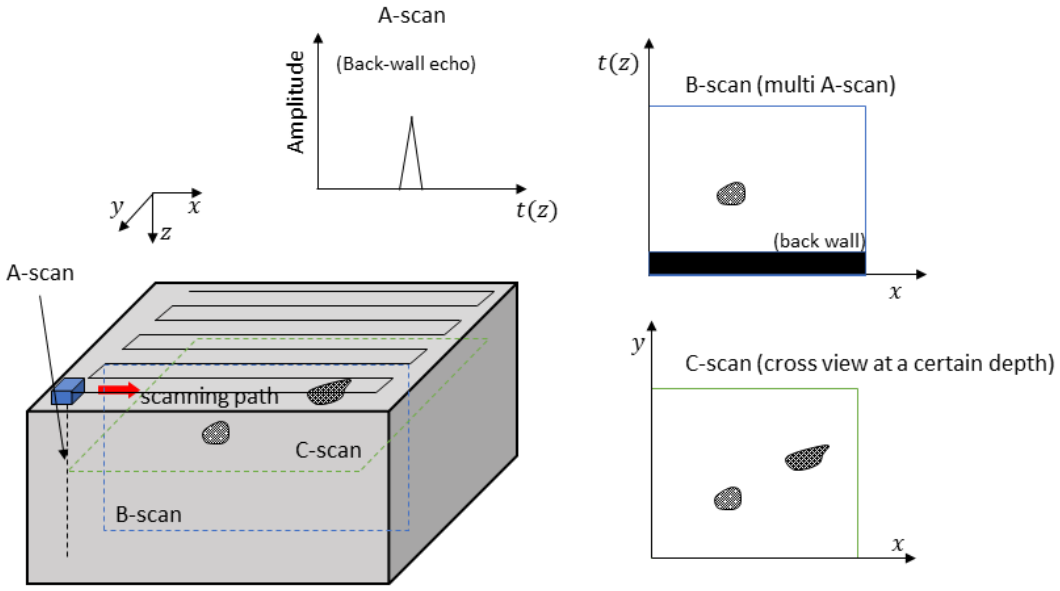

Figure 1.5: Formats of ultrasonic data representation; A-scan is from a single point showing the amplitude information at a certain time/depth trace. A B-scan consists of multiple A-scans. It is formed by combining all A-scans obtained after scanning along a line in the x-direction. A C-scan is the cross section view of the workpiece at a certain depth.

A-scan is the most basic form, showing the ultrasonic amplitude as a function of time or distance at a single location. B-scan and C-scans contain imaging information. A B-scan normally consists of multiple A-scans obtained from moving the transducer along a certain path. In a B-scan display, the x-axis indicates time (or depth) and the y-axis is the location of the transducer, or vice versa. A C-scan normally contains information about a cross section through the sample. The transducer is scanned over the xy-plane. The amplitude at a certain depth/time point is extracted to form the image of the scanned plane. In this work, A-scans and B-scans were mostly used.

UT methods exhibit many advantages over other NDE techniques. Firstly, instantaneous results can be available from the UT display. The three display formats can be used together [25], with the ability to provide rich information about a crack including its location, size and shape. Also, surface, subsurface or bulk defects are detectable using UT, depending on measurement configuration, and its penetration depth is larger than the other techniques listed above. However, materials with coarses grain, irregular shape or very small size can be unfavourable for UT examination. Conventional UT using piezoelectric transducers requires an extra medium of couplant between transducer and sample surface to reduce the transmis-

sion loss due to acoustic impedance mismatch, and this can cause beam divergence and unrepeatable results. The use of couplant can also require a flat and relatively clean surface to be inspected (surface preparation), which may further reduce the inspection efficiency. EMATs, as a non-contact ultrasonic technique, can overcome some of these drawbacks. Additionally, equipment calibration may be needed before implementing the UT, and an experienced operator is required. More details of ultrasound transduction methods can be found in section 2.3 and chapter 3.

Throughout this work, EMAT transducers arranged in pitch-catch mode were developed. Surface wave transmission to evaluate surface-breaking defects was studied in chapters 5 and 6. In chapter 7, both bulk waves and surface waves were used. An alternative reflection and transmission method was developed for surface crack characterisation.

1.4 Established UT techniques

The above section gave a basic introduction to the NDE UT method. Selected specialist ultrasonic techniques that have been established for advanced uses are described in this section. They are; time-of-flight diffraction (TOFD), guided wave ultrasonic inspection, and phased array (PA) UT for enhanced beam performance and imaging convenience.

1.4.1 Time-of-Flight Diffraction

TOFD is a method using wave diffraction to give information about crack size and depth. The ability of high accuracy and automated inspection has brought TOFD more attention since the 1980s [26]. It is now considered as an alternative to replace conventional pulse-echo ultrasonics and radiography for weld inspection [27].

Figure 1.6(a) shows the typical arrangement for a TOFD test using a longitudinal wave [26]. A pair of transducer consisting of an ultrasonic transmitter and receiver is used in pitch-catch mode on the same side of the sample. The wide beam of the transmitter allows the longitudinal wave to cover a wide sectoral region. There is also a lateral wave propagating along the near surface. On the receiver side, two waves are expected to be detected where no defect is present; the incident lateral wave (LW) and the longitudinal wave reflected from the back wall (BW), whose ray paths are illustrated in the figure. When a crack is at a depth that is located between the lateral wave and the back wall, additional diffracted waves from the crack tips (the top, 'diffract 1', and the bottom, 'diffract 2') are created and will be detected by the receiver. With knowledge of the sound speed, the transit time

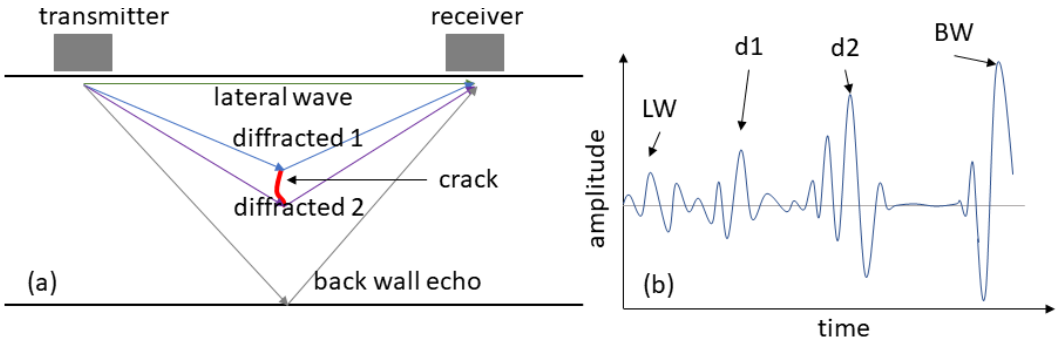

Figure 1.6: Typical TOFD arrangement, after [2]. (a) Ultrasound transducers are placed in pitch-catch mode. Ray paths of the lateral wave (LW), the diffracted waves (diffract 1 and 2) and the back wall echo (BW) are indicated. (b) A typical TOFD A-scan display, according to the waves in (a).

of different waves can be found, so the corresponding waveforms in the received A-scan trace can be identified. By solving simple trigonometric relations, crack size and depth can be obtained. Figure 1.6(b) gives a typical TOFD A-scan [26]. Four waves can be observed; the incident lateral wave, the diffracted wave from the crack top, the diffracted wave from the crack bottom, and the back wall echo.

The existence of the lateral wave hinders the detection of surface/near-subsurface defects using TOFD. A modified Hough transform method was studied to remove the interference from the surface waves [28]. The directed/reflected surface wave patterns on the TOFD image were partially removed and the signal-to-noise ratios of the desired diffracted waves were significantly increased. It can also be seen that the effective region of a TOFD inspection is reduced when the sample thickness is decreased, as the back wall echo starts to overlap with the incident lateral wave in the A-scan. Miniaturising the transducer and increasing the pulse frequency can be helpful. A combined immersion-TOFD system (conventional TOFD used under water) was proposed to enhance the performance on thin materials [29]. The beam angle and the transducer separation are more flexible and can be adjusted under the water, so a higher angle longitudinal wave can be generated to detect a shallower crack.

1.4.2 Long range guided wave ultrasonics

Conventional UT methods send ultrasound into bulk media. Arrangements such as the pulse-echo mode are a typical inspection type and can be very time consuming and costly when a large scale is under test, as every point on the sample needs to be tested. Using ultrasonic guided waves for long-range screening is an attractive

alternative [3, 30]. Unlike pulse-echo piezoelectric ultrasound, where waves with high frequency (small wavelength) are used, guided wave ultrasonics normally uses sound waves with much lower frequency (greater wavelength). When the sound wavelength is comparable to the thickness of the sample, or the sample has a curved geometry, the sample becomes a waveguide, where the stress waves will travel along the boundaries with special characteristics [3]. Such waves are typically from tens of kilohertz to hundreds of kilohertz (depending on the material geometric properties), as these show a lower degree of attenuation during propagation (see section 2.1.4 for ultrasound attention). The possible travel distance of guided waves is from several to tens of metres, overcoming the drawback of the short travelling distance exhibited by conventional UT [3]. Guided wave ultrasonics in plates or cylindrical structures has been extensively developed, and has been applied in many situations, such as composite plates, rails, vessels, tubes or pipelines diagnostics in all major industries [30, 31, 32, 33].

Guided waves show some complexity during propagation, and the material and its geometry will determine the characteristics of the guided waves that it may support. The dispersion of guided waves describes that waves with different frequencies may travel at different velocities. Lamb waves and shear-horizontal (SH) guided waves are two examples of guided waves that can occur in a plate (or shell) with finite thickness. Section 2.1.3 gives the scientific basis for Lamb waves, from which the solution (equations 2.41 and 2.42) suggests the wave motion can be categorised into asymmetric and symmetric modes, as demonstrated in figure 2.5. The SH guided wave is a group of waves that propagates in a free plate. The particle vibration of SH guided wave is parallel to the surface of the waveguide. An attractive property of SH guided waves is that the fundamental mode is non-dispersive on flat samples, where both group and phase velocities are the same at all frequencies [3]. SH guided waves are also capable of travelling around a bend with very limited energy loss [34], showing the potential to inspect a long distance in the presence of bends or other obstacles. This type of wave is not easy to generate using conventional pieozoelectric transducers, but can be generated by EMATs very efficiently. SH EMATs have been applied for weld inspection, and more details are given in sections 3.4.2 and 3.4.4.

Guided wave modes become more complex in pipeline or tubes. There are two axisymmetric wave modes that can be identified in a pipe; longitudinal wave (L-mode) and torsional wave (T-mode), which propagate in the pipe axial direction. L-mode and T-mode are analogous to Lamb wave and SH wave, respectively, if the pipe is approximated as a curved plate, but the circumferential geometry of the pipe

causes another layer of complexity. The flexure mode of the pipe can also give rise to another type of wave, flexural waves (F-mode), which are non-axisymmetric [30].

Typical instrumentation for a guided wave system employs a ring of transducers, when a tubular structure is under test [32]. The large volumetric length inspection is undertaken by a single shot of the probe at a single position. The transducer array is arranged circumferentially for sending and receiving the ultrasound, which is similar to the conventional pulse-echo method when reflection of the sound wave is used to evaluate discontinuities. Nevertheless, the complexity of wave modes and the dispersive nature make guided waves hard to interpret in a complex structure. Highly experienced technicians are required to operate GWT. One of the effective methods to simplify the data processing is to implement mode selection on the transducer side, such that only a single mode can be sent and received from the sample [35, 36].

1.4.3 Phased Array UT

The phased array method is an advanced technique that has been extensively used in a variety of different areas, including radar, acoustics and ultrasonography [37, 38, 39]. Development of ultrasonic phased arrays (PAs) for NDE purposes benefits from recent advances in electronics and material science. The ability of a PA UT system, such as dynamic beam control and slice imaging through the object, make it accepted in many demanding practices [40].

The common arrangement of an UT inspection (explained in section 1.3.5) is undertaken by a single-element transducer to emit the sound wave with fixed beam characteristics. In a PA system, a probe contains multiple elements, and each of them is individually driven by a pulse with an appropriate time delay factor. The delay sequence of the entire array is programmable, known as focal law, and the beam characteristics of the array are electronically tunable. Figure 1.7 demonstrates three basic beam profiles transmitted from a typical PA system. In figure 1.7(a), when all elements are pulsed simultaneously (no phasing is applied), a plane wave propagating in the normal direction is generated. This is similar to the performance of a single-element transducer, where the beam width is determined by the transducer aperture size. The beam can also be steered into a certain direction, as can be seen in figure 1.7(b). The time delay between the neighbouring elements is progressively increased, so the corresponding phase shift between different elements leads to coherent constructive interference primarily in the desired direction. Similarly, focusing at various depths is achievable via a PA. Figure 1.7(c) exemplifies a simple PA array accompanied with a symmetric focal law. The combined wavefront

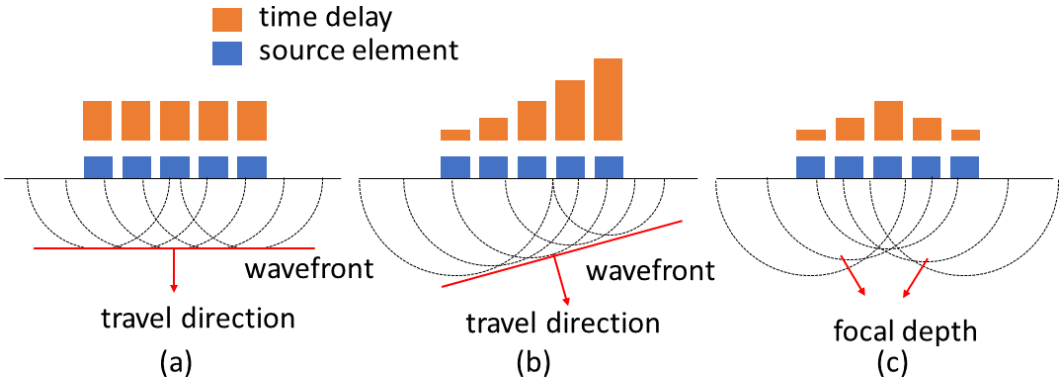

Figure 1.7: Phased array modalities: (a) array without phasing. (b) Beam steering. (c) Beam focusing.

is chosen to be symmetric around the central element. With the propagation of the wave, a final focal point can be obtained at a calculated depth, if the velovity of the wave is known precisely.

PA ultrasonics is replacing conventional pulse-echo ultrasonics in many applications due to its superb sensitivity and the controllable electronic unit. Mechanical moving of a single transducer is required to form a B-scan display, while a B-scan is obtainable with a single PA probe by simply combining the results from multiple elements (elements are working as both transmitters and receivers with multiplexing) [40]. The ability of beam steering also allows a sector scan over a wider area, and this has been applied to inspect complex weld structures [41]. Recently, many efforts have been made on data post-processing and imaging techniques, including full-matrix capture (FMC) and the total focusing method (TFM) [42]. FMC is a data-acquisition method for subsequent imaging post-processing. It allows collection of all possible data from a PA probe. Each element is fired in turn and the rest are used to receive the reflected signals, for example, a 16-element probe will capture a 16 by 16 matrix dataset. Each cell contains a time-domain signal from a transmit-receive pair. The algorithm of TFM allows one to focus at each point of interest, by mapping the amplitude in the A-scan in the FMC matrix from the calculated time-of-flight point [42]. Visual imaging with higher resolution can be obtained. However, the complexity of PA electronics makes the system more expensive than traditional UT systems. With a large number of pixels, the post-processing for a high quality image can be computation and time consuming. Additionally, a small size and a large number of ultrasonic elements are always needed for high resolution imaging. A piezoelectric PA system with hundreds of elements can be very expensive, and the need for couplant for NDE uses is sill a major drawback.

1.5 Electromagnetic Acoustic Transducers (EMATs) for ultrasonic NDE

The established ultrasonic methods introduced in this chapter show powerful capability to provide a wealth of information about a component, nondestructively. Sending and receiving of the chosen ultrasonic signals are crucially important in an ultrasonic NDE system. The common methods of ultrasound transduction are introduced in chapter 2. While piezoelectric transducers are by far the most popular choice, EMATs, as a counterpart, are gaining more attention due to their unique advantages. After decades of research and development, EMATs have been applied for different purposes, for example, NDE damage detection (including thickness gauging) [43, 44], physical acoustics studies (evaluation of material elastic constants, attenuation, grain size etc.) [11] and ultrasonic communication [45]. This work focuses on EMAT applications in NDE. Details of the EMAT technique are given in chapter 3.

An EMAT typically consists of a coil and a permanent magnet. The coil is used to introduce the electromagnetic field into the sample, and the magnet is to provide a biasing field. Together these cause elastic motion in the sample. This allows EMATs to work without the need of direct contact with the sample surface (see more in sections 3.2 and 3.3), and removes issues relating to required flatness of the sample, and surface preparation, and couplant.

The non-contact characteristic equips EMATs with more suitability over traditional piezoelectric transducers (which need couplant), especially for applications within a harsh environment (hot, dry, corrosive etc.) [46, 47, 48]. EMATs also show great potential for on-line inspection with fast speed [49]. In fact, the flexibility of spatial configuration for the EMAT coil and magnets makes it possible to generate all kinds of wavemodes, from conventional bulk waves and surface acoustic waves (SAWs) to guided waves in different structures (see section 3.4). The beam shape can also be customised, giving either straight beam or angle beam.

EMATs can be configured in all common arrangements such as pulse-echo, through-transmission and pitch-catch [11]. However, EMATs are widely recognised as having low efficiencies and are only used on conducting and/or magnetic materials. These drawbacks have hindered EMATs from being further applied. The element size in an EMAT array system can never be as small as that in a piezoelectric system by a significant margin, hence a lower imaging resolution can be expected. However, PA EMATs are suitable for some special applications, in particular under harsh industrial environments or for inspection with wavemodes that are

hard to generate using piezoelectric transducers. More details of PA EMAT designs are introduced in section 3.4.4. The phased EMAT arrays proposed in this work focus on extended ultrasonic surface wave applications. Instead of tuning the beam to cover a wider inspection area, the phasing technique was used to enhance the wave generation ability of EMATs.

Despite the above limitations, there is still much more that can be done with EMATs. This work presents new designs of EMAT with a phased array concept (chapters 5 and 6) and extended use of EMAT multiple wavemode generation (chapter 7) for enhanced metal surface crack detection. Below gives the outline of these designs;

1. Chapter 5. Illustration of the array design of EMAT proposed in this work, from basic coil element formation to spatial performance of the entire array. A Rayleigh wave was chosen as the ultrasonic wave required when configuring a linear array system. This was to make use of the EMAT convenience, where surface waves can be easily generated to inspect on a large scale with fast speed (e.g. for RCF in railways) [50], or characterise a material under corrosive conditions (e.g. for SCC) [48]. The lift-off effect of the proposed EMAT will be thoroughly studied, as this behaviour can influence the non-contact advantage of EMATs (see section 3.2.4 for EMAT lift-off problem).

2. Chapter 6. Implementing phasing onto the array EMAT proposed in chapter 5. The possible number of channels in the EMAT driver in this work was four (introduced in chapter 4), but full control of Rayleigh wave characteristics (frequency, bandwidth) was achieved via the phased EMAT system. The new design significantly improved the performance of surface crack detection compared to a conventional EMAT system. Comparison of the lift-off performance between the phased and non-phased array EMAT is discussed.

3. Chapter 7. A multi-mode EMAT pitch-catch system is proposed. An EMAT generating both an angle beam shear wave and direct surface wave was characterised and used. A comprehensive scan of the near- and far-surfaces of a metallic material was achievable through the use of the proposed EMAT pair.

Chapter 2

Ultrasound basics and review

This chapter considers the ultrasonic technique in more detail. First the basic theory of ultrasonic bulk waves, Rayleigh surface waves and Lamb waves propagation is presented. Ultrasonic attenuation in a homogeneous media is also briefly introduced, though this factor did not crucially influence the experimental results presented in chapters 4 to 7. The behaviour of sound waves at interfaces is described in detail, so that the behaviour of Rayleigh surface waves can be used to characterise surface-breaking defects (chapters 5 to 7). Common methods of ultrasound transduction are briefly introduced, including piezoelectric transducers, flexural air-borne transducers and laser ultrasound, and the laser interferometer was used for ultrasound detection in the later chapters. EMATs are described separately in chapter 3.

2.1 Ultrasonic waves in elastic media

2.1.1 Elastic behaviour of materials

Before understanding wave propagation in elastic media, a fundamental knowledge of the deformative behaviour of an elastic solid is required. A mathematical framework is included in this section to review the basic concepts and formulae of static elasticity, such as the strain, the stress and Hooke's law. Physical quantities demonstrated below are represented in tensor notation.

The stress, $\underline{\underline{\sigma}}$, is a measure of internal forces in a body between its particles. When an elastic material is subjected to an applied stress, the deformation undergone is described through the strain, $\underline{\underline{\varepsilon}}$ [51]. In three-dimensions, the stress is described by a stress tensor of rank two, σ_{ij}, where i, j take values 1,2 or 3 (mapping to x_1, x_2 and x_3 axes respectively). The first index indicates the direction of the surface normal for the surface onto which the stress is applied and the second

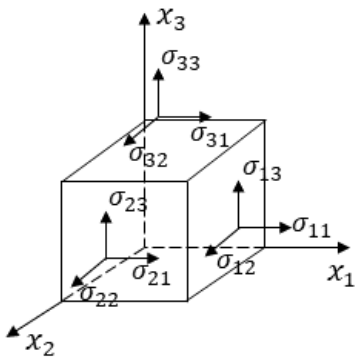

Figure 2.1: The stress tensor on a differential element [3].

indicates its direction [51]. The strain tensor, ε_{ij}, is also a tensor of rank two. These tensors are given below for three dimensional materials,

$$\underline{\underline{\varepsilon}} = \begin{pmatrix} \varepsilon_{11} & \varepsilon_{12} & \varepsilon_{13} \\ \varepsilon_{21} & \varepsilon_{22} & \varepsilon_{23} \\ \varepsilon_{31} & \varepsilon_{32} & \varepsilon_{33} \end{pmatrix} \quad \text{and} \quad \underline{\underline{\sigma}} = \begin{pmatrix} \sigma_{11} & \sigma_{12} & \sigma_{13} \\ \sigma_{21} & \sigma_{22} & \sigma_{23} \\ \sigma_{31} & \sigma_{32} & \sigma_{33} \end{pmatrix}. \tag{2.1}$$

Figure 2.1 shows the definition of the stress tensor in Cartesian coordinates.

For materials that behave linearly and elastically, and for a deformation that is sufficiently small, the constitutive relationship between the applied stress and the strain can be written as [51],

$$\sigma_{ij} = C_{ijkl}\varepsilon_{kl}. \tag{2.2}$$

This is known as Hooke's law and $\underline{\underline{C}}$ is the elastic constant. Since $\underline{\underline{C}}$ links $\underline{\underline{\sigma}}$ and $\underline{\underline{\varepsilon}}$, the elastic tensor C_{ijkl} is a 4^{th} order tensor which contains 81 components. For any elastic body, these components are not always independent, and the tensor can be simplified [52];

- using the symmetry of the stress and strain tensors ($\sigma_{ij} = \sigma_{ji}$ and $\varepsilon_{ij} = \varepsilon_{ji}$) leads to a reduction of the number of independent components of C_{ijkl} from 81 to 36. This must hold as a result of the condition of static equilibrium. If it was not the case, the paired stresses along any one axis could not be balanced and this would cause acceleration and rotation. The symmetries lead to only six independent components in σ_{ij} or ε_{ij}, including three diagonals and three off-diagonals. Such symmetry is reflected in the matrix of $\underline{\underline{C}}$, as $C_{ijkl} = C_{jikl} = C_{ijlk} = C_{jilk}$.

- The elastic constant matrix is symmetric, $C_{ijkl} = C_{klij}$. This condition is

satisfied for all elastic bodies, which further reduces the number of independent constants of $\underline{\underline{C}}$ to a maximum of 21.

There is a convention to use reduced notation to represent the elastic constants, due to the above symmetries [51, 53, 54]; this is written as $C_{IJ} \equiv C_{ijkl}$, and I, J go over values 1,2,3...6, since ij and kl are used in pairs. The conversion between the normal indices and the reduced indices is

$$11 \rightarrow 1,\ 22 \rightarrow 2,\ 33 \rightarrow 3,\ 23, 32 \rightarrow 4,\ 31, 13 \rightarrow 5,\ 12, 21 \rightarrow 6. \tag{2.3}$$

Using the tensor-to-matrix notation, Hooke's law (equation 2.2) in reduced notation is rewritten as,

$$\begin{bmatrix} \sigma_{11} \\ \sigma_{22} \\ \sigma_{33} \\ \sigma_{23} \\ \sigma_{31} \\ \sigma_{12} \end{bmatrix} = \begin{bmatrix} C_{11} & C_{12} & C_{13} & C_{14} & C_{15} & C_{16} \\ & C_{22} & C_{23} & C_{24} & C_{25} & C_{26} \\ & & C_{33} & C_{34} & C_{35} & C_{36} \\ & & & C_{44} & C_{45} & C_{46} \\ & & & & C_{55} & C_{56} \\ s & & & & & C_{66} \end{bmatrix} \begin{bmatrix} \varepsilon_{11} \\ \varepsilon_{22} \\ \varepsilon_{33} \\ \varepsilon_{23} \\ \varepsilon_{31} \\ \varepsilon_{12} \end{bmatrix}, \tag{2.4}$$

where the letter s indicates the symmetry of the $\underline{\underline{C}}$ matrix.

Some of the elastic constants are further reducible depending on the structural properties of the material. For example, in isotropic cubic crystals, each of the axes, x_1, x_2 and x_3, are equivalent and so are the planes x_1x_2, x_2x_3 and x_1x_3. This leads to an elastic behaviour where $C_{11} = C_{22} = C_{33}$, $C_{12} = C_{13} = C_{23}$ and $C_{44} = C_{55} = C_{66}$ [54]. The elastic constant matrix for such a medium is reduced to [54],

$$\underline{\underline{C}} = \begin{pmatrix} C_{11} & C_{12} & C_{12} & 0 & 0 & 0 \\ C_{12} & C_{11} & C_{12} & 0 & 0 & 0 \\ C_{12} & C_{12} & C_{11} & 0 & 0 & 0 \\ 0 & 0 & 0 & C_{44} & 0 & 0 \\ 0 & 0 & 0 & 0 & C_{44} & 0 \\ 0 & 0 & 0 & 0 & 0 & C_{44} \end{pmatrix} \tag{2.5}$$

The Lamé parameters, λ (bulk modulus) and μ (shear modulus), historically are used to represent $\underline{\underline{C}}$ for an isotropic material; $C_{12} = \lambda$, $C_{44} = \mu$ and $C_{11} = \lambda + 2\mu$. Hence, Hooke's law (equation 2.2) for an isotropic bulk material can be written as,

$$\sigma_{ij} = \lambda \varepsilon_{kk} \delta_{ij} + 2\mu \varepsilon_{ij}, \tag{2.6}$$

here δ_{ij} is the Kronecker delta, which is equal to 1 if $i = j$, or 0 otherwise.

Hooke's law (equation 2.2 or 2.6) is one of the three essential relations (along with equations 2.7 and 2.8) for deriving the ultrasound wave motion in elastic materials. In the following two sections, waves in unbounded and bounded media will be introduced. Waves travelling in isotropic materials are emphasised since all test samples used in this work are aluminium bar samples with the top 3 mm removed to avoid grain structure issues, and for the wavelengths used, can be taken as isotropic [55].

2.1.2 Bulk waves in elastic media

In this section, ultrasonic harmonic motion (i.e. motion with a time factor of $e^{i\omega t}$, where ω is the angular frequency and t is time) in an unbounded isotropic elastic media is introduced. The derivation reviewed below mainly follows the methods by Rose [3] and Auld [54].

Firstly, the equation of motion is defined by Newton's second law of motion, which states the kinetic relation between an object and the force acting on it. Equation 2.7 gives the law in index notation that is commonly used in elastic-dynamics [3, 53, 54, 56],

$$\sigma_{ij,j} = \rho \ddot{u}_i, \tag{2.7}$$

where $\sigma_{ij,j} = \sum_i \sum_j \frac{\partial \sigma_{ij}}{\partial x_j}$ and $\ddot{u}_i = \sum_i \frac{\partial^2 u_i}{\partial t^2}$. ρ indicates the material density and u is the particle displacement. The material particles undergo harmonic motion, with $\ddot{u} = -k^2 u$, where k is the wavenumber. The ultrasonic deformation is on a small scale such that a linear approximation can be made between the strain and the particle displacement, hence [51],

$$\varepsilon_{ij} = \frac{1}{2}(u_{i,j} + u_{j,i}). \tag{2.8}$$

The sections below introduce first the basic two types of wave motions in an unbounded material; shear and longitudinal motions, and then the bulk wave propagation in an isotropic solid.

Shear and longitudinal motion

By substituting Hooke's law (equation 2.6) and the deformation relation (equation 2.8) into Newton's law (equation 2.7), the wave equation can be obtained, and is given by,

$$(\lambda + \mu) u_{j,ij} + \mu u_{i,jj} = \rho \ddot{u}_i. \tag{2.9}$$

This is the famous Navier's governing equation. For clearer demonstration of the physical quantities (the space, the time and the motion), the following derivation is represented by vector notation. Using the Hamiltonian[1] and Laplacian[2] operators, ∇ and ∇^2, equation 2.9 in vector form is written as,

$$(\lambda + \mu)\nabla(\nabla \cdot \mathbf{u}) + \mu\nabla^2\mathbf{u} = \rho\frac{\partial^2}{\partial t^2}\mathbf{u}. \tag{2.10}$$

To understand the wave motion described by the above governing equation, the method of potentials can be used to find the harmonic solution. $\mathbf{u}$ is decomposed via Helmholtz decomposition,

$$\mathbf{u} = \nabla\phi + \nabla \times \boldsymbol{\psi}, \quad \nabla \cdot \boldsymbol{\psi} = 0, \tag{2.11}$$

where ϕ and $\boldsymbol{\psi}$ are scalar and vector potentials, respectively. By substituting equation 2.11 into equation 2.10 and rearranging, and separating terms in ϕ and $\boldsymbol{\psi}$, one obtains the expression

$$\nabla\left[(\lambda + 2\mu)\nabla^2\phi - \rho\frac{\partial^2}{\partial t^2}\phi\right] + \nabla \times \left[\mu\nabla^2\boldsymbol{\psi} - \rho\frac{\partial^2}{\partial t^2}\boldsymbol{\psi}\right] = 0. \tag{2.12}$$

This can be separated to give,

$$\nabla^2\phi - \frac{1}{c_L^2}\frac{\partial^2}{\partial t^2}\phi = 0, \tag{2.13}$$

$$\nabla^2\boldsymbol{\psi} - \frac{1}{c_T^2}\frac{\partial^2}{\partial t^2}\boldsymbol{\psi} = 0, \tag{2.14}$$

where c_L and c_T are longitudinal and shear velocities, respectively, with $c_L^2 = \dfrac{\lambda + 2\mu}{\rho}$ and $c_T^2 = \dfrac{\mu}{\rho}$. The above equations allow the description of two independent motions; firstly, if $\nabla \times \boldsymbol{\psi} = 0$ and hence $u = \nabla\phi$, then the displacement only has longitudinal (dilatational) motion with a velocity c_L. Similarly, if $\nabla\phi = 0$ and $\mathbf{u} = \nabla \times \boldsymbol{\psi}$, the displacement only has shear motion, with a velocity c_T. These two wavemodes can propagate in an infinite elastic body without any interaction.

---

[1] $\nabla = \dfrac{\partial}{\partial x_1}\vec{i} + \dfrac{\partial}{\partial x_2}\vec{j} + \dfrac{\partial}{\partial x_3}\vec{k}$

[2] $\nabla^2 = \dfrac{\partial^2}{\partial x_1^2} + \dfrac{\partial^2}{\partial x_2^2} + \dfrac{\partial^2}{\partial x_3^2}$

Bulk wave propagation

Unlike the simple isotropic elastic wave behaviour (equation 2.9), waves travelling in anisotropic media is far more complex. The Christoffel equation given below is more general and can be used to study waves propagating in either isotropic or anisotropic bodies [3, 53, 54],

$$(\Gamma_{ij} - \rho c^2 \delta_{ij}) u_j = 0, \tag{2.15}$$

where Γ_{ij} is the Christoffel acoustic tensor and is dependent on the material crystal structure. $\Gamma_{ij} = C_{iklj} n_k n_l$, where n_k and n_l are the direction cosines of the normal to the wavefront. Equation 2.15 can be used to solve the bulk wave propagation in a certain direction. For example, in an isotropic crystal, assuming the plane harmonic waves are travelling in the direction of $[n_1, n_2, n_3]$=[0,0,1] (wavevector $\mathbf{k} = |\mathbf{k}| \cdot [n_1, n_2, n_3]$), the Christoffel tensor is [3, 54],

$$\underline{\underline{\Gamma}} = \begin{pmatrix} C_{44} & 0 & 0 \\ 0 & C_{44} & 0 \\ 0 & 0 & C_{11} \end{pmatrix}. \tag{2.16}$$

Substituting the above Γ-matrix into equation 2.15 enables solution of the particle displacement, which contains a group of three eigen-wavemodes;

1. A horizontally-polarised shear wave (SH shear wave), with speed $c_1 = c_T$. The particle displacement, $\mathbf{u}_1$, is in the direction [1,0,0].

2. A vertically-polarised shear wave (SV shear wave), with speed $c_2 = c_T$. The particle displacement, $\mathbf{u}_2$, is in the direction [0,1,0].

3. A longitudinal bulk wave (L shear wave), with speed $c_3 = c_L$. The particle displacement, $\mathbf{u}_3$, is in the direction [0,0,1].

Figure 2.2 illustrates the wave motions in Cartesian coordinates x_1-x_2-x_3. These waves are the most commonly used ultrasonic waves in ultrasonic NDE and are relevant to the physical phenomena described in chapter 7, where surface breaking defects on the far side of a sample were scanned using the shear bulk wave.

2.1.3 Guided elastic waves

When bulk waves are coupled to the media boundaries, elastic motions with special properties occur. Chapters 5 and 6 focus on detecting material surface breaking

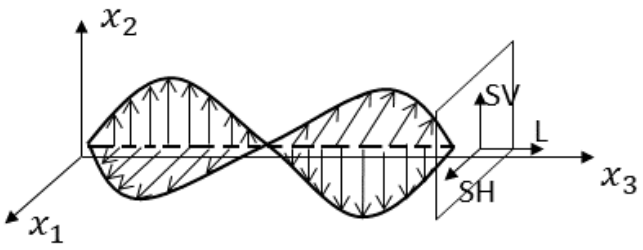

Figure 2.2: Schematic showing the propagation of plane waves in x_3-direction. Three eigenmodes, SH, SV and L, correspond to the three solutions of wavevector in the [1,0,0], [0,1,0] and [0,0,1] directions, respectively.

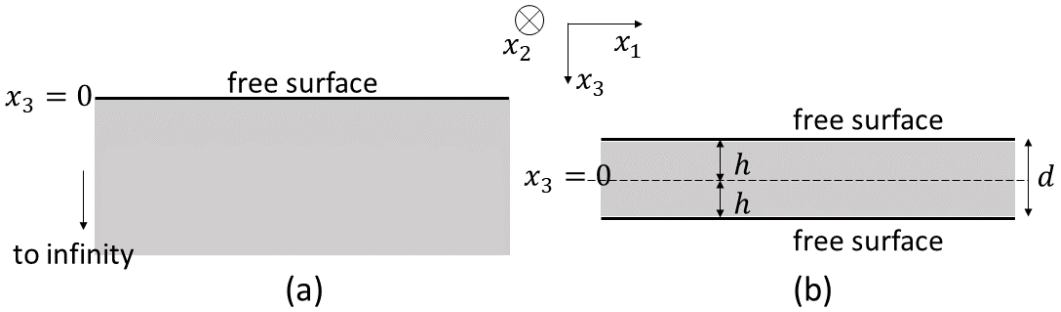

Figure 2.3: Geometries showing samples in which (a) Rayleigh waves or (b) Lamb waves will propagate.

defects using Rayleigh surface waves. Such a wave propagates along the material surface, showing a unique sensitivity to surface discontinuities [57]. The elastic model of the testpiece material is considered as a half-space with one free surface, since the sample thickness is usually much greater than the Rayleigh wavelength used. The coupling of the longitudinal and shear motions at the free surface results in the special Rayleigh motion, which will be detailed in section 2.1.3.

A brief introduction is also given to Lamb waves in section 2.1.3. These waves arise in plate structures when the sample thickness becomes comparable to or less than the ultrasound wavelength. The Rayleigh-Lamb frequency dispersion relation will be introduced, showing the numerical link between the Rayleigh surface wave and Lamb wave when the sample thickness decreases from more than five times the wavelength to zero.

Figures 2.3(a)&(b) demonstrate the geometry of the half-space and the plate problem, respectively. The geometries are described in two dimensions where the sagittal wave is formed only by the displacements in the x_1 and x_3 directions. It is assumed that the size of the solids are infinitely large in the x_2 direction and no particle motion is in the x_2 direction ($u_2 = 0$).

There are several classical methods to solve the above free half-space and plate problems, for example, the method of displacement potentials [3, 53, 56, 57] or the method of partial waves [53, 54]. The following introduces the derivation through the former method. First, the displacement $\mathbf{u}$, for the case of these two-dimensional problems, can be written as,

$$\mathbf{u} = (u_1, 0, u_3). \tag{2.17}$$

The Helmholtz decomposition of the displacement (equation 2.11) states that ϕ and $\boldsymbol{\psi}$ can be expressed as

$$\phi = \phi(x_1, x_3, t), \tag{2.18}$$

$$\boldsymbol{\psi} = (0, \psi_2, 0) \text{ and } \psi_2 = \psi_2(x_1, x_3, t), \tag{2.19}$$

where x_1 and x_3 are the particle locations in the x_1 and x_3 dimensions. Under the two-dimensional framework, $\boldsymbol{\psi}$ is simplified to a one-dimensional plane wave propagation, ψ_2 from here on. The above expressions for ϕ and ψ can be substituted into equation 2.11, allowing the displacements u_1 and u_3 to be written in terms of ϕ and ψ [3, 53],

$$u_1 = \frac{\partial}{\partial x_1}\phi - \frac{\partial}{\partial x_3}\psi, \tag{2.20}$$

$$u_3 = \frac{\partial}{\partial x_1}\psi + \frac{\partial}{\partial x_3}\phi. \tag{2.21}$$

Equations 2.20 and 2.21 are used to find the stress components, σ_{13} and σ_{33}, which are critical for solving the boundary conditions later. This is done by substituting equations 2.8, 2.20 and 2.21 into equation 2.6, to obtain,

$$\sigma_{13} = \mu\left(\frac{\partial^2}{\partial x_1^2}\psi + 2\frac{\partial^2}{\partial x_1 \partial x_3}\phi - \frac{\partial^2}{\partial x_3^2}\psi\right), \tag{2.22}$$

$$\sigma_{33} = \lambda\frac{\partial^2}{\partial x_1^2}\phi + (\lambda + 2\mu)\frac{\partial^2}{\partial x_3^2}\phi + 2\mu\frac{\partial^2}{\partial x_1 \partial x_3}\psi. \tag{2.23}$$

For Rayleigh and Lamb waves, different boundary conditions should be satisfied, leading to different wave properties. The sections below give a brief review for both waves.

Rayleigh surface acoustic waves

Following the geometry given in figure 2.3(a), the boundary condition for Rayleigh waves is,

$$\sigma_{13} = \sigma_{33} = 0 \text{ at } x_3 = 0. \tag{2.24}$$

Recalling equations 2.13 and 2.14, which are the longitudinal (ϕ) and shear (ψ) wave equations in an unbounded isotropic medium, a general harmonic solution for ϕ and ψ can be written as,

$$\phi = Ae^{-kqx_3}e^{i(kx_1-\omega t)}, \tag{2.25}$$

$$\psi = Be^{-ksx_3}e^{i(kx_1-\omega t)}, \tag{2.26}$$

in the x_1-x_3 plane, where $q^2 = 1 - \dfrac{c^2}{c_L^2}$ and $s^2 = 1 - \dfrac{c^2}{c_T^2}$. A and B are unknown constants. Equations 2.25 and 2.26 imply plane waves travelling in the direction of x_1 ([1,0,0]).

To solve for A, B, and find the Rayleigh velocity, c_R, the boundary condition described in equation 2.24 must be used. Substituting equations 2.25 and 2.26 and equations 2.22 and 2.23 into the boundary condition yields,

$$A = i\frac{2s}{1+s^2}B \quad \text{or} \quad -\frac{1+s^2}{i2q}B, \tag{2.27}$$

which holds if,

$$(s^2+1)^2 - 4qs = 0. \tag{2.28}$$

This is the Rayleigh wave characteristic equation. The roots of the equation contain the Rayleigh wave velocity. Equation 2.28 is rewritten by Viktorov [57] as,

$$\eta^6 - 8\eta^4 + 8(3-2\xi^2)\eta^2 + 16(\xi^2-1) = 0, \tag{2.29}$$

where $\eta = c/c_T$ and $\xi = c_T/c_L$. Viktorov also provides an approximate solution of the root, that is,

$$\eta_R \approx \frac{0.87 + 1.12\nu}{1+\nu}, \tag{2.30}$$

where ν is the material Poisson's ratio. According to this approximation, the Rayleigh velocity c_R ($c = c_R$) in an aluminium is about 2906 m/s for $c_T = 3111$ m/s and $\nu = 0.345$ [58].

Another thing of note is the elliptical trajectory of the particle motion with Rayleigh waves. This can be demonstrated from solving the displacement u_1 and

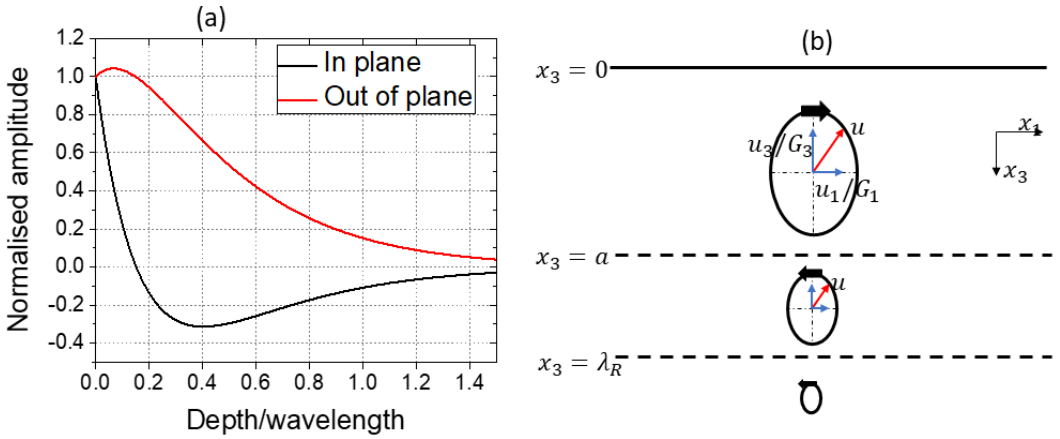

Figure 2.4: Rayleigh wave motion in an aluminium sample. (a) Normalised in-plane (u_1) and out-of-plane (u_3) motions as a function of depth into the sample. (b) The Rayleigh displacement vector at different depths, after [3]. a is the depth when the particle motion reverses from that at the surface.

u_3. Substituting equations 2.25, 2.26 and 2.27 into equations 2.20 and 2.21 gives,

$$\begin{aligned} u_1 &= \frac{kB}{2q}\left[(1+s^2)e^{-kqx_3} - 2qse^{-ksx_3}\right]\cos(kx_1 - \omega t) \\ &\equiv G_1(x_3)\cos(kx_1 - \omega t), \end{aligned} \tag{2.31}$$

$$\begin{aligned} u_3 &= \frac{kB}{2}\left[-(1+s^2)e^{-kqx_3} + 2e^{-ksx_3}\right]\sin(kx_1 - \omega t) \\ &\equiv G_3(x_3)\sin(kx_1 - \omega t). \end{aligned} \tag{2.32}$$

$G_1(x_3)$ and $G_3(x_3)$ are functions that describe the amplitude of the displacements u_1 and u_3, receptively, as x_3 is increased. An elliptical numerical relation can then be identified from manipulating equations 2.31 and 2.32 into [3, 57],

$$\left[\frac{u_1}{G_1(x_3)}\right]^2 + \left[\frac{u_3}{G_3(x_3)}\right]^2 = 1. \tag{2.33}$$

While the original displacements u_1 and u_3 refer to longitudinal and shear motions, respectively, equation 2.33 indicates that the sum of these wavevectors results in an elliptical particle motion. This motion decays into the material thickness, and has a minor axis of $|G_1|$ and a major axis of $|G_3|$. Figure 2.4 demonstrates the motion properties of Rayleigh waves. The displacement amplitude is given in figure 2.4(a), where both u_1 and u_3 values are normalised to their values at the surface ($x_3 = 0$). The in-plane motion refers to u_1 and the out-of-plane motion refers to u_3. Most of the wave motion is concentrated within one wavelength of the surface. This is

a key point that can be used for detecting surface cracks [57] and details will be introduced in section 2.2.2. Figure 2.4(b) shows the Rayleigh elliptical motion at different depths. The orientation of the motion is reversed at a depth, $x_3 = a$, and the motion occurring at deeper thicknesses (more than a wavelength, $x_3 > \lambda_R$) is insignificant, indicated by a much smaller size of the ellipse trajectory of $\mathbf{u}$.

Lamb waves

Following the geometry given in figure 2.3(b), the boundary conditions for Lamb waves are,

$$\sigma_{13} = \sigma_{33} = 0 \quad \text{at } x_3 = \pm h, \tag{2.34}$$

where h equals to half of the sample thickness. Similar to the Rayleigh derivation, expressions for harmonic motion in ϕ and ψ are first suggested,

$$\phi = \Phi(x_3)e^{i(kx_1-\omega t)}, \tag{2.35}$$

$$\psi = \Psi(x_3)e^{i(kx_1-\omega t)}, \tag{2.36}$$

where Φ and Ψ are unknown functions indicating the wave distributions only in the transverse direction (x_3 dependences). Equations 2.35 and 2.36 are plane waves that travel in the x_1 direction ([1,0,0]) and are standing waves in the x_3 direction ([0,0,1]). Recalling the wave equations for ϕ and ψ (equations 2.13 and 2.14), a general solution for Φ and Ψ can be found as [53],

$$\Phi(x_3) = A_1 \sin(k_{3_L} x_3) + A_2 \cos(k_{3_L} x_3), \tag{2.37}$$

$$\Psi(x_3) = B_1 \sin(k_{3_T} x_3) + B_2 \cos(k_{3_T} x_3), \tag{2.38}$$

where k_{3_L} and k_{3_T} are defined as the longitudinal and transverse (shear) wavenumbers in the x_3-direction, and $k_{3_L}^2 = \dfrac{\omega^2}{c_L^2} - k^2$ and $k_{3_T}^2 = \dfrac{\omega^2}{c_T^2} - k^2$. The boundary condition represented in equation 2.34 is satisfied only if Φ and Ψ are of opposite parity [3, 53, 57]. Hence,

$$\Phi(x_3) = A_2 \cos(k_{3_L} x_3 + \gamma), \tag{2.39}$$

$$\Psi(x_3) = B_1 \sin(k_{3_T} x_3 + \gamma), \tag{2.40}$$

where $\gamma = 0$ or $\pi/2$. When $\gamma = 0$, σ_{13} is odd and σ_{33} is even about the axis of $x_3 = 0$ (middle of the x_1-x_3 plane). When $\gamma = \pi/2$, σ_{13} is even and σ_{33} is odd about the axis of $x_3 = 0$. Substituting equations 2.39, 2.40, 2.35 and 2.36 into equations 2.20

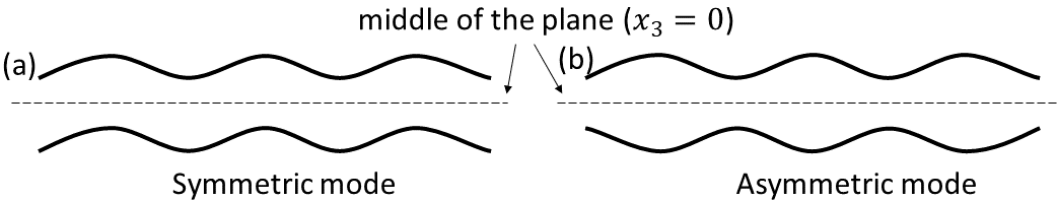

Figure 2.5: Illustration of Lamb wave modes. (a) Symmetric mode (S-mode). (b) Asymmetric mode (A-mode).

and 2.21 yields the results,

$$u_1 = ikA_2 \cos(k_{3_L} x_3 + \gamma) + k_{3_T} B_1 \cos(k_{3_T} x_3 + \gamma), \tag{2.41}$$

$$u_3 = k_{3_T} A_2 \sin(k_{3_L} x_3 + \gamma) + ikB_1 \sin(k_{3_T} x_3 + \gamma). \tag{2.42}$$

Note, the factor $e^{i(kx-\omega t)}$ has been omitted for simplicity. When $\gamma = 0$, the above displacements represent the symmetric mode (S-mode) for Lamb waves which imposes wave motion that is symmetric about $x_3 = 0$, while $\gamma = \pi/2$ leads to the antisymmetric mode (A-mode) that moves anti-symmetrically about the axis $x_3 = 0$ shown in figure 2.5.

Substituting equations 2.39, 2.40, and equations 2.22 and 2.23 into the Lamb wave boundary condition (equation 2.34) gives the Rayleigh-Lamb frequency equations [3, 57],

$$\frac{\tan(k_{3_T})h}{\tan(k_{3_L})h} = -\left[\frac{4k^2 k_{3_T} k_{3_L}}{(k_{3_L}^2 - k^2)^2}\right]^{\pm 1}, \tag{2.43}$$

where '+' is for symmetric modes while '-' is for antisymmetric modes. There are an infinite number of Lamb wave modes that can be supported within a thin plate, and these equations can be used to determine the phase velocity of a Lamb wave at a particular frequency (f) or at the product of the frequency and the sample thickness (fd). The dispersive nature and the complex wave modes make the Lamb wave problem more complicated than that of the bulk wave or the Rayleigh surface wave.

Equation 2.43 can only be solved numerically. One of the typical methods is to use the bi-section method, from giving a proper initial value of phase velocity at a certain value of fd, as described in section 6.3 of reference [3]. Figure 2.6 shows a sample dispersion curve for phase velocity derived in aluminium material. It can be seen that, with increasing fd, the phase velocities of the S_0 and A_0 reach that of the Rayleigh mode, while the other modes have the shear velocity.

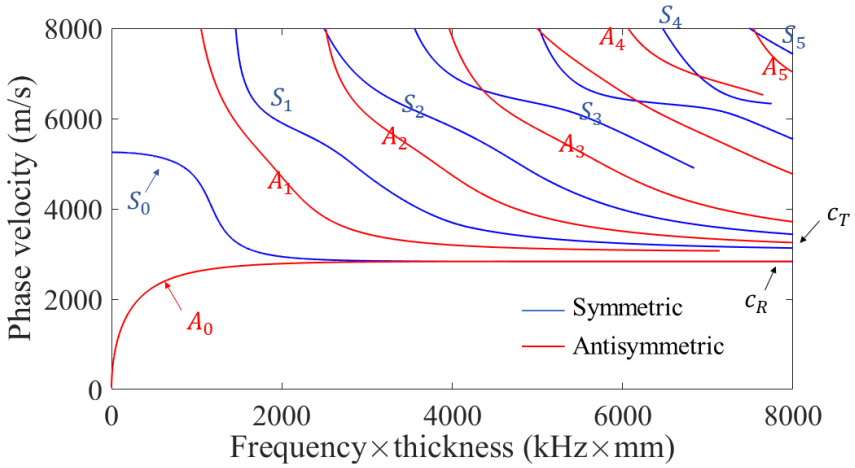

Figure 2.6: Lamb wave dispersion curve showing phase velocity, after [4]. The sample material is a free isotropic aluminium plate.

2.1.4 Ultrasonic wave attenuation

So far, the ultrasonic waves have been assumed to propagate in an idealised media without energy loss of any kind. However, the ultrasound energy will always be reduced throughout the propagation in a standard material. For a plane wave, the wave amplitude after propagating a distance x, A_x, often follows the below relationship to the amplitude A_0 at the initial position [53, 59],

$$A_x = A_0 e^{-\alpha x}, \tag{2.44}$$

where α is the attenuation coefficient in the x-direction. The above equation is determined phenomenologically, which states that the acoustic energy decays exponentially with an increased propagation distance[3].

The analysis of the wave attenuation is complex as it is attributable to multiple aspects, such as the wave property (frequency, polarisation), the material properties, the temperature and so on [53]. In general, two mechanisms are primarily responsible for causing attenuation, they are, *absorption* and *scattering* [59];

1. Absorption is a direct energy conversion from the mechanical energy of the ultrasound into heat. It arises from many mechanisms; for example, dissipation due to the internal molecular friction with the ultrasonic vibration in a solid

[3]The acoustic attenuation contributed by the beam geometric spreading is not included here. This phenomenon comes from the expanding of the acoustic wavefront with the wave propagation, while the total acoustic energy in the medium stays the same. For a spherical wave, the sound intensity I follows an inverse square law with propagation distance R, i.e. $I \propto 1/R^2$. For a cylindrical wave, it follows an inverse law, $I \propto 1/R$ [23].

with a high degree of elastic hysteresis [60]. The heat flow from the hot regions (compressions) to the cooler regions (rarefactions) created by a longitudinal motion can cause opposite elastic deformation due to the thermal-elastic effect, which leads to more ultrasonic attenuation [61]. The absorption is linked closely to the material properties of viscosity, thermal conduction and the hysteresis effect at a microscopic level, etc. The absorption coefficient is defined as α_a.

2. Scattering is when a sound wave encounters discontinuities in a material, such as grain boundaries, dislocations, inclusions or phase changes in a metal. Reflections, refractions and diffractions can occur, causing additional energy diminishing in the propagation direction. The scattering attenuation depends on the geometric shape and the distribution of the scatterers within the material [23]. Unlike the absorption, scattering is not an energy conversion process, but also follows an exponential decay law (equation 2.44) [62]. The scattering coefficient is defined as α_s.

The attenuation coefficients in many liquids and metals are frequency dependent [60, 62, 63]. Both α_a and α_s obey a frequency power law,

$$\alpha_a \propto |f|^m, \tag{2.45}$$

$$\alpha_s \propto |f|^n, \tag{2.46}$$

where m and n are material-dependent. For absorption, α_a increases linearly with frequency ($\alpha_a \propto |f|$) in many metals [53, 60], while it follows a square law ($\alpha_a \propto |f|^2$) in water [64]. The effect in other media of interests, such as human tissues, is often between that in water and metals [65]. Scattering can be categorised into three regimes by comparing the sound wavelength, λ, with the average diameter of the scatterer, $\bar{D}$ [62]; when the wavelength is much greater than the size of the scatterer or $\lambda > 10\bar{D}$, it is Rayleigh scattering, where $\alpha_s \propto |f|^4$. When the wavelength is large but comparable to the scatterer size (e.g. $4\bar{D} < \lambda < 10\bar{D}$), it is stochastic and follows a square rule, $\alpha_s \propto |f|^2$. When the wavelength is comparable or smaller than the scatter ($\lambda < 4\bar{D}$), it is treated as a diffusion phenomenon where α_s is independent of the wave frequency but is inversely proportional to the scatterer diameter, $\alpha_s \propto 1/\bar{D}$. The functional dependence of the attenuation coefficients upon frequency is summarised in table 2.1.

In this work, the material to be tested is aluminium. The grain size of aluminium is of the order of 0.1 mm, while the sound frequency used is less than 1.5 MHz, corresponding to a 2 mm shear wavelength and 4.2 mm longitudinal wave-

Table 2.1: Functional dependence of the attenuation on wave frequency, state of materials (for absorption), and scatterer size (for scattering). m and n are defined in equations 2.45 and 2.46. f is the ultrasonic frequency and $\bar{D}$ indicates the average size of the scatterer.

Absorption, α_a			Scattering, α_s		
dependence	m	materials	dependence	n	range (in solids)
$\|f\|$	$m \approx 1$	metals	$\|f\|^4$	n=4	$\lambda > 10\ \bar{D}$
$\|f\| \sim \|f\|^2$	$1 < m < 2$	human tissues	$\|f\|^2$	n=2	$4\bar{D} < \lambda < 10\bar{D}$
$\|f\|^2$	$m = 2$	water	$1/\bar{D}$	n=0	$\lambda < 4\ \bar{D}$

length or larger. Mason and Maskimin [66, 67] give an estimation of attenuation of shear and longitudinal waves in aluminium and some other solids, in which the attenuation coefficient is fitted as,

$$\alpha = B_1 f + A_4 f^4, \tag{2.47}$$

where B_1 and A_4 are constants. The first linear term is attributed to the absorption due to the elastic hysteresis while the second fourth order power term is contributed by the Rayleigh scattering when the given wavelength is greater than one-third of the grain size. Equation 2.47 represents a case that fits with the description in table 2.1.

Due to the lower frequencies excited by the EMATs in this work (normally less than 1 MHz) and the limited separation between the transmitter and receiver (normally less than 150 mm), the attenuation effect was extremely small in this work for surface crack detection, and hence is not considered in the explanation of the results.

2.2 Ultrasonic waves at interfaces

The reflection and transmission of waves at an inhomogeneity in the medium is essential for ultrasound to be used as a tool for NDT and medical diagnosis. In fact, such wave behaviours are so general and important that they must always be considered when ultrasound moves from one medium to another, including for transducer design and crack detection. This section introduces two topics; firstly, the basics of ultrasound reflection, refraction and mode conversion at an interface. Secondly, the interaction between Rayleigh surface waves and a surface defect. This is a highly relevant topic for the work of chapters 6 and 7 and needs to be reviewed in detail.

2.2.1 Reflection, refraction and mode conversion

Like other waves, ultrasonic waves can experience reflection and refraction at an interface between two media. Such interfaces can be categorised as; fluid-fluid, fluid-solid, vacuum-solid, solid-solid etc., according to the materials of interest. The situation of fluid-fluid is briefly introduced for illustrative purpose as it is the simplest case; only longitudinal waves can propagate within the fluids without any mode conversion at the interface. The basic concepts of wave reflection and transmission are demonstrated by this case. Considering the ultrasound propagation in this work (e.g. the wave is directly induced into a bar sample by EMATs and using surface waves to target the surface defects on both the near and far side surfaces), the scenario of air-solid is of most interest and needs to be well understood. It is approximated as vacuum-solid because only a small amount of ultrasound wave (nearly zero) will leak into the air because of the large acoustic impedance mismatch between the two mediums.

The derivation given below follows by procedure summarised by Cheeke [53]; firstly, define the interface and the coordinate system to be used. Secondly, identify all possible reflected and transmitted waves. Finally, apply the boundary condition at the interface to solve for the unknown parameters, such as the refracted angle, the reflection coefficients, etc,. In this section, a plane pressure wave, p, with unity amplitude in the general form $p = e^{i\mathbf{k}\cdot\mathbf{r}-i\omega t}$ is used; $\mathbf{k}$ is the wavevector that has been defined in section 2.1 and $\mathbf{r}$ denotes the propagation distance of the wave.

For the case of a fluid-fluid interface, assuming a wave is incident from the upper medium ($x_3 > 0$, medium 1) upon the interface at $x_3 = 0$, a reflected wave in medium 1 and a transmitted wave in the lower medium ($x_3 < 0$, medium 2) could occur, demonstrated in figure 2.7. Medium 1 and 2 have acoustic properties described by wavenumbers, k_1, k_2, sound speeds, c_1, c_2 and densities, ρ_1, ρ_2, respectively. p is used to represent a pressure wave. For an incident angle of θ_1, $\mathbf{k}$ is in the direction of $[\sin\theta_1, \cos\theta_1]$, and the incident ($i$), reflected ($r$) and transmitted ($t$) pressure waves can be represented as [68],

$$p_i = e^{ik_1(\sin\theta_1 x_1 - \cos\theta_1 x_3)}, \tag{2.48}$$

$$p_r = R_p e^{ik_1(\sin\theta_1 x_1 + \cos\theta_1 x_3)}, \tag{2.49}$$

$$p_t = T_p e^{ik_2(\sin\theta_2 x_1 - \cos\theta_2 x_3)}. \tag{2.50}$$

Here the time oscillator $e^{-i\omega t}$ has been omitted for simplicity. $k_1 = \omega/c_1$ and $k_2 = \omega/c_2$. R_p and T_p are defined as the pressure reflection and transmission coefficients. To solve for θ_2, R_p and T_p, the boundary conditions must be considered;

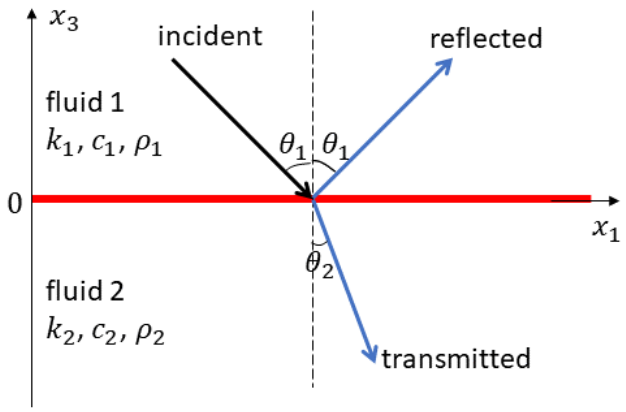

Figure 2.7: Schematic diagram showing a longitudinal wave incident from medium 1 to medium 2. The wave is travelling in x_1-x_3 plane.

first is the conservation of horizontal momentum along the x-axis, which implies that the horizontal wavevector for p_i, p_r and p_t should remain the same, yielding,

$$\frac{\sin\theta_1}{\sin\theta_2} = \frac{c_1}{c_2} = \frac{k_2}{k_1} = \frac{n_2}{n_1}. \tag{2.51}$$

This is the Snell's refraction law, where n_1 and n_2 are the refractive index for medium 1 and medium 2, respectively.

The second boundary condition is the continuity of pressure and velocity at the interface, $x_3 = 0$. The results of applying these conditions are that [53, 68],

$$R_p = T_p - 1, \tag{2.52}$$

$$R_p = (Z_1^* - Z_2^*)/(Z_1^* + Z_2^*), \tag{2.53}$$

$$T_p = 2Z_1^*/(Z_1^* + Z_2^*), \tag{2.54}$$

where $Z_j^* = \rho_j c_j/\cos\theta_j$ is defined as the normal acoustic impedance of the medium j. There are a few special cases;

1. $\theta_1 = 0$, normal incidence. $\theta_2 = 0$, $R_p = (Z_1 - Z_2)/(Z_1 + Z_2)$ and $T_p = 2Z_1/(Z_1 + Z_2)$. $Z = \rho c$ is referred to as the acoustic characteristic impedance of the medium.

2. $\theta_1 = 90°$, parallel incidence. This gives $R_p \to 1$ and $T_p \to 0$.

3. $0 < \theta_1 < 90°$. This scenario needs to consider n as an addition. If $n > 1$, the refraction angle θ_2 is always less than the incident angle θ_1. If $n < 1$, total reflection will occur at a critical angle $\theta^* = \tan^{-1}(\sin n_2/n_1)$. When

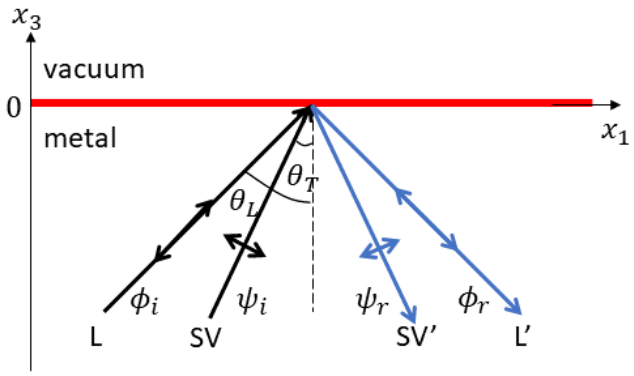

Figure 2.8: The coordinate system of waves in reflection at a boundary of solid-vacuum. The incident waves are implied in back while reflections are in blue. Wave motions are indicated by the double-sided arrows on the wave beams.

$0 < \theta_1 < \theta^*$, the refraction angle increases as the incident angle increases. When $\theta^* \leq \theta_1 < 90°$, it is a total reflection with $|R_p| = 1$, but both reflection p_r and refraction p_t exhibit a phase shift compared to the incident p_i [68].

Another scenario of interest in this work is when the ultrasound is incident onto a metal-air interface. A metal-vacuum interface is used to demonstrate this, as explained in the beginning of this section. Unlike a fluid, that can only support longitudinal waves, metals can support both longitudinal and shear waves, leading to more complicated results at the interface, including mode conversion.

Figure 2.8 demonstrates the wave in reflection at a boundary of metal and vacuum. Recall equation 2.11 in section 2.1.2 where the plane wave is represented in the form of potentials ϕ and $\boldsymbol{\psi}$ as $\mathbf{u} = \nabla\phi + \nabla \times \boldsymbol{\psi}$. ϕ indicates the longitudinal wave and $\boldsymbol{\psi}$ indicates the shear wave. $\boldsymbol{\psi}$ can describe both shear-horizontal and shear-vertical waves. In this section, the former is not considered and $\boldsymbol{\psi}$ is simplified to a scalar form, ψ. This can be applied because the polarisation of the particle displacement of a shear-horizontal wave is perpendicular to the x_1-x_3 plane. No mode conversion would occur in this wavemode at a metal-vacuum interface, similar to the case when longitudinal waves are in liquids, and so this is not considered here. Hence the incident (with subscribe i) and reflected wave (with subscribe r) displacements can be represented as,

$$\mathbf{u}_i = \nabla\phi_i + \nabla \times \psi_i, \tag{2.55}$$

$$\mathbf{u}_r = \nabla\phi_r + \nabla \times \psi_r, \tag{2.56}$$

with wavevectors $\mathbf{k}_i$ and $\mathbf{k}_r$, respectively, where $\mathbf{k}_i = -\mathbf{k}_r$.

Figure 2.8 shows a bulk wave combining both longitudinal (L, ϕ_i) and shear-vertical (SV, ψ_i) components, incident from the metal (lower medium, $x_3 < 0$) to the surface ($x_3 = 0$); a reflected longitudinal (L', ϕ_r) and a reflected shear-vertical (SV', ψ_r) occur. The incident angles for ϕ_i and ψ_i are θ_L and θ_T, respectively, $\theta_L \neq \theta_T$. These hold because the speeds of longitudinal motion and shear motion are different and the horizontal momentum along the x_1-axis must conserved (see discussion for equation 2.51). The corresponding wavevectors for ϕ_i and ψ_i are in the directions [$\sin\theta_L$, $\cos\theta_L$] and [$\sin\theta_T$, $\cos\theta_T$], respectively. Similarly, the wavevectors for ϕ_r and ψ_r are [$\sin\theta_L$, -$\cos\theta_L$] and [$\sin\theta_T$, -$\cos\theta_T$], respectively. The total potentials contributed by both incident and reflected waves can be written as,

$$\phi = \phi_1 e^{ik_L \cos\theta_L x_3} + \phi_2 e^{-ik_L \cos\theta_L x_3}, \tag{2.57}$$

$$\psi = \psi_1 e^{ik_T \cos\theta_T x_3} + \psi_2 e^{-ik_T \cos\theta_T x_3}, \tag{2.58}$$

where $k_L = \omega/c_L$ and $k_T = \omega/c_T$. The oscillation $e^{ikx_1 - i\omega t}$ where $k = k_L \sin\theta_L = k_T \sin\theta_T$, is omitted for simplicity. ϕ_1 and ψ_1 are the incident amplitudes, while ϕ_2 and ψ_2 are for the reflections. To solve for ϕ_2 and ψ_2, the boundary condition of a free surface (both normal and shear stresses at the surface vanish, $\sigma_{13} = \sigma_{33} = 0$ at $x_3 = 0$) needs to be applied. This is analogue to the derivation of the Rayleigh surface wave given in section 2.1.3; by substituting equations 2.57, 2.58 and equations 2.22, 2.23 into the boundary condition, a mathematical relation between the incident amplitude and reflection amplitude can be obtained,

$$\begin{bmatrix} \phi_2 \\ \psi_2 \end{bmatrix} = \begin{bmatrix} R_{LL} & R_{TL} \\ R_{LT} & R_{TT} \end{bmatrix} \begin{bmatrix} \phi_1 \\ \psi_1 \end{bmatrix}. \tag{2.59}$$

Let $[S] = \begin{bmatrix} R_{LL} & R_{TL} \\ R_{LT} & R_{TT} \end{bmatrix}$, which is known as the scattering matrix (S-matrix). Each term has its own physical meaning [68];

1. R_{LL} indicates the reflection coefficient of a longitudinal wave where the incident wave is also a longitudinal wave. Similarly, R_{TT} is the reflection coefficient from a shear to shear wave. The full expressions of R_{LL} and R_{TT} are given by,

$$R_{LL} = R_{TT} = \frac{k_L k_T \cos\theta_L \cos\theta_T - k_T^2 \cos^2\theta_T \cot^2\theta_T}{k_L k_T \cos\theta_L \cos\theta_T + k_T^2 \cos^2\theta_T \cot^2\theta_T}. \tag{2.60}$$

2. R_{TL} is the transformation coefficient from an incident shear wave to a reflected

longitudinal wave. R_{TL} is written as,

$$R_{TL} = \frac{2k_T^2 \cos^2\theta_T \cot\theta_T}{k_L k_T \cos\theta_L \cos\theta_T + k_T^2 \cos^2\theta_T \cot^2\theta_T}. \tag{2.61}$$

3. R_{LT} is the transformation coefficient from an incident longitudinal wave to a reflected shear wave. R_{LT} is written as,

$$R_{LT} = \frac{-2k_L k_T \cos\theta_L \cos\theta_T \cot\theta_T}{k_L k_T \cos\theta_L \cos\theta_T + k_T^2 \cos^2\theta_T \cot^2\theta_T}. \tag{2.62}$$

Having knowledge of the scattering matrix allows for understanding of the whole system, from ultrasonic probing characteristics to testing medium properties. Information provided by such a matrix can therefore work for multiple purposes. One of the promising topics to NDT is to use the S-matrix to accurately size a defect-like structure within a solid [69, 70], including its location, angle and shape. This idea is similar to the principle of using Rayleigh surface wave to characterise surface-breaking defects.

2.2.2 Rayleigh wave interaction with surface-breaking defects

As stated in chapter 1, surface-breaking defects occur in various industrial components, from tight fatigue cracks in aerospace engineering to surface cracks in concrete structures [50, 71, 72, 73, 74, 75, 76]. Quantitative identification of such cracks at an early stage before they develop to the hazardous stage is important.

Some well-known ultrasonic NDT techniques using bulk waves have been developed for bulk/near-surface crack characterisation, such as time-of-flight diffraction (TOFD), as introduced in chapter 1. There are also numerous studies on using Rayleigh surface waves for surface crack NDT. As introduced in section 2.1.3, a Rayleigh wave is a guided elastic wave that propagates along the material surface. The wave displacement, both in the in-plane and the out-of-plane, exponentially decays through the material thickness (see terms $G_1(x_3)$ and $G_3(x_3)$ in equations 2.31 and 2.32), thereby the majority of the wave energy remains highly confined to a thin layer near the free surface during the propagation. It can be seen from figure 2.4 that the depth of this layer is of the order of one Rayleigh wavelength. This unique wave property makes Rayleigh waves a very sensitive tool for finding surface discontinuities. The wave scattering of Rayleigh waves at a surface crack has been used for crack characterisation (the size, shape and orientation) since the 1960s [57].

A Rayleigh wave encountering a surface-breaking defect will experience wave

phenomena including reflection, transmission and mode-conversion [74, 77, 78, 79, 80]. A Rayleigh wave can be considered as a combination of a longitudinal (in-plane) motion and a shear vertical (out-of-plane) motion. When such a wave impinges onto the solid-air interface created by a crack, a portion of the wave will be reflected whilst the rest will be transmitted and mode-converted. Figure 2.9(a) is a schematic showing the problem of simple normal incidence Rayleigh waves on a surface-breaking defect of depth d. f and λ represent the ultrasound frequency and wavelength, respectively, and the incident Rayleigh wave (R_i) is assumed to be broadband, consisting of both smaller wavelength components (high f, small λ) and larger components (low f, large λ). The penetration depth of the high f component in the figure is smaller than the crack depth, whereas that of the low f is deeper than the crack depth. For simpler interpretation, the frequency of the high f incident wave is assumed to be high enough that the wave can be approximated as propagating along the surface ($\lambda \ll d$), while that of the low f incident wave is assumed small enough that the penetration depth is much larger than the crack depth ($\lambda \gg d$). Incident waves with any other frequency/wavelength components will follow a propagation behaviour between the above two cases.

To demonstrate the wave phenomena, the interaction between the incident Rayleigh wave (R_i-wave) and the crack is considered from two spatial aspects: the backscattered field and the forward-scattered field, demonstrated in figures 2.9(b) and (c), respectively. In the backscattered field, the high frequency component and the portion of the low frequency energy near the surface can first be considered by using the ray-tracing approximation, where the wave is taken as travelling along the sample surfaces. At the crack mouth, these waves can be reflected, giving R_{r1}. The wave can also be transmitted down the open face of the crack. At the crack tip, a second reflection can occur back towards the crack mouth, labelled R_{r2}. Further reflections between crack mouth and tip can occur, with increasingly small amplitudes [80]. Some of the energy contained in the lower frequency wave may reflect from the crack face (R_{r3}), while a portion will be transmitted directly underneath the defect into the forward-scattered field. Each time the wave is reflected, mode conversion may occur. In experiments, a significant mode conversion into a surface-skimming longitudinal wave is observed from the crack mouth (R_{h1}, shown by green arrow and circle). At the crack tip, mode conversion into bulk wave modes is found (R_{h2}) [80, 81, 82].

In the forward-scattered field (figure 2.9(c)), multiple transmitted waves can again be seen. Following again the ray-tracing approximation, wave R_{r2} can be transmitted around the bottom of the crack and propagates along the crack face,

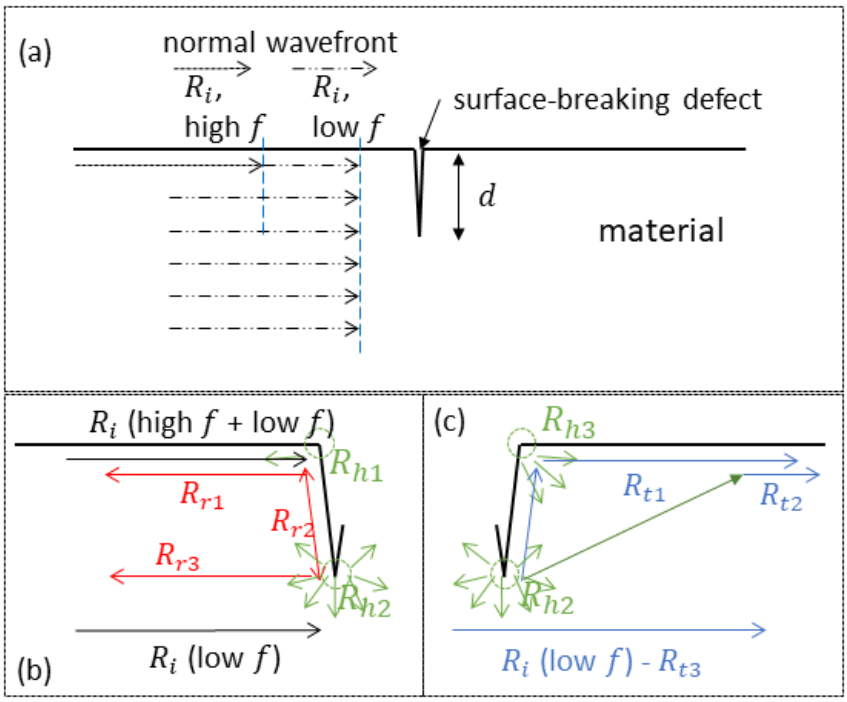

Figure 2.9: (a) Schematic of a Rayleigh wave interaction with a surface-breaking defect. A plane Rayleigh wave is normally incident onto the edge crack. The crack depth is d and the incident Rayleigh wave (R_i) contains various wavelength components, including $\lambda \ll d$ (square dot line near the surface) to $\lambda \gg d$ (long dash dot dot lines from surface to depths larger than d). (b) The back-scattered field. (c) The forward-scattered field. The ray paths for high-frequency R_i and low-frequency R_i are distinguished.

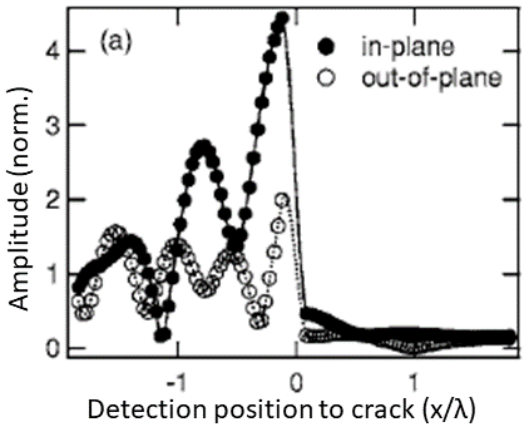

Figure 2.10: The near-field enhancement effect of Rayleigh wave characterising surface-breaking defects, after [5].

around the mouth opening, and along the sample surface, giving R_{t1}. This will arrive at a later time than the directly transmitted low frequency wave, R_{t3}. For waves which have undergone mode conversion at the crack tip, a portion of the wave may travel through the bulk of the sample and be reflected or mode-converted back into a Rayleigh wave when it reaches the top surface (R_{t2}). The arrival time of this wave will show a dependence on the position at which it is detected, and the geometry of the crack [82]. It should be noted that only a small amount of mode conversion may occur at the crack mouth, illustrated by the green circle.

Near-field enhancement effect

A near-field enhancement effect has been observed and studied by a few researchers [5, 6, 83, 84]. It states that the detected Rayleigh signal can be drastically increased when the detector is in the proximity of the surface crack.

Figure 2.10 demonstrates the Rayleigh wave near-field enhancement effect. This is the result from a finite element analysis where a wideband Rayleigh wave signal centred at 590 kHz interacted with a 3 mm deep surface crack. Rayleigh velocities at various detection points were collected. It is clearly shown that the amplitude of the reflected signal gives an overall trend of enhancement as the detection position was moved closer to the crack. Both in-plane and out-of-plane components show similar results, while the enhancement of the latter was smaller. There are also some minima occurring among the maxima. This can be explained by wave interference between the incident Rayleigh and the reflected and mode converted waves, such as the surface skimming longitudinal waves at the crack opening mouth, caus-

ing a significant amplitude enhancement when a constructive interference is formed, or a signal cancellation when a deconstructive interference is formed.

The enhancement factor of the incident wave amplitude can be as high as to 2∼5 times, depending on crack geometry [5]. This effect can be used as a powerful tool to identify the presence of a surface crack [50], or even provide information about the crack geometry [82, 85, 86], including the crack depth, length and inclined angle.

Quantitative study on crack geometry

The propagation properties of Rayleigh waves provide a method of quantitative NDE for surface-breaking defects. This is an inverse problem using the scattering of Rayleigh wave to extract information about the crack geometry. One of the established methods to estimate the crack depth is to measure the delayed arrival-time of the Rayleigh wave that is diffracted from the crack tip [73, 74, 87]. The crack depth can be calculated from comparing signals with a reference signal taken in the absence of the crack. This is similar to TOFD but using a Rayleigh surface wave instead. The small signal-to-noise ratio of the desired diffracted signal can be an issue for signal processing. This method can also be problematic for shallow surface cracks when the time resolution is limited [73].

Other techniques are mostly founded on the physical principle that the Rayleigh wave reflection/transmission is frequency dependent, as explained above. Numerous studies have been undertaken to quantify the Rayleigh transmission and reflection when surface cracks vary from shallow to deep. Different methods, from theoretical predictions to experimental validations, were employed. For example, Achenbach et al. [88] analytically predicted the R-wave reflection and transmission for backscattered and forward-scattered fields respectively by considering the contribution from each eigen-wavemode. Numerical simulations, such as finite difference method [89, 90] or finite element analysis [80, 81], were used to model the Rayleigh-crack system, enabling the relation between the wave transmission/reflection and the crack depth to be studied. Also, many experiments have been done to validate the analytical or numerically simulated results, including using wedge piezoelectric transducers to generate Rayleigh waves [6, 73, 89], validating via laser-based ultrasound systems [78] or EMAT-based systems [50, 80, 85]. All of the studies show that the Rayleigh transmission decreases with increasing crack depth, while the reflection increases. An example can be found in figure 2.11. It should be noted that the use of such transmission/reflection curves with varying crack depth for crack characterisation is more suitable when $d/\lambda < 1$ [88, 89]; for deeper cracks, most of the wave energy will be blocked, thereby the transmission will show a constant low

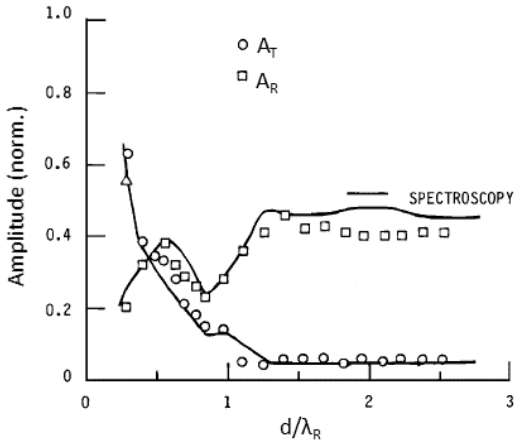

Figure 2.11: Rayleigh wave transmission/reflection curve, after [6]. A_T refers to the transmission coefficient and A_R refers to the reflection coefficient. The wedge transducer result (discrete points) was compared to the ultrasonic spectroscopy (solid lines).

value and reflection can tend towards a constant value.

Methods using spectrum analysis in the frequency domain were also investigated to extract crack information. Different ultrasound systems can generate/detect Rayleigh waves with various frequency properties, for example a pulsed-laser or EMAT based system can be designed to give a broadband wave [78, 81], while the wedge piezoelectric transducer systems are more narrowband [73]. Because a crack will effectively block the high frequency components and partially block lower frequencies, the spectrum of the transmitted or reflected signals in the far field differs significantly from that of the original incident signal. Longo et al. [91] modelled the crack as a low-pass filter and determined the crack depth by relating it to the cut-off frequency of this filter. Masserey et al. [73] used the shift of the central frequency in the transmission spectrum to estimate the crack depth. Edwards et al. [92] used linear fitting to the fast Fourier Transform (FFT) of the transmitted signal. A cut-off frequency defined as being at the zero-crossing of the x-axis was identified to be related to the crack depth. Complex geometries, such as angled or branched cracking, can also be characterised by the laser-EMAT or the pitch-catch EMAT systems [82, 86].

2.3 Common methods of ultrasonic transduction

2.3.1 Conventional piezoelectric transducers

Ultrasonic transducers working through the mechanism of piezoelectricity are by far the most common technique in research and industry areas, including ultrasonic NDT. The piezoelectric phenomenon was first described by Curie brothers and is reversible; the direct piezoelectric effect explains that in certain materials, an electric charge can be generated in response to an applied mechanical stress. Such an effect has been widely applied for designing of acoustic sensors/receivers [53, 93]. The reverse piezoelectric effect, where deformation of these materials could occur when an electrical field is applied, is used for generation. Many acoustic actuators/emitters work principally on the latter reverse effect [53, 93].

For a piezoelectric material, a common approach to describe the electromechanical coupling through the piezoelectric effect is through a physics framework, briefly introduced below. The behaviour can be described by [93, 94];

$$P_i = d_{ij}\sigma_j. \tag{2.63}$$

The above equation is given in matrix notation, where the physical quantities of electrical polarisation, $\mathbf{P}$, and mechanical stress, $\boldsymbol{\sigma}$, are written in the tensor forms, P_i and σ_j. P_i is a first rank tensor where i goes over $i = 1, 2, 3$, indicating a three-dimensional polarisation through the Cartesian coordinate system. σ_j is a second rank tensor but j goes from 1 to 6 for the simplified stress indices, as explained in section 2.1. The piezoelectric coefficient tensor is defined as d_{ij}, where the first subscript demonstrates the direction of the induced or the applied electric field, and the second subscript indicates the direction of the applied stress.

Depending on the orientation of the electrical field and the resultant mechanical stress (or vice-versa), the piezoelectric coefficient, d_{ij}, can be categorised into four groups to describe the material piezoelectric behaviour [93];

1. Coefficients d_{11}, d_{22} and d_{33} (three in total) to characterise the longitudinal piezoelectric effect or L-effect. This refers to the piezoelectrically induced electrical moment whose direction of polarisation is in the same direction as the applied stress (normal to the surface). Figure 2.12(a) exemplifies the piezoelectric phenomenon represented by d_{33}.

2. Coefficients d_{12}, d_{13}, d_{21}, d_{23}, d_{31} and d_{32} (six in total) to characterise the transverse piezoelectric effect or T-effect. This refers to the induced electrical moment whose direction of polarisation is perpendicular to the applied

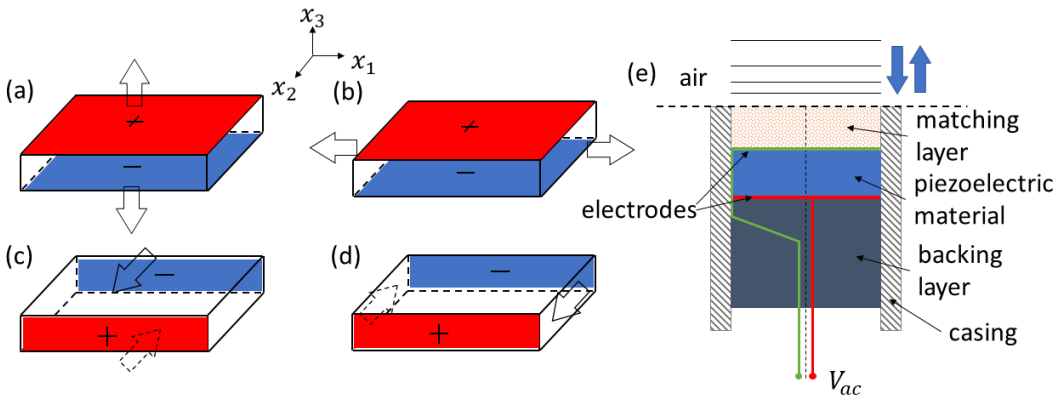

Figure 2.12: Several piezoelectric coefficients are illustrated from (a) to (d) upon a piezoelectric cut. The electrical response of the cut, indicated by a pair of electrodes to show the induced electrical field, is the result of applied mechanical stress, indicated by a pair of arrows acting on the corresponding surfaces. The polarisation of the stress is indicated by the arrow direction. (a) d_{33}-mode. (b) d_{31}-mode. (c) d_{24}-mode. (d) d_{26}-mode. (e) demonstrates the sandwich structure of a classical single crystal piezoelectric transducer.

stress (normal to the surface). Figure 2.12(b) exemplifies the piezoelectric phenomenon represented by d_{31}.

3. Coefficients d_{14}, d_{25} and d_{36} (three in total) to characterise the longitudinal shear piezoelectric effect or L_S-effect. This is when a tangential stress is applied, and a longitudinal electrical polarisation can be induced which is perpendicular to the original stress direction. Figure 2.12(c) exemplifies the piezoelectric phenomenon represented by d_{24}.

4. The rest of the coefficients, d_{15}, d_{16}, d_{24}, d_{26}, d_{34} and d_{35} (six in total), to characterise the transverse shear piezoelectric effect or T_S-effect. Similarly, this effect corresponds to the application of a tangential stress with a corresponding transverse electrical polarisation. Figure 2.12(d) exemplifies the piezoelectric phenomenon represented by d_{26}.

There are 18 individual components in total in the tensor d_{ij}, however, the number of independent components can be much smaller in common practical piezoelectric materials, such as quartz (2), Rochelle salt (RS) (8), the family of barium titanate (BaTi) or the family of lead zirconate titanate (PZT), etc. [94].

In practice, a single piezoelectric element is not able to generate or detect the sound vibration directly into or from either fluids or solids very efficiently. This is due to the large mismatch of the acoustic impedance between the piezoelectric

material ($\sim 10^1$ MRayl) and other media, especially gas ($\sim 10^{-4}$ MRayl), hence significant energy loss occurs [58]. To reduce the loss, an additional impedance 'matching' layer is used before the sound is directed into the target media. The acoustic impedance of the matching layer is optimised to the geometric mean value of that of the neighbouring media, $\sqrt{Z_1 Z_2}$ [95], though this is hard to achieve practically. Some composites with porous structures are used as common matching layer materials [96]. Designing of multiple matching layers can also be an option to improve the transduction efficiency [96, 97]. This, however, could increase the fabrication complexity undesirably. A typical structure of a basic piezoelectric module is shown in figure 2.12(e). A three-layer sandwich structure is presented, where the piezoelectric material is arranged between a matching layer and a backing layer. The generated sound wave is expected to propagate unidirectionally to the air (or vice versa) due to the presence of the backing layer, which is designed for improving the mechanical damping, reducing the waveform distortion and energy loss. Another important consideration when optimising the transducer structure is to ensure that the thickness of the matching layer is equal to a quarter of the wavelength [23, 97]. This is to form constructive interference for waves that have bounced back and forwards in the layer, so they are in-phase and can be superposed at the boundaries. This method will also decrease the transducer bandwidth.

Many NDT applications use ultrasound for flaw detection in solid materials, with piezoelectric transducers used as the sound emitters/receivers. A layer of couplant is normally used to reduce the transduction loss from piezoelectric transducer to the solid material. One way to couple the transducer and the test sample is to use an immersion test, since water is a natural medium for effective transferring of acoustic waves from transducer to sample [98, 99, 100]. The other way is to use an extra layer of couplant gel (or dry couplant). This is also to overcome the issue of impedance mismatch between the air and the materials, so waves can be transmitted into the sample or vice versa more efficiently. It is the use of the couplant that hinders the development of fast, repeatable UT for large field inspection, or application in harsh industrial environments.

Generation or reception of surface acoustic waves (SAWs), such as Rayleigh or Lamb waves, for detecting surface/near surface defects can also use standard piezoelectric transducers, with an additional use of a wedge between transducer and sample [7, 101, 102]. Figure 2.13 is a schematic digram showing a pair of transducers arranged in pitch-catch mode for Rayleigh wave generation and detection. The transducer configuration is known as the angle-beam wedge transducer, working on the principle of wave refraction and mode conversion. The transducer positioned on

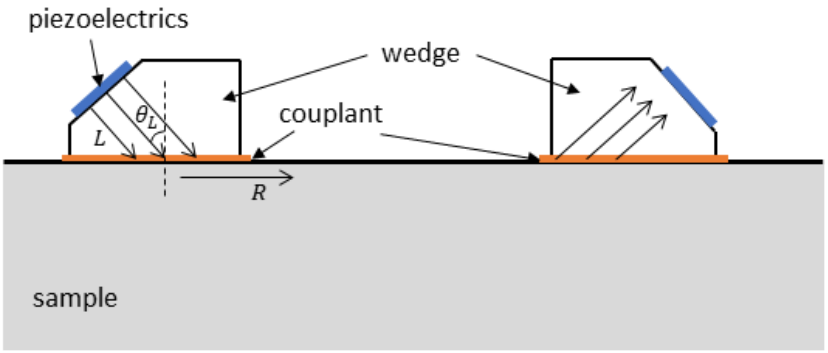

Figure 2.13: Geometry of Rayleigh wave generation and detection using angle-beam wedge transducers, after [7]. L refers to longitudinal wave and R refers to Rayleigh wave. Couplant gel is also used for increasing the transferring efficiency.

the left is the wave emitter while the right one is the receiver. During generation, a longitudinal bulk wave is first generated and propagates into the medium of the wedge, before obliquely impinging onto the interface between the wedge and the sample surface. Mode conversion will then occur with both longitudinal and shear waves occurring at the boundary, as explained in section 2.1.2. If the incident angle θ_L is properly chosen, both bulk waves will propagate along the surface (critical angle for total reflection, as explained in section 2.2.1), leading to the Rayleigh wave. The wave reception through the wedge transducer can be simplified to a reciprocal process to the generation process, but other issues such as beam spreading in the wedge or leaky waves need to be considered [7].

2.3.2 Flexural mode ultrasonic transducers

The development of ultrasonic transducers is now benefiting from improvements to the technology of micro-electromechanical systems (MEMS) and new material science. There are trends of producing transducers which are miniaturised, thin-filmed, electronically-integrated and low-power consuming [53, 103, 104, 105, 106].

One of the most successful subjects of research and development has to be the micro-machined ultrasonic transducers (MUTs). The MUTs family includes capacitive micro-machined ultrasonic transducers (cMUTs) and pieozoelectric micro-machined ultrasonic transducers (pMUTs) [107, 108, 109, 110]. Unlike the traditional piezoelectric transducers where the acoustic excitation happens within the piezoelectric layer, cMUTs and pMUTs generate ultrasound through the vibration of a thin-film structure that is directly coupled to the fluids. Figure 2.14 is a schematic diagram showing a basic cell of cMUTs [107]. It can be considered as a capacitor

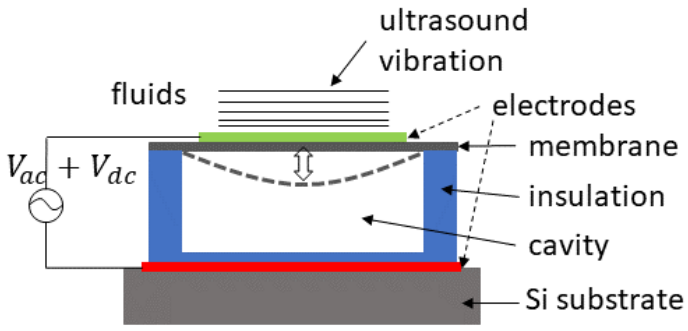

Figure 2.14: Typical cross-section view of a basic cell of cMUTs.

cell which consists of a top metallised suspended membrane and a bottom rigid metallised Si substrate. By applying a bias voltage (V_{dc}) between the electrodes, the membrane will deflect into the cavity as a result of the attractive electrostatic forces towards the substrate. By superimposing an AC voltage (V_{ac}), ultrasound can then be generated via the subsequent mechanical vibration of the membrane. The transducer bandwidth is closely related to the resonant frequency of the flexural mode of the membrane. A pMUT cell transfers the energy in a similar way but the above membrane is replaced by a piezoelectric membrane. The vibration of the membrane is caused by the lateral strain induced by the piezoelectric effect [109, 110].

The mechanical impedance of the thin-membrane is much lower than its acoustic impedance, hence the energy transformation of cMUTs and pMUTs is higher than that of conventional piezoelectric transducers. A wider bandwidth can also be provided due to the absence of the matching layer [107, 109]. Modern microfabrication techniques are enabling these MUTs to be good candidates for phased array imaging in medical diagnostics [105, 111]. However, some of their intrinsic properties, such as the requirement of the large bias field for cMUTs or the fragile membrane structure, can hinder NDT application in hostile environments, such as at high pressure.

An alternative air-coupled flexural design has been investigated for gas flow measurement under elevated pressure levels [112, 113, 114]. In there, the piezoelectric ceramic was bonded onto a metal cap, working as the actuator to cause resonant vibration of the front surface and so ultrasound can be generated. The long waveform caused by the cap vibration can be an issue, but the ceramic can be protected under those high pressure working conditions.

Many attempts have been made to identify different piezoelectric materials for harsh condition NDT applications [115, 116]. Bernhard et al., [116] investigated various candidates, including both single-crystals and ceramics. The materials were

exposed to an environment that was up to 2000°, and/or under a test of nuclear radiation. Aluminium Nitrate (AlN) was concluded as a viable candidate to survive these harsh environments.

2.3.3 Laser-based ultrasound

Some other methods, such as laser ultrasound or EMATs, for ultrasound generation and detection are gaining more interest in the field of NDT. These are both non-contact techniques and show great potential for implementing repeatable scans when compared to conventional piezoelectric methods [11, 117]. While EMATs will be introduced in the next chapter in detail as they are the focus of this work, this section gives a brief introduction to laser ultrasound.

Generation of ultrasound via laser irradiation in a metal can be categorised into two regimes; the thermoelastic regime and the ablation regime [117]. The localised heating of the sample surface by a laser pulse can cause significant, rapid heating over a small region. Thermal expansion occurs during the heat diffusion, giving rise to elastic waves as a result of the associated strains. When the applied laser power density is increased and reaches a threshold, the ablation of the sample surface occurs. A plasma is formed during the material melting phase, with an extra expansion (normal to the sample surface) causing ultrasound generation. Applications at higher power densities within the ablative regime are not optimal as the technique is no longer nondestructive.

Ultrasound generation and detection via lasers are through different principles. This means a separate laser detector is required to capture the sound vibration in the system. Several laser measuring systems, such as the Michelson interferometer, which works on a polished surface, Doppler vibrometer (insensitive to very small disturbances) or Fabry-Perot interferometer, have been widely applied in ultrasonic detection over the past few decades [118].

The lift-off work on the single coil presented in chapter 5 employed a two-wave mixing interferometer (Intelligent Optical Systems (IOS), AIR-1550-TWM) to receive the EMAT generated surface waves. This equipment requires scattered light for detection of ultrasound, hence a sample with rough surfaces can be used. Also, the workable bandwidth of the IOS is from 0 to 125 MHz, allowing a relatively accurate measurement under the frequency variation designed in this work. The Rayleigh surface displacement in the out-of-plane direction can be measured. This system is more sensitive than the Doppler velocity vibrometer which is more commonly used in NDT. Figure 2.15 is a schematic showing the basic units of the IOS interferometer [119]. Two coherent light beams, a plane-wave reference beam

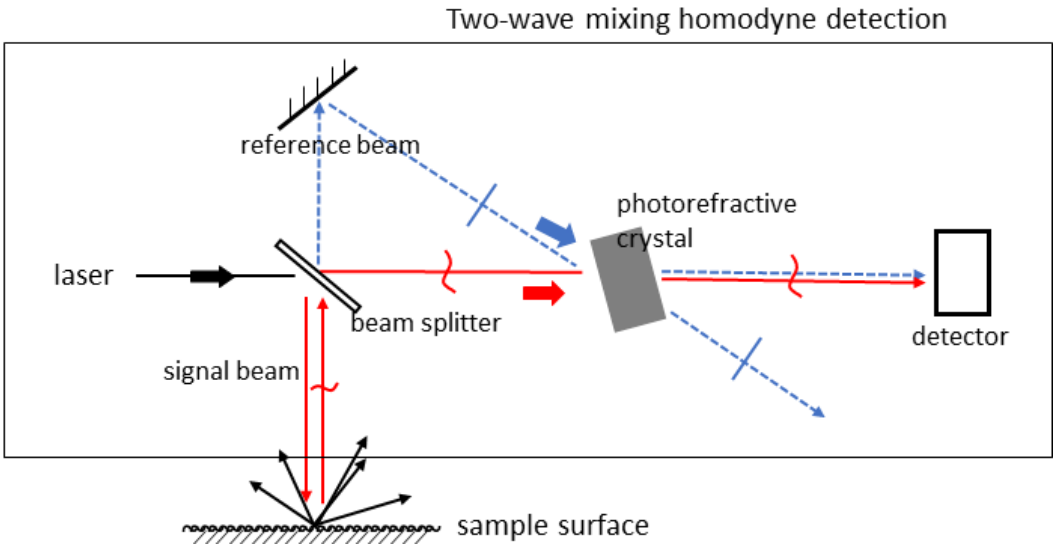

Figure 2.15: A basic schematic showing the two-wave mixing interferometer as an ultrasonic detector.

(blue dashed line) and a signal beam (red solid line) are produced by a common laser source via a beam splitter. The two beams are mixed within a photorefractive crystal (PRC); the signal beam is first directed towards the sample surface and hence a reflection carrying the information about the vibrating sample surface can be combined with the reference beam in the PRC. The PRC acts as an adaptive beam splitter to diffract the reference beam, allowing a perfect wavefront matching between the transmitted signal beam and the diffracted reference beam for coherent detection [119, 120, 121]. Any of the reference beam that hasn't been diffracted correctly by the PRC will be wasted.

Laser ultrasound offers unique non-contact benefits, but it also brings many safety concerns. Lab operation is generally required for appropriate implementation of the safety procedures. Some high power lasers can only work in sealed chambers, which hinders its wide application in industry. Also, laser ultrasonics is generally more costly than other methods.

Chapter 3

Electromagnetic acoustic transducers (EMATs) introduction

EMATs are an established non-contact method in the field of ultrasonic NDE, and are also the major topic of this work. So far, there are a small number of major EMAT solution providers on the market, including Innerspec, Olympus, ROSEN Group, Sonomatic and Sonemat. Most of these focus on producing simple, standard designs of EMAT, but there are many bespoke solutions that are possible using this type of transducer. Advanced NDT systems using EMAT techniques are presented here.

This chapter reviews the operation of EMATs. The first part introduces the EMAT acoustic principles, including the three generation mechanisms and the receiving mechanism. The second part introduces the EMAT electronics, mainly focusing on the electrical characteristics of the system comprised of the EMAT driver, EMAT and the testpiece material. The last part reviews EMAT design for different ultrasonic wavemodes, from conventional single-coil EMATs to the state of the art array designs of EMATs.

3.1 Basic EMAT configuration

EMATs are a type of transducer that can transform electrical energy to elastic wave motion inside a material. An EMAT typically consists of a coil to introduce a dynamic magnetic field into the material, and a permanent magnet (or electro-magnet) to introduce a static biasing magnetic field. Figure 3.1 shows a schematic

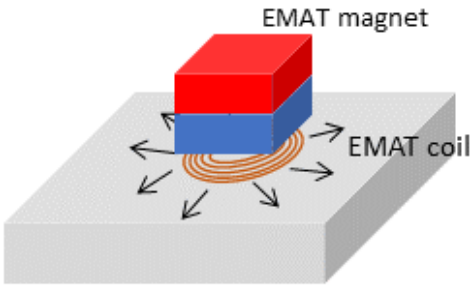

Figure 3.1: Sketch of basic EMAT configuration; a magnet and a coil.

of the basic EMAT configuration. A flat spiral coil is used to generate ultrasound omni-directionally. More details on this design can be found in section 3.4.1. The electromagnetic coupling between the EMAT and the material under test are detailed in the following section.

3.2 Acoustic mechanisms

EMATs can generate ultrasound via three different mechanisms, depending on sample properties; Lorentz force, magnetisation, and/or magnetostriction mechanisms [11, 122]. The Lorenz force can occur in all electrically conductive materials, whereas the latter two mechanisms only arise in magnetic materials.

The understanding of the EMAT-material electromagnetic interaction is introduced here. Maxwell's equations are the governing equations of this process, as given here in the differential form [123],

$$\nabla \cdot \mathbf{D} = \rho_f, \tag{3.1}$$

$$\nabla \cdot \mathbf{B} = 0, \tag{3.2}$$

$$\nabla \times \mathbf{E} = -\frac{\partial \mathbf{B}}{\partial t}, \tag{3.3}$$

$$\nabla \times \mathbf{H} = \mathbf{J} + \frac{\partial \mathbf{D}}{\partial t}. \tag{3.4}$$

Here $\mathbf{D}$ denotes the electric flux density, ρ_f the free charge density, $\mathbf{B}$ the magnetic flux density, $\mathbf{E}$ the electrical field, $\mathbf{H}$ the magnetic field, $\mathbf{J}$ the conduction current density and $\mathbf{J}_D = \dfrac{\partial \mathbf{D}}{\partial t}$ the displacement current density. The constitutive relations

between **B** and **H** and **D** and **E** are

$$\mathbf{B} = \mu\mathbf{H}, \tag{3.5}$$

$$\mathbf{D} = \epsilon\mathbf{E}, \tag{3.6}$$

where μ and ϵ are the material permeability and permittivity respectively. The final essential equation is Ohm's law, relating **J** and **E** via

$$\mathbf{J} = \sigma\mathbf{E}, \tag{3.7}$$

where σ is the material conductivity.

3.2.1 Electromagnetic skin depth

For the inductive coil wire which forms part of an EMAT, which is driven by a dynamic (time-varying) current $\mathbf{I}_c$, there will be an associated dynamic magnetic field, $\mathbf{H}_c$ surrounding it, as defined by Ampère's law. When this AC driven coil is in close proximity to a conductive material ($\sigma > 0$), this time-varying magnetic field (or magnetic flux, $\mathbf{B}_c$) will penetrate into the material, causing a secondary flow of electric charge (known as an eddy current) within the material, as defined by Faraday's law (equation 3.3). At the material surface (the interface between the air and the material), the eddy current is out-of-phase to the primary driving current and will generate a secondary magnetic field which opposes the magnetic field that creates it, as stated by Lenz's law.

The mutual cancellation between the eddy current (or the secondary varying magnetic field) and the coil driving current (or the primary varying magnetic field) leads to the rapid fall-off of the electromagnetic (EM) fields as they penetrate to larger depths within the material. The eddy current is therefore constrained into a thin layer below the material surface. This phenomenon is known as the electromagnetic skin effect.

Assuming that the coil current is oscillating at an regular frequency ω ($\omega = 2\pi f$), and that f is far below 100 MHz in most EMAT applications [11], the displacement current, $\mathbf{J}_D$, and the conduction current, $\mathbf{J}_c$, can be compared as $\frac{|\mathbf{J}_D|}{|\mathbf{J}_c|} = \omega\frac{\epsilon}{\sigma}$ [123], where in conductive metals, the term $\frac{\epsilon}{\sigma}$ is of the order of 10^{-17} [124]. $\mathbf{J}_D$ in equation 3.4 is hence neglected in this work. The EM fields induced by the EMAT coil in the material then can be described by the updated

Maxwell's equations,

$$\nabla \cdot \mathbf{D} = 0, \tag{3.8}$$

$$\nabla \cdot \mathbf{B} = 0, \tag{3.9}$$

$$\nabla \times \mathbf{E} = -\frac{\partial \mathbf{B}}{\partial t}, \tag{3.10}$$

$$\nabla \times \mathbf{H} = \mathbf{J}_c. \tag{3.11}$$

Here, the net charge density (ρ_f) in equation 3.8 is zero. This holds because the material is electrically neutral on a macroscopic level, as the electron density matches the ion density on the microscopic level.

The constitutive relationships (equations 3.5 and 3.6) and Ohm's law (equation 3.7) are substituted into equations 3.10 and 3.11 to find the **E**-field. Manipulations are given below based on [123];

$$\begin{aligned} \nabla \times \mathbf{E} &= -\mu \frac{\partial \mathbf{H}}{\partial t} \\ \nabla \times (\nabla \times \mathbf{E}) &= -\mu \frac{\partial}{\partial t}(\nabla \times \mathbf{H}). \end{aligned} \tag{3.12}$$

The right hand side of the above equation can be rewritten using the electric field from Ampère's equation (equation 3.11). The left hand side can be represented as $\nabla \times (\nabla \times \mathbf{E}) = -\nabla^2 \mathbf{E} + \nabla(\nabla \cdot \mathbf{E})$ through the vector identity. This can be further simplified to $-\nabla^2 \mathbf{E}$, as $\nabla \cdot \mathbf{E} = \frac{\rho_f}{\epsilon} = 0$, as defined by Gauss' law (equation 3.8). Equation 3.12 hence is rewritten as

$$\nabla^2 \mathbf{E} - \mu\sigma \frac{\partial \mathbf{E}}{\partial t} = 0. \tag{3.13}$$

The **H**-field equation can be derived using a similar procedure, giving

$$\nabla^2 \mathbf{H} - \mu\sigma \frac{\partial \mathbf{H}}{\partial t} = 0. \tag{3.14}$$

By considering a plane wave propagating in the z-direction (the direction through the material thickness), the Laplacian operator can be simplified to $\nabla^2 = \frac{\partial^2}{\partial z^2}$. Solutions to equation 3.13 and 3.14 can then be easily found as [123]

$$\mathbf{E}_z(z,t) = \tilde{E}_{z_0} e^{i\omega t} e^{-\frac{z}{\delta}} e^{-i\frac{z}{\delta}}, \tag{3.15}$$

$$\mathbf{H}_z(z,t) = \tilde{H}_{z_0} e^{i\omega t} e^{-\frac{z}{\delta}} e^{-i\frac{z}{\delta}}, \tag{3.16}$$

where $\tilde{E}_{z_0}$ and $\tilde{H}_{z_0}$ are the complex magnitudes of the electric field and magnetic

field at the material sample surface, respectively. δ is defined as the standard depth of the penetration of the wave into the the material or the skin depth, and is given by

$$\delta = \sqrt{\frac{2}{\omega\mu\sigma}}. \tag{3.17}$$

This indicates the value of the depth in the material thickness direction when the EM wave amplitude has attenuated to $1/e$ of its value at the material surface ($|\mathbf{E}_{z|_{z=\delta}}| = |\tilde{E}_{z_0}|/e$). It can be seen that this skin depth is highly dependent on the frequency of the wave (ω) and the material properties (μ and σ). The terms $e^{-\frac{z}{\delta}}$ in equations 3.15 and 3.16 show that the EM fields would exponentially decay into the material depth, and the term $e^{-i\frac{z}{\delta}}$ illustrates the corresponding spatial phase information.

By substituting Ohm's law (equation 3.7) into equation 3.15, the coil induced current density in the conducting material, $\mathbf{J}_z$, can be obtained,

$$\begin{aligned} \mathbf{J}_z(z,t) &= \sigma\mathbf{E}_z(z,t) \\ &= \tilde{J}_{z_0} e^{i\omega t} e^{-\frac{z}{\delta}} e^{-i\frac{z}{\delta}} \end{aligned} \tag{3.18}$$

where $\tilde{J}_{z_0}$ denotes the complex value of the current density at the conductor surface. Figure 3.2 demonstrates the amplitude and the phase information of $\mathbf{J}_z$ as a function of depth z for a 500 kHz current in an Aluminium bar sample. It can be seen from figure 3.2(a) that the induced eddy current in Aluminium is mostly concentrated in a small depth, where the skin depth δ is only 0.12 mm. Such a current field also shows a phase shift with the increased z, with a 180° phase shift at around z=0.39 mm with respect to that at $z = 0$ mm (material surface).

From equation 3.17, it can be seen that a higher frequency can lead to a thinner skin depth. For the EMATs developed in this work, the EM skin depths (tens of micro-meters) are always much smaller than the generated/detected ultrasound wavelength (of the order of millimetres, see chapter 2) in the target samples. The current is therefore approximated as an effect occurring only at the material surface (a surface effect).

3.2.2 Generation mechanisms

Lorentz force

The first generation mechanism to be introduced and the one most relevant to the work in this thesis, is generation via the Lorentz force. The Lorentz force is the force which acts on moving charged particles in electric and magnetic fields. The

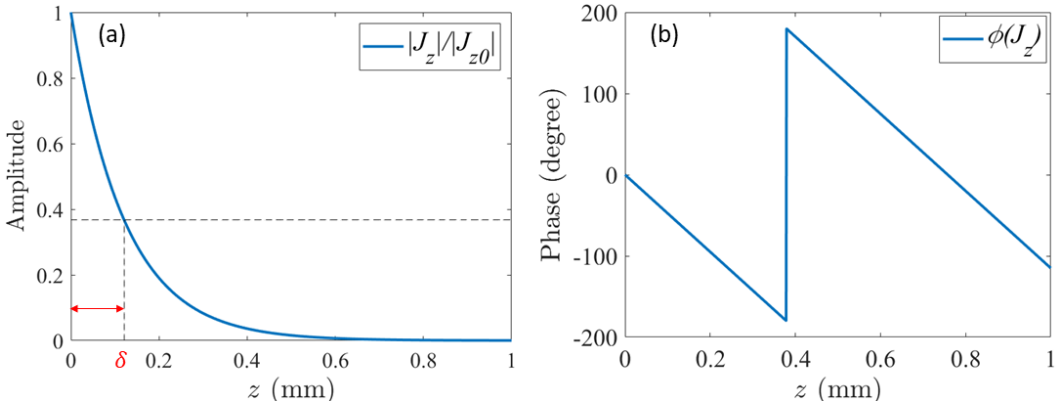

Figure 3.2: Current density for a plane wave propagating of frequency 500 kHz in an Aluminium sample. (a) and (b) are the amplitude and the wrapped phase information of current density at different depths (z-direction). The skin depth, δ, is illustrated in (a).

Lorentz force formula is

$$\mathbf{F} = q(\mathbf{E} + \mathbf{v} \times \mathbf{B}), \tag{3.19}$$

where q denotes the particle electric charge and $\mathbf{v}$ is the particle velocity [125]. The first term, $q\mathbf{E}$, is the Coulomb force (electric force) and the second term, $q\mathbf{v} \times \mathbf{B}$, refers to the magnetic force.

On the macroscopic level, the test sample is electrically neutral, hence the Lorentz force induced in the conducting material can be simplified to $\mathbf{F}^{(L)} = q\mathbf{v} \times \mathbf{B}$. On the atomic scale, the generation mechanism can be understood from the motion of the electrons. Firstly, the motion of the charged electrons is given by [11]

$$m_e \dot{\mathbf{v}}_e = -e(\mathbf{E} + \mathbf{v}_e \times \mathbf{B}) - \frac{m_e \mathbf{v}_e}{\tau}. \tag{3.20}$$

Here $-e$, m_e and $\mathbf{v}_e$ denote the electron charge, mass and velocity respectively. The electron experiences a Lorentz force given by the term $-e(\mathbf{E} + \mathbf{v}_e \times \mathbf{B})$. The term $-\frac{m_e \mathbf{v}_e}{\tau}$ arises from scattering due to random particle thermal motion, and τ denotes the mean time of the electron-ion collision [11, 126]. For common metals, τ is of the order of 10^{-14} s at room temperature [11], which is a much shorter time scale than the oscillation of the driving electrical field, $2\pi/\omega$. The electron-ion collision is therefore approximated as a continuous momentum transfer process such that no overall acceleration occurs, and $\dot{\mathbf{v}}_e = 0$. Equation 3.20 for the motion of an electron is then reduced to

$$\frac{m_e \mathbf{v}_e}{\tau} = -e(\mathbf{E} + \mathbf{v}_e \times \mathbf{B}). \tag{3.21}$$

The above process of the momentum transfer causes motion of the ions. For an isotropic conductor with a certain volume, which is neutral in terms of the total electric charge ($N_i Z_i = n_e e$, where Z_i is the ion charge and N_i and n_e are the charge densities of ions and electrons respectively), the forces that are applied to the ions by the fields and the moving electrons in unit volume of the material can be written as [11]

$$\mathbf{F} = N_i Z_i(\mathbf{E} + \mathbf{v}_i \times \mathbf{B}) + n_e \frac{m_e \mathbf{v}_e}{\tau}, \tag{3.22}$$

where $\mathbf{v}_i$ denotes the ion velocity. Equation 3.22 for the ions includes the Lorentz force from the magnetic field and the collision force transferred from the electrons. It is known that $\mathbf{v}_i \ll \mathbf{v}_e$ since the ions are less free to move than the electron, hence the collision force is the predominant force on the ions causing elastic motion, rather than the Lorentz force on the ion. By substituting equation 3.21 into equation 3.22 and rearranging, the force on the ions reduces to

$$\mathbf{F} = -n_e e \mathbf{v}_e \times \mathbf{B} = \mathbf{J}_e \times \mathbf{B} \equiv \mathbf{F}^{(L)}. \tag{3.23}$$

$\mathbf{J}_e = -n_e e \mathbf{v}_e$, is equal to the induced eddy current density, $\mathbf{J}_z$ (equation 3.18). $\mathbf{B}$ represents the total magnetic field, and consists of the AC coil induced time-varying magnetic field, $\mathbf{H}_z$, demonstrated in section 3.2.1, and the static biasing magnetic field, $\mathbf{B}_0$, produced by the EMAT magnet, if one is used. Substituting $\mathbf{J}_e$ by $\mathbf{J}_z$, and $\mathbf{B}$ by the sum of static and dynamic fields, equation 3.23 can be further decomposed to

$$\begin{aligned} \mathbf{F}^{(L)} &= \mathbf{J}_z \times (\mathbf{B}_0 + \mu \mathbf{H}_z) \\ &= \mathbf{J}_z \times \mathbf{B}_0 + \mu \mathbf{J}_z \times \mathbf{H}_z \\ &\equiv \mathbf{F}^{(L)}_{static} + \mathbf{F}^{(L)}_{dynamic}, \end{aligned} \tag{3.24}$$

where the relationship $\mathbf{B} = \mu \mathbf{H}$ has been used. Note, $\mathbf{B}_0$ is a static or slowly time-varying biasing field, whereas $\mathbf{J}_z$ and $\mathbf{H}_z$ oscillate at a frequency of ω (see expressions in equations 3.16 and 3.18, respectively). The Lorentz force contributed by the static field, $\mathbf{F}^{(L)}_{static}$, vibrates at the same frequency (ω) as the coil driving current (see equation 3.18), whereas the contribution from the coil dynamic magnetic field, $\mathbf{F}^{(L)}_{dynamic}$, vibrates at the doubled frequency, 2ω (see equations 3.16 and 3.18).

Equation 3.24 states that the direction of the induced Lorentz force is perpendicular to the plane containing the current and magnetic field. Figure 3.3 illustrates the EMAT induced Lorentz forces that are produced by either (a)&(b) static magnetic fields in different orientations or (c) the coil self-generated dynamic field for

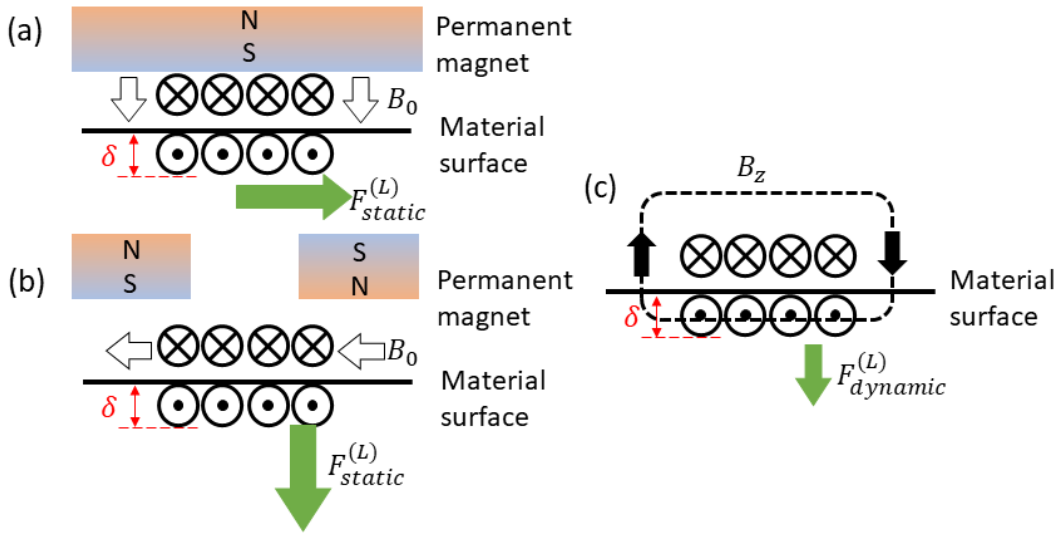

Figure 3.3: EMATs schematic diagram showing the Lorentz force ultrasonic source. The skin depth δ is given and the coil induced eddy-current is assumed to be concentrated in the depth region of δ. Direction of the generated Lorentz force is given by green arrows. (a)&(b) demonstrate the generation of the Lorentz force by applying a permanent magnet with normal or tangential fields. (c) demonstrates the coil self-field Lorentz force. The dynamic magnetic flux is shown by the dashed circle.

a simple linear coil. The induced eddy currents are perpendicular to the sample surface and are approximated as purely out-of-phase to the driving current within a skin depth [127]. The direction of the Lorentz force depends on the configuration of the external magnetic field and the coil, for example in figure 3.3(a), a shear (in-plane) Lorentz force arises from the interaction between an out-of-plane biased external magnetic field and the eddy currents. Figure 3.5(b) shows a normal (out-of-plane) Lorentz force when the static field is instead in-plane. Figure 3.3(c) shows the coil-self induced out-of-plane Lorentz force arising from the interaction between the coil self-induced EM fields.

Figure 3.3 illustrates the most basic Lorentz force configuration for ultrasound generation. In fact, the generation efficiencies for different wavemodes are far more complex in practical use. The coil self-generated out-of-plane force always exists whether the magnet is used or not. Hence, the generation of shear wave (in-plane) requires careful design of the external magnet, from the geometric size to the orientation of the field, and similar for the longitudinal wave (out-of-plane). Work to optimise the EMAT design is essential, not only to ensure the proper wavemode selection but also to maximise the generation efficiency. More information about EMAT designs for generating different wavemodes is given in section 3.4,

with demonstrations of various coil and magnet layouts.

Additionally, the requirement for an external magnetic field for Lorentz force application depends on the intensity of the generation current. If the coil self-generated fields are strong enough and $\mathbf{F}^{(L)}_{dynamic}$ can produce enough signal, the external field is not a necessity, as EMATs can work solely with AC pulsed coils. There are a few applications based on such a concept [128, 129], mainly under high temperature conditions when piezoelectric transducers or the magnet in an EMAT will quickly fail when it surpasses the Curie-temperature. Reference [130] shows that the contribution from the self-generated dynamic field is relatively small when the driving current is below 100 A. In this work, the EMAT driver can produce a current pulse with a peak amplitude of around 70 A, as will be introduced in chapter 4. The Lorentz force effect in this case is dominated by the static magnetic field provided by external magnets, and self-field generation is inefficient.

Magnetoelastic mechanisms

Besides the Lorentz force that can be generated in all electrically conducting materials, EMATs can cause ultrasonic vibration through two other magetoelastic mechanisms in a magnetic material, including *magnetisation force* and *magnetostrictive force* [11, 122]. In a ferromagnetic material exposed to an external magnetic field (considering both the dynamic field induced by the EMAT coil, $\mathbf{H}$, and an external biasing field if one is applied), the magnetisation force arises as a result of the interaction between the external field and the magnetic dipoles within the material. The magnetic dipoles tend to align with the external field. The magnetisation force for ultrasound generation is given by [131],

$$\mathbf{F} = \int_V \mu_0 \mathbf{M} \cdot \nabla \mathbf{H} dV + \frac{1}{2}\mu_0 \int_S \mathbf{n} M_{n_S}^2 dS, \tag{3.25}$$

where $\mathbf{M}$ denotes the magnetisation, $\mathbf{n}$ is the unit vector normal to the material surface and M_{n_S} is the normal component of the magnetisation at the surface. The first integrand term represents the force acting in the material volume, and the second the force on the surface. Following the method reported in [11], equation 3.25 is reduced to

$$\mathbf{F} = (\nabla \mathbf{H}) \cdot \mu_0 \mathbf{M}_0 \equiv \mathbf{F}^{(M)}, \tag{3.26}$$

where the surface traction is not considered. Here $\mathbf{M}_0$ denotes the material magnetisation within the biasing field. $\mathbf{B}$, $\mathbf{H}$ and $\mathbf{M}$ have the relationship $\mathbf{B} = \mu_0(\mathbf{H} + \mathbf{M})$, where μ_0 is the magnetic permeability of free space. Equation 3.26 for estimating

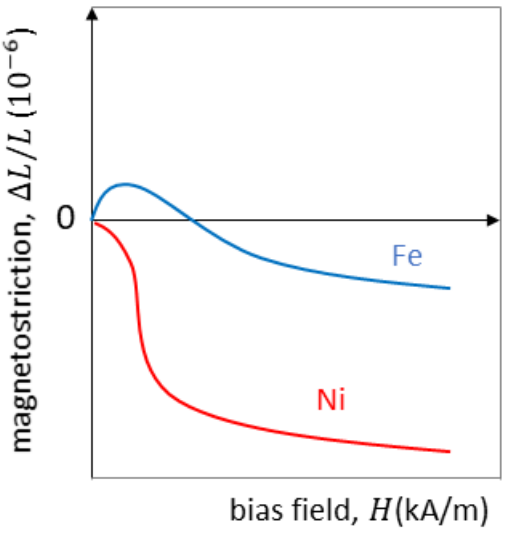

Figure 3.4: Sketch of magnetostriction characteristic curves (λ_S-H) of iron (blue) and nickel (red).

the magnetisation force works for most cases, but it can cause discrepancy when a high frequency and high material permeability are used, due to the underestimation of the surface traction [132].

Magnetostriction is a phenomenon where a magnetic body shrinks or expands due to the change in magnetisation. It arises because the magnetic domains within the material tend to rearrange in the presence of an external magnetic field, causing mechanical strain of the body [133]. Figure 3.4 is a sketch of typical magnetostriction curves for iron and nickel. λ_S is the variation of the relative deformation and is given by $\lambda_S = \frac{\triangle L}{L}$, where L is the length of the magnetic sample. It can be seen that a pure nickel sample shrinks in the direction of the applied field, whereas an iron sample would expand first and then shrink as the biasing field intensity is increased. When the relevant biasing field is time-varying, as with the dynamic field for EMATs, this strain can be exploited to cause ultrasonic motion. For a ferromagnetic material, a high λ_S and a high d_S (magneto-mechanical strain coefficient $\left(\frac{\partial \lambda_S}{\partial H}\right)_\sigma$) are the basic requirements for generation of ultrasound [133].

The magnetostriction effect is far more complicated in polycrystalline materials, as suggested by the highly non-linear λ_S-H behaviour for iron shown in figure 3.4. Precise prediction of the ultrasonic transduction efficiency of a magnetostrictive EMAT is difficult on ferromagnetic materials. Thompson [126] investigated this for iron and nickel and showed that the magnetostrictive force can dominate the generation process at low bias fields, but will become relatively insignificant after

the magnetisation saturation, when compared to Lorentz force generation. This conclusion conflicts with the arguments made by Ogi [134], who states that the magnetostriction can donate the EMAT detection and generation in many steels. A more recent work corrects this to show that the Lorentz force is the major contribution, while the magnetostrictive force only takes a small part in generation in steel samples [135].

In this work, ferromagnetic materials are not the focus as all samples are aluminium. The magnetoelastic mechanisms for generating the ultrasound are therefore not considered when designing the EMAT system used in chapters 5 to 7.

3.2.3 EMATs as receiver

EMATs can also be used as ultrasound detectors. This section gives an introduction to EMAT detection via the Lorentz force mechanism. The latter two are only briefly introduced, since the testing material in this work was aluminium.

Ultrasound propagation within a conductive material leads to dynamic deformation of the body. If such a vibrating body is exposed to a magnetic field (by e.g. using an external magnet to provide a biasing field), a dynamic electric field can be induced by the internal charge carriers i.e. the electrons and ions within the conductor due to the Lorentz force [11],

$$\mathbf{E}_r^M \propto \frac{\partial \mathbf{u}}{\partial t} \times \mathbf{B}_0, \tag{3.27}$$

$$\mathbf{J}_r^M \propto \sigma \frac{\partial \mathbf{u}}{\partial t} \times \mathbf{B}_0. \tag{3.28}$$

Here, $\mathbf{E}_r^M$ and $\mathbf{J}_r^M$ denote the induced electric field and the current density within the material (superscript 'M') for the receiving process (subscript 'r'), respectively. This induced electrical field due to the interaction between the ultrasonic motion ($\mathbf{u}$) and the biasing field ($\mathbf{B}_0$) will cause potential differences across the length of a coil wire if it is placed in close proximity to the sample surface. An EMAT coil placed above the material can thus be used as a receiver to measure the ultrasound signal. However, the above equations do not imply that EMAT detection is merely a reversed Lorentz force process with respected to the generation (equation 3.23). This is because only electrons with energies above or around the Fermi level are free to move and so create the charge current for generation [136], though both ions and electrons can experience the Lorentz force. The momentum transfer from ion to electron for detection process is more efficient than generation who is transferred from electron to ion.

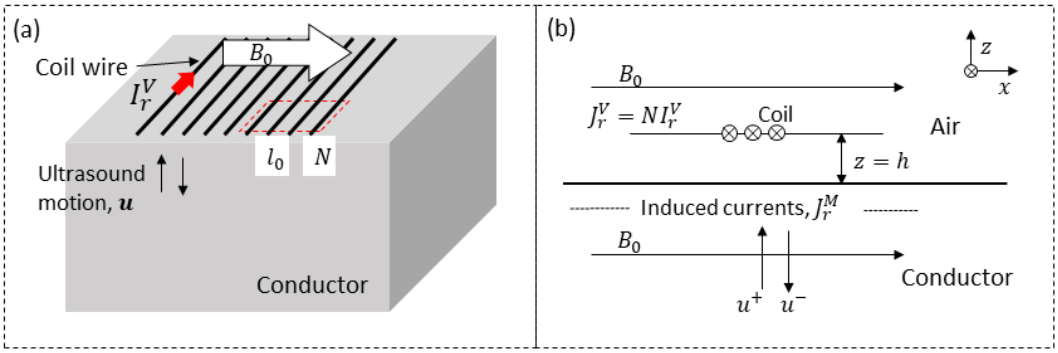

Figure 3.5: Schematic diagram of EMAT detection of a longitudinal wave through the Lorentz force mechanism. (a) 3D view. An EMAT with a single planer linear coil is placed above the conductor. The static bias field is parallel to the material surface in the in-plane direction. (b) Cross section. The EMAT detection coil is at a lift-off h above the surface. The induced current field within the material, J_r^M, is shown by the dashed line and that in the air (J_r^V) is shown in solid line. Both the incoming wave from the positive z-direction (u^+) and the reflected wave into the negative direction (u^-) are shown.

Figure 3.5 shows an example when an EMAT is used to detect a longitudinal wave, with displacement **u** (out-of-plane, the wave travels through the direction of the material thickness). As can be seen in the schematic of figure 3.5(a) the chosen EMAT consists of planar linear coil wires, and the static magnetic field, $\mathbf{B}_0$ is applied parallel to the material surface (in-plane, x-direction). The EMAT coil can be approximated as a conducting sheet. N and l_0 denote the wire density and length, respectively. The induced current in the EMAT coil sheet (superscript 'V') is defined as I_r^V for clarity, and so the current density in the coil is $J_r^V = NI_r^V$. Figure 3.5(b) shows the cross section. The coil is above the sample at a lift-off h.

Assuming that the ultrasound **u** is a plane wave travelling in the z-direction; it will firstly propagate from the material bulk (u^+, in positive z-direction), then reflect at the material surface and back into the far field (u^-, in negative z-direction). **u** therefore can be expressed as,

$$\mathbf{u}(z) = u(z)\vec{k} \quad \text{where} \quad u(z) = u_0(e^{-ikz} + e^{ikz}), \tag{3.29}$$

where the time oscillator $e^{i\omega t}$ is omitted for $\mathbf{u}(z)$. Assuming that $\mathbf{B}_0$ is uniformly distributed across the xz-plane,

$$\mathbf{B}_0 = B_0\vec{j}. \tag{3.30}$$

Substituting the above equations into equation 3.27, the induced current in the

sample material by motion $\mathbf{u}$ can be expressed as

$$J_r^M(z) \propto \sigma \frac{\partial u(z)}{\partial t} B_0 = i\omega\sigma u_0 (e^{-ikz} + e^{ikz}) B_0. \tag{3.31}$$

This disruption (dynamic electric field) will propagate into the air and be measured by the EMAT coil as the change of electromotive force. To find the coil detected signal, the magnetic vector potential[1] in the air, $\mathbf{A}_r^V$, is solved for first. This quantity is produced as a result of the whole $\mathbf{J}_r^M$ (the sum of $J_r^M(z)$ over all depths). The work reported in [137, 138, 139] has given the details of the derivation of $\mathbf{A}_r^V$, which uses Maxwell's equations and the EM fields boundary conditions at the material surface. The result is,

$$\mathbf{A}_r^V \propto 2\mathbf{u}_0 B_0 \left(1 - i\frac{1}{2}k^2\delta^2\right)^{-1}, \tag{3.32}$$

where δ and k denote the EM skin depth and wavenumber within the material, respectively. u_0 is the ultrasonic displacement at the material surface ($z = 0$). The potential difference that is induced in a linear coil with a length l_0 for a unit width is

$$\begin{aligned} \mathbf{V}_r^V &\propto -Nl_0 \frac{\partial}{\partial t} \mathbf{A}_r^V \\ &\propto -2Nl_0 (i\omega\mathbf{u}_0) B_0 \left(1 - i\frac{1}{2}k^2\delta^2\right)^{-1}. \end{aligned} \tag{3.33}$$

Note, the term in the first bracket $i\omega\mathbf{u}_0$ is the value of the ultrasonic velocity at $z = 0$. Taking both the time oscillation and spatial parameter, z, into account, the EMAT detected voltage signal can be expressed as [137],

$$\mathbf{V}_r^V(t, z) \propto -2Nl_0 B_0 \left(1 - i\frac{1}{2}k^2\delta^2\right)^{-1} \frac{\partial}{\partial t}(\mathbf{u}(t, z = 0)). \tag{3.34}$$

This equation illustrates that an EMAT is a particle velocity sensor and it measures the temporal signal of the wave velocity at the sample surface. The work reported by Dixon [140] generalises this conclusion and argues that the detected velocity signal will be enhanced by a factor of ω compared to displacement sensing methods such as laser interferometry [141], due to the differential term.

Apart from the Lorentz force mechanism, magnetoelastic mechanisms can also contribute when using EMATs as a detector in a ferromagnetic material [11].

[1] $\mathbf{B} = \nabla \times \mathbf{A}$ and $\nabla \cdot \mathbf{A} = 0$

The ultrasonic vibration disturbs the equilibrium (steady state) of the magnetisation of the magnetic domain within the body, causing extra magnetic flux. This is the reverse of the magnetostrictive force generation mechanism [133]. The constitutive relationship of the magnetic field is given by [11, 142, 143]

$$\mathbf{B} = \mu_0(\mu_r)_{\mathrm{S}}\mathbf{H} + \tilde{e}^{(\mathrm{MS})} \times \boldsymbol{\varepsilon}^{\mu}, \tag{3.35}$$

where $(\mu_r)_{\mathrm{S}}$ denotes the magnetic permeability tensor at a constant strain, $\tilde{e}^{(\mathrm{MS})}$ denotes the mechanical-magneto coefficient and $\boldsymbol{\varepsilon}^{\mu}$ denotes the strain caused by the ultrasound.

Precise evaluation of EMAT detection through the magnetostrictive effect is difficult. In detecting bulk waves using a spiral coil, it is reported that shear wave detection is more efficient than longitudinal wave detection in steel samples, no matter how the bias field is polarised [143]. This is because the out-of-plane magnetostrictive force will always be cancelled by the magnetisation force or the Lorentz force if they are configured parallel. The detection efficiency of the longitudinal wave is sample thickness dependent in steel samples [144], that is, a smaller thickness can give a larger wave amplitude due to the reduced attenuation after multi-reflections between the upper and lower surfaces. As a result, detection of Rayleigh waves is also possible using EMATs, but the in-plane component (shear) is normally easier to detect than the out-of-plane (longitudinal) in magnetic samples.

3.2.4 Lift-off performance

An EMAT does not need direct contact with samples, allowing for fast scans and the potential to be used in high temperature testing [49] or on conductive samples covered with thin non-conductive coatings [44]. The lift-off (the distance between transducer and the sample surface, as illustrated in figure 3.5(b)) performance of an EMAT is a very important characteristic to be considered during practical use. EMATs are only effective for a lift-off range of a few millimetres [11], with the range dependent on EMAT design and the frequency used.

The EMAT generation/detection mechanisms given in sections 3.2.2 and 3.2.3 can be strongly affected by variation in lift-off. Firstly, increasing lift-off causes a signal amplitude reduction [139, 145, 146]. On generation, the transmitted EM field into the sample is reduced due to the further distance between the driving coil and sample. This is shown by the fact that the values of $\tilde{E}_{z_0}$ and $\tilde{H}_{z_0}$ at the surface in solutions of equations 3.15 and 3.16 decay exponentially, and so does the generated sound signal amplitude. On detection, similarly, the induced electromotive force in

the detection coil (equation 3.34) is reduced because the magnetic flux is less intense at a greater distance from the sample.

Secondly, both theoretical models explained in section 3.2 assume the coil is large enough that the transmitted/received EM fields can be approximated as a plane wave. However, EMATs are of finite size, and the edge effect cannot be ignored in some situations. Solving the field distribution of an AC driven coil is a very classical topic in electromagnetism [123]. There are many relevant works that can be reviewed to solve the EMAT problem [147, 148, 149, 150]. One of the most classical solutions is from [147] where a planar spiral (pancake) coil is placed above a conductor. Figure 3.6(a) demonstrates the system geometry. The magnetic vector potential in the conductor when a spiral coil carries an AC current is,

$$A(r,z) = \mu I_0 r_0 \int_0^{r_0} \int_0^{\infty} \Gamma_1(\alpha r_0)\Gamma_1(\alpha r) e^{-\alpha h} \alpha \frac{e^{\alpha_1 z}}{(\alpha + \alpha_1)} dr_c d\alpha. \tag{3.36}$$

This is solved in the rz-plane, where r is the radial position and z is the depth. r_0 is the radius of the spiral coil and I_0 is the magnitude of the driving current pulse. Γ_1 refers to the Bessel function of first kind. r_c is a continuous variable from 0 to the value of r_0. α is also a continuous variable from 0 to positive infinity, and α_1 is defined as $\alpha_1 = \sqrt{\alpha^2 + i\omega\mu\sigma}$. h denotes the coil lift-off.

Figure 3.6(b) shows an example of the lift-off effect on the distribution of the magnetic vector potential underneath the coil. It illustrates the shape of the magnetic potential in the material near surface region ($z = -0.01$ mm) when a 1.0 mm radius coil is driven by a 500 kHz pulse, and the coil is placed at various lift-offs. It is worth noting that the increasing lift-off h broadens the distribution from a narrower sinusoidal shape to a broader shape. Such a shape distortion is very sensitive to the variation of lift-off since a change of less than millimetre can cause a significant change (e.g. the width of A at 1 mm lift-off is twice as wide as that at 0.25 mm). This lift-off effect has several consequences on the ultrasound generation, for example, the shape of the ultrasound waveform is distorted, making the measurement inaccurate [151, 152, 153]. As a result, one cannot use EMATs for accurate measurements when lift-off needs to be changed significantly, without consideration of the lift-off. This is discussed in detail in chapters 5 and 6.

Several efforts have been made to quantify the EMAT lift-off effect, mainly by evaluating the system electrical characteristics [152, 154, 155]. This is a similar problem to one which occurs in eddy-current testing (ECT) [156]. The mutual interaction between the primary fields and the secondary fields caused by eddy currents must be taken into account. The coil impedance is also significantly lift-off depen-

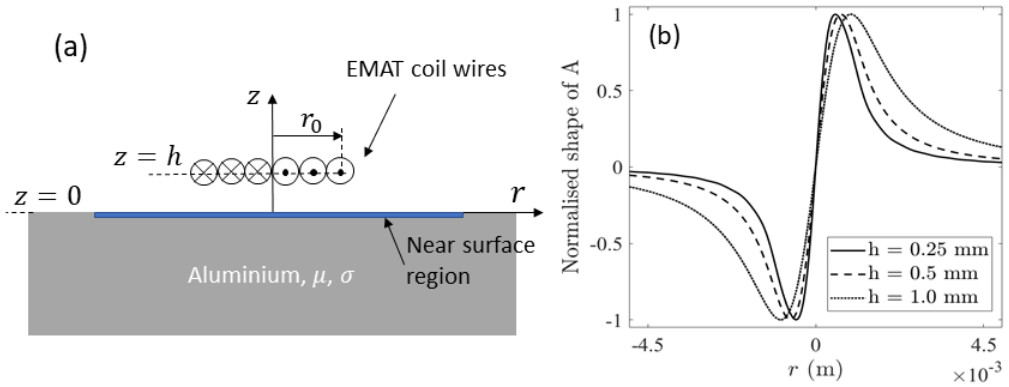

Figure 3.6: Distribution of a pancake coil induced magnetic potential in an aluminium testpiece. The coil is at different lift-offs; 0.25, 0.5 and 1.0 mm.

dent [127]. The work reported in [154] emphasises the coil inductance behaviour, showing a shifted electrical resonance of the EMAT coil when coupled to a conductor at various lift-offs. The resultant broadband ultrasound experienced a frequency shift. A lift-off compensation was made for accurate velocity measurement [152].

The EMAT magnet can also contribute to the lift-off effect. Models discussed in section 3.2.2 assume the static magnetic field is uniform across the entire domain. This is not always true however, especially when the permanent magnet used is not large enough [139], or an electromagnet is used [157]. The magnetic flux in such cases is not evenly distributed in a single direction and can have some edge effects. As the lift-off is increased, the flux density at the material surface drops by a certain amount. The signal-to-noise is thereby reduced.

A ferrite backing method proposed in [158, 159] was used to enhance Rayleigh wave EMAT lift-off performance [146]. Instead of having a permanent magnet, a simple ferrite was used as a back plate to the coil. The ferrite was magnetised by the magnetic field surrounding the excitation coil, and so the induced eddy current can be enhanced to give a larger signal.

The lift-off performance of the array EMAT designed in chapter 5 and 6 is investigated in detail. The study focuses on the Lorentz force spatial behaviour when a single linear coil is used as a finite ultrasonic source, and its effect on building a linear coil array. The dependence of the system electrical characteristics is not considered. This is to emphasise the coil spatial behaviour. The investigated lift-off region (less than 1.5 mm) was small and the variation of the electrical characteristics was minimal. The magnet field divergence was not considered, since the chosen lift-off region was very small. Section 5.3 details the variation of the coil electrical characteristics and the magnetic field drop, so the simplification of the

lift-off problem in this work can be applied.

3.3 EMAT electronics

3.3.1 Electrical impedance matching

As introduced in section 3.2, an EMAT can transfer electrical energy into elastic motion and vice versa. However, the transdution efficiency is very low compared to that of piezoelectric transducers. It is therefore necessary to minimise the energy loss during the transmission of energy from an electrical pulser to a generation EMAT.

A basic EMAT generation system consists of the pulser generator, EMAT, test sample and the associated cables [11, 154, 155], as shown in figure 3.7(a). The pulser generator normally has an internal resistance of the order of tens of ohms. An EMAT coil is less resistive but more inductive. Hence, good impedance matching is needed to reduce the energy loss. L-type impedance matching has been applied and figure 3.7(b) shows the basic diagram of the system impedance network [11]. The pulser and the EMAT have impedances of Z_p and Z_E, respectively, taking the forms,

$$\begin{aligned} Z_p &= R_p + jX_p, \\ Z_E &= R_E + jX_E. \end{aligned} \tag{3.37}$$

R_p, R_E and X_p, X_E represent values of resistance and reactance of the pulser and the EMAT, respectively. Components A and B on figure 3.7(b) can be used as reactive components (inductor and capacitor) to improve the transmission efficiency. For the coupling between the EMAT and the sample, the equivalent capacitance is very small and the coupling is mostly inductive [156]. The equivalent inductance for this part depends significantly on the properties of the test sample, the coil geometry and the transducer lift-off [147, 156, 160]. The resultant inductance that can be measured for the EMAT coil, L_E, can be decomposed into [154]

$$L_E = L_{air} - L_{eddy} + L_{ampere}, \tag{3.38}$$

where L_{air} denotes the coil inductance when no sample is in proximity, L_{eddy} is the contribution from the induced eddy currents in the sample and L_{ampere} is the inductance arising from the Ampère current from the sample magnetisation. These inductance sources are inter-dependent through Maxwell's governing equations. Because the induced eddy currents oppose the excitation currents, the inductance of

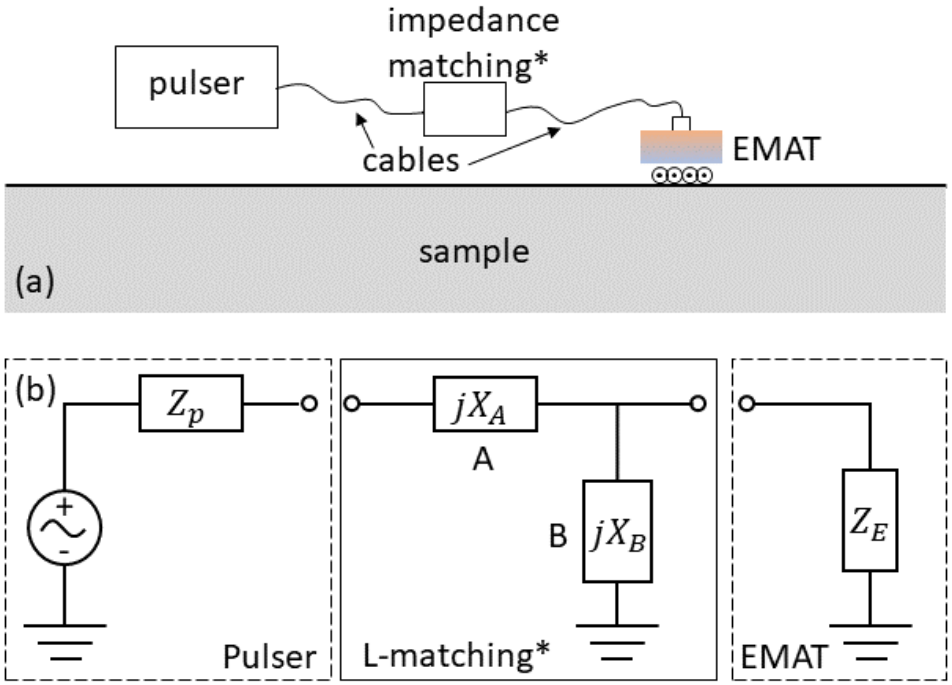

Figure 3.7: (a) Schematic of a basic EMAT generation circuit. The use of impedance matching unit is optional ('$*$'). (b) Block diagram showing the EMAT impedance network with L-type impedance matching method.

the excitation coil can be reduced [127]. The Ampère current can be ignored in paramagnetic and diamagnetic materials, but is very strong in ferromagnetic materials [154]. The capacitance possessed by the transducer connection cables also needs to be considered during the measurements [155].

Design of the above matching network requires that the electrical characteristics of the pulser and the EMAT are both measurable. Once Z_p and Z_E are known, values for components A and B can be found from [11]

$$X_A = GR_E - X_E \quad \text{and} \quad X_B = -\frac{R_p^2 + X_p^2}{X_p + GR_p}, \tag{3.39}$$

where G is a dimensionless quantity given by $G = \sqrt{\frac{R_p}{R_E}\left[1 + \left(\frac{X_p}{R_p}\right)^2\right]} - 1$. This solution is obtained under the condition that the pulser impedance is equal to the equivalent impedance of components A and B and the EMAT combined, which gives a maximised transmission power to the EMAT. However, as discussed earlier in section 3.2, given that it is the EM field that transmits the driving energy, a maximum current would be more desirable for EMAT use. Such a requirement is

satisfied when the reactance of the pulser and EMAT is matched so that the whole circuit is at electrical resonance [161, 162, 163].

The 'L-matching' network was used in the work of [163], where a simple capacitor was employed to cancel the reactance of the EMAT coil inductance. This was applicable because the pulser used was relatively ideal with a constant 50 ohm internal resistance, and nearly zero reactance throughout its frequency range. Also, the EMAT coil application in that design was fixed to only a few frequencies, allowing accurate measurements of the EMAT impedance, and so the design of the 'L-matching' components.

The in-house built EMAT driver used in this work exhibited a dynamic impedance behaviour under different frequency use (see figure 4.4). This frequency behaviour was not standardised (or compensated for) for the multi-frequency EMAT array used during the experiment. Using a simple L-matching network to match the EMAT-driver impedance was not applicable as this would have meant that only one frequency of operation was optimised. Future work can include the optimisation of the EMAT driver internal circuit, and a matched EMAT-driver circuit. The electrical system would then expect an improved high frequency performance. The drawback of the trial pulser will be described in chapter 4, and details of designing a multi-frequency EMAT ultrasonic system are given in chapters 5 and 6.

3.3.2 Detection amplification

As EMATs often suffer from low signal-to-noise ratio, careful design of the electronics is desired. EMATs as the ultrasonic generator often require for high power driving as discussed in section 3.3.1. Although the receiving Lorentz force process is much more efficient (see section 3.2.3), the detected signal by an EMAT receiver can still be weak and is sometimes contaminated by the surrounding noise, such as EM disturbance or other mechanical/electrical noise from the associated setup [164]. The level of signal without amplification is normally too small to be read on a standard oscilloscope. Design of the amplification unit for the received signal is important and is also critical to the data processing. A pre-amplifier with low noise and good impedance matching is essential with designs discussed in references [164, 165, 166, 167, 168].

There have been some attempts to incorporate EMATs with chirp pulse compression methods [169, 170]. The received signals have been improved by a factor of tens of decibels and the level of signal averaging (a signal processing method to enhance the SNR) required was significantly reduced. However, an extra hardware unit or post-processing module is required, which can sometimes lower the EMAT inspection speed.

3.4 EMAT designs for different wavemodes

As explained in section 3.2, EMATs generating/detecting ultrasound act mainly via the electromagnetic coupling between the EMAT coil, the biasing field and the testpiece sample. The direction of the acoustic source (Lorentz force or magnetostrictive force) solely depends on the arrangement between the current flowing through the EMAT coil and the applied biasing field. By carefully designing the EMAT coil and the static magnetic field, different ultrasonic wavemodes can be achieved.

This section gives a brief introduction to EMAT designs that have been developed for generating bulk waves (shear and longitudinal waves) and surface waves (Rayleigh, Lamb waves, and shear-horizontal (SH) guided waves) in metallic materials. Some special designs, such as focused EMATs for enhanced bulk or surface inspection, are also mentioned. EMATs using the phased array concept will be introduced at the end. Note, the Lorentz force mechanism for EMATs to generate/detect ultrasound is emphasised in this section, since the testpiece samples of interest in this work are all non-magnetic.

3.4.1 Conventional EMATs

Conventional EMATs consist of a single conductive coil and a permanent magnet (or electromagnet [171]). To customise the desired Lorentz force for different wavemodes, there are two main aspects to consider; the shape of the EMAT coil and the design of the magnetic field, such as the field orientation and the magnet layout. This determines the spatial distribution of the Lorentz force. The spatial effect of the coil can be understood from the eddy-current theory demonstrated in section 3.2.1, and the calculation of the eddy-current distribution given by Dodd and Deeds [147] detailed in section 3.3. The latter consideration is to determine the polarisation of the resultant Lorentz force into the material; for example, the ideal normal magnetic field illustrated in figure 3.3(a) will lead to a shear force for shear wave generation. For the full picture one must also consider any self-field generation. This section summarises some basic EMAT configurations based on the work presented in [11, 122, 172, 173, 174, 175, 176].

There are four common shapes of EMAT coils for bulk wave applications; linear, spiral, racetrack (elongated spiral/pancake) and butterfly (double racetrack), shown in figures 3.8 and 3.9. Figures 3.8(a) and (b) represent the linear and butterfly coils. Both are used to create the basic linear pattern of the eddy current over the plane (the birds eye view on the left). By introducing a single permanent magnet, a Lorentz force with a linear pattern can be induced into the material to excite

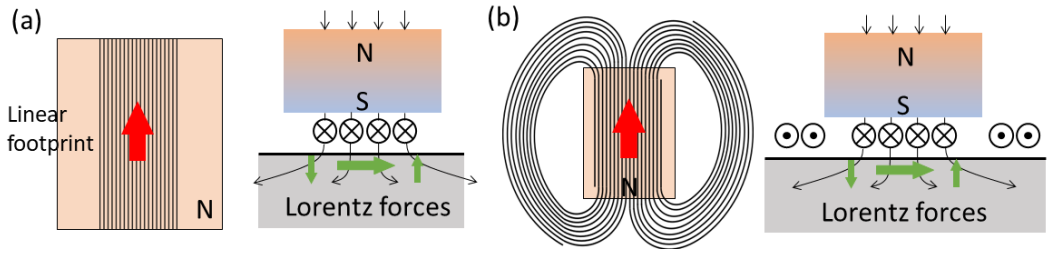

Figure 3.8: Schematic showing two linear polarised EMATs consisting of a single block permanent magnet and (a) a linear coil wrapped around the magnet, or (b) a flat butterfly coil.

bulk waves. To produce the coil shown in figure 3.8(a), a wire is wrapped onto a block magnet [172]. An example EMAT application of this type of coil is given in figure 7.3(c) in chapter 7 for multi-mode surface scanning. The butterfly coil shown in figure 3.8(b) is easier to produce as it is planar [122, 175, 176]. This also allows for the flexible design of the magnet to enhance the EMAT performance, for example, using multiple magnets to increase the normal flux density while suppressing the radial flux [176, 177]. However, there is also a huge waste of the coil when using the butterfly coil design to provide a linear pattern, compared to the linear coil, since the coil in its outer reaches is away from the magnet, and the increased inductance and the potential self-field generation from the sides of the coil needs to be considered.

For the applied static magnetic field shown in figure 3.8, the edge effect of a practical magnet cannot be neglected, hence both normal and tangential components of the biasing field under the sample surface are produced. The resultant Lorentz force contains both shear force and normal force (illustrated by green arrows) components for shear and longitudinal wave generation. In addition, a Rayleigh surface wave can also be generated because of the coupling between the shear and longitudinal waves at the sample surface.

The spiral coil EMAT is demonstrated in figure 3.9(a) with the use of a single permanent magnet. This is the most basic configuration of EMATs, with simple production of the spiral coil and arrangement of the magnet. The spiral coil is radially polarised and the spatial distribution of the eddy currents is symmetric but out-of-phase on opposite sides of the centre. While the magnet provides primarily a normal component of the static magnetic field but also some radial components, the resultant Lorentz forces will contain both shear and normal components to excite both longitudinal and shear waves. The longitudinal wave is generally small due to the small intensity of the shear component of the magnetic field. A Rayleigh surface wave can also be induced when two bulk wavemodes are coupled at the

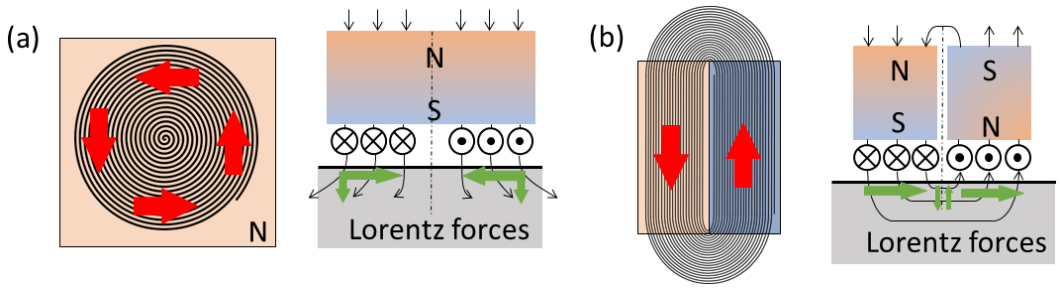

Figure 3.9: Schematic of (a) spiral coil and (b) racetrack coil EMATs. Both coils can provide a symmetric layout of the currents. Two magnet configurations can be used with each designs. Using a single magnet as shown in (a), the induced shear Lorentz forces are symmetric, while they are identical when using two magnets with alternating polarisation shown in (b).

surface. Because of the symmetric distribution of the induced Lorentz forces due to the currents symmetry, these generated waves are omni-directional, propagating into the bulk or surface at the same time [174]. However, the primary wavemode generated by this set-up is a radially polarised shear wave.

The racetrack coil, or elongated spiral coil, can be used similarly to the spiral coil with only one magnet, or with two magnets for shear wave generation and detection [11, 122, 173], with the latter demonstrated in figure 3.9(b). Unlike the spiral coil usage in figure 3.10(a), where the EMAT is radially polarised, the racetrack coil can imprint linear patterns by carefully choosing the magnet size. If the two magnets are in alternating orientations, the resultant shear Lorentz forces are identical and in-phase on either side of the centre. A small normal Lorentz force for longitudinal wave excitation arises in the centre due to the presence of the edge tangential magnetic field. This design has been proved to be very effective for shear wave generation in ferromagnetic materials, since the normal Lorentz force for longitudinal wave generation in those cases is cancelled by the magnetisation force [11]. The Rayleigh surface wave is also minimised.

Meander-line coil EMATs

Another conventional design is the meander-line coil EMAT, shown in figure 3.10. The coil is fabricated into a meander-shape, so that the multiple turns of coil generate enhanced ultrasound waves. Each turn can be considered as a single linear coil with a small width. Using a normal biasing magnetic field (provided by a permanent magnet), a shear Lorentz force array that is parallel to the surface is induced. The direction of the neighbouring Lorentz force elements changes alternately with

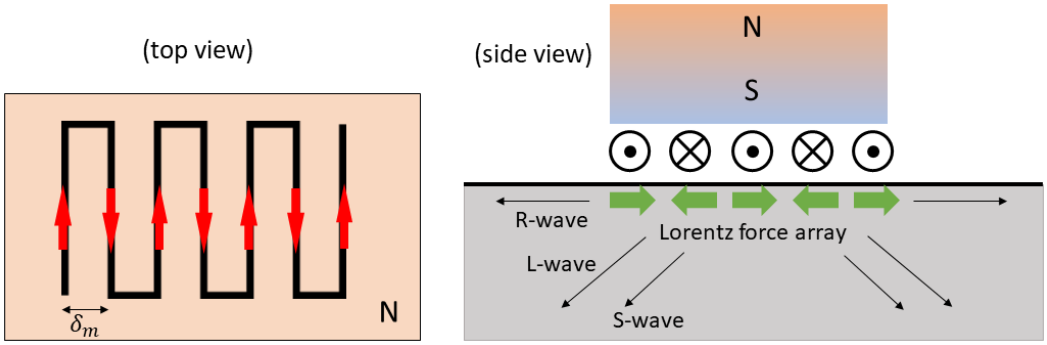

Figure 3.10: Schematic of a meander-line coil EMAT.

respect to each other, as shown in figure 3.10.

The meander-line coil is capable of generating multiple modes, giving bulk waves and surface waves simultaneously [122]. This is understandable as each coil turn is approximated as a linear element where the shear wave, longitudinal wave and the surface coupled Rayleigh wave will be excited. The array property of the meander-line coil can provide many benefits. Firstly, for bulk waves, the ultrasound beam is obliquely emitted into the material, showing a certain directivity that can be used to improve the detection sensitivity [178, 179]. The directional characteristics also show a frequency-dependence [172, 180], making it possible to electronically tune the beam directivity for enhanced detection. Secondly, for surface waves; the meander-line geometry is similar to a comb structure where a narrowband signal can be generated [181]. An approximate relationship between the spacing of the coil turns and the optimal wavelength for generation is given by,

$$\delta_m = (m + \frac{1}{2})\lambda, \tag{3.40}$$

where δ_m is the coil turn spacing and m is an integer. This property has been used for wavelength selection of Rayleigh surface waves [181] or mode selection of Lamb waves [182], since the transducer bandwidth in this case is dominated by the number of turns and the meander spacing [122]. Chapter 6 (section 6.3) discusses the performance of the conventional meander-line coil EMAT as compared to the linear coil array EMAT developed in this work for Rayleigh surface wave generation.

3.4.2 Periodic Permanent Magnet EMATs

Recently, the periodic permanent magnet (PPM) EMAT design has gained more interest [11, 122]. Figure 3.11 demonstrates the schematic of a typical PPM EMAT.

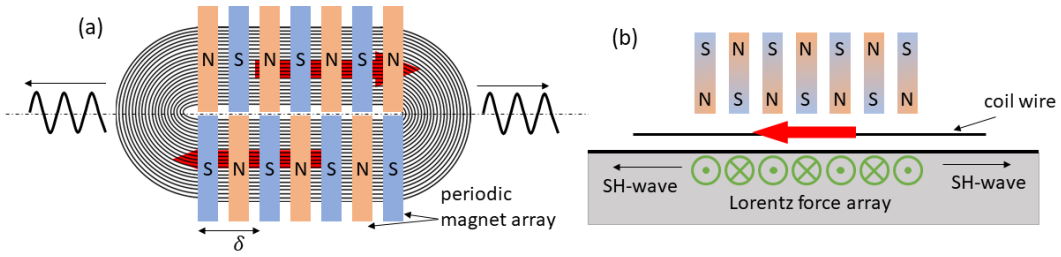

Figure 3.11: Schematic of a periodic permanent magnet (PPM) EMAT generating SH guided waves on a plate surface.

This design aims to generate horizontally-polarised shear waves (SH-waves) in different materials, especially SH guided waves in thin structures. A simple racetrack coil is used with a permanent magnet array, as can be seen in figure 3.11(a). The polarisation of each neighbouring magnet is changed alternately, leading to an alternating Lorentz force whose direction varies with the same period as the magnet array. The induced array of Lorentz forces is parallel to the surface, and so the generated shear wave is polarised horizontally to the sample surface, propagating to the far field in both directions. Figure 3.11(b) gives the cross-section view. This design is similar to the concept of the meander-line coil where a pseudo source array is formed, but the force distribution here is dominated by the magnet separation. The properties of the generated SH waves, i.e. the wavelength, are determined by the layout of the magnet array; the wavelength for the generation pulse should equal the period of the magnet array to maximise the output amplitude.

SH-wave PPM EMATs have been applied in different applications. Hill and Dixon [183] investigated the directivity characteristics of the SH bulk wave beam emitted from a PPM EMAT. The frequency-dependence of the beam directivity was confirmed. Beam steering was achieved by simply tuning the input frequency rather than using a phased array system, due to waves from each section interfering constructively [184]. This PPM system with beam-steering capability has been used for weld inspections [185, 186, 187]. Additionally, PPM EMATs have been used in pipeline inspections. The SH waves are different in different structures, providing more possible inspection strategies. For example, the PPM generated SH guided wave travelling in the circumferential direction around a pipe was used to monitor corrosion, using a pitch-catch EMAT arrangement moving in the axial direction [188], or by using a modified PPM design to generate a torsional wave whose particle displacement is in the circumferential direction and the wave propagates in the axial direction [189]. The latter wave type provides a means of inspecting over a large distance within a single measurement [190].

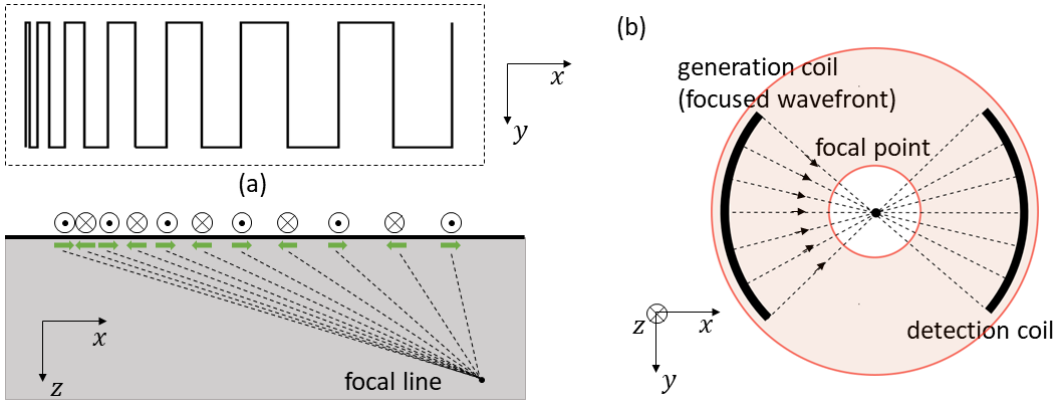

Figure 3.12: (a) Line-focusing for bulk inspection (in xz-plane), after [8]. (b) Point-focusing for surface inspection (in x-$y$plane), after [9].

3.4.3 Wave focusing EMATs

Recently, there has been a group of interesting designs of EMATs using wave focusing for enhanced ultrasonic inspection. The main reason for applying the focusing principle using an EMAT is to concentrate the ultrasonic energy to the target flaw/crack through a narrowed beam. The method can be effective at overcoming the drawbacks of EMAT low signal amplitude, and the low detection accuracy due to the broad beam profile generated by a conventional EMAT design [8, 9, 191, 192]. Tiny cracks can be detected using focused EMATs before they develop into the hazardous stage [134].

Two focusing EMAT designs are illustrated in this section. First is the line-focusing shear wave EMAT for bulk inspection, shown in figure 3.12(a) [8]. This is a modified meander-line coil EMAT where the generated shear-vertical wave is focused in the xz-plane. By continuously varying the spacing between each of the meander-line turns, the shear wave emitted from each coil turn is superimposed in a way where their combined wavefront is directed at a certain angle through constructive interference. A beam-steered EMAT with good directivity can be obtained by using different frequencies, offering great potential for oblique ultrasonic inspection. The prototype design presented in [8, 191] shows a sharpened directivity of a 4.0 MHz shear wave line-focusing EMAT at around 40°, allowing for the detection of tiny slits that are deeper than 0.05 mm. It can be expected from the above example that, by carefully tuning of the geometry of the meander-line coil, different focal lengths and depths can be obtained. However, this is not flexible for multiple applications since the focal law of each line-focusing EMAT is fixed due to their fixed physical designs.

Another design shown in figure 3.12(b) is the focused surface wave EMAT for enhanced surface crack detection [9]. The Rayleigh wave generated by the EMAT was used to detect a surface crack. With the use of a normal biasing field (in the z-direction, indicated by the red shadow region), the shear Lorentz force was induced underneath the AC driven coil for Rayleigh wave generation. The wavefront of the emitted cylindrical waves followed the coil curvature and was geometrically focused at a point, and this can be used for small surface crack detection. A symmetric detection coil was used to receive the transmitted Rayleigh wave. A pair of focused coils used the racetrack design and the Rayleigh frequency was set to 2.0 MHz, allowing for detection of small cracks that were of the order of 0.5 mm depth and 1.0 mm length. This single generation-detection design can be improved in multiple ways, for example, by using multiple detection coils to capture the signal scattered by the crack from arbitrary scan orientations [192] or using a meander-line coil to further improve the signal amplitude of the inspection [9].

There are some other interesting focusing designs. Takishita et al. [193] proposed a point-focusing EMAT for bulk inspection. This new design was based on the previous line-focusing concept where a meander-line coil with continuously varied spacings was first used to make a focal line in the x-z plane. Meanwhile, the meander-line coil was geometrically curved at the sample surface, similarly to the Rayleigh focusing design, to form a focal point in the x-y plane. The resultant geometry led to a focal point in the material in three-dimensions. Sun et al. [194] developed a fan-shaped PPM design to focus an SH wave in a plate. The magnet array was made into a fan shape whose outer and inner edges were concentric, and so the generated SH guided waves were focused unidirectionally in the plane. It can be seen that the flexibility of EMAT design, either through the customisable coil shape or different magnet arrangements, brings great opportunities. By combining these with the EMAT advantage of being non-contact, the potential can be maximised.

3.4.4 Phased Array EMATs

As introduced in chapter 1, the phased array (PA) technique has been widely applied in many industrial and scientific areas as well as in medicine. PA ultrasonics allows for programmable beam patterns such as beam steering or focusing, by controlling the wavefront superposition from multiple coherent acoustic elements. PA enhanced ultrasound allows for better sensitivity and efficiency for ultrasonic testing (UT) [40].

The design of PA EMAT systems is gaining more interest, although the size and the low transduction efficiency of EMAT are widely recognised as the major drawbacks that hinder its development. Unlike a piezoelectric PA system that can

contain hundreds of very small individual elements/channels, an EMAT system is much more power-consuming, and the EMAT source element is much larger. A 32-channel PA SH wave EMAT [166] is the maximum reported in the published literature for welds inspection. One of the methods to reduce EMAT energy requirements is to evaluate data in conjunction with the digital techniques of pulse compression [169] or coded excitation [195]. An 8-element pulse-echo EMAT PA system was proposed based on the latter, claiming that the peak excitation power was less than 5 W per channel [196]. This system used an angled shear-vertical (SV) bulk wave to detect the surface crack located on the sample far-side surface. The prolonged excitation signal can however, degrade the axial resolution of the imaging. Learning from the evolution of piezoelectric ultrasonics, there is a chance to update the EMAT technique using advances in electronics.

Despite the disadvantages for PA operation, the unique advantages of EMATs, such as the generation/detection flexibility for different wavemodes and the capability of operating without couplant, make it the best candidate for some special applications. Up to date, there have been three types of PA EMATs that are noteworthy; the SH-wave EMAT PA system for welding inspection [166, 185, 197], the longitudinal-wave EMAT PA system for the nuclear power industry [198] and the coil-only EMAT PA system for high temperature inspection [129]. Below gives a brief introduction to these techniques.

SH EMATs for austenitic weld inspection: Conventional UT methods were not considered for the application because of the high degree of acoustic distortion, anisotropy and scattering arising from the large grains of the weld material (see section 2.1.4 for ultrasonic attenuation). The SV or L waves generated by conventional piezoelectrics are impractical because they will be skewed into certain directions [185], and associated with the issue of mode conversion (see section 2.2.1). A low frequency (below 2 MHz) SH wave thereby exhibits great potential for improving UT scans of austenitic welds, since its attenuation is not significant and the propagation angle will not be obviously skewed. This type of wave can be easily generated by a PPM EMAT (see section 3.5.2) but not by conventional piezoelectric transducers. The combination with the PA technique equips the PPM EMAT (or SH meander-line EMAT [178]) with a better signal to noise ratio and the ability of beam steering for testing over a wider angular range (up to 90°). Details of the performance of PA SH EMATs designed by different groups can be found in [166, 197, 185], for example, Sawaragi et al. [197] proposed an 8-segment PA PPM EMAT system for pipe welding detection and Gao et al. [185] developed a high-power integrated 8-channel phased driving system via an H-bridge circuit for

PPM EMAT steering.

Longitudinal wave PA EMATs have been developed for in-service nuclear reactor inspection, for the ASTRID reactor launched by the French government [198]. While optical methods and conventional piezoelectric ultrasonics are considered to be impractical for inspecting the sodium cooled fast reactor, EMATs are an option that can work properly in the hot and irradiated liquid sodium environment. The on-going progress of system development can be seen from their annual conference papers [199, 200, 201]. To improve the PA EMAT performance, the configuration of the magnet array has been optimised, the electronics has been optimised to maximise the output current via the resonance phenomenon (see section 3.4.1) and the number of the EMAT driving channels has been increased from 8 to 12.

Another special design of longitudinal wave PA EMAT was for as-cast steel testing [129]. This was a coil only generation design based on the Lorentz force principle demonstrated in figure 3.3(c), which was expected to work in the extremely high temperature (up to 2000°C) environment. The EMAT driver consisted of four individual phased channels, allowing for operating a four-coil phased array. The driving system was equipped with a high energy unit that could deliver a current pulse with a peak value of 1.75 kA from each channel, and so each coil element could be sufficiently driven to produce enough ultrasound.

There is still room for PA EMATs to be extended for other NDE applications, due to their flexibility of design for different wavemodes and their non-contact advantages. The phased EMAT arrays proposed in this work focus on using Rayleigh surface waves for surface crack characterisation and will be detailed in chapters 5 and 6. The lift-off performance of an array EMAT (see problem described in section 3.3) will also be studied to better characterise the ultrasonic behaviour of the system.

Chapter 4

Experimental and modelling methodologies

This chapter outlines the experimental and modelling methodologies used in this work. The method for EMAT production is firstly introduced, from coil making to manufacture of the transducer holder. The specialised electrical driving system (four-channel phased EMAT pulser) that was developed for this work is then detailed. The major functional parts of the driver are illustrated. The driving signals for EMAT use are exemplified. The behaviour is studied for different load components, such as low reactance resistor and typical EMAT coils.

Finite element analysis was used for EMAT modelling in this work. The procedure of forming the finite element EMAT model is introduced at the end of this chapter, from the EMAT electromagnetic generation to the wavefield modelling and the target Aluminium samples.

4.1 EMAT production

The work of this thesis required the production of several new designs of EMAT coil. The method of EMAT production has yet not been standardised. One of the popular ways to make an EMAT is through the printed circuit technique [11]. However, all the EMAT prototypes used in this work were made by hand-winding wires. This is good for conceptual design where novel transducer configurations can be achieved easily. In addition, the wire density can be improved compared to the printed circuit method, and EMATs with a better generation/detection efficiency can be expected. Also, the hand-made EMAT provides a better lift-off performance than the printed ones as no extra circuit board is placed between the coil wire,

magnet, and the sample surface.

Making flat EMAT coils was done through the method developed by Y. Fan in the Ultrasound Group, University of Warwick. This method is based on the technique described in [11]. Details of the fabrication procedure can be found in reference [163], and here only a brief introduction is given. The procedure consists of four steps; 1. producing a paper template of the coil design. In this work, the geometric shape of the coil (to scale) was designed using an open source painting package, InkSpace. 2. Etching the coil shape onto a substrate. The coil template was stuck onto a glass plate using multiple layers of scotch tape and Kapton tape. A scalpel was used to etch the design into the tape layers by cutting along the coil profile provided by the template, so that the wires could be wound into the etched layer to produce the required shape. 3. Hand-winding the copper wire into the desired shape. 4. Encapsulating the coil using Kapton tape to protect the prototype design.

The permanent magnets used in this work were NdFeB magnets, produced by Supermagnete Llc. The size of the magnet was $25 \times 15 \times 6$ mm^3 (45N). A 3D printer was used to make the EMAT holders. Though the 3D printing material is plastic and hence offers no shielding, it is good enough to provide a solid casing and electrical insulation to the EMAT high currents and provides a good means of EMAT prototyping for rapid research studies.

4.2 Four-channel EMAT driver

As introduced in chapter 3, the coils of the EMAT are essential to the system as they are used as the driving source of the EMAT ultrasound generation. The multiple channel electronic system for driving the coils is therefore fundamental to making the novel designs presented in the later chapters achievable.

The version of the EMAT ultrasonic driver used in this work can only support a maximum of 4 sensors working at the same time. It is a prototype for a more advanced device which could be developed now the promise has been shown. For using it to configure a conventional phased array system, the limited number of driving channels (only 4) means limited performance of the ultrasound bream directivity, and also the imaging performance.

In this thesis, a new array EMAT system was developed with a different phasing modality. Four very basic linear EMAT coils were chosen to implement the fundamental/feasibility study for this idea. The surface wave inspection performance has been proven when using just 4 coils/channels; a better signal-to-noise

ratio (SNR), and the capability of wavelength selectivity (see figure 6.10). The array performance of 4 coils was better than using just 2 coils, but worse than would be expected if using 6 coils or more (see discussions around figures 5.14 and 6.12), for both SNR and wave selectivity performance.

The pulser was designed and built by David Greenshields from the Electronics Workshop (Department of Physics, University of Warwick) for this research. Common phased array electronics are available on the market, but their power level is normally significantly less than the requirement for EMAT driving. The pulser contains four individual EMAT drivers that can support four separate EMATs working simultaneously. Figure 4.1 demonstrates the pulser block diagram of the major units; PIC processor as the interface to the user, radio frequency (RF) burst generator which is field-programmable gate array (FPGA)-based, four EMAT drivers (CH0 to CH3) to deliver high current sinusoidal outputs, and power supply. Users can customise their EMAT driving signals by setting multiple aspects; the central frequency, the number of cycles (linked to bandwidth), the number of channels that are activated, and the time delay on each channel. The signal amplitude level and the pulser repetition rate can also be varied. The desired sinusoidal burst would then be produced by the FPGA burst generator before more power is added on to the output by the EMAT driver. The main functional part of the EMAT driver contains a MOSFET current source and a voltage booster transformer, as can be seen in the figure. The time delay between each channel can be customised, which plays a key role for varying the EMAT array performance in chapter 6.

This pulser design is the next generation of the design compared to the one presented in [129, 202]. The difference between the two is the ability of signal delivery. For example, the signal generated by this pulser is under the full control of the user, allowing control of frequency and bandwidth, while that in [202] delivers a wideband pulse signal with around 1.5 μs duration. The price for the level of control is that the amplitude level of the output in this pulser is much lower than that of the original version. The original has an output of up to 1.75 kA, as it is powered by a bank of capacitors, while this system has a maximum output of 72 A ideally. The two different pulsers are therefore suitable for different practical applications.

In the following sections, the performance of the pulser used in this work will be described in more detail. The output signals will be shown and the pulser frequency-dependent characteristics are studied through a simplified Norton circuit.

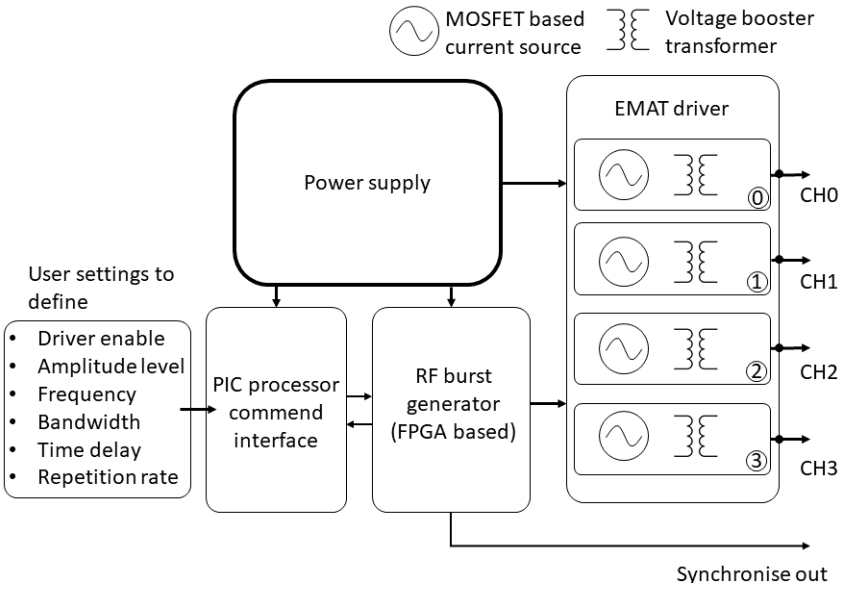

Figure 4.1: Block diagram showing the major parts of the EMAT pulser used in this work.

4.2.1 Time-delayed high current output

The performance of the in-house built pulser largely depends on the FPGA signal generator unit. The programmed module allows for varying the duration of the burst signal from one cycle to ten cycles, and the central frequency from 10 kHz to 10 MHz. The time delay between channels can be set from 0 to 10 s in 5 ns steps. Figure 4.2(a) shows the voltage outputs from all four channels for a 1 MHz three-cycle driving signal, with a time delay between the successive channels of 4 μs. Full amplitude level (100%) was set. It should be noted that there is a small oscillation after the voltage burst signal. This implies that the MOSFET has been disabled. For the power MOSFET chosen in this pulser, a threshold voltage to the gate is required for conduction. To stabilise and linearise the MOSFET gate voltage with drain current, source transistors were pre-used to produce a small current before the MOSFET. This helped the MOSFET to work in the region where it was more linear, instead of starting from 0 V. The small perturbations outside the pulse waveform envelope were caused by the switching on and off of the transistors. Additionally, the signal shapes for the different channels are not completely identical. This could be due to the 50 Hz mains ripple on the high voltage DC supply that was not regulated, and so appeared directly on the output. The hand-wound transformer for each channel may not be identical, which can also affect the relative amplitude level of each channel. Figure 4.2(b) shows the magnitude frequency spectrum (fast

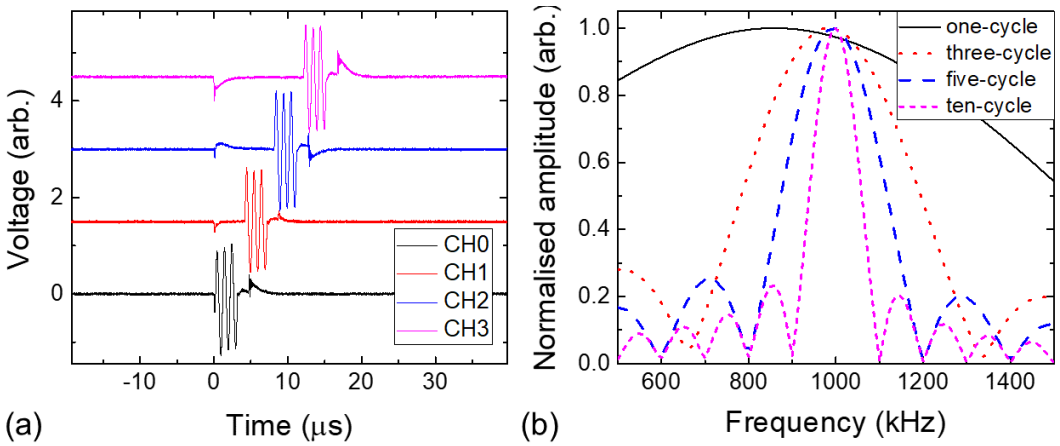

Figure 4.2: Driving signal at 1 MHz, showing (a) output of each channel for three-cycle operation, and (b) frequency information (after fast Fourier Transform, FFT) for different numbers of cycles.

Fourier Transform, FFT) of the signals generated from one of the channels for different numbers of cycles. The central frequency was also 1 MHz. The abilities of broadband (one cycle) or narrowband driving are shown.

4.2.2 Norton equivalent circuit

Understanding the pulser frequency characteristics is essential to this work, as array EMATs described in chapters 5 and 6 have considered operation at different frequencies (wavelengths). Since the pulser internal network is complex, one way to simplify the circuit is implementing the Norton equivalent circuit [161]. Though this method could be an oversimplification, a good approximation can be obtained as a preliminary study for this trial pulser. Figure 4.3(a) shows the diagram of the equivalent circuit. The system has been considered as being composed of two parts; the current source and the load. The Norton circuit of the former consists of an ideal voltage source (about 72 A as the maximum peak-to-peak current value for an ideal load) with a damping resistor, Z_P, mainly contributed by the primary winding of the transformer, while that of the load is mainly decomposed into the EMAT, with an internal impedance of Z_E. The transformer in the EMAT pulser is 1:1, so the turns ratio is 1 and the impedance ratio is 1. Therefore the impedance seen at the primary will be the same as that of the EMAT if the frequency is within the specified operating range of the transformer.

The transformer has a complex electromagnetic behaviour, with frequency-dependent characteristics that will also be expected from the pulser behaviour. Pre-

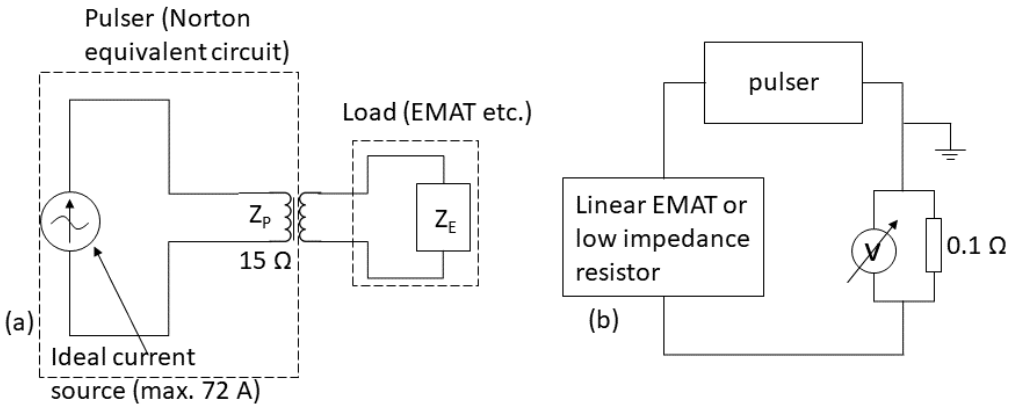

Figure 4.3: Schematic of (a) the pulser Norton equivalent circuit, and (b) the method used to test the pulser frequency characteristics.

cise prediction of the transformer efficiency is difficult since it can be contributed to by multiple factors, such as the transformer construction, magnitude, frequency as well as the signal types. There are two sources of loss, the copper loss and the core loss. The copper loss is the heat loss due to the resistance of the wire. The core used in this transformer is ferrite core that has an effective frequency up to 1 MHz. Beyond this, the efficiency will be drastically limited. Also when the current is bigger than the core 'saturation current', the magnetic field stops increasing, and the primary begins to be more resistive, so the power waste is increased.

To evaluate the pulser behaviour, a measurement based on the method shown in figure 4.3(b) was undertaken. A low reactance 0.1 Ω resistor (ten low reactance 1 Ω resistors connected in parallel) was connected in series with the pulser and the EMAT coil, and a voltmeter was used to detect the potential difference across it when the pulser was activated. This unit was used to measure the current flowing in the pulser-load system for a range of driving frequencies. The current was obtained by dividing the potential difference by the resistance (0.1 Ω). A load of one resistor or a choice of two different EMAT coils were tested, and their impedance information (without connection to the pulser) between 0 to 6 MHz is given in figure 4.4(a). The impedance of the load was measured by a HP impedance analyser. The loads used were,

1. A low reactance 4.7 Ω resistor. It can be seen that its impedance value from 0 to 6 MHz remains at about 4.7 Ω. This resistor was chosen to evaluate the general behaviour of the pulser.

2. Two linear coils (see figure 3.8(a)); one was made from 6 turns of wires of 0.1 mm diameter (approx. 0.6 mm width in total), and the other was 7 turns

of wires with 0.2 mm diameter (approx. 1.5 mm width in total). Two different coils were used to evaluate the EMAT coil influence on the pulser system. It can be seen that the two coils show similar impedance values within the chosen frequency change, although the 0.6 mm one has slightly higher amplitude (the difference is smaller than 3 Ω). From 0 to 6 MHz, the impedance is increased from 0 to about 25∼28 Ω.

Following this, the loads were connected to the pulser (CH0) to evaluate the performance of the pulser at different frequencies. All driving signals were set to three-cycles so a good bandwidth and time resolution could be guaranteed. As explained in section 3.2, EMAT generation efficiency depends largely on the driving current intensity; the peak-to-peak current values were therefore found and plotted. The measurements were undertaken via the set-up illustrated in figure 4.3(b) and the results are given in figures 4.4(b) and (c). Figure 4.4(b) shows the currents when the 4.7 Ω resistor was used. The central frequency of the driver was varied from 300 kHz to 5.5 MHz with a 50 kHz step. Amplitude levels (size of the pulser output) of 25%, 50%, 75% and 100% were measured. It can be seen that the pulser gave an overall non-linearly decreasing behaviour with frequency. The 75% and 100% levels show a steep drop from 300 to 750 kHz and a moderate drop from 950 kHz to 1.8 MHz, compared to that at 1.8 MHz or above. The 25% and 50% levels show steep drops from 300 to 750 kHz, but experienced a relatively steady output range from about 750 kHz to 2.5 MHz (highlighted in the red rectangle) before the current started dropping again at higher frequencies. The behaviour of the current output was complex and can be attributable to multiple factors; firstly, it could be due to the behaviour of the power op-amp that was used to drive the MOSFET gates, where the signal amplitude can drop off at higher frequencies. Secondly, the RC filter ('R' by the gate drive resistor and 'C' by the MOSFET input capacitance) formed in the MOSFET gate drive circuit can cause the signal decrease at higher frequencies. Thirdly, the drain-source capacitance on the MOSFET took more current at higher frequencies, so the available output current was reduced. The transformer, which has its own frequency characteristics, can also contribute to the effect. The coil wire wound onto the transformer shows mostly inductive behaviour and may behave inconsistently at high frequencies.

The results when using the EMAT linear coils as a load are given in figure 4.4(c). The driving frequency was varied from 500 kHz to 6 MHz with a 100 kHz step. The data for the 4.7 Ω load resistor is also included for better comparison. It can be seen that similar trends were provided for both EMAT coils at both amplitude levels (whether 100% or 50%). The current amplitude was generally smaller

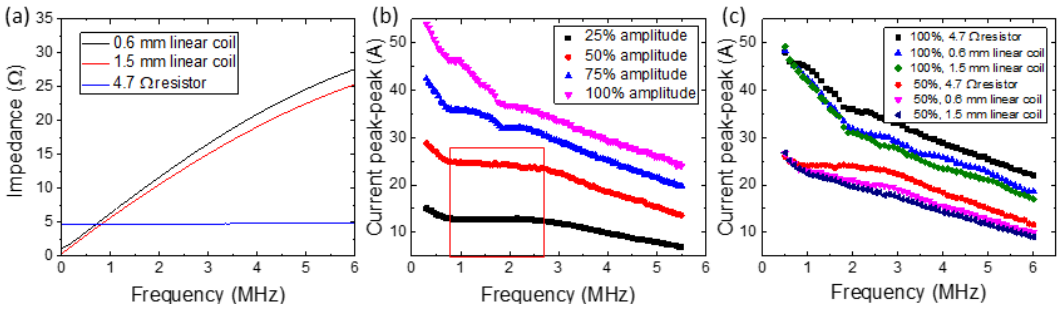

Figure 4.4: (a) Frequency characteristics of different test loads. Measured using a HP impedance analyser. (b) Current measurements using the standard 4.7 Ω resistor at different amplitude levels. (c) Full results of the current measurement on all components in (a). 50% and 100% amplitude levels were tested.

compared to that obtained with the 4.7 Ω resistor, due to the larger impedance of the linear coils (tens of ohm). However, this amplitude reduction is not significant (less than 3 A difference below 1.7 MHz). The difference reached about 5 A when the frequency was increased to 6 MHz. This implies that the electrical influence from the EMAT coil will not majorly affect the system over the frequency range used. The electrical characteristics of the whole system depend mostly on the intrinsic properties of the pulser system. Pulser optimisation therefore can be one of the future directions for research, when high currents and higher frequency EMATs are required.

The absolute value of the output currents through the EMAT ranged from 50 A at lower frequencies, when the pulser was set to an output amplitude of 100%, and decreased to only 17 A when the frequency was 6 MHz. The self-field ultrasound generation contributed by these current intensities can therefore be reasonably neglected [130]. In chapters 5 to 7, the EMATs were used primarily in the frequency range from 300 kHz to 1.5 MHz with 100% amplitude level, so enough signal-to-noise (SNR) can be guaranteed.

There are some constrains in this system; 1. the requirement of high-power consumption, and 2. the reduced device portability. Optimisations such as the design of more efficient EMAT coil/magnet layouts or using digital electronics can be part of future work. This will be dependent on the particular NDT purpose.

4.3 Generic experimental procedure

The EMAT systems developed in this work were used in pitch-catch configuration with a separate detector coil. On the transmission side, the pulser and EMAT were

used on the target sample for ultrasonic generation. On the detection side, signals were captured by different ultrasonic detectors. For example, a racetrack coil EMAT detector (see section 3.4.1) was used for studying the Rayleigh wave array EMAT performance in chapters 5 and 6, and also for the shear wave multi-mode EMAT study in chapter 7. The received sound wave signals were amplified by a low-noise amplifier before being displayed on a digital oscilloscope. Also, the signals were digitalised and saved using the same oscilloscope. The IOS laser interferometer described in section 2.3.3 was used for single coil lift-off performance as described in section 5.3. Full details of the experimental set-up will be given in the relevant sections.

4.4 Finite element method (FEM)

Finite element method (FEM) is an analysis method that can give approximate numerical solutions to mathematical models of physical problems [203]. The core concept of a FEM is to perform finite element formulation, in which the physical domain is geometrically discretised into a set of non-overlapping small regions of space known as elements, so the unknown physical variables can be more easily calculated by computers. The FEM method provides a good way of solving the behaviour of complex physical structures, from beams and shells to bridges or aircraft etc., making it a powerful tool to solve engineering problems.

A typical FEM procedure can contain the following steps [203]; identify the physical problem (e.g. sample geometry, measurement type), construct the mathematical model (normally the governing partial differential equations (PDEs) and boundary conditions), implement and obtain the finite element solution, and implement the post-processing (data interpretation, visualisation, etc.). The central focus of this work is to develop different EMAT systems for multiple purposes (phased array and multi-mode EMATs, see chapters 6 and 7). Conducting FEM modelling gives a good validation of the EMAT performance at different design stages.

As introduced in chapters 2 and 3, the phenomenon of EMAT generation is a multi-physics problem, which must consider both electromagnetism and elastodynamics. Figure 4.5 illustrates a basic EMAT generation problem in 2D. The EMAT generator is coupled with the conductive material via electromagnetic forces. Here the Lorentz force is emphasised as this is the major interest in this work (see section 3.2). The induced Lorentz force plays the role of ultrasonic source to generate the desired wavemode in the material. The entire system can be separated into two aspects for simplicity; the induction of the ultrasonic force, and the ultrasound

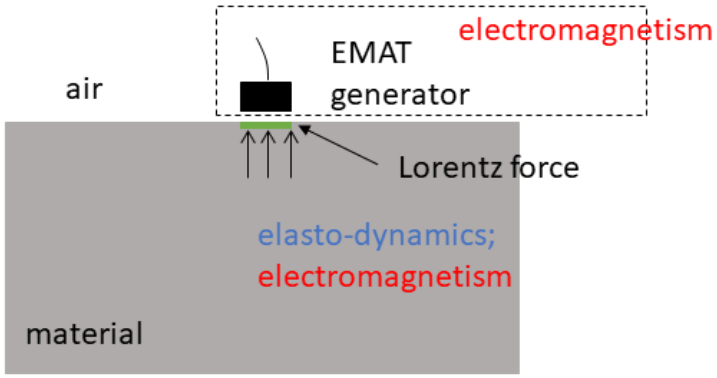

Figure 4.5: Simple 2D model of EMAT generation problem described for FEM solution.

generation. The benefits of doing so are obvious; firstly, it allows for quantitative study of EMAT characteristics. This is essential for an EMAT designer when the physical configuration of the coil and the magnet can significantly affect the ultrasonic source distribution. Secondly, it can significantly save the computation time. The geometric scale of the ultrasonic wavefield (the material) is normally of the order of tens of millimetres, while the EMAT generator is several millimetres. One can hugely improve the efficiency if different geometric discretisation (domain size, meshing fine degree etc) and different analysers (static or transient, in frequency or time domain) are allocated at different modelling stages. For example, a single EMAT model with finer meshing and static solver can be used for understanding the transducer electromagnetic behaviour, while a separate dynamic model for sample wavefield modelling on a larger scale can be formed to understand the beam directivity.

The modelling of the Lorentz force in the EMAT-material system (see red parts in figure 4.5) was undertaken using the commercial package COMSOL Multiphysics 5.5. The modelling was conducted on a computer managed by the Warwick Centre for Scientific Computing (CSC). This was done to understand the Lorentz force distribution when different EMAT lift-offs were used (see section 5.3.1). The relevant physical equations are Maxwell's equations (equations 3.1 to 3.4), applied on the EMAT magnet, coil and material. Figure 4.6(a) demonstrates the basic computational model of the problem. From the top to the bottom, there were five domains that were constructed[1]; air (Ω_1), permanent magnet (Ω_2,), coil (Ω_3), skin

[1]With support from Z. Li, Ultrasound Group, University of Warwick.

effect region (Ω_4) and material (Ω_5). The key domains in the model are the coil (Ω_3) and the skin effect region (Ω_4). While the coil and skin region are normally of the order of a millimetre or less, depending on the driving frequency, the magnet, material and air are much larger, normally of the order of tens of millimetres and hundreds of millimetres, respectively. These are not drawn to scale in the figure for simplicity, but the brightness of the blocks indicates the fineness of their meshing, for example, the meshing for the coil and the skin effect region were much denser than that of the air, magnet and the rest of the material. There are several features of note regarding this model;

1. The coil was modelled by the COMSOL built-in module (the 'Coil' feature in the regime of 'Magnetic Fields' Physics) where the flowing current can be customised. In this work, sinusoidal bursts with the desired number of cycles and central frequency were defined.

2. The polarisation of the biasing magnet field was set according to the real magnet used in the experiment.

3. The size of the skin region (Ω_4) element was rectangular meshed (0.017 mm, 351 per 487 kHz Rayleigh wavelength). This is to ensure the spatial accuracy of the desired eddy-currents field when it is borrowed to generate an ultrasound. The thickness of the material (Ω_5) was set to ten times the skin region. In the rest of Ω_5, the meshing was set to fine (16 per Rayleigh wave length). The EM wave wavelength is much larger for the selected frequency.

All the above manipulations were to make a good tradeoff between the computation accuracy and speed. The finite analyser was stationary and the data of the electromagnetic fields and Lorentz force could be extracted at each set point in the time domain.

The next step for solving the above finite element problem is to transform the governing PDEs and boundary conditions (strong form) into the weak form (integral equations with weaker requirements on the continuity of field variables). Numerical methods or algorithms further approximate the weak formulation into a set of algebraic equations, and so the numerical solution can be obtained easily using computers. More details about the theory of finite element analysis can be found in [203] and on the COMSOL website [204].

The result of COMSOL modelling can be used later for other purposes. Section 7.3.2 used FEM to study the wave directivity from an EMAT generator. The target material thickness was of the order of tens to hundreds of millimetres, and

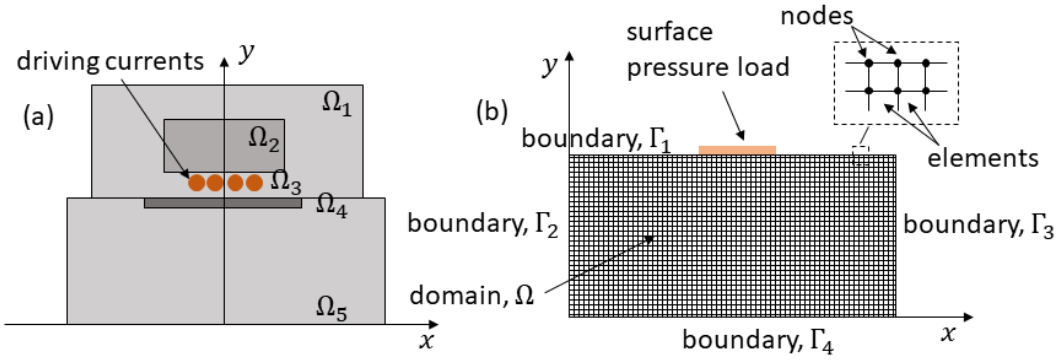

Figure 4.6: Sketches to illustrate the FEM computational model corresponding to the physical model described in figure 4.5. Each physical domain is geometrically discretised into a set of elements with nodes at corners and this is demonstrated in the inset in (b). (a) EMAT FEM model in COMSOL package. Each domain has been discretised but not shown for simplicity. (b) Wavefield model in PZFlex package.

in this case the ultrasonic wavefield modelling (see blue part in figure 4.5) was undertaken by a commercial package PZFlex (now OnScale) for faster transient computation. The modelling was conducted on a dedicated modelling computer on the central server of the Ultrasound Group.

Figure 4.6(b) demonstrates the basic computational model of the problem. There is only a single domain (Ω) which represents the material with several boundaries (Γ_1 to Γ_4). This is a problem that has been simplified, where the EMAT generation was replaced by a surface pressure load onto the material surface to match the load from the chosen EMAT design. This holds because the EMAT generation phenomenon (the Lorentz force mechanism) can be approximated as a surface effect (see section 3.2). The distribution and intensity of the pressure load was identical to the EMAT induced Lorentz force that was studied in COMSOL. The governing equations here are Newton's law (equation 2.7) and Hooke's law (equation 2.2). PZFlex allows users to customise the boundary condition from 'free', 'fixed', 'absorption' and 'symmetric'. While the first two are most common, 'absorption' is very useful for acoustic problems when many wavemodes exists in the same media but only one is of interest, and reflections need to be minimised, and 'symmetric' is useful for further reducing the computation time. It should be noted that absorbing boundaries in this program are set for longitudinal waves and are not perfectly valid for other wavemodes. The FEM in chapter 7 used 'absorption' to study the shear wave behaviour. The meshing fineness of the model formed in chapter 7 was 20 elements per ultrasonic wavelength. This can ensure a good tradeoff between

the modelling accuracy and the computation time [205]. The obtained dataset (displacement/velocity information at each node for the entire wave travelling time) was post-processed in MATLAB.

The full modelling details of each EMAT and the test sample will be given in the relevant sections in chapters 5 and 7. The variables were mainly EMAT geometric size, magnetic field orientation, characteristics of the driving currents (frequency and bandwidth) and the geometry of the test samples.

Chapter 5

Array EMATs: Lorentz force model for Rayleigh wave generation

5.1 Introduction

EMATs used in arrays have drawn more attention recently. Different set-ups have been suggested to configure the geometry of an ultrasonic source array. For example, a meanderline coil with multiple coil turns can be approximated as an array, and this design is dedicated for narrowband surface acoustic wave (SAW) output [182]. Formation of a surface wave array model is therefore the basis of surface crack detection purpose in this thesis, which forms the central focus of this chapter.

In this chapter, the mathematical model of a one-dimensional linear coil array EMAT developed for understanding the behaviour of surface wave (Rayleigh) generation is presented. The ultrasonic generation is through the Lorentz force mechanism. A single linear coil was used as the ultrasonic element. The analytical model in two-dimensions provided by the work [11] was firstly verified, and was used to form the full array EMAT model. The chapter will start from the basics of the single coil generation, with a full discussion of its electromagnetic field distribution for ultrasound generation, then build a one-dimensional linear coil array model.

The spatial behaviour of the model was the main focus of this chapter and the discussion focused on two main aspects; the coil/coil array frequency behaviour in terms of the surface Rayleigh wave generation (at zero lift-off), and the lift-off performances of the coil/coil array when a lift-off between EMAT and sample was applied. In the former, the effect caused by different coil array layouts will be

discussed including the changing of coil width, coil separation and the number of applied coils. For the latter, the calculated spatial behaviour with lift-off was used to verify the lift-off phenomenon described in chapter 2 where the ultrasound frequency will shift with lift-off variation. Both coil and coil array lift-off behaviour will be discussed, including both the time domain and the frequency domain information. The coil electrical variation due to the lift-off effect was not considered in this model, as its electrical characteristics remained similar over the lift-off range studied.

5.2 Experimental set-up for EMAT lift-off study

The experimental work undertaken in this chapter was used for understanding the EMAT lift-off performance and verifying the theoretical model. Two experiments were designed; 1. for single-coil (section 5.3.3) and 2. for two-coil (section 5.6.2) ultrasonic behaviour studies.

The generated experimental process has been introduced in section 4.3. The schematic for the full set-up used in this chapter is given in figure 5.1(a). The in-house built four-channel pulser detailed in chapter 4 was used to drive the EMAT coil. Two non-contact ultrasonic detectors were used to capture the generated Rayleigh signal. The broadband IntOpSys laser interferometer (see section 2.3.3) was first used to measure the signals generated by the single coil EMAT to give a broadband measurement. A racetrack EMAT detector (see section 3.4.1) was then used to measure the signals generated by two-coil EMATs, as this gave a better signal-to-noise ratio (SNR). The effective bandwidth of the EMAT detector was from 0 to 4 MHz [206]. The detected ultrasound signals were recorded by a digital oscilloscope after being amplified. Data processing, including a 50 kHz high-pass filter and smoothing (Savizky-Golay, IR filter, of polynomial order 3), was then performed. All tests were undertaken on an aluminium bar sample whose thickness was 60 mm. Varying the generation EMAT lift-off was done through inserting plastic spacers of thickness 0.1 mm between the EMAT and the sample surface, as indicated in figure 5.1(b), to a maximum of 12 plastic sheet spacers (total lift-off of 1.2±0.1 mm).

Three configurations of linear generation EMAT (see introduction in section 3.4.1) were used, demonstrated in figures 5.1(b) to (d). Each coil was near-identical and had a width of 1.5 mm. The magnet was 25×15×18 mm^3, producing an out-of-plane static field in the z-direction at its centre, and coils were placed onto the magnet in the required positions and held in place using spacers. The magnetic field was predominantly in the z-direction for all coil positions. The configurations

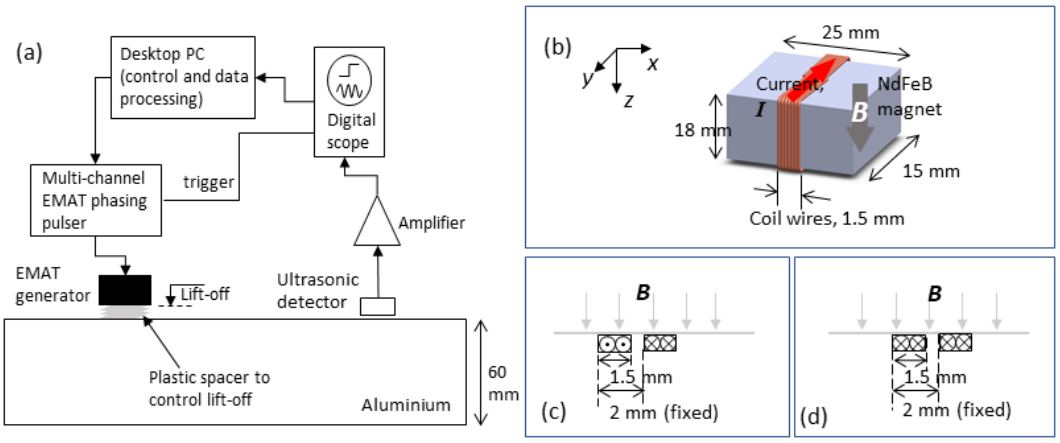

Figure 5.1: Schematic diagram showing the set-up for EMAT lift-off study.

are summarised here:

1. figure 5.1(b); single coil experiment, coil in the centre of the magnet.
2. Figure 5.1(c); meander configuration (opposing currents) for two coils. A fixed physical separation of 2 mm was used. Coils were positioned equidistant from the magnet centre.
3. Figure 5.1(d); normal array configuration (same direction currents) for two coils. The physical separation was also fixed at 2 mm and coils were equally separated from the magnet centre.

5.3 Model of the coil as a finite source

In this work, a coil is used as the source element to form an array EMAT. The desired wavelength of the Rayleigh wave is of the order of sub-millimetres to millimetres for surface crack characterisation, and is comparable to the coil width, which is normally of the order of a millimetre. A coil therefore works as an ultrasonic element with a finite source field whose edge effect cannot be ignored.

A linear coil EMAT (without magnet) is demonstrated in figure 5.2(a) in two-dimensions. The system includes the electromagnetic coupling between the coil and the conductive material. The single coil consists of a series of copper wires and is driven by an alternating current. As introduced in chapter 3, a mirror current (eddy current), $\mathbf{J_e}$, will be induced into the material skin depth region when the coil is placed in close proximity to a conductive material. Three approximations are

given below to simplify the derivation of the coil induced mirror currents when a finite coil width is considered:

1. the physical gaps between the wires are small enough that they can reasonably be ignored. This holds for the EMAT production method used in this work as each loop of wire is wrapped tightly onto the magnet by hand, and gaps will be minimal.

2. The electrical charges are distributed uniformly across the coil width direction. This also holds because the wire is reasonably thin (0.08 or 0.2 mm diameter) and the wire density in a single coil is large enough to make this approximation.

3. The driving (primary) current was of the order of tens of amperes (see section 4.2 for the pulser introduction). The coil induced mirror (secondary) current was weak enough that the mutual effect between the coil primary dynamic magnetic field and the mirror current associated secondary magnetic field [130] was not considered for ultrasound generation. This holds for aluminium samples in this work. There will always be some mutual effect between the primary and secondary fields when the coil electrical characteristics are considered, but this will have minimal impact on the spatial behaviour discussed in this work.

In the two-dimensional space domain (the xz-plane) shown in figure 5.2(a), the mirror current can be calculated using Maxwell's equations (see section 3.2.1). The induced secondary currents in the y-direction (into the page), $J_{e,y}$, are given by [11]:

$$J_{e,y} = \frac{\partial H_x^M}{\partial z} - \frac{\partial H_z^M}{\partial x}, \tag{5.1}$$

where H_x^M and H_z^M are the horizontal and vertical magnetic components of the dynamic magnetic field in the material's skin depth (the superscript 'M' indicates that the physical quantities are within the material). The time oscillator $e^{i\omega t}$ is omitted in the following derivations for simplicity.

The term H_z^M in equation 5.1 is typically neglected in this flat coil set-up, as it is only significant at the edges of the coil and can be very small (approximately zero) under the coil. Equation 5.1 can hence be simplified to,

$$J_{e,y}(x,z) \approx \frac{\partial H_x^M(x,z)}{\partial z}. \tag{5.2}$$

The component H_x^M generated by a current through a single wire for an infinite coil

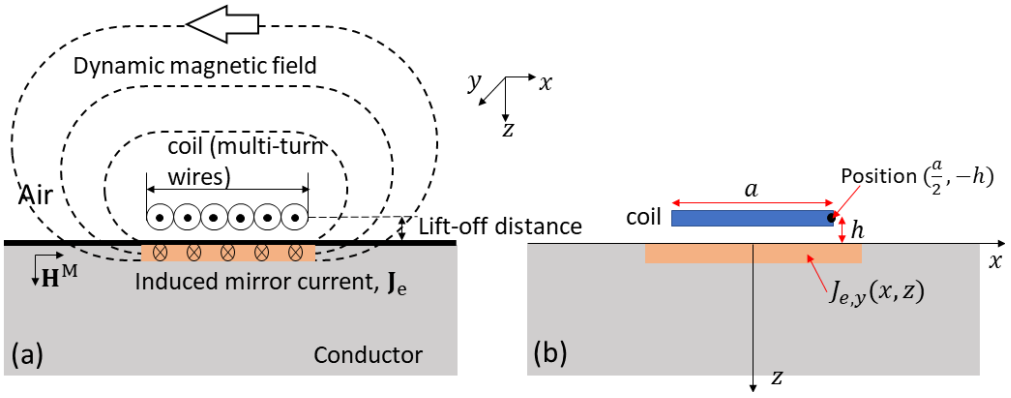

Figure 5.2: (a) The transient electromagnetic fields generated using the EMAT coil. The dashed lines show the direction of the dynamic magnetic field surrounding the coil. A second electrical field (mirror current) is induced in the material. The secondary magnetic field and the mutual effect between primary and secondary fields are not indicated. (b) Simplified calculation model.

width along the x-axis has been calculated in [11],

$$H_x^M = \frac{\bar{\mu} I}{(1+\bar{\mu})\pi} \frac{h}{h^2 + x^2} \exp\left[-\frac{(1+i)z}{\delta}\right], \tag{5.3}$$

where h is the coil lift-off (the vertical distance between the coil and the material surface), δ is the electromagnetic skin depth (see section 3.2.1) and $\bar{\mu}$ is the relative permeability of the material.

A linear coil has multiple turns and therefore a finite width which must be considered when analysing the mirror currents induced. The simplified calculation model is demonstrated in figure 5.2(b). A coil with a finite width a, and a lift-off h is assumed to be located at the coordinate origin. By applying approximations 1 and 2 from the start of this section, the model of the coil is approximated as a very thin sheet of current of width a with a uniform charge (wire) density along x-axis. Using (x_T, z_T) to represent the coil position in the xz-plane in the figure, (x_T, z_T) can be described as being evenly distributed from $(-a/2, -h)$ to $(+a/2, -h)$ under the approximations. The magnetic component H_x^M contributed by a single coil position $(x_T, -h)$ (z_T has been replaced by $-h$) can be found as,

$$dH_x^M = \frac{\bar{\mu} I}{(1+\bar{\mu})\pi} \exp\left[-\frac{(1+i)z}{\delta}\right] \frac{h dx_T}{h^2 + (x - x_T)^2}, \tag{5.4}$$

where x_T continuously varies from $-a/2$ to $+a/2$. The total magnetic field in the

xz-plane can therefore be found by integrating over the coil width, that is,

$$\begin{aligned} H_x^M(x,z) &= \frac{\bar{\mu}I}{(1+\bar{\mu})\pi}\exp\left[-\frac{(1+i)z}{\delta}\right]\int_{-a/2}^{a/2}\frac{h dx_T}{h^2+(x-x_T)^2} \\ &= \frac{\bar{\mu}I}{(1+\bar{\mu})\pi}\exp\left[-\frac{(1+i)z}{\delta}\right] \\ &\qquad \times\left[\arctan\left(\frac{x+a/2}{h}\right)-\arctan\left(\frac{x-a/2}{h}\right)\right]. \end{aligned} \tag{5.5}$$

This equation includes the *spatial* information of the coil induced H_x^M-field in the xz-plane.

Substituting equations 5.3 and 5.5 into equation 5.2 gives:

$$J_{e,y}(x,z) \approx -\frac{(1+i)}{\delta}H_x^M(x,z), \tag{5.6}$$

$$J_{e,y}(x,z) \propto \exp\left[-\frac{(1+i)z}{\delta}\right]\times\left[\arctan\left(\frac{x+a/2}{h}\right)-\arctan\left(\frac{x-a/2}{h}\right)\right] \tag{5.7}$$

Equation 5.7 shows that the distribution of $J_{e,y}$ induced in the y-direction depends on the position (x,z) within the material, but also depends on the coil geometry and its location, given by (a,h). Note that this follows the methods outlined in reference [11] where the time variation is omitted for the calculations. The eddy current contains an extra factor of ω due to the eddy current being related to the time differential of the dynamic magnetic field [127], but this is omitted in this work as it will have a limited effect on the spatial behaviour. The nonlinear factor $\exp\left[-\frac{(1+i)z}{\delta}\right]$ indicates that the induced $J_{e,y}(x,z)$ will exponentially decay into over the material depth (z direction), as expected.

In the work of [130], $J_{e,y}(x,z)$ at a single depth of $z = 0.01$ mm was chosen to present the distribution along the x-axis. A square or sinusoidal shape of coil induced $J_{e,y}$ was shown. For typical ultrasonic frequencies in metals, the effective region over which there is a non-negligible $J_{e,y}$ is relatively thin. The coil field of the EMAT can therefore be approximated by calculating the total mirror current contribution from all depths,

$$\begin{aligned} \tilde{J}_{e,y}(x) &= \int_0^\infty J_{e,y}(x,z)dz \\ &\propto \left[\arctan\left(\frac{x+a/2}{h}\right)-\arctan\left(\frac{x-a/2}{h}\right)\right]. \end{aligned} \tag{5.8}$$

This allows one to simplify the distribution of mirror current from a two-dimensional (xz-plane) description to a one-dimensional (x-axis) problem.

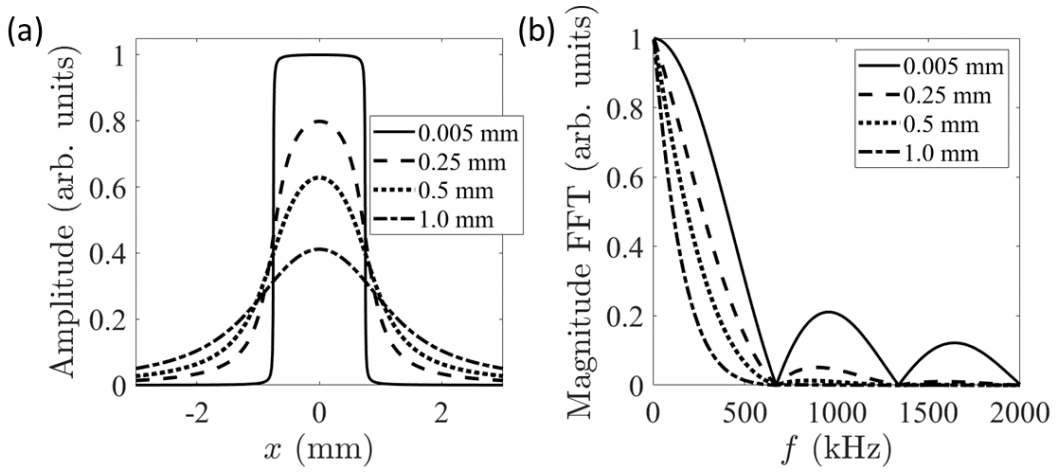

Figure 5.3: The changing profile of the EMAT coil induced mirror current field with the lift-off. (a) the coil profile in space domain. (b) The response of (a) in frequency domain. The single coil is with a 1.5 mm width. Different lift-offs are indicated by the legend.

5.3.1 Distortion of the induced electromagnetic fields with lift-off

Equation 5.8 was used to calculate the spatial behaviour of the mirror current as the lift-off was increased. Since a practical EMAT coil is a finite rather than a point source, the mirror current will experience a visible distortion when the lift-off is increased by the same order of magnitude as the coil width, as described by equation 5.7.

An example of $\tilde{J}_{e,y}$ calculations are given in figure 5.3. The linear coil was set to a width of a =1.5 mm and the current profile is given at different lift-offs (h varied from 0.005 mm to 1.0 mm). It can be observed that the mirror current exhibits a significant change as lift-off is increased, with the current intensity dropping and the profile of the induced mirror current broadening. The corresponding frequency response of the coil profile is given in figure 5.3(b). The coil gives the maximum response at 0 Hz (or a DC signal) at zero lift-off, and the first minimum occurs at around 600 kHz. The single linear coil has been extensively used for low frequency generation, driven by a wideband pulse [81, 207]. As lift-off increases, the higher frequency peaks experience significant magnitude reduction. The bandwidth of the low frequency region is also reduced, and so the single coil performance is limited to low frequencies.

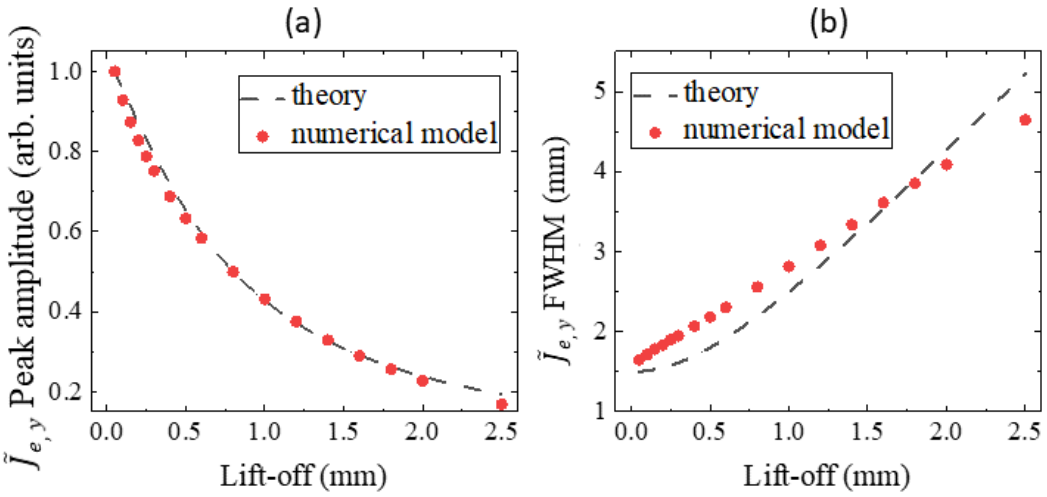

Figure 5.4: Comparisons between the COMSOL numerical modelling and the theoretical calculation. (a) shows the peak amplitude of the mirror current as a function of lift-off and (b) is the full width half maximum (FWHM) of the current profile.

Validation of the theory using a FEM model

Numerical modelling was performed to validate the behaviour of $\tilde{J}_{e,y}$ for a more realistic set-up where the wires in the coil were considered separately rather than a uniform current block. The commercial package COMSOL MultiPhysics 5.5 was used. The modelled coil consisted of seven turns of wire, each with a diameter of 0.2 mm, giving a total width for the coil of 1.5 mm when including a small physical gap between each wire. Aluminium was chosen as the testpiece, with dimensions of 15×5 mm (width×thickness). The frequency of the current was 487 kHz, chosen to match a frequency where the ultrasound experiments gave a good signal-to-noise ratio. The lift-off of the coil was varied from 0.05 mm to 2.5 mm (from 0.05 to 0.3 mm with a 0.05 mm interval, from 0.3 to 0.6 mm with a 0.1 mm interval and from 0.6 to 2.0 mm with a 0.2 mm interval). The total current density over the depths within the material was found at each lift-off.

Figure 5.4 shows the results for the theory (equation 5.8, black dash lines) and the COMSOL numerical model (red points). Two parameters, the peak amplitude and the full width half maximum (FWHM) of the FFT of the current density are plotted. Good agreement is seen between the predictions and the numerical modelling, particularly in the peak amplitude. The FWHM shows a small discrepancy, due to the simplifications of the analytical model which assumes the current profile is a single rectangular block of current. Despite this small discrepancy, over the practically usable lift-off range of the EMAT there is reasonably good agreement,

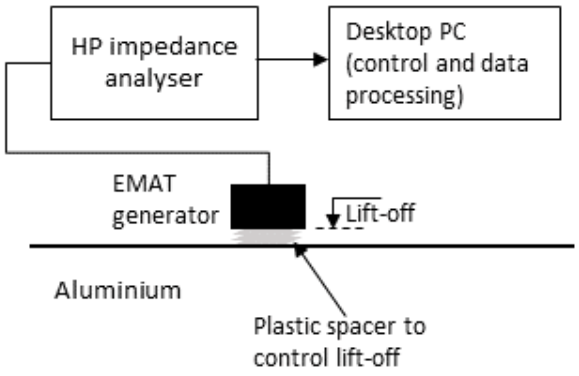

Figure 5.5: Experimental set-up for coil impedance test. A HP impedance analyser was used.

and the current amplitude and spatial behaviour are the primary considerations when interpreting the lift-off behaviour. Therefore the simplified model described by equation 5.8 is used for comparison with the experimental data as it offers ease of interpretation of the behaviour.

5.3.2 Validation of the coil electrical characteristics

The coil electrical characteristics with lift-off were assumed to remain constant in the mode developed. However, significant changes with lift-off have been found in some broadband EMAT systems (see problem described in section 3.2.4). This section provides the experimental validation that for this system the driving current signal and electrical characteristics of the coil can be approximated as constant.

The single coil EMAT shown in figure 5.1(b) was tested. The experiment includes two tests measuring; the driving current flowing through the EMAT coil, and the coil impedance change, both with lift-off. The driving signal was a single-cycle burst centred at 487 kHz. This is to match with the lift-off study given in section 5.3. The experimental set-up for measuring the driving current was the same as that in figure 4.3(b). The lift-off change was made by inserting plastic spacers between coil and sample. The set-up for measuring coil impedance change with lift-off is shown in figure 5.5, where an HP impedance analyser was used to test the coil resistance and inductance. The testing range of the lift-off for these tests was from 0.1 (no spacers, but considering the Kapton tape layer between the coil and the sample surface) to 1.5 mm (14 spacers).

The current output of the pulser in the time domain was plotted as a function of lift-off, with results given in figure 5.6(a). A FFT was then taken and the peak

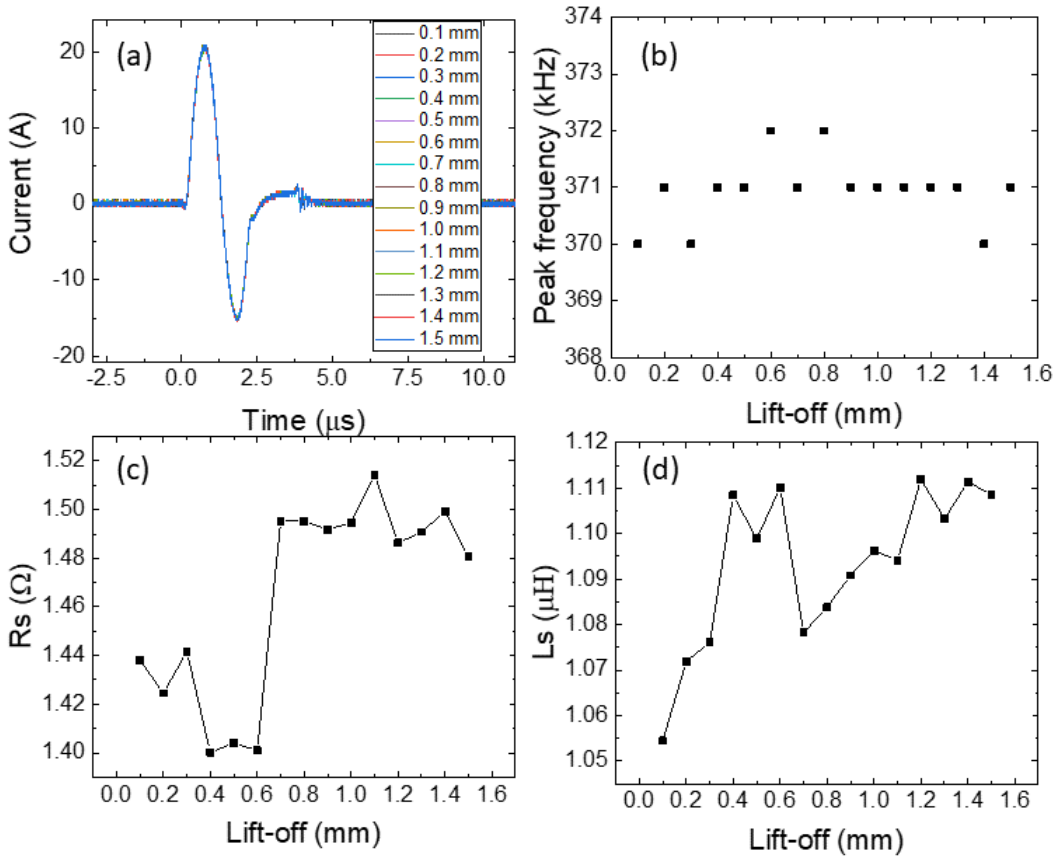

Figure 5.6: Lift-off test of the coil electrical characteristics. (a) Driving current profile with lift-off. (b) Peak frequency in the fast Fourier Transform (FFT) of (a). (c) and (d) are the coil resistance and inductance information, respectively.

(frequency at which the FFT showed a maximum value) is plotted as a function of lift-off in figure 5.6(b). This was to evaluate the current frequency shift effect with lift-off. It can be clearly seen that the current through the coils was approximately constant over this range with no consistent variation with lift-off. Therefore the input current for the models can be treated as constant.

Figures 5.6(c) and (d) show the resistance and inductance of the coil, respectively. Both show only very small variations (less than 7.5% for resistance and less than 4% for impedance) over the lift-off range considered. Again, the changes show only a small trend with increasing lift-off and hence the coil electrical characteristics can be taken as being approximated constant.

Finally, the self-field generation mechanism was tested by removing the magnet. No self-field generation was observed. Therefore, the approximations in the model of the generation being due to just the static field, and a constant behaviour of the input current, are appropriate.

5.3.3 Surface wave generation via Lorentz force mechanism

In this work, the surface wave generation is through the Lorentz force mechanism, as the testing samples were aluminium and are non-magnetic. For the 2-D model presented in figure 5.2(a), with a large static magnetic field directed into the sample ($B_{0,z}$), and assuming that the dynamic magnetic field generation (self-field) can be ignored, the Lorentz force (equation 3.24) can be considered using scalars for simplicity. Only the x-component needs to be calculated,

$$\mathbf{F}^{(L)} \approx \mathbf{F}_s^{(L)} = F_s^{(L)} \vec{\boldsymbol{\imath}}, \tag{5.9}$$

where $F_s^{(L)}$ is the magnitude of the Lorentz force generated by the static magnetic field and the mirror current. Combining equations 3.24, 5.8 and 5.9 gives,

$$F_s^{(L)}(x) = \tilde{J}_{e,y}(x) B_{0,z}. \tag{5.10}$$

If the static field is treated as a constant over all lift-offs, the Lorentz force magnitude is proportional to $\tilde{J}_{e,y}$, and the spatial profile of the EMAT force is then identical to that of the mirror current. The generated force due to the static field is then in-plane. The approximation of the static magnetic field as being constant is not true when lift-off is changed; however, the primary effect is a reduction in field at the surface which will affect the amplitude of the generated ultrasound waves, but not the frequency behaviour.

The OP component of the magnetic field ($B_{0,z}$) provided by the block magnet was measured using a Gauss meter for multiple lift-offs, and incorporated into the model via equation 5.10 such that the appropriate value was used for each lift-off. An approximately exponential drop-off of field with lift-off was observed. The field effect will be illustrated with the coil spatial calculation in the discussion later.

The convolution model for surface wave generation

The generic process of surface wave generation using single coil EMATs has been described previously using the coupling between the EMAT source field and the lattice field [56, 57, 130]. This is a convolution between the temporal driving function $y(t)$ and the spatial profile of the coil. Where there are multiple wires in a coil, each separate piece of wire can be treated as a single linear source, and a linear sum of the contributions from each line source gives the final detected signal. For Rayleigh surface wave generation, one should consider the phase lag between each generated signal, and the total displacement contributed by all the wire turns in a complete single linear coil is given by [10, 130],

$$u^y(t, x, z) \propto F^{(L)}(x, z) \otimes y(t), \tag{5.11}$$

where $\otimes$ denotes convolution, $y(t)$ indicates the driving signal of the EMAT coil (input current) and the spatial profile of the coil ($F^{(L)}(x, z)$) can be described by equations 5.8, 5.9 and 5.10 for this work. The above convolution model has also been validated for EMAT detection [206, 208] where a racetrack coil was used for receiving the ultrasound.

The wave motion u^y can be measured as a function of time at a point P. For example, the out-of-plane component (motion in z-direction) can be measured by using the laser interferometer introduced in section 2.3.3, defined as $s(t)$. Combining equations 5.8 to 5.11, the measured displacement signal, $s(t)$, can hence be written as,

$$s(t) \propto F_s^{(L)}(x) \otimes y(t), \tag{5.12}$$

$$s(t) \propto \tilde{J}_{e,y}(x) \otimes y(t)\ . \tag{5.13}$$

Converting the spatial signal, which is a function of x, to one written as a function of time t by using $t = x/c_R$, where c_R is the phase velocity of the Rayleigh wave, equation 5.13 can be rewritten as,

$$s(t) \propto \tilde{J}_{e,y}(t(x)) \otimes y(t). \tag{5.14}$$

This is to simplify the calculation from the spatial-temporal domain to a single temporal domain. The above equation forms the central theoretical basis of this chapter. It shows that the behaviour of the generated Rayleigh wave depends on the mirror current distribution, which is affected not only by the driving current signal temporal behaviour, but also by the coil geometry (width a) and lift-off (h). To evaluate the distortion of the EMAT field with lift-off, broadband signals (one-cycle inputs) for the EMAT driving current were used for all lift-off analysis. The ultrasonic behaviour of the single coil with lift-off will be studied in the following section, and that for the coil array (section 5.4) will be given in section 5.6.

5.3.4 Ultrasonic frequency shift with lift-off

The ultrasonic behaviour due to the changing spatial profile of the mirror current for a single linear coil with lift-off is discussed here. An experimental study was undertaken to validate the effect described by the theoretical model, with the set-up shown in figure 5.1(a).

The lift-off results for the single coil lift-off are given in figure 5.7. The theoretical prediction for ultrasonic generation is first shown. This uses $\tilde{J}_{e,y}$, as shown in figure 5.3, for a coil positioned at the origin with a width of $a = 1.5$ mm. The simulated driving signal $y(t)$ was a single-cycle sinusoidal wave, centred at 487 kHz. Figures 5.7(a) and (b) show the behaviour calculated using equation 5.14 in both the time and the frequency domain for h from 0.2 to 0.8 mm. Similarly to the spatial change of $\tilde{J}_{e,y}$ with lift-off, the generated ultrasound also experiences a waveform broadening. The corresponding frequency spectrum shows not only that the amplitude is reduced with increasing lift-off, but the peak frequency in the FFT is also decreased. The frequency shift effect is primarily due to the distortion of the current profile as the same driving signal ($y(t)$) was used for all lift-offs. Figure 5.7(c)&(d) shows the corresponding experimental results. Good agreements can be observed between the theory and the experiment in both the time domain and the frequency domain. The signal-to-noise ratio in the experiment is smaller, limiting the lift-off range in the practical use.

To compare the theoretical and experimental results more precisely, quantified studies on the change in peak frequency and the change in amplitude of the signals with lift-off were performed. The outputs were measured as a function of lift-off, shown in figures 5.8(a) for peak frequency shift and (b) for amplitude drop, respectively. The shift in peak frequency was approximately linear, and a linear fit was made to quantify the trend for experiment and calculated results. It can be seen that the linear fit lines for experiment and calculation show a small offset of around

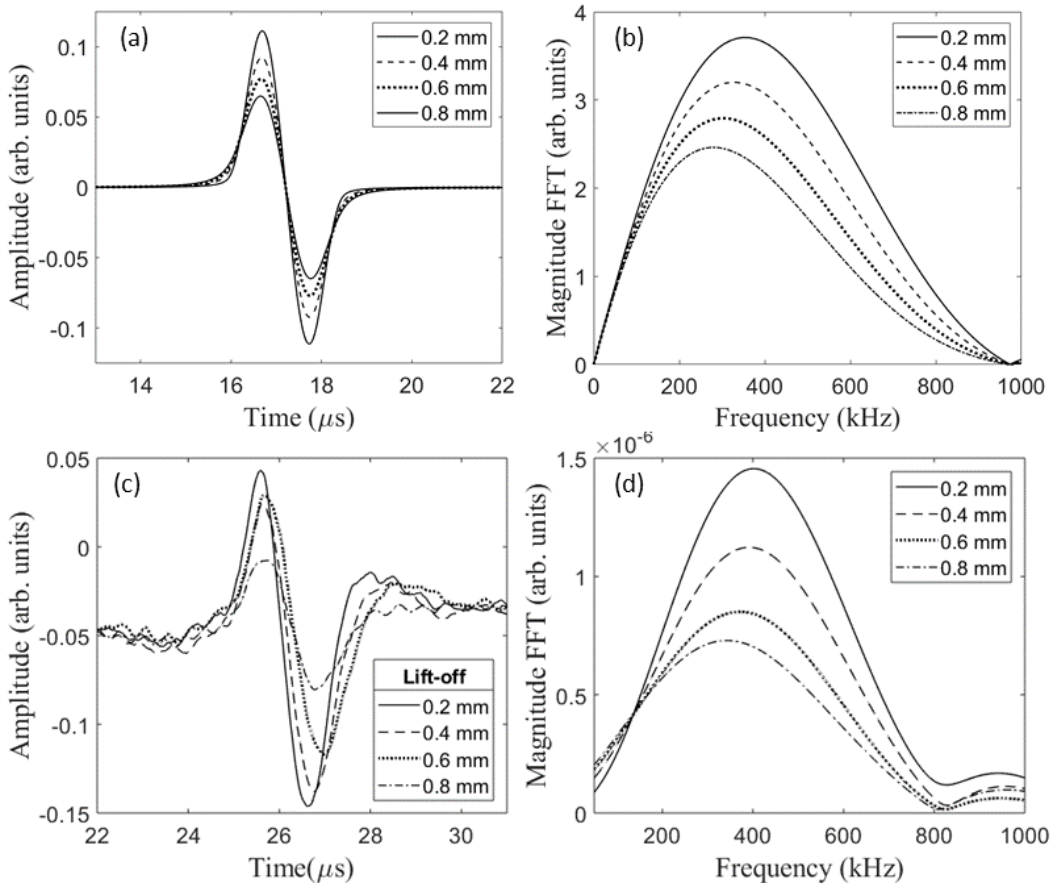

Figure 5.7: The generated ultrasound signal using a 1.5 mm wide single linear coil EMAT with lift-off. (a) and (b) are the predicted signals using the calculations of equation 5.14. (c) Signals measured using laser interferometer and (d) FFTs of the data presented in (c).

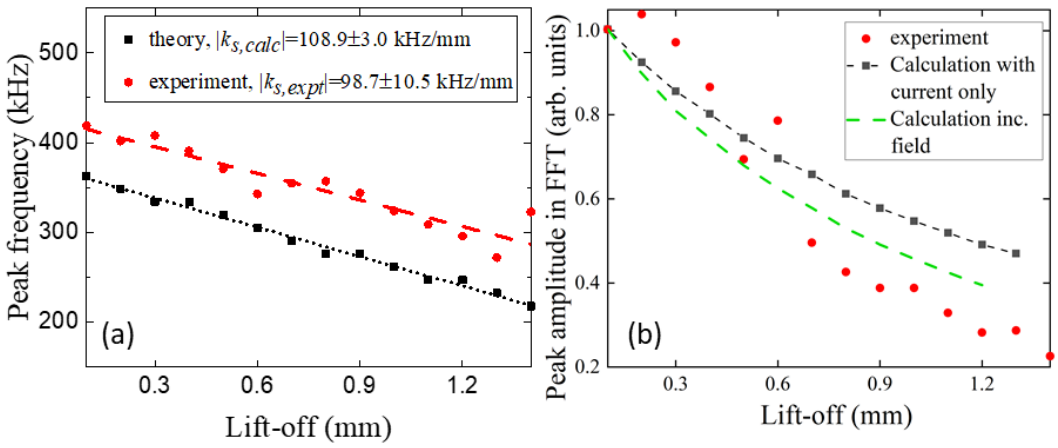

Figure 5.8: Comparison between the experiments and the theoretical prediction. (a) The shift of the peak frequency, (b) the magnitude decrease of the peak in FFT with lift-off.

50 kHz, but have very similar slopes. Multiple factors contribute to this offset; mismatch between the simulated ideal driving frequency and the EMAT pulser output (the latter was not as broadband as a perfect single-cycle pulse, so the resultant ultrasound shows a reduced bandwidth), the physical gap due to the glue and tape used to seal the coil that cannot be accurately controlled for in the measurement lift-off value, and the small variation of the permanent magnetic field [146]. Some scatter is observed in the experiment at higher lift-offs, and this is due to the limited signal to noise ratio during the experiment, especially at high lift-offs. The slopes k, which give the rate of frequency shift with lift-off, agree well within errors, with slopes of $k_{s,expt} = 99 \pm 11$ kHz/mm and $k_{s,calc} = 109 \pm 3$ kH/mm obtained.

Figure 5.8(b) shows the change in magnitude of the FFT peak, normalised to a value of one for the smallest lift-off (0.1 mm here). An exponential fit to the data of the form $A\exp[-\alpha h]$ gives values of $\alpha_{calc} = 0.71$ and $\alpha_{expt} = 1.44$. The calculated model only considers the spatial effect; other factors will also significantly affect the lift-off. The model using the calculation of the current and a constant magnetic field is shown by the black points and line, while a model incorporating the measured variation of the magnetic field with lift-off is shown in green. The current-only model underestimates the change in magnitude, as expected, while the calculation including the field shows a much better prediction of the behaviour. This model does not exactly describe the behaviour, and a full model including the coil electrical behaviour and change in impedance with lift-off would show better agreement; however, this very simple model explains the majority of the change in signal amplitude for a single coil EMAT with lift-off.

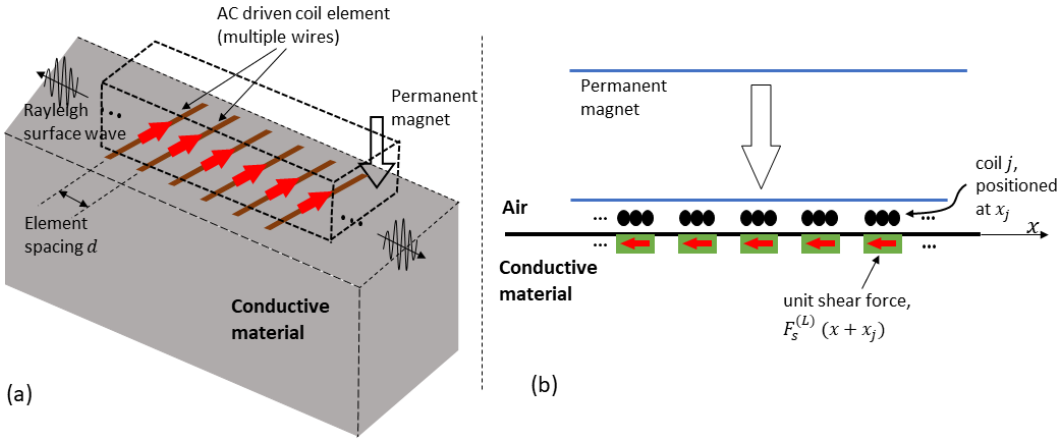

Figure 5.9: Geometry of the linear coil array. (a) 3-D schematic diagram showing a linear coil array EMAT on a conductive material. (b) Cross-section view of the array presented in (a). The generated Lorentz force is emphasised, shown in green blocks under the sample surface. Coil element j is positioned at x_j on the surface, and its force expression is $F_s^{(L)}(x + x_j)$ using the single coil model $F_s^{(L)}$ in section 5.3.2.

Despite the disagreement between the prediction based on the model and the experimental results, the single coil behaviour when considered as a finite ultrasonic element fits well to the predictions of this simple spatial model. The following sections will discuss the formation of a coil array EMAT for Rayleigh wave generation and its corresponding lift-off performance, treating the single linear coils as elements of the array.

5.4 Formation of linear coil arrays for Rayleigh wave generation

A normal array EMAT could consist of multiple linear coils. The development of the work in this thesis starts from configuring a 1-D coil array. Figure 5.9(a) demonstrates the array EMAT geometry on a conductive material. Multiple linear coils with a fixed spacing, d, are used as the array elements. Each coil is driven by an AC current. A block permanent magnet is used to provide the static magnetic field that is directed into the sample surface ($B_{0,z}$). The testing sample is non-magnetic, and the EMAT generation is through the Lorentz force mechanism. The coil induced mirror current is small enough in this work that the self-field generated Lorentz force is again not considered here.

Figure 5.9(b) shows the array cross-section view. Each coil element is identical to the single coil model introduced in section 5.3. The mirror current polarisation

is approximated as out-of-phase to the driving current, but not shown here. Explanations of the single coil model and the mirror current characteristics are given in sections 5.3.1 and 3.2.1, respectively. The generated Lorentz force from each coil is due to the interaction between the out-of-plane static magnetic and the mirror current, and is shown by green blocks. The force direction is in-plane (shearing), illustrated by the red arrows.

The array generated Lorentz force is a superposition of the force components contributed by each of the coil elements ($F_s^{(L)}(x)$ for a single linear coil, section 5.3.2). The Rayleigh surface wave that is generated by such an ultrasonic force array will propagate along the material surface in the positive or negative x-direction. For a coil element (coil j) located at position x_j, the force expression along x-axis is $F_s^{(L)}(x + x_j)$. Taking a linear combination of these forces, the total Lorentz force model of the coil array can be written as

$$f_s^{(L)}(x) = \sum_{j=1}^{N} F_s^{(L)}(x + x_j), \tag{5.15}$$

when N linear coils in total are applied to form the array.

The 1-D linear array given in figure 5.9(a) shows all currents on the coils acting in the same direction. A meander coil, another important array configuration, has the currents acting in alternating directions, i.e. anti-parallel to the neighbouring coil. Considering both ways of coil polarisation, a coefficient l is added to amend equation 5.15, giving

$$\begin{aligned} f_s^{(L)}(x) &= \sum_{j=1}^{N} l \times F_s^{(L)}(x + x_j) \\ \text{where } \; l &= \begin{cases} (-1)^{j+1} & \text{coils with alternating polarisation,} \\ 1 & \text{coils with parallel polarisation.} \end{cases} \end{aligned} \tag{5.16}$$

The full expression of $F_s^{(L)}$ can be found in equations 5.8 and 5.10. The spatial performance of the coil array is discussed from two aspects in the following two sections: 1. the array spatial performance for Rayleigh surface generation without lift-off variation. This includes the analysis of coil parameters, a (coil width), d (coil spacing) and N (applied coil number). 2. the array lift-off performance. This includes analysis of the array behaviour when lift-off h is varied.

5.5 Array spatial impulse response

The narrowband nature of an ultrasonic array with a linear periodic source pattern, such as a meander-coil, has previously been used to select a Lamb wave mode or Rayleigh wave wavelength [3, 57]. Constructive interference occurs when the source element spacing is carefully designed such that the undesired Rayleigh wavelengths or Lamb wave modes can be efficiently suppressed. Full constructive interference can be obtained by an ideal point source array. However, for a surface wave EMAT, the coil elements are of finite width, and the wavelength selectivity performance is limited. Very thin coils, such as the design of a meander coil in [192], were used to give 2.0 MHz frequency Rayleigh wave operation for detection of sub-mm surface cracks, but the signal-to-noise ratio and the lift-off performance was reduced due to the thin coils required.

The array EMAT performance, either as a meander coil or the linear coil array constructed in this work, needs to be optimised. Section 5.3.2 showed that the single coil model gave a surface wave displacement that can be predicted by the convolution between the coil force distribution in the space domain ($F_s^{(L)}$) and the driving signal in the time domain (y). This section focuses on the force distribution characteristics of the coil array, for its capability of pure wavelength/frequency generation. By separating out the driving signal effect, just the force model is studied, giving the spatial impulse response.

The spatial response of the linear array with an arbitrary coil number N, coil element width a and element spacing d is discussed. The aim is to find the upper limit of the workable frequency range for a certain array design, and identify the maximal coil element width to achieve the chosen frequency. This allows accurate frequency control with a good signal to noise ratio.

Firstly, the EMAT is operated without any lift-off ($h = 0$). The Lorentz force for a single linear coil with a width a (equations 5.8 and 5.10) at zero lift-off, that is positioned at $x = 0$, can be normalised to a rectangular function, $\bar{F}_s^{(L)}$,

$$\bar{F}_s^{(L)}(x) = \begin{cases} 1 & |x| \leq a/2, \\ 0 & \text{otherwise.} \end{cases} \tag{5.17}$$

The behaviour of an ultrasonic array when all elements are identical ($l = 1$ in equation 5.17) has been studied previously, for example in [23, 35, 57]. This work focuses on the meander configuration as it is more commonly used for EMAT design. The shear force array for such an array can also be updated to a set of rectangular functions at zero lift-off. Given that a coil spacing d is applied, equation 5.16 for

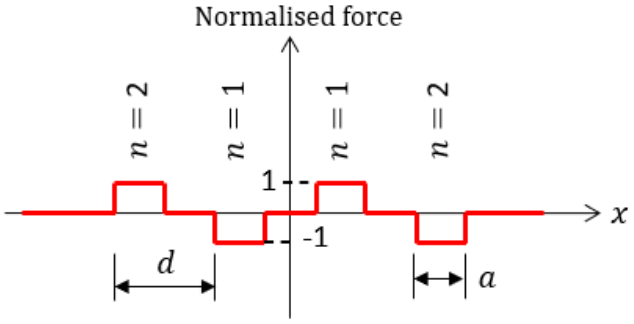

Figure 5.10: Normalised force profile for two pairs of coils. The current is taken to be passing through each coil in alternating directions. This forms the spatial model of the EMAT induced Lorentz force array.

$l = (-1)^{j+1}$ (array operated in pseudo-meander configuration) is updated to,

$$\bar{f}_s^{(L)}(x) = \sum_{n=1}^{N_{di}} (-1)^n \times \left\{ \text{rect}\left[\frac{x - (n-1/2)\,d}{a}\right] - \text{rect}\left[\frac{x + (n-1/2)\,d}{a}\right] \right\}$$

$$\text{where} \quad \text{rect}(u) = \begin{cases} 1 & |u| \leq \dfrac{1}{2}, \\ 0 & \text{otherwise}, \end{cases} \tag{5.18}$$

where N_{di} indicates the total number of coil dipoles, i.e. the number of coil pairs with alternating current directions, and n denotes which pair is being considered, with each coil in the pair equidistant from the origin. A schematic diagram of the normalised force array generated by this array is given in figure 5.10 for $N_{di} = 2$, showing the coil pair numbering used throughout.

To obtain the spatial impulse response of the coil array, equation 5.18 is transformed into the wavenumber domain by taking the Fourier transform of $\bar{f}_s^{(L)}(x)$, that is,

$$\begin{aligned} \hat{\bar{f}}_s^{(L)}(k) &= \int_{-\infty}^{\infty} \bar{f}_s^{(L)}(x) e^{-ikx} dx, \\ &= \sum_{n=1}^{N_{di}} (-1)^n \left[\int_{-a/2+(n-1/2)d}^{a/2+(n-1/2)d} e^{-ikx} dx - \int_{-a/2-(n-1/2)d}^{a/2-(n-1/2)d} e^{-ikx} dx \right]. \end{aligned} \tag{5.19}$$

Given that $\int e^{-ikx}dx = \frac{i}{k}e^{-ikx}$, the above expression can be simplified to,

$$\begin{aligned}
\hat{\tilde{f}}_s^{(L)}(k) &= \sum_{n=1}^{N_{di}}(-1)^n \frac{i}{k}\left[\left(e^{ik(n-\frac{1}{2})d} - e^{-ik(n-\frac{1}{2})d}\right)\left(e^{\frac{ika}{2}} - e^{\frac{-ika}{2}}\right)\right] \\
&= \sum_{n=1}^{N_{di}}(-1)^n \frac{i}{k}\left\{2i\sin\left[k\left(n-\frac{1}{2}\right)d\right]2i\sin\frac{ka}{2}\right\} \\
&= -\frac{4i}{k}\sin\left(\frac{ka}{2}\right)\sum_{n=1}^{N_{di}}(-1)^n \sin\left[k\left(n-\frac{1}{2}\right)d\right] \\
&= -4di\sin\frac{ka}{2}\sum_{n=1}^{N_{di}}(-1)^n\left(n-\frac{1}{2}\right)\mathrm{sinc}\left[k\left(n-\frac{1}{2}\right)d\right], \qquad (5.20)
\end{aligned}$$

where k is the wavenumber.

The above equation states that the response of the array spatial model has a functional dependence on both a, d and N_{di}. In practice, ultrasound generation is normally defined by the temporal frequency f. For a non-dispersive Rayleigh wave, c_R shows no dependency on k, and hence the Fourier response in k-domain (equation 5.20) can be updated into the f-domain by substituting the relationship $k = 2\pi f/c_R$. Thus, the spatial response of the coil array in the temporal frequency domain, $g(f)$, can be obtained,

$$g(f) = -2di\sin\left(\frac{\pi a}{c_R}f\right)\sum_{n=1}^{N_{di}}\left\{(-1)^n(2n-1)\,\mathrm{sinc}\left[(2n-1)\frac{\pi d}{c_R}f\right]\right\}. \qquad (5.21)$$

The modulus of $g(f)$ is used to define the frequency behaviour for the linear coil array, and the terms can be separated,

$$\begin{aligned}
&|g(f)| \equiv T(f) = \alpha(d)D(f,a)H(f,d,N_{di}), \\
&\text{where } \alpha(d) = 2d, \\
&\qquad D(f,a) = \left|\sin\left(\frac{\pi a}{c_R}f\right)\right|, \qquad (5.22) \\
&\qquad H(f,d,N_{di}) = \left|\sum_{n=1}^{N_{di}}\left\{(-1)^n(2n-1)\,\mathrm{sinc}\left[(2n-1)\frac{\pi d}{c_R}f\right]\right\}\right|.
\end{aligned}$$

Here α is a separation-dependent coefficient, $D(f,a)$ is defined as the spatial function of the coil element width, a, and $H(f,d,N_{di})$ is the spatial function of the array geometry, depending on the coil spacing, d, and the number of coil dipole pairs, N_{di}.

$D(f,a)$ and $H(f,d,N_{di})$ both exhibit periodicity. Figures 5.11(a) and (b)-

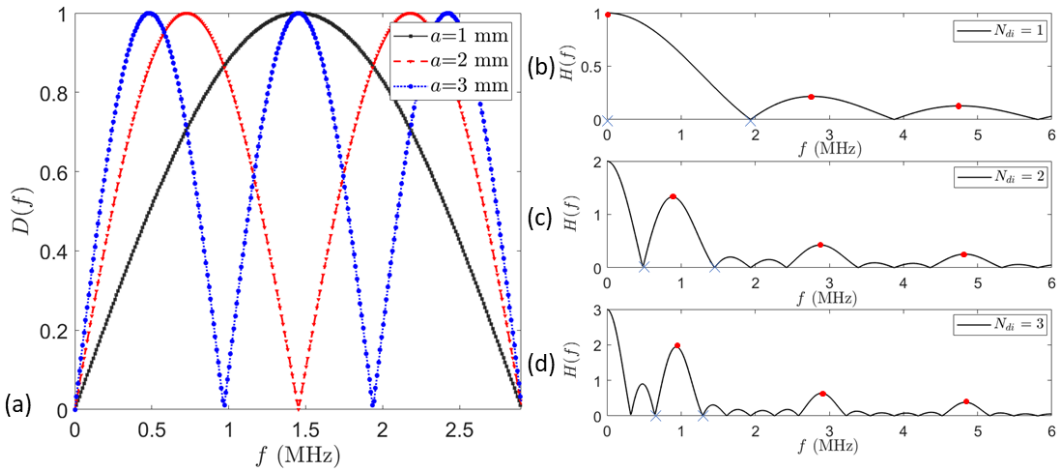

Figure 5.11: Example $D(f,a)$ and $H(f,d,N_{di})$. c_R=2906 m/s. (a) $D(f,a)$ is shown for a =1, 2 and 3 mm. (b)-(d) $H(f,d,N_{di})$ is shown for d =1.5 mm and N_{di} = 1, 2 and 3 respectively.

(d) show several examples for function $D(f,a)$ and $H(f,d,N_{di})$ respectively. For function $D(f,a)$, the spatial period is found as c_R/a from the 'sin' function. On increasing a from 1 to 3 mm, the value of the period is reduced and more peaks appear within the same chosen frequency range, i.e. one peak at 1.45 MHz for a=1 mm, two peaks at 0.72 and 2.2 MHz for a=2 mm, and three peaks at 0.5, 1.45 and 2.4 MHz for a=3 mm. The peak frequencies appearing in each spatial period can be calculated by the relation $f_p^D = (2m-1)c_R/2a$, where f_p^D is used to represent the peak frequency of function $D(f,a)$ and m is an integer, denoting the mth period in the f-domain.

The behaviour of $H(f,d,N_{di})$ is not sinusoidal, as can be seen from figures 5.11(b) to (d). Examples for N_{di}= 1, 2 and 3 and d =1.5 mm are shown. A series of main peaks occur in the spectrum of $H(f,d,N_{di})$, and become sharper with increasing N_{di}, as expected. The periodicity depends on both d and N_{di}. Unlike $D(f,a)$, where the term $\left|\sin(\frac{\pi a}{c_R}f)\right|$ is repeated in each spatial period (c_R/a), $H(f,d,N_{di})$ is expressed by the 'sinc' function, and its amplitude exhibits a non-linear damping with increasing f. The value of the spatial period of $H(f,d,N_{di})$ can be found as c_R/d, and is about 1.94 MHz for d = 1.5 mm in the figure. Single or multiple maxima can occur within each spatial period, for example, when N_{di} = 1, there is only one peak in each spatial period (see figure 5.11(b)), i.e. 0 MHz is the peak from 0 to 1.94 MHz (first period), 2.75 MHz is the peak from 1.94 to 3.88 MHz (second period) and so on. When $N_{di} \geq 2$, more peaks are observed within each period. The number of peaks is determined by the coil dipole number, N_{di}, i.e.

$2N_{di}+1$ when $N_{di} \geq 2$, for example 3 peaks per period for $N_{di}=2$, 5 for $N_{di}=3$ and so on. The target peaks that dominate the array wavelength/frequency are highlighted by the red spots in figure 5.11(b)-(d). Note, the peak of 0 MHz is not considered for $N_{di} \geq 2$. With the increasing of N_{di}, the bandwidth of these target peaks become sharper. Quantitative study of these peaks is given below to better study the array frequency behaviour.

The peak frequency that provides the greatest magnitude in each period is defined as f_p^H for $H(f,d,N_{di})$. To find f_p^H, several procedures are taken,

1. find the zero-crossing of $H(f,d,N_{di})$. This was undertaken by using the mathmactical property of the 'sinc' function. The two nearest zero-crossings within a period are approximated as $\frac{N_{di}-1}{2N_{di}-1}\frac{c_R}{d}$ (left) and $\frac{N_{di}}{2N_{di}-1}\frac{c_R}{d}$ (right) on the f-axis, when N_{di} is used. These correspond to 0 and 1.94 MHz for $d=1.5$ mm and $N_{di}=1$, 0.65 and 1.29 MHz for N_{di}=2, and 0.77 and 1.16 MHz for N_{di}=3, highlighted by blue crosses in figures 5.11(b) to (d).

2. The value of the peak frequency (f_p^H) is therefore between the left zero-crossing and the right zero-crossing.

3. The bandwidth between the two zero-crossings can be calculated by their difference, that is, $\frac{c_R}{(2N_{di}-1)d}$ from the zero-crossings given in procedure 1.

4. The bandwidth ($\frac{c_R}{(2N_{di}-1)d}$) is decreased with increasing N_{di}.

5. If N_{di} becomes infinitely large, the bandwidth $\frac{c_R}{(2N_{di}-1)d}|_{N_{di}\to\infty}=0$ holds and the peak frequency f_p^H is given by $\frac{N_{di}-1}{2N_{di}-1}\frac{c_R}{d}|_{N_{di}\to\infty}=c_R/2d$.

It can be concluded that f_p^H approaches the limit $c_R/2d$ when N_{di} is large. This matches well with the rule of thumb that $f=c_R/2d$ due to the coil spacing setting the wavelength, and is defined as the limit frequency $f_p^*=f_p^H|_{N_{di}\to\infty}=c_R/2d$ in this section for later comparison.

The frequency behaviour of the full response $T(f)$ depends on the product of $D(f,a)$ and $H(f,d,N_{di})$, and will give a peak magnitude response at a frequency f_p^T. The behaviour splits into three regimes which depend on the array geometry: $d>a$, $d=a$ and $d<a$.

For $d>a$ and $N_{di} \geq 2$, the layout of the coil array matches with a conventional meander coil. Figure 5.12 shows examples of $T(f)$ when a =1.5 mm, d =2.0 mm, and N_{di} =2, 3 or 4. Since $a<d$, the spatial period of function $D(f,a)$

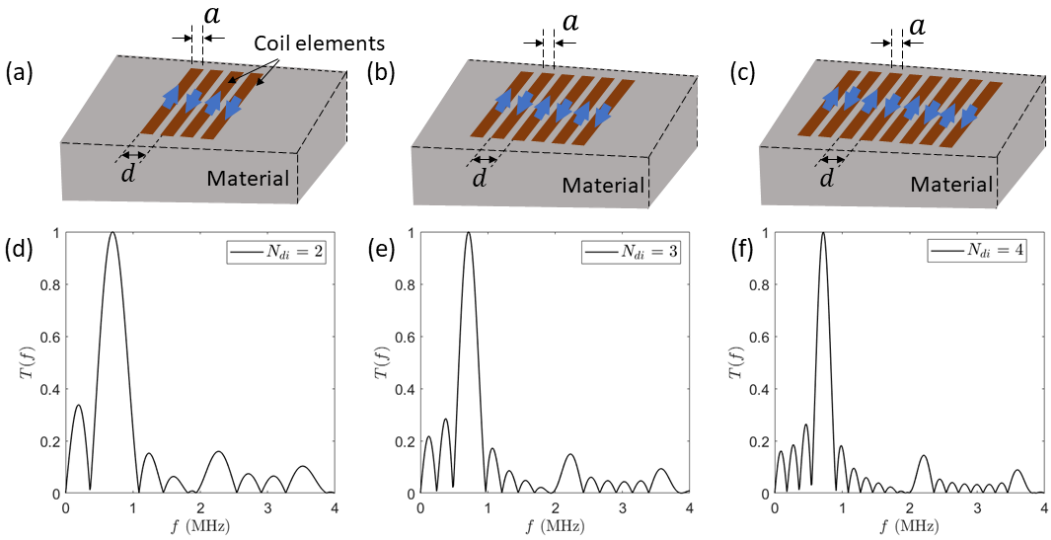

Figure 5.12: Examples showing the behaviour of the linear coil array when it is configured as a meander coil. a = 1.5 mm, d =2 mm and N_{di} for (a) 2, (b) 3 and (c) 4. c_R = 2906 m/s. The corresponding frequency behaviour, $T(f)$ is shown from (d) to (f).

is much larger than that of the function $H(f, d, N_{di})$, and hence the position of the resultant f_p^T is dominated by f_p^H. When N_{di} is increased from 2 to 4, the resultant bandwidth to $T(f)$ at f_p^T becomes narrower, as expected (due to the narrower bandwidth of $H(f, d, N_{di})$). f_p^T =0.70, 0.71 and 0.72 MHz for N_{di} =2, 3 and 4 respectively, and will reach $f_p^* = c_R/2d = 0.73$ MHz when N_{di} is large enough.

For $N_{di} = 1$, the system has a single pair of coils. The behaviour of function $H(f, d, N_{di})$ for $N_{di} = 1$ is different from that of $N_{di} \geq 2$, as shown in figure 5.11(b), and $f_p^H = 0$ in the first spatial period for $N_{di} = 1$. This would have an impact on $T(f)$. The resultant f_p^T will be determined by both the period of functions $D(f, a)$ and $H(f, d, N_{di})$. Figure 5.13 shows the scenario when only a single coil pair is used. The width of each coil is fixed at 1.5 mm while the coil spacing d decreases from 2.5 mm ($d > a$) to 1.5 mm ($d = a$). The behaviour of the full response $T(f)$ is shown in (a) and the geometry of the single pair array in 2-D is shown in (b) to (d) for d =2.5, 2.0 and 1.5 mm, respectively. A more broadband spectrum of $T(f)$ for $N_{di} = 1$ compared to $N_{di} \geq 2$ (figure 5.12) can be observed. The target f_p^T (highlighted by the red spots in figure 5.13(a)) continuously increases with the decrease of d. f_p^T is 0.52, 0.62 and 0.72 MHz for d =2.5, 2 and 1.5 mm, respectively. Note, f_p^T for d = 2.0 mm here matches well with the peak frequency of the two-coil out-of-phase model for the lift-off study in figure 5.17(a) (zero lift-off model), confirming the consistency of this chapter.

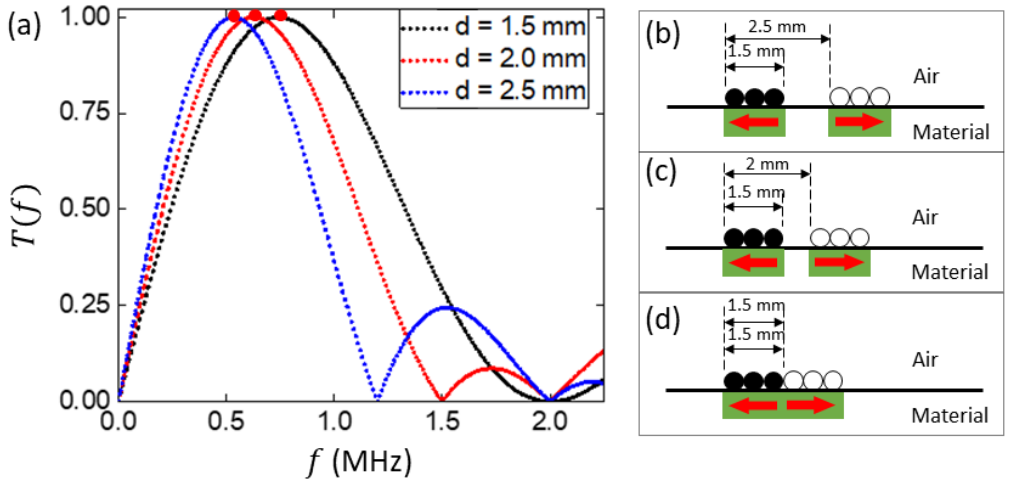

Figure 5.13: Behaviour of a single dipole pair array ($N_{di} = 1$). $c_R = 2906$ m/s and $a = 1.5$ mm. Different coil spacings (d =1.5, 2 and 2.5 mm) are shown. (a) shows the behaviour of their full response $T(f)$. (b)-(d) show the array 2D configuration when different d was used. The current direction is indicated by wire colour (black and white meaning alternating polarisation). The coil induced Lorentz force is shown in green blocks and the arrow indicates the direction of the shear force.

A special case was formed when $d = a = 1.5$ mm (figure 5.13(d)). In this case, there is no space between the coils. This configuration recreates a racetrack coil EMAT (see section 4.1). In the work of [206], a square wave model for a ractrack coil was proposed and the peak frequency of the model was found to be $0.761c_R/2d$, when the total width of the coil was 1.5 mm. The same behaviour of f_p^T can be found by numerically solving $T(f)$ (equation 5.22) if the array parameters are set to $a = d = 0.75$ mm and $N_{di} = 1$, mimicking the same racetrack shape. This agreement confirms the reliability of this work.

Since the value of d is critical to the frequency behaviour of an array coil, the demand for high frequency operation requires a small d. The physical design limit is where more coil pairs ($N_{di} \geq 2$) are used but no physical gap is present between each nearest neighbour ($d = a$). This is the limit when fabricating a meander coil, and it is hard to physically achieve. The regime when $d < a$ is not practical for an EMAT array design since the coils start to overlap with each other. The electromagnetic fields of the array become complicated and are not discussed in this work. Chapter 6 introduces the concept of phasing to obtain smaller effective separations.

It is essential to know the frequency at which operation of a coil array will be optimal for different design parameters. Considering the results of f_p^T for $N_{di} = 1$ and $N_{di} \geq 2$ at $d = 2$ mm (figures 5.13(c) and 5.12), f_p^T =0.6, 0.7, 0.71 and 0.72 MHz

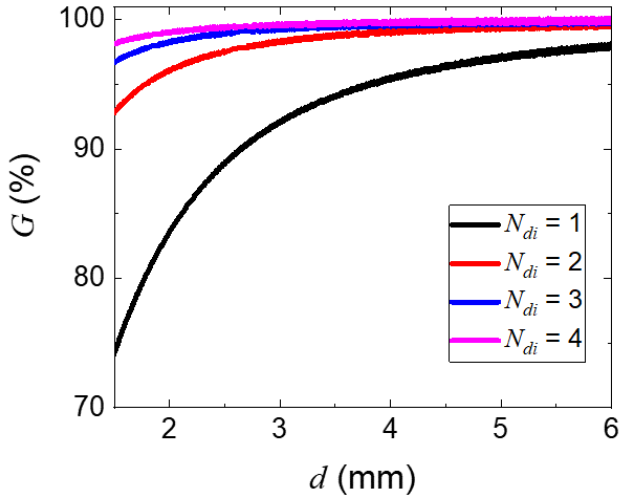

Figure 5.14: Behaviour of the ratio of the frequency generated to that designed (equation 5.22). a is fixed at 1.5 mm. d increases from 1.5 mm to 6.0 mm. N_{di} at 1, 2, 3, 4 are chosen to compare.

as N_{di} is varied from 1 to 4. To study in more detail the influence caused by the coil number, a dimensionless quality G is defined,

$$G = f_p^T(d, N_{di})/f_p^*(d) \tag{5.23}$$

by comparing the peak obtained with the limiting frequency f_p^*, which is the upper limit that will be obtained by an infinite N_{di}. f_p^T was numerically solved using equation 5.22 at each chosen d and N_{di}. a was fixed at 1.5 mm. G is plotted as a function of d in figure 5.14 for $N_{di} = 1$ to 4 and $d \geq a$.

It can be seen that f_p^T always approaches f_p^* when d increases. However, there is a dependence on N_{di} when d becomes smaller. When the system desired peak frequency (or wavelength) is low (large), d is much larger than a and the coil element can be approximated as a point source, giving closer to the ideal frequency output. However, when d becomes comparable to a, the drop of f_p^T is obvious and the influence of the coil finite width a cannot be neglected. Meanwhile, an array with a large N_{di}, for example N_{di} =3 or 4 in the figure, can lead to a higher f_p^T than that for a small N_{di} (N_{di} =1 or 2 in the figure). The reduction of f_p^T due to the effect of a can be compensated for by using more coils (large N_{di}), especially for a high frequency purpose when d is required to be small. The result of $N_{di} = 2$ providing a $f_p^T = 0.928 f_p^*$ is better than $N_{di} = 1$, which only provides $0.744 f_p^*$ at $d = a = 1.5$ mm. The results of N_{di} =3 or 4 are better, as they are $0.968 f_p^*$ and $0.98 f_p^*$, respectively.

In summary, an array with more elements is a better spatial filter (wavelength/frequency) than that one using fewer elements. In practice, arrays with N_{di} =2 to 3 are suitable designs, making a good balance between the transducer size and the frequency performance.

5.6 Array performance with lift-off

Section 5.3 describes the lift-off effect of a single linear coil when generating Rayleigh surface waves. The effect of lift-off on the designed linear coil array also needs to be understood, particularly when the interaction between the neighbouring coils with finite coil separations is non-neglegable. This section discusses the ultrasonic behaviour when a coil array EMAT is applied with lift-off. The single coil model described in section 5.3 was used to predict the array behaviour, and both theoretical analysis and experiments using the array were undertaken. The spatial distortion of the mirror current of the array is extensively studied in this section. Other factors such as the coil electrical variation with lift-off or the magnet field distortion with lift-off are not emphasised, as they will be similar to the behaviour for a single coil.

5.6.1 Cross-talk from the neighbouring coil

Sections 5.4 and 5.5 discuss the EMAT array behaviour using multiple linear coils without lift-off. In such an 1-D linear array, the coil induced mirror currents within the sample surface region will experience interaction with the currents generated by their nearest neighbours, with the interaction changing as the spatial behaviour of the currents changes with lift-off. Figure 5.15 illustrates such a cross-talk effect when a four-coil array is applied for two lift-offs, (a) h_1 and (b) h_2. It can be seen that the mirror currents partially overlap with each other. The spatial area of the overlapping region is widened when the lift-off is increased ($h_2 > h_1$). This indicates that the cross-talk between coils becomes more significant at higher lift-offs.

5.6.2 Two-coil model

The simplest form of a coil array is considered in this section using two identical linear coils ($N_{di} = 1$). The two coils are separated by a distance of d and are located symmetrically about the origin, with each having the same value of lift-off (h). Considering the single coil mirror current (equation 5.8), the induced mirror currents from each of the coils can be represented as $\tilde{J}_{e,y}(x - d/2)$ for the right hand coil, and $\tilde{J}_{e,y}(x + d/2)$ for the left hand coil.

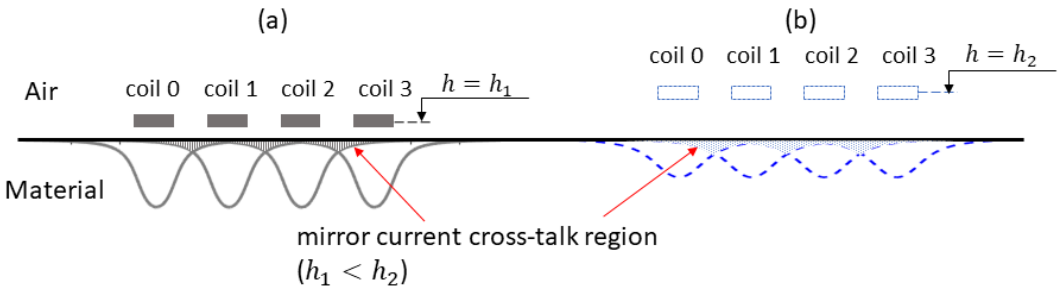

Figure 5.15: Schematic showing the interaction of the underneath mirror currents when a four-coil array is applied at lift-off (a) h_1 and (b) h_2 where $h_1 < h_2$. The spatial profile of the coil induced currents is shown in the material surface region and the cross-talk from the neighbouring is filled by gray color in (a) and blue color in (b).

To form a general model, the two coils are assumed to be independent. Any phase lag between the coils need to be considered. Here, an extra time factor $\exp(i\omega t^{'})$ is added. This is applied for the coil located at $(-d/2, h)$ (left hand coil), where $t^{'}$ indicates the time delay of the current activation between the two coils. The total current distribution contributed by these coils is,

$$\tilde{J}_{e,y}^{tot} = \tilde{J}_{e,y}(x - d/2) + \exp(i\omega t^{'}) \times \tilde{J}_{e,y}(x + d/2). \tag{5.24}$$

From the above equation, different distributions of the model can be obtained by varying the delay factor $t^{'}$. Assuming that $t^{'}$ is within one time period of the particle motion T_0 ($T_0 = 1/f$), that is $0 < t^{'} \leq T_0$ and $-1 \leq \exp(i\omega t^{'}) \leq 1$, two scenarios can be classified and are illustrated below,

- when $T_0/4 \leq t^{'} < 3T_0/4$ and $\exp(i\omega t^{'}) \leq 0$, the two coils are polarised in opposite directions and behave like a dipole, with the limiting result of $\exp(i\omega t^{'}) = -1$ describing the meander-coil-like set-up;
- when $0 < t^{'} < T_0/4$ or $3T_0/4 \leq t^{'} \leq T_0$ and $\exp(i\omega t^{'}) \geq 0$, two coils are polarised in the same current direction, with $t^{'} = 0$ or T_0 corresponding to currents in the same direction with the same phase.

The above discussion is demonstrated in figure 5.16. The figure shows the current profile of two coils, coil 1 (right hand) and coil 2 (left hand). While coil 2 is modulated by the factor $\exp(i\omega t^{'})$, coil 1 is fixed in the temporal domain. A small lift-off is applied to both coils and the desired profile is slightly distorted along the x-direction. This is to distinguish from the standard rectangular shape for zero lift-off analysed in sections 5.4 and 5.5. The figure focuses on the effect of $t^{'}$ as it

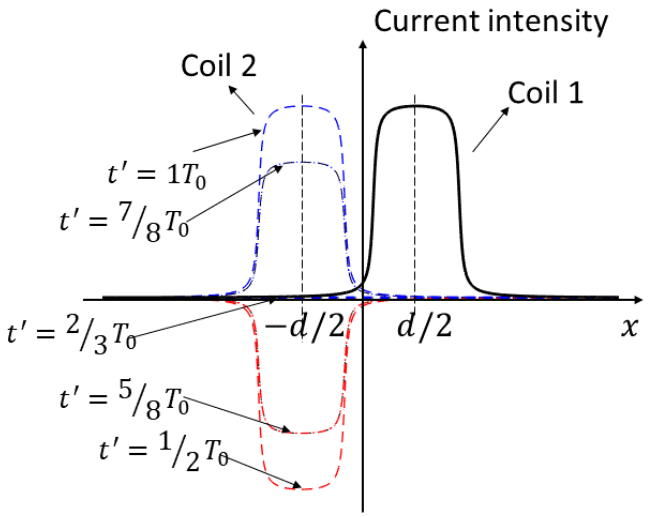

Figure 5.16: Schematic showing the effect of the phase difference between the two coils. Two identical linear coils are assumed to be located at $-d/2$ and $d/2$. The figure shows the induced current distribution of the two coils as two individual sources. $t^{'}$ applied to coil 2 is varied from $t^{'} = T_0/2$ to $t^{'} = T_0$. A small lift-off is assumed.

is increased from the half period point $T_0/2$ to a whole period T_0. The other half period will repeat the results. Coil 2 is shown by the red dashed line from $t^{'} = T_0/2$ to $t^{'} = 2T_0/3$. The current is in the opposite direction to that in coil 1, and the current amplitude decreases from the negative maximum to zero. The cross-talk region near the origin is cancelled due to the presence of such a dipole effect. Coil 2 is then shown by blue dashed lines from $t^{'} = 2T_0/3$ to $t^{'} = T_0$. The amplitude increases from zero to the positive maximum. The two coils have currents flowing in the same current direction in this situation, and the cross-talk region is enhanced.

While figure 5.16 indicates the two-coil with an arbitrary phase lag, this thesis emphasises two extreme conditions; 1. $t^{'} = T_0$, the two coils are in phase (a standard array configuration). 2. $t^{'} = T_0/2$, the two coils are out of phase (mimicking a meander-coil). The total currents for these configurations are written as,

$$\tilde{J}^{tot\pm}_{e,y} = \tilde{J}_{e,y}(x - d/2) \pm \tilde{J}_{e,y}(x + d/2), \tag{5.25}$$

where '$-$' denotes out-of-phase behaviour and '$+$' is in-phase. The effect of the coil width a and the lift-off variation h on the field distribution $\tilde{J}_{e,y}(x)$ is immediately obvious as these factors are included in.

Calculation of these currents ($\tilde{J}^{tot\pm}_{e,y}$) are shown in figure 5.17 (red solid

lines) for two-coil is operated out-of-phase (figures 5.17(a) to (e)) and in-phase (figures 5.17(f) to (j)). The behaviour for a single coil centred on the origin (black dashed lines) is also shown for comparison. The coils had $a = 1.5$ mm, coil spacing $d = 2.0$ mm, and lift-off distances of 0 to 0.8 mm. The upper panels show $\tilde{J}_{e,y}^{tot\pm}$ after normalisation in the spatial domain, such that the single coil behaviour has a peak value of 1 at each lift-off. The lower panel shows the corresponding behaviour in the frequency domain.

For figures 5.17(a) to (e) (out-of-phase configuration), it can be seen that the coils give a spatial behaviour similar to a square wave (spatial domain) at zero lift-off, as expected. The frequency of the peak in the frequency behaviour of the current is at about 625 kHz. This is different from the prediction obtained by the simple equation $\lambda = 2d$, where one would expect a frequency of 725 kHz in aluminium. This has been explained in section 5.5 and is mainly due to the finite width of the coils. As lift-off is increased, the current profile becomes a dipole, and the peak in the frequency behaviour shifts to about 330 kHz at 0.8 mm.

For figures 5.17(f) to (j) (in-phase configuration), two identical rectangular shapes in the spatial behaviour can be observed at zero lift-off. As lift-off is increased, the two currents 'merge' to become effectively a single coil with a larger width at very high lift-off. This distortion has a significant impact on the frequency behaviour, especially on the high frequency bandwidth. Although the FFT of the two-coil remains at about twice the magnitude of that for the single coil at low frequencies, there is a significant attenuation at higher frequencies (above 1 MHz in this set-up) with increased lift-off. This variation in the generated mirror currents will have a significant impact on the frequency of the generated ultrasound.

5.6.3 Time domain waveform distortion

A single coil EMAT can experience an ultrasound frequency shift due to the lift-off distortion effect, and EMATs in the coil array design will also exhibit a similar phenomenon due to the distortion, but with different behaviour due to the cross-talk between the neighbouring coils. This section discuss the ultrasonic behaviour of the two-coil model formed above, including both the out-of-phase and the in-phase configurations. The ultrasonic frequency behaviour is the central focus here. Details of the experimental set-up are as given in section 5.2.

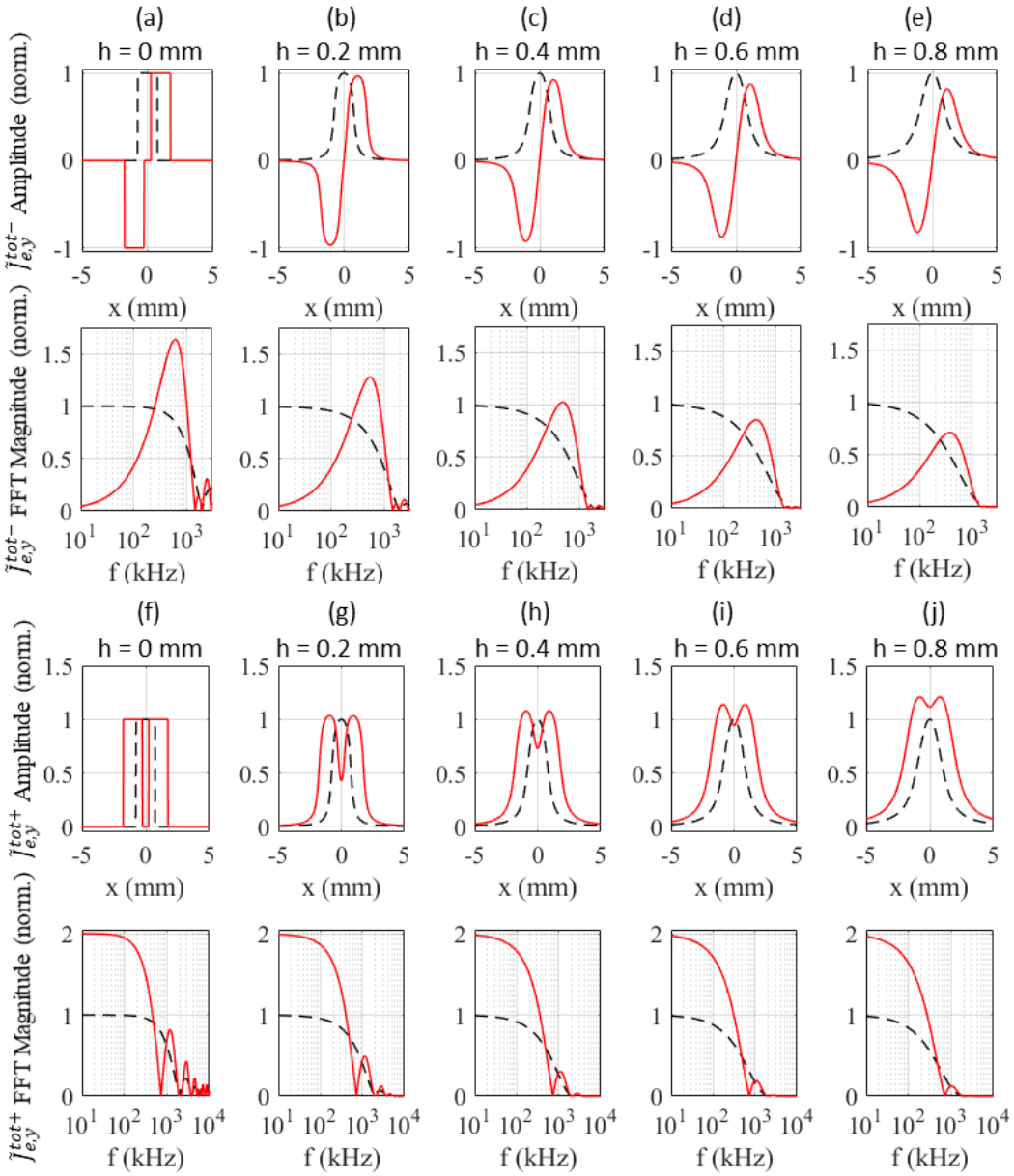

Figure 5.17: Underneath cross-talk from the neighbouring coil. (a) to (e) show the lift-off behaviour of the two-coil model (solid red lines) when two coils are out-of-phase (mimicking a meander-line coil). (f) to (j) show when two coils (solid red lines) are in-phase (mimicking a normal 1D array). The spatial behaviour is given in the upper panel while the corresponding frequency behaviour is given in the lower panel. The single coil behaviour is given by dashed black lines for comparison.

Two-coils out-of-phase

There is a preferred frequency which is related to the separation of coils when multiple (two) coils are used in an array, as explained before. As shown in figure 5.17, a peak at around 625 kHz for 2 mm separation is shown for the two-coil out-of-phase configuration. A singe-cycle pulse with 625 kHz ($y(t)$) was therefore used to drive these coils for both theoretical predictions and experiential measurements. Results are shown in figure 5.18. The prediction for ultrasound generation using equations 5.14 and 5.25 is given in figures 5.18(a) and (b) in the time and frequency domains, respectively. The FFTs have been normalised so that the peak value at each lift-off had a maximum magnitude of 1. This is to emphasise the frequency shift effect. The corresponding experimental results are given in (c) and (d). The lift-off was varied from 0.1 to 1.2 mm, but only 0.2, 0.4, 0.6, 0.8 and 1.0 mm are shown for clarity.

It can be seen that the overall shape of the time domain waveform is maintained during the increase of lift-off, but an elongation is observed alongside a reduction in amplitude. Note that the experiment was polarised in the opposite direction to the model. The corresponding frequency behaviour exhibits a decrease in the peak frequency, which is similar to the behaviour of the single coil. For the experimental results shown in figures 5.18(c) and (d), the signals keep a similar shape with some distortion, and are in qualitative agreement with the calculation results.

To compare the frequency shift effect between the experiment and theoretical prediction, the peak frequency in the FFTs are plotted as a function of lift-off, shown in figure 5.19. The frequencies have been normalised, so that the peak frequency at zero lift-off had a maximum value of 1. The decreasing trends are clearly seen. A generally good agreement is obtained. Some discrepancies occur at high lift-offs ($h \geq 0.6$ mm). This is attributable to two factors; firstly, the inaccuracy of the analytical model for higher lift-offs explained in figure 5.4. Secondly, the reduced signal-to-noise ratio in the experiment when lift-off was increased.

Two-coils in-phase

A high frequency that was predicted to give a large amplitude signal (see figure 5.17(f)) was chosen for the two-coil in-phase configuration (see figure 5.17(f)). A frequency of 900 kHz (a frequency between the first maximum (0 kHz) and the second maximum (1200 kHz)) was chosen to drive the coils. This should be high enough to validate the high frequency attenuation behaviour with lift-off. Figure 5.20 shows the results of both the theoretical prediction (figures 5.20(a) and (b)) and the exper-

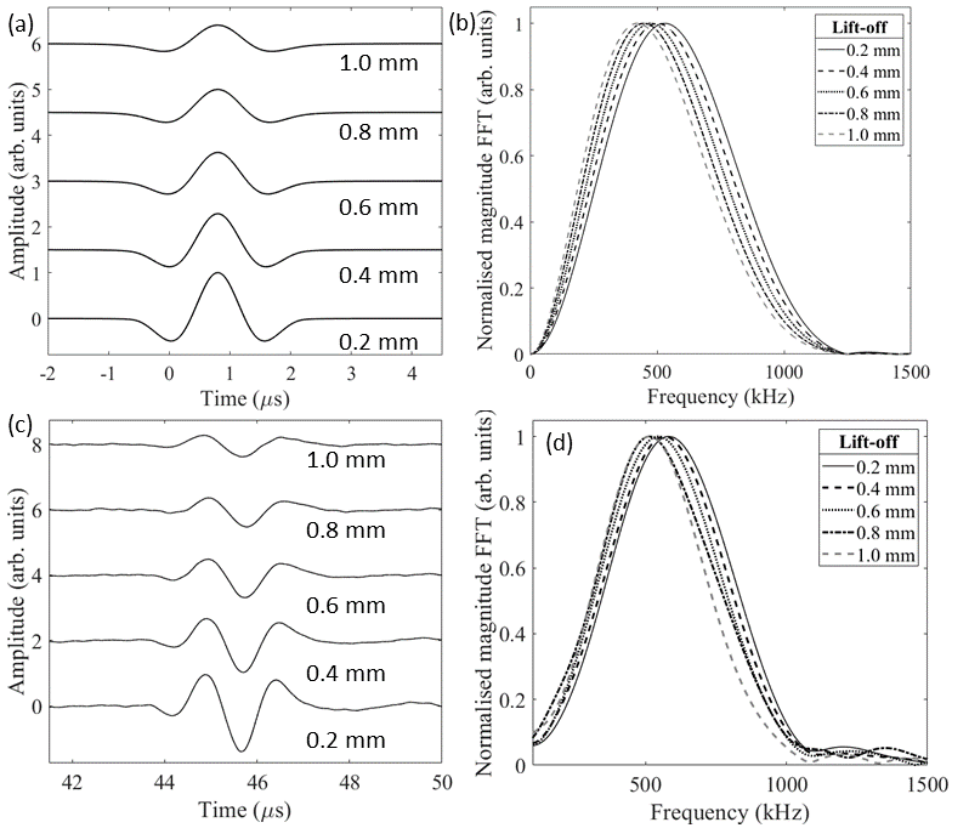

Figure 5.18: Lift-off behaviour for the two-coil out-of-phase EMAT generating a Rayleigh surface wave. The physical separation between the coils was 2.0 mm and the driving frequency was 625 kHz. The theoretical prediction is in (a) and (b), while the measured signal using an EMAT detector is given in (c) and (d). (a) and (c) are A-scans while (b) and (d) are the corresponding FFTs.

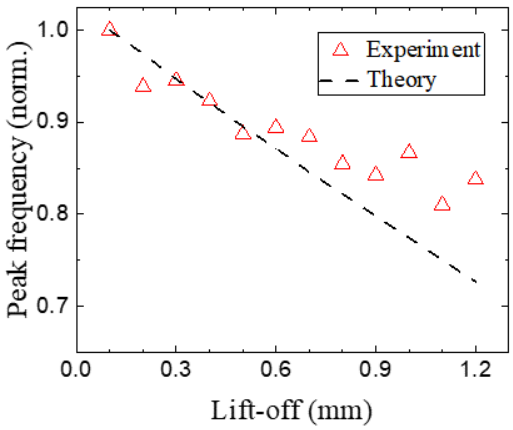

Figure 5.19: Comparing the shift of peak frequency in the FFT of the theoretical calculation (data shown in figure 5.18(b)) and experiment (data shown in figure 5.18(d)).

iment (figures 5.20(c) and (d)) in the time domain and the frequency domain. The theoretical calculation was based on equations 5.14 and 5.25. The driving signal, $y(t)$, was single-cycle centred at 900 kHz.

In the theoretical prediction, a clear waveform distortion with lift-off can be seen in the time domain. At 0.2 mm lift-off, the waveform is a non-standard two-cycle wave. The waveform was significantly distorted when the lift-off was increased; two cycles merged into only one cycle as with the final result in the single coil. The in-phase signals from the two coils overlap at the centre of the pulse train, giving the distinction waveform pattern observed. The shape of this depends on the coil separation and the frequency chosen for operation. There are two maxima observed in the frequency spectrum, corresponding to the low frequency peak and the high frequency peak, respectively, as expected (the low frequency bandwidth and the first harmonic shown in figures 5.17(f)-(j)). The magnitude FFT has been normalised to the value of second peak ('1'), so that the variation of the two peaks can be compared at different lift-offs. It can be seen that the low frequency peak dominates as lift-off is increased. This observation agrees well with the coil frequency predicted expected in figure 5.17. The experimental results (figures 5.20(c) and (d)) show qualitative agreement with the prediction, although an extra half cycle is observed in the time domain. This can be attributable to two aspects; 1. influence from the EMAT detector. The model was assumed to be captured by a point detector, while the used racetrack detector has a finite bandwidth. 2. The actual driving signal was not as ideal as the modelled single-cycle pulse used for prediction.

A quantitative study on ultrasound frequency characteristics was then per-

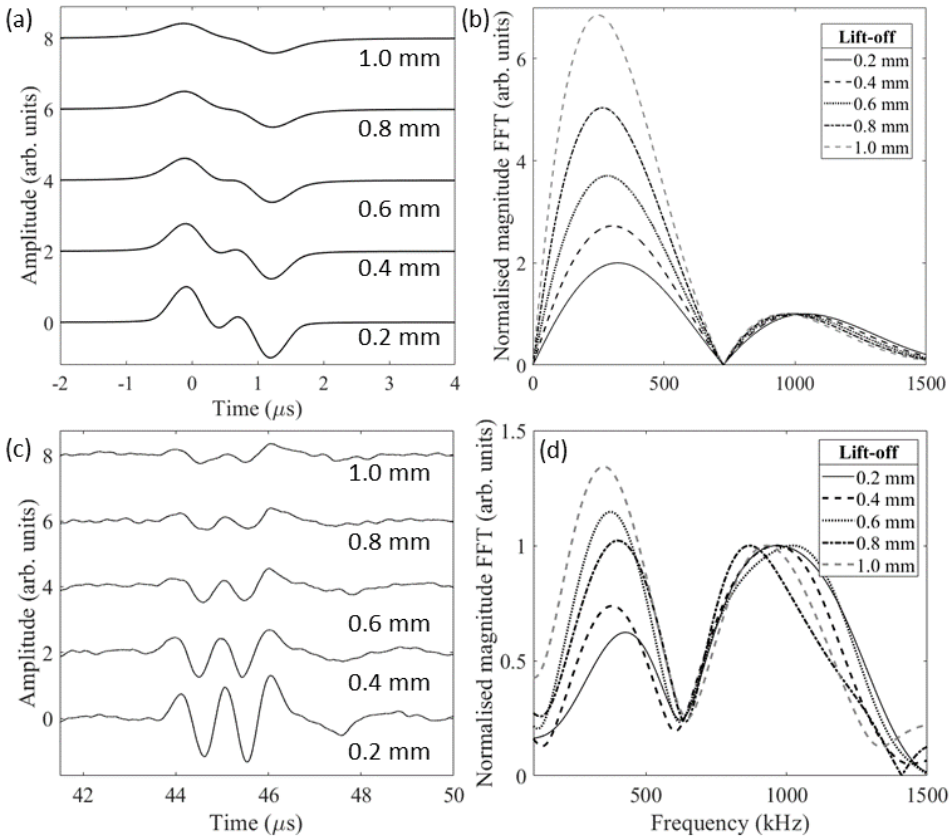

Figure 5.20: Lift-off behaviour for the two-coil in-phase EMAT generating a Rayleigh surface wave. The physical separation between the coils was 2.0 mm and the driving frequency was 900 kHz. Theoretical prediction is in (a) and (b) while the measured signal using EMAT detector is given in (c) and (d). (a) and (c) are A-scans while (b) and (d) are the corresponding FFTs.

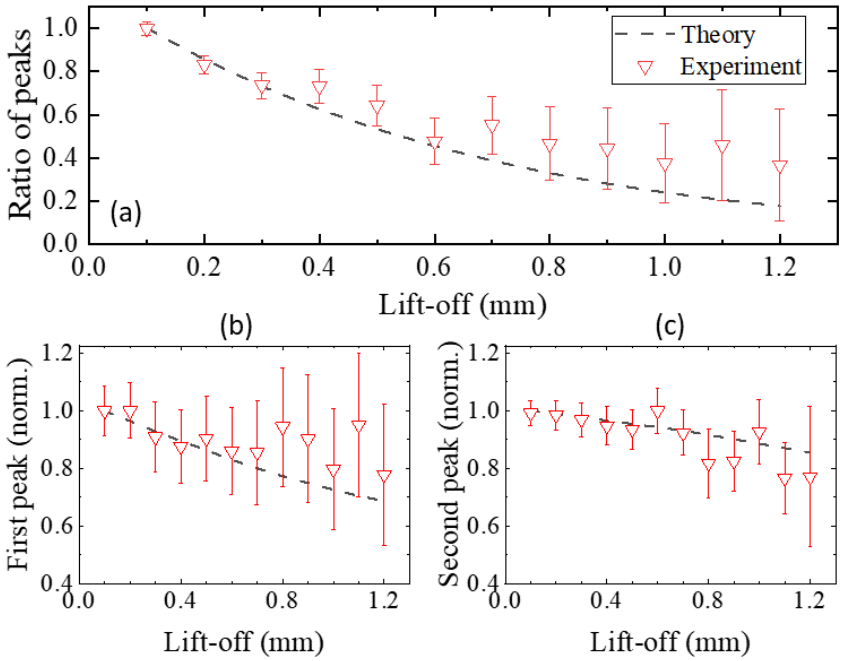

Figure 5.21: Comparing the relative change of peak frequencies in the FFT of the theoretical calculation (data shown in figure 5.20(b)) and experiment (data shown in figure 5.20(d)). (a) shows the amplitude ratio of the two peaks. (b)&(c) compare the shift of the first peak frequency and second peak frequency, respectively.

formed. Three comparisons were made between the theoretical and experimental results. They are: the amplitude ratio of the second peak (high frequency) to the first peak (low frequency) in the FFTs; the value of the first peak; and the value of the second peak. The results were found at each lift-off and are shown in figures 5.21(a) to (c), respectively. All have been normalised to maximum value at zero lift-off, so that the spatial variation of the generated signal can be easier clarified.

For amplitude comparison (figure 5.21(a)), a good agreement between the theory and experiment is observed, though the speed of the decrease from the theory is slower than that of the experiment. Similarly, the decreasing trends of frequency shifts of the two peaks (figures 5.21(b)&(c)) match well between the theory and experiment, but the slopes of the former are larger than the latter. This shows that the model has overestimated the lift-off effect at large lift-offs. The reduced signal-to-noise in the experiment when the lift-off was above 0.7 mm could also have a strong effect here, as shown in figure 5.20(c).

5.7 Summary

This chapter demonstrates the array EMAT model for Rayleigh surface wave generation used in this thesis. The generation is mainly through the Lorentz force mechanism. With a constant static magnetic field applied, the theoretical emphasis was given to the coil electromagnetic fields for mirror (eddy-) currents induction and their spatial behaviour.

The single layer, flat, linear coil was chosen as the array element for building the one-dimensional linear array. The spatial effect of the coil element with a finite width has been detailed, mainly from the aspect of the spatial distortion of the induced mirror currents with lift-off. The subsequent ultrasound behaviour can exhibit a peak frequency decrease of the order of 100 kHz/mm for a 1.5 mm width coil as lift-off is increased.

Formation of the 1-D linear coil array is given. The coil array was represented by the coil induced shear Lorentz force array to generate a Rayleigh wave. The force array has been standardised to a series of rectangular functions at zero lift-off. The frequency behaviour of the standardised array has been discussed when an arbitrary layout of the array, including the parameters of coil width, a, coil separation, d and the number of coil pairs (dipole), N_{di}, is applied. Several features are of note,

1. the array frequency largely depends on the values of a and d. If the desired wavelength is much larger than a, the simple rule $\lambda = 2d$ or $f_p^* = c_R/2d$ holds, where c_R is the Rayleigh speed.

2. The frequency cannot be increased to an infinitely large value by simply decreasing d. If the wavelength is comparable to a, the real frequency hits a maximum value when d decreases to $d \approx a$.

3. By increasing the number of applied coil pairs (dipoles), N_{di}, a higher frequency can be obtained for a same a and d used above.

The lift-off behaviour of the formed coil array was then discussed. It shows that the cross-talk (or spatial overlap) between the induced mirror currents from the neighbouring coils can cause a significant impact on the array generated ultrasound. The studies were undertaken on a two-coil model, for an out-of-phase configuration mimicking the function of a simplified meander coil, and an in-phase configuration mimicking a simplified normal coil array. The result of the out-of-phase two-coil is similar to that of the single-coil, showing that a frequency shift can occur with lift-off. Care must be taken, such as lift-off compensation [152], when using EMATs

with this configuration where a precise frequency is required. The result of the in-phase two-coil shows a significant attenuation at high frequency with lift-off. The natural conflict between good lift-off capability and a high frequency output for the in-phase array was observed.

These lift-off results suggest that, for the design of an array EMAT, a good lift-off performance always conflicts with the need for high frequency narrowband operation. A trade-off must be formed during practical use.

Chapter 6

Phased EMAT arrays for surface crack detection

6.1 Introduction

Ultrasonic testing with Rayleigh waves has been used for material characterisation [209, 210] and surface defect sizing [78, 211, 212, 213]. EMATs , with their non-contact advantage, provide a method of Rayleigh wave excitation and have good potential for fast inspection over a large area and in harsh conditions, such as high temperature [46, 171] or corrosive environments [48].

Since the particle motion for a Rayleigh wave follows an elliptical trajectory and the wave penetration depth is of the order of a wavelength [57], appropriate selection of the wavelength is critical when using Rayleigh waves to detect a surface crack. A broadband Rayleigh signal with multiple wavelength content is sensitive to different crack depths [92]. A narrowband Rayleigh wave, on the other hand, can provide more signal to noise ratio in a certain bandwidth, but the sensitivity range to different crack depths is limited [181]. Conventional EMATs use a meander coil design to generate narrowband Rayleigh waves with a fixed choice of central wavelength. The use of a single meander EMAT limits inspection to the designed wavelength, which limits the sensitivity to different size defects. Additionally, when operated at short wavelength (high frequency) to detect small defects, the coil dimensions are very small, leading to difficulties in manufacture. An alternative EMAT method which could offer narrowband operation but with a tunable frequency would bring many benefits in crack characterisation.

This chapter proposes an advance in EMAT design, using a phased coil array EMAT system for Rayleigh wave generation. Array EMATs with four linear

coils were developed. Each coil was individually controlled using the in-house built multi-channel pulser introduced in chapter 4. Different working wavelengths can be selected by delaying the firing time of each coil element (phasing) to give different effective separations between the coils. The practical performance of the four-coil phased array is comprehensively presented, including the comparison with standard meander EMATs, the capability of multi-wavelength generation, and the use for surface crack detection and depth gauging. Limits for the crack sensitivity are discussed, giving directions for future optimisation.

The lift-off performance of the phased array is also discussed. In chapter 5, it has been seen that a significant frequency shift could occur with lift-off for a meander-coil. Comparison between the phased array formed in this chapter and the standard meander-coil is given. The influence of the coil physical or effective spacing after phasing is detailed, since it is the key factor for adjusting the workable wavelength/frequency of both the meander-coil or the phased array configuration presented in this chapter.

6.2 Experimental set-up

In this chapter, the experimental development was undertaken to validate the practical performance of the proposed phased EMAT arrays. This focused on two topics; the performance of enhanced multi-wavelength Rayleigh wave surface crack detection (section 6.4), and the lift-off performance compared to normal array EMATs or meander coils (section 6.5). Details of the experimental set-ups used are given below.

The instrumentation used to implement the surface crack inspection followed the procedure introduced in section 4.3. The exact system schematic is given in Figure 6.1(a). The four-channel high energy pulser introduced in chapter 4 was used to drive the array EMATs. In this chapter, the array EMATs were designed for two purposes; firstly, a four-coil prototype was used to inspect the surface crack. This EMAT design will be detailed in section 6.4.1. Secondly, two-coil prototypes, either phased or non-phased, were used to compare the array lift-off performance. These EMATs were similar to the two-coil models developed in section 5.6.2, and will be introduced briefly in the next section. The broadband racetrack EMAT detector (see section 3.4.1) was used to receive the generated Rayleigh wave signal, with a total width of 3 mm, length of 25 mm, and using a NdFeB magnet ($25 \times 15 \times 6$ mm^3). The sensitivity range of the detector was between 0 and 4 MHz [206]. The detected ultrasound signal was passed through an amplifier and a 2.5 MHz low pass filter

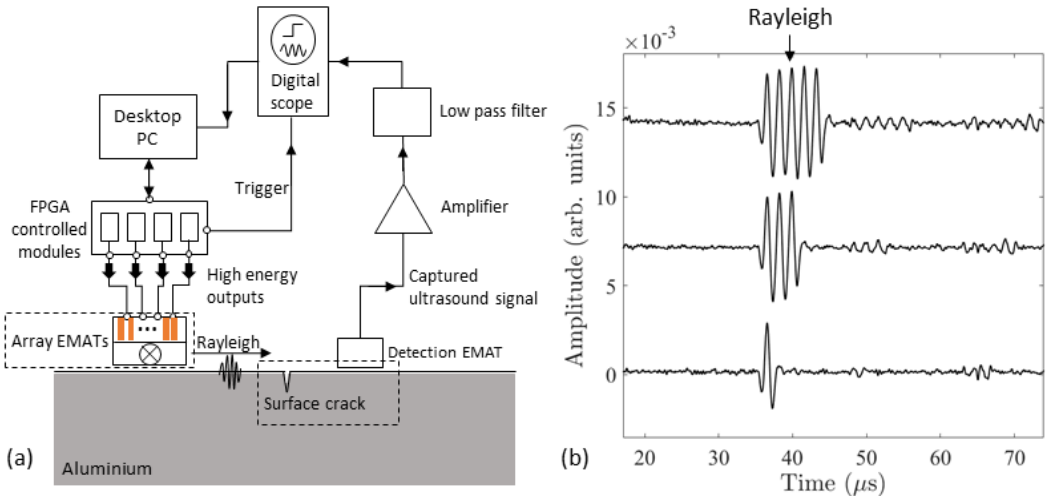

Figure 6.1: (a) Schematic diagram showing the instrumentation used in this chapter. The generation array EMATs are either four-coil (section 6.4) or two-coil models (section 6.5). Machined surface slots were present for experiments in section 6.4.3, while other samples were clean. (b) Detected Rayleigh wavefront from the array EMAT with a single coil activated for different numbers of cycles.

before being recorded by a digital oscilloscope. The separation between the generator (the farthest coil element) and the detector was 100 mm for all experiments in this chapter. All testing samples were aluminium. For the surface crack detection experiments described in section 6.4, the inspection used a 60 mm thick bar containing several machined slots. The slots were across the sample full face (in the y-direction), and the opening width was 1 mm (in the x-direction). The crack depth is given in the relevant section for clarity. For the lift-off study in section 6.5, the used sample was clean and without surface slots.

Figure 6.1(b) shows the basic Rayleigh waveform (appears at around 35 μs) that was generated from a single channel (coil 0, the farthest from the detector) without a surface crack. The centre frequency of the driving signal was 600 kHz, and the number of cycles of the driving signal was chosen to be one-cycle, three-cycle or five-cycle. The ultrasound shape is rectangular windowed, as expected. The single-cycle pulse provided a lower signal-to-noise ratio compared to the three-cycle or the five-cycle, but the latter provided less resolution in the time domain. The experiments designed in section 6.4 used three-cycle driving, while those in section 6.5 used single-cycle broadband driving.

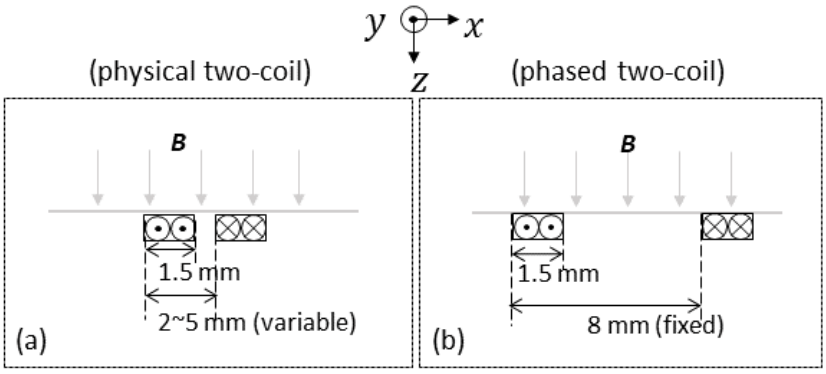

Figure 6.2: Cross view of the two-coil EMAT for (a) the varied and (b) fixed separation configurations.

6.2.1 Two-coil EMATs for lift-off performance comparison

The two-coil prototypes built for lift-off performance comparison are shown in figure 6.2. In this chapter, multiple coils with opposing currents (i.e. in a meander configuration, or a phased array giving pseudo-meander behaviour) were focused on to compare the behaviour of coils with different physical and effective separations. The coils were hand made followed by the method introduced in chapter 4. Each coil was near-identical, with a 1.5 mm width. Configuration of the EMAT magnet was the same as that in section 5.2 where the dimensional size was $25 \times 15 \times 16$ mm^3, producing an out-of-plane static field in the z-direction. The coils were placed onto the magnet in the required positions and held in place using spacers. Figure 6.2(a) shows the meander configuration for two coils, with physical separations of 2, 2.5, 3, 4 and 5 mm between coil centres used. Coils were positioned equidistant from the magnet centre. Figure 6.2(b) shows the two coils used to give a fixed physical separation of 8 mm, for opposing currents. The coil pair was also at equivalent positions under the magnet. Phasing was then used to vary the effective separation (see explanation in section 6.3.2) from 2 to 5 mm, corresponding to the physical separations used. The magnetic field was predominantly in the z-direction for all coil positions.

6.3 Phased spatial domain for the coil array

Before presenting the concept of phasing, the general idea of EMAT arrays used as a transmitter for narrowband ultrasound generation is demonstrated. The behaviour of the generated wave can be considered as an phenomenon of wave interference.

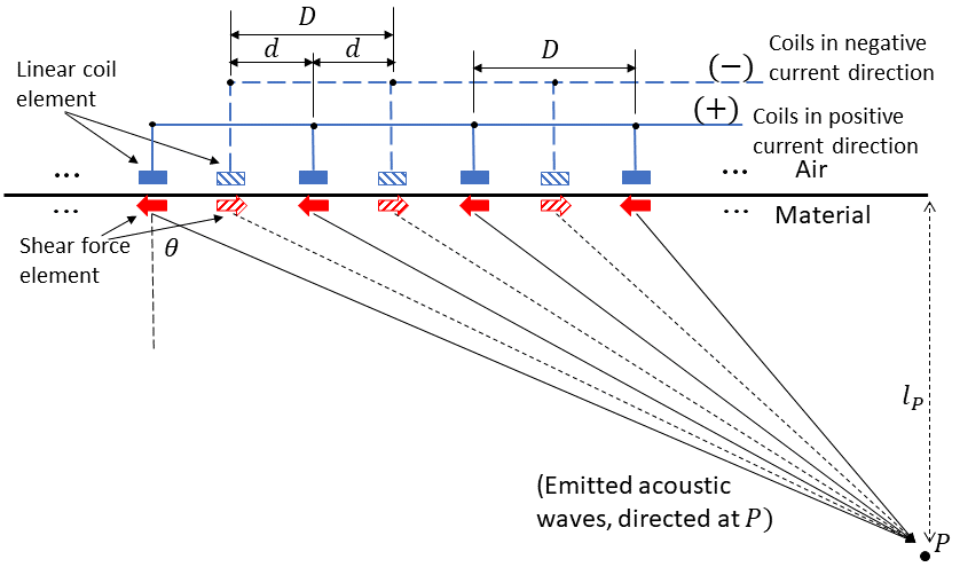

Figure 6.3: The ultrasonic wave interference from a coil array EMAT. Linear coils are polarised either in the positive current direction ('+') or in the negative current direction ('-'). Position P is an observation point in the far field ($l_P \gg D$). Waves from each force interfere at P, and fringes in the x-direction can be formed.

Figure 6.3 shows how constructive ultrasound interference can be obtained for a shear wave by using an EMAT coil array. The static magnetic field produced by a magnet is not shown here for simplicity. The linear coil elements are shown as blue blocks above the sample surface. Each coil generate a wave, and the waves will interfere with each other.

In order to discuss the array behaviour comprehensively, the coil array configuration is divided into two sets defined by the direction of the current polarisation; one is when currents are in the negative current direction (inwards, '−') and the other is when they are in the positive direction (outwards, '+'). The sizes of the coil elements in both arrays are the same, including the width (a) and the number of coils (N). The separation between the neighbouring coils with the same polarisation in both groups is D[1]. Two groups are intersected evenly, giving an inter-distance d between the coils with alternating polarisations, where $d = D/2$.

The induced Lorentz force array is shown by the red arrows under the material surface. The direction of the induced shear force depends on the coil polarisation, and is illustrated by the direction of the force arrows. The ultrasonic waves emitted by the force element will travel into the material or along the material surface, depending on the generated wavemodes; for example a shear-vertical wave with in-

[1] D is used in this chapter to be distinct from d used in chapter 5.

cident angle, θ, will propagate into the material bulk, or a Rayleigh surface wave will propagate on the material surface (see section 3.4.1). These waves will then interfere. For bulk waves, at an observation point, P, in the far field ($l_P \gg D$, where l_P is the distance between the sample surface and the observation point), the propagation paths of the incoming waves from different elements can be approximated as parallel, but with coherent phase differences due to their different path lengths. Interference fringes will be formed in the the detection plane [23].

The behaviour observed at P is due to the linear superposition contributed by each source element [23]. A constructive interference can be obtained, depending on the path length differences and whether a coil array with appropriate spatial layout, i.e. the coil separation, was applied. In section 5.4, two configurations of linear coil arrays are discussed; all coils used in the same current direction, or in alternating directions to mimic a meander coil. To achieve the former, the coil array either in the '-' direction OR in the '+' direction in figure 6.3 can be used. For the latter, both groups need to be used at the same time. The condition that needs to be satisfied to form constructive interference for shear waves generated by two different configurations are [23],

$$D\sin\theta = m\lambda, \quad \text{or} \quad d\sin\theta = (m+\frac{1}{2})\lambda \quad (m = 0, 1, 2...), \tag{6.1}$$

where λ is the ultrasound wavelength and θ is the incident angle of the desired wavemode. m is zero or an integer, indicating the mth harmonic contained in the interference. The use of D or d depends on the array configuration, i.e whether the neighbouring coil is purely in the same current direction or alternating directions.

For a guided wave or Rayleigh wave EMAT whose generated waves will propagate along the material surface ($\theta = 90°$ and $\sin\theta = 1$), the directional effect in two-dimensions is neglected. Equation 6.1 for a Rayleigh EMAT array can be modified to

$$D = m\lambda, \quad \text{or} \quad d = (m+\frac{1}{2})\lambda \quad (m = 0, 1, 2...). \tag{6.2}$$

This implies that the wavelength/frequency of the array system for Rayleigh generation is dominated by the choice of the coil spacing, as discussed in chapter 5. However, this equation is not fully comprehensive for a practical coil array EMAT; the efficiency of different harmonics (m is 1 or higher) is not included, nor is the effect of the coil finite width a or the coil number N (for D) or the coil dipole number N_{di} (for d). Mathematical analysis of the array model is covered in sections 5.4 and 5.5.

In this chapter, phasing is applied onto the above coil array such that the

time at which an element is activated is controlled, for Rayleigh wave generation. Electronic tuning of D or d is implemented, thereby the effective spatial layout of the array can be changed. Different Rayleigh wave characteristics will be obtained, providing more possibilities for surface crack detection.

6.3.1 Unidirectional signal enhancement

Signal-to-noise improvement

The in-house built multi-channel EMAT driver (see chapter 4) can firstly be used as a phased array system to provide an improved signal to noise ratio compared to a conventional single coil EMAT. Demonstration of this strategy starts from equation 6.2. The coil array with all coil elements polarised in the same current direction is chosen (see coil group '+' in figure 6.3). The condition for such an array to offer a constructive interference is when $D = 0$ ($m = 0$) or $D = m\lambda$ ($m = 1, 2...$). $D = 0$ will give a strong signal as the wave generated by each coil will be overlapped, but is not practical. However, by using the phased pulser, a time delay factor can be applied onto the each element, so that the time point of coil activation (wave generation) can be controlled, and it is possible to set the delay such that effectively $D = 0$ ($m = 0$). Sufficient delays for coils are applied, for example, by delaying the coils closet to the detector, the wave signal generated by coil 0, wave 0, will propagate first along the material surface. Coil 1 is then fired at the time point when wave 0 has propagated to the location under coil 1. The two waves (wave 0 and 1) will superpose and propagate until they reach coil 2, at which point coil 2 is activated, etc. In other words, the spatial differences between the coils are cancelled by the time delay. All coils are electronically 'overlapped'. This is equivalent to a physical array where there are no separations between the neighbouring elements ($D = 0$). The signal-to-noise ratio can then be maximised.

Figure 6.4 demonstrates a four-coil $D = 0$ operation. The four coils are in the same current direction and are indicated by the blue blocks. The delay factor for coils 3 to 0 are 0, $\Delta\tau$, $2\Delta\tau$ and $3\Delta\tau$ respectively, where $\Delta\tau$ is a time delay unit. The Rayleigh wave generated by a coil is bidirectional, propagating in both the positive and negative x-directions. The schematic shows the time point when coil 3 has just been fired. The bi-directional waves generated by a coil are shown on different vertical layers to act as a guide to the wave behaviour, with the vertical distance corresponding to the time delay. For example, coil 0 is $3\Delta\tau$ ahead of coil 3, and coil 3 is the last one being fired in the figure. The four waves that travel in the negative x-direction are superimposed at the position just underneath coil 3. A

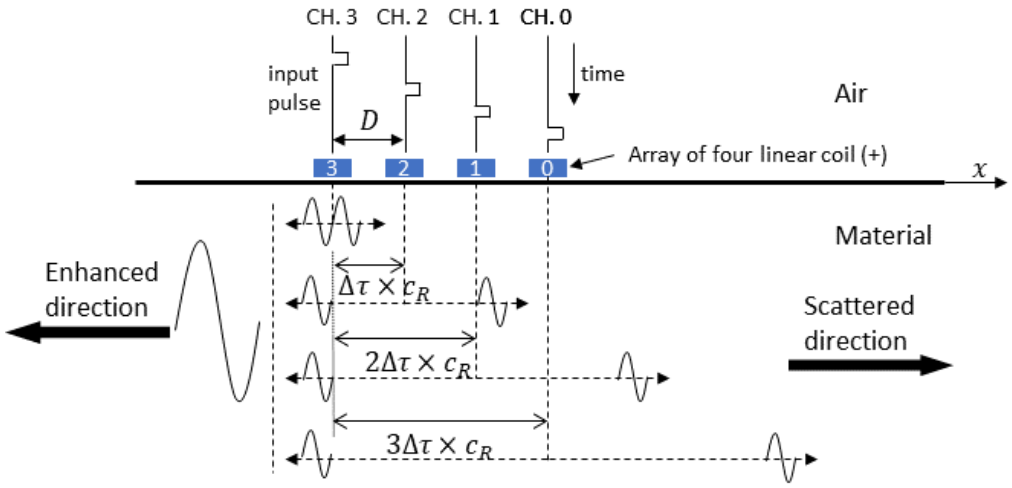

Figure 6.4: Unidirectional signal enhancement by implementing a four-coil phased array system. The EMAT coil is bidirectional. Each coil is individually controlled and a time delay sequence is used. At the time point when coil 3 has just been fired, waves moving in the -x direction are superimposed, while in the +x direction waves are not. $\Delta\tau$ is the time delay unit and $\Delta\tau = D/c_R$.

signal enhancement is obtained. The physical spacing D between coils is cancelled by using a time delay that satisfies the relation $D = \Delta\tau \times c_R$ or $\Delta\tau = D/c_R$.

Meanwhile in the positive $x-$direction, the effective separation between the four waves becomes larger. For example, coil 2 was driven $\Delta\tau$ ahead coil 3, and the corresponding generated wave has travelled a distance $\Delta\tau \times c_R + D = 2D$ further. By carefully choosing the delay factor $\Delta\tau$ for the array, the effective layout of the array is changeable such that constructive interference could instead be obtained in the positive x-direction.

This concept has been previously investigated in the work [10]. The Rayleigh wave coils were sequentially delayed by a four-channel phased broadband pulser. The time delay factor was calculated using $\tau_{0,j} = d_{j,0}/c_R$, where $d_{j,0}$ was the physical separation between the jth element and the reference element. Figure 6.5 shows the result of their four-coil broadband enhanced system. The signal improvement of the Rayleigh wave is immediately shown, although the waveform is not a standard sinusoidal wave. This might be due to the coil self-field generation and the resultant wave frequency doubling [129].

An experimental investigation for Rayleigh signal improvement using a more controllable pulser (see chapter 4) was undertaken later in this chapter. A narrow-band signal with a good signal to noise ratio was obtained, with results given in section 6.4.2.

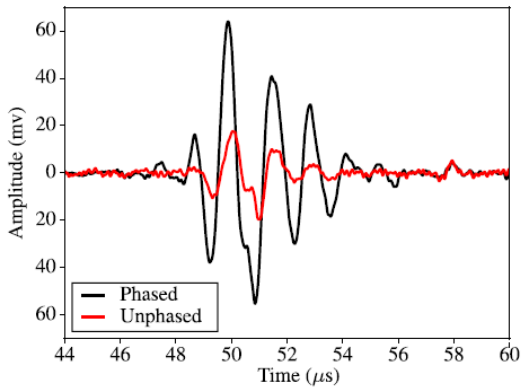

Figure 6.5: Enhanced Rayleigh wavefront from a four-coil phased system. Comparison of a single coil activation (unphased) is given. The coil sources have 3.0 mm width and the coil spacing is 3.8 mm (date taken from [10]).

Multi-wavelength emitting

Apart from the advantage that one can use phasing to improve the signal amplitude, generation of multiple wavelengths for Rayleigh inspection is another important benefit to be discussed. The motivation of this is to extend the sensitivity range for sizing the surface crack depths, as introduced in section 2.2.2.

Both coil array groups, either in the positive polarisation or negative polarisation, demonstrated in figure 6.3, can deliver such a benefit. To generate multiple wavelengths, the relation to form constructive interference (equation 6.2) needs to be satisfied. Two layout scenarios can be identified; use of a single group ('+' or '-') or use of both array groups ('+' and '-').

Figure 6.6 demonstrates the phasing modality applied for both scenarios. In figure 6.6(a), a single array with four identical coils is used. All coils are polarised in the same current direction. By using the phased four-channel pulser, the coils can be separately controlled and delayed. The time delays from coil 0 to 3 are $3\Delta\tau$, $2\Delta\tau$, $\Delta\tau$ and 0, respectively. Here, unlike the special case where $\Delta\tau = D/c_R$ for signal improvement purpose, $0 < \Delta\tau < D/c_R$, so that multiple wavelengths can be generated. The coils show bi-directivity, and the delayed waves that travel in both the positive and negative x-directions show the effect of geometric scattering or gathering (reducing the effective separation of the coils such that the waves 'gathered' together) with respect to their original activated positions. This produces an 'elongated' coil array when looked at from the positive x-direction or a 'narrowed' array when looked at from the negative x-direction. Constructive interference (equa-

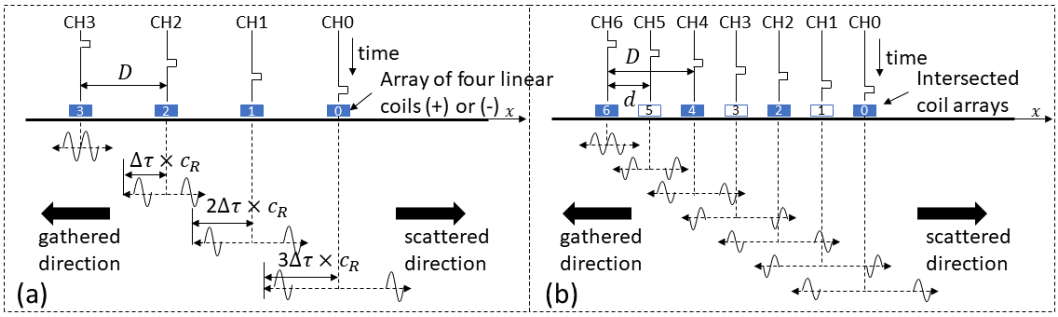

Figure 6.6: Schematic diagram showing the Rayleigh waves generated from the coil array when it is delayed for multi-wavelength generation. (a) A single coil group is used. All coils are polarised in the same current direction, and the coil spacing is D. (b) Two coil groups with different polarisations are used, $d = D/2$. (a) is at the time point when coil 3 has just been fired, and (b) is at the time point when coil 6 has just been fired. $\Delta\tau$ is $0 < \Delta\tau < D/c_R$ in (a) and is $0 < \Delta\tau < d/c_R$ in (b).

tion 6.2) occurs when

$$D_{eff}^{\pm} = m\lambda, \tag{6.3}$$

where D_{eff}^{-} and D_{eff}^{+} are the effective coil spacing after phasing for the wave propagating in the negative x-direction or positive x-direction, respectively. The values of D_{eff}^{-} and D_{eff}^{+} are linked to the time delay $\Delta\tau$, using $D_{eff}^{-} = D - \Delta\tau \times c_R$ and $D_{eff}^{+} = D + \Delta\tau \times c_R$.

In figure 6.3(b), both coil groups polarised in '+' and '−' are used. The two groups are intersected evenly and the coil spacing between the nearest neighbour coils is $d = D/2$. The schematic uses 7 coils, mimicking the configuration of a typical meander coil (see section 3.4.1). By controlling and delaying the coil elements separately, the effective array layout can be electronically changed. A delay sequence $[6\Delta\tau\ 5\Delta\tau\ 4\Delta\tau\ 3\Delta\tau\ 2\Delta\tau\ \Delta\tau\ 0]$ is applied to coils 0 to 6, and $\Delta\tau$ is $0 < \Delta\tau < d/c_R$. The condition that gives constructive interference (equation 6.2) in this case is,

$$d_{eff}^{\pm} = (m + \frac{1}{2})\lambda, \tag{6.4}$$

where d_{eff}^{-} and d_{eff}^{+} are the effective coil spacings after phasing in the negative x-direction and positive x-direction, respectively. The values of d_{eff}^{-} and d_{eff}^{+} are linked to the time delay via $d_{eff}^{-} = d - \Delta\tau \times c_R$ and $d_{eff}^{+} = d + \Delta\tau \times c_R$.

From equations 6.3 to 6.4, the wavelength λ provided by the effective coil spacings (either D_{eff} or d_{eff}) can be varied by changing the time delay $\Delta\tau$. This means one can design a multiple-wavelength EMAT array system by applying phasing (time delay) to a single physical array. A large flexibility is immediately shown

by this proposed concept.

Equations 6.3 and 6.4 show that both arrangements of linear coil arrays (a single coil group or two group intersected) can offer the ability of multi-wavelength Rayleigh wave generation. For a practical design, the latter arrangement is preferred. This is because the coil spacing in the meander configuration d is only half of D in the first arrangement, and so the coil density in the d-configuration is much higher. This is very beneficial for EMAT design. By employing more coils, a better signal-to-noise ratio can be obtained for a given transducer size requirement.

In the following sections in this chapter, the design of the coil array with alternating current polarisation was used. Development was focused on the phasing advantage of multiple-wavelength generation. The relation that the array layout needs to satisfy for constructive interference is,

$$d_{eff} = \frac{1}{2}\lambda, \quad \text{or} \quad \lambda = 2d_{eff} \ , \ \text{or} \quad f = \frac{c_R}{2d_{eff}}, \tag{6.5}$$

where $m = 0$ is chosen. The reason is that the mode at $m = 0$ can provide the most efficient frequency/wavelength in a meander configuration (see sections 5.4 and 5.5). d_{eff} can either be d^{-}_{eff} or d^{+}_{eff}, depending on the desired propagation direction of the surface wave.

The above discussion offers the basic principle for phased multi-wavelength operation. The phased four-channel high current driver introduced in chapter 4 allows experimental validation. The procedures used to implement the phased four-coil EMAT system for multi-wavelength Rayleigh wave generation are summarised in the cartoon given in figure 6.7. The four-coil system is unidirectionally enhanced to give variable d_{eff} and λ. The details are summarised below;

- coil 1 could be activated at time $t = 0$, coil 2 at time $t = \Delta\tau$, coil 3 at a time $2\Delta\tau$, etc. The surface wave generated by coil 1 would then have moved closer to coil 2 before it is activated, making the separation of the coils appear to be smaller for waves travelling to the right.

- Conversely, for $N^{'}$ coils, coil $N^{'}$ could be activated at time $t = 0$, coil $N^{'}$-1 at time $\Delta\tau$, coil $N^{'}$-2 at time $2\Delta\tau$...For this configuration, shown in figures 6.7(b)&(c), the wave from coil $N^{'}$ would travel at a set distance before coil $N^{'} - 1$ is activated, making the separation between the coils appear larger.

- By the above phasing process, an effective separation between coils d_{eff} can be defined. The designed wavelength of the system is then $\lambda = 2d_{eff}$. The

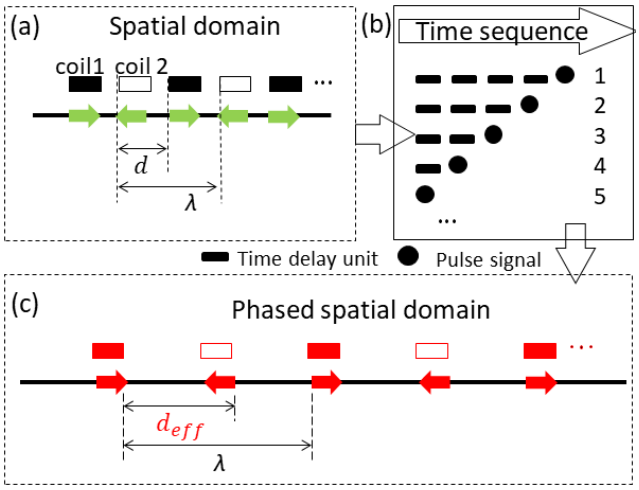

Figure 6.7: The modality of the phased EMAT array. (a) shows the physical separation of the coils. Coils which are filled or non-filled indicate alternating current directions; (b) shows the delay (dash) and pulse time (spot) of each channel; (c) shows the effective separation obtained by the delay process, where red indicates the coils are delayed.

time delay factor for element j to choose a d_{eff} is

$$\tau_j = j\frac{d - d_{eff}}{c_R} = j\Delta\tau. \tag{6.6}$$

The proposed strategy was experimentally validated on a four-coil system in the next section. The parameter N_{di} (the number of dipole coil pairs) was used to represent the applied coil number, where $N_{di} = N/2$ for the meander configuration array. For small values of N_{di}, the achieved wavelength will be slightly offset for the designed wavelength, as described in section 5.5. However, improved behaviour can still be obtained.

6.3.2 Controlled surface wave bi-directivity

Section 6.3.1 detailed the possible phasing strategies to change the array EMAT spatial characteristics (effective separation). The bi-directivity of surface waves generated by an EMAT coil has been illustrated (see figures 6.4 and 6.6). By carefully choosing the time delay factor $\Delta\tau$, the effective layout of the array for waves propagating in the -x-direction or +x-direction can be varied, and so the surface waves are controlled in both directions.

Another interesting phasing application is to control the wave directivity, i.e. controlled surface wave generation direction. The special case demonstrated in sec-

tion 6.3.1 for pure signal improvement purposes ($\Delta\tau = D/c_R$ and $D_{eff} = 0$) can be modified to solve this problem. When using the meander coil configuration (alternating current polarisation) and careful choice of $\Delta\tau$, the amplitude enhancement direction in the $-x$ for currents in the same direction (see figure 6.4) will be replaced by a signal cancellation instead, as the overlapping waves are now out-of-phase. Zero output can be therefore obtained by the alternating coil polarisation. This design can be used for complex geometry inspection, where a reduced bi-directivity can reduce the spurious signal reflected from multiple directions. This idea is suggested as one of the future directions, and more details are given in chapter 8.

6.4 Experimental development: Four-coil phased operation

6.4.1 EMAT configuration

Experimental development of the array EMAT followed the method introduced in chapter 4. A four-coil (number of coil pairs N_{di}=2) transducer prototype was built to implement the phasing concept proposed in this section. Figure 6.8(a) shows the 3-D sketch of the four-coil array EMAT. A permanent NdFeB block magnet of dimensions $25 \times 15 \times 6$ mm^3 was used to introduce the static magnetic field. Copper wires were tightly wrapped onto the magnet to produce four identical coils, each with seven turns of 0.2-mm-diameter copper wire and a total coil width of 1.5 mm including spacing. The physical separation between the coils was fixed at $d = 6$ mm with the variation of the static magnetic field minimal over this range. Figures 6.8(b) and (c) show the photographs of the transducer in a 3-D-printed holder. Four insulated BNC connectors were used for the coils. The signal enhancement experiment (see figure 6.9) was done using the normal array configuration (coils polarised in the same direction), and the rest in this chapter were done using the pseudo-meander array configuration.

6.4.2 Enhanced Rayleigh wave generation

Enhanced signal amplitude & geometry dependence

As demonstrated in section 6.3, a phased Rayleigh array EMAT can provide two benefits; a large signal to noise ratio or the ability to deliver multiple wavelengths, depending on the time delay $\Delta\tau$. In this section, typical examples obtained by the four-coil phased array are given. Experimental set-ups were introduced in section 6.2. The detector was fixed on one of the generation array for unidirectional

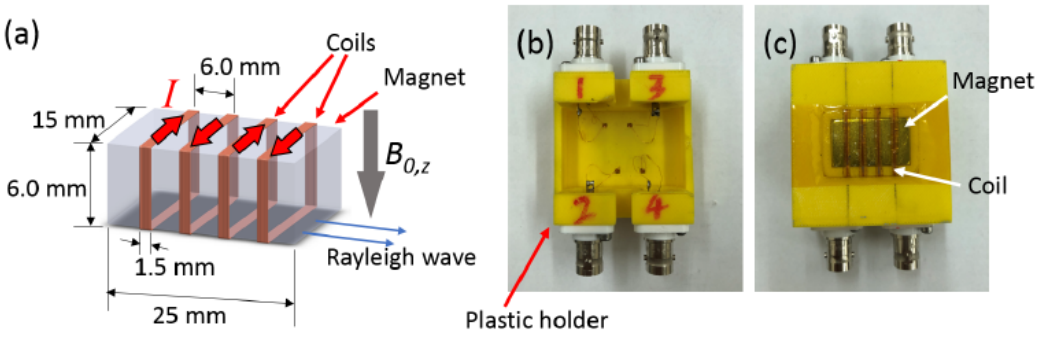

Figure 6.8: Schematic of the Rayleigh wave array EMAT. Parameters of the array are: coil width $a = 1.5$ mm, coil physical separation $d = 6.0$ mm, and the number of coil dipoles N_{di} =2. (a) Configuration of the coils and the permanent magnet. The 3-D printed transducer holder from (b) top and (c) bottom.

enhancement study.

Firstly, coils in the '+' array were delayed to provide the largest possible signal. The time delay for coils 0 to 3 were 0, $\Delta\tau$, $2\Delta\tau$ and $3\Delta\tau$, where $\Delta\tau = D/c_R$, and coil 0 was used as the reference coil (farthest from the detector). D is 6 mm, c_R is 2906 m/s on aluminium material and $\Delta\tau$ was calculated as 2065 ns. The test result is given in figure 6.9 for three cycle operation. A large signal-to-noise ratio (SNR) improvement is immediately shown by comparing the phased four-coil model to the single coil. Additionally, the waveform engineered by the narrowband system shows a clear sinusoidal shape, giving improvement compared to the signal obtained from the broadband design (figure 6.5) [10].

Equation 6.4 describes the spatial relation between the desired wavelength and the coil spacing. Using phasing (τ_j) allows one to vary the array effective layout (d_{eff}), but the issue due to the coil element finite width is not addressed by this equation (see section 5.4). The four-coil prototype used a 1.5 mm coil width, which can decrease the wavelength performance when d or d_{eff} approached 1.5 mm (see figure 5.14). It is therefore important to verify the spatial behaviour of the phased array with different $\Delta\tau$ (or d_{eff}), i.e. ensure the spatial spectrum of the array (see section 5.4) matches well with the input current signal, so that the Rayleigh wave output can be optimised. The convolution model demonstrated in section 5.3.2 can be used to predict the behaviour of the final resultant Rayleigh wave. The spatial profile of the EMAT array induced Lorentz force array and the driving signal are in the spatial domain (x-domain) and the time domain (t-domain), respectively. To predict both domains accurately, the ultrasound signal in the Fourier domain is

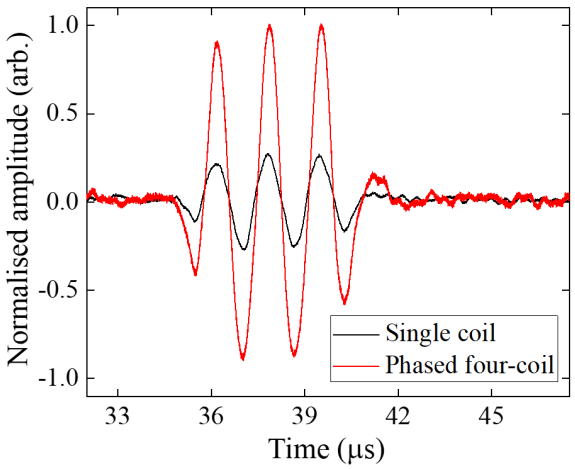

Figure 6.9: The enhancement Rayleigh wave by the narrowband phased four-coil system. The single-coil is given for comparison. The signal centre frequency is 600 kHz.

described in the form of a 2-D Fourier transform,

$$\begin{aligned}\hat{S}(k,\omega) &= \int_{-\infty}^{\infty}\int_{-\infty}^{\infty} S(x,t)e^{-i2\pi(kx+\omega t)}dxdt \\ &= \mathcal{F}(\bar{f}_s^{(L)}(x)) \times \mathcal{F}(y(t)),\end{aligned} \tag{6.7}$$

where $S(x,t)$ indicates that the sound wave generated by the array EMAT with a normalised Lorentz force profile $\bar{f}_s^{(L)}(x)$ is driven by a temporal signal $y(t)$, propagating in the x-direction. Note, equation 6.7 is just the Fourier form of equation 5.12.

Examples of designing wavelengths of 3.06 mm and 4.84 mm using the presented four-coil phased system are given in figure 6.10. Coil 0 was used as the reference coil and the time delay sequence for the coil array was calculated from equation 6.6. d is 6 mm and d_{eff} was 1.5 and 2.4 mm for the two designed wavelengths, respectively. The centre frequency f_0 of the driving signal was set as f_p^T, obtained by numerically solving equation 5.22. It should be noted that small discrepancies occur in the output wavelengths (3.06 and 4.84 mm) by using $2d_{eff}$ =3 and 4.8 mm. This is due to the effect of the coil finite width (1.5 mm) which is comparable to the desired wavelengths here.

Figures 6.10(a) and (b) show the calculation results using equation 6.7, for a driving signal $y(t)$ of the frequency indicated on the temporal axis, and the frequency due to the array structure behaviour in the spatial axis. Frequency parameters ω (rad/s) for the temporal domain and k (m^{-1}) for the spatial domain were transformed into f (Hz) using the relations $\omega = 2\pi f$ and $k = 2\pi f/c_R$. The driving

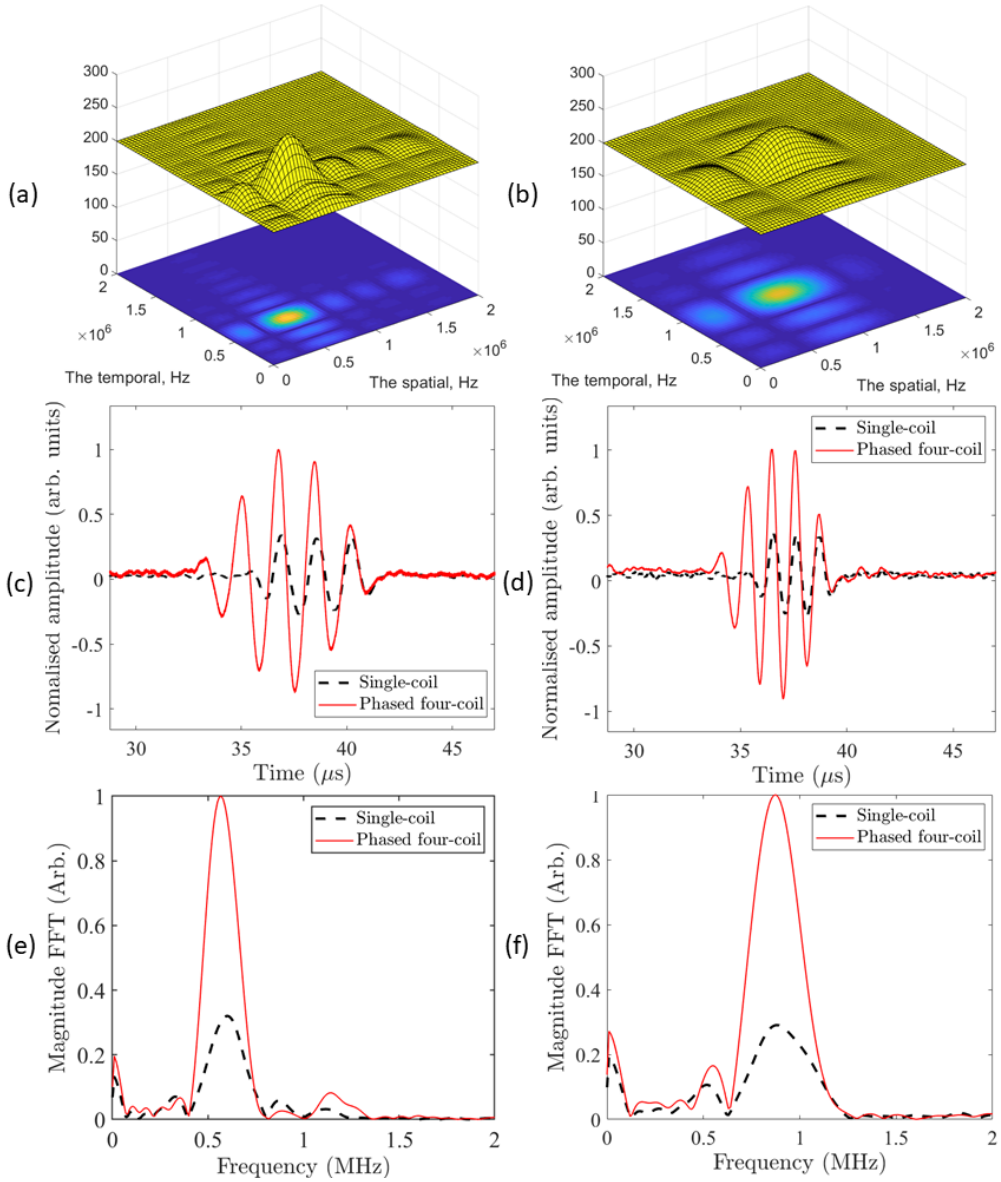

Figure 6.10: Generation of Rayleigh waves for wavelengths 3.06 mm and 4.84 mm. (a) and (b) show the calculated frequency spectra for the temporal driving signal and the spatial response from the array structure. (c) and (d) are the experimental Rayleigh signals in time domain, while (e) and (f) are frequency domain. (a),(c) and (e) are for $\lambda = 4.84$ mm and a centre frequency of the driving signal of $f_0 =$ 600 kHz for d_{eff}=1.5 mm. (b),(d) and (f) are for $\lambda = 3.06$ mm, $f_0 = 950$ kHz and $d_{eff} = 2.40$ mm. Due to the effect of coil 1.5 mm width, the resulted wavelength is a little larger than $2d_{eff}$, as explained in section 5.4.

signal was modelled by a rectangular windowed sine wave centred at the selected frequency. The duration was three time periods, modelling the three-cycle driving signal. The calculation was undertaken in MATLAB. Both frequency/wavelength operations predicted a peak at the designed frequencies, which are 600 and 950 kHz for the two wavelengths. Figures 6.10(c) to (f) show the experimental results detected by the racetrack EMAT detector, with the comparison of the output signals between the single coil and four-coil operations. The captured A-scans are given in figures 6.10(c) and (d), respectively, showing the enhanced Rayleigh wave amplitude when four coils were used. The time delays used to obtain different values for d_{eff} led to a small increase in waveform cycle number. This means the resultant waveforms are tone-burst shaped rather than rectangular shapes. Figures 6.10(e) and (f) are the corresponding frequency spectra of the A-scans given in figures 6.7(c) and (d), respectively, showing the bandwidth centred at around 600 and 950 kHz, as expected.

Although the EMAT coils had a 1.5 mm width, the wave signals generated by the coil array confirm the designed frequency characteristics, with a good signal to noise ratio. This implies that a good constructive interference can still be obtained by the finite coil width, as long as both spatial and temporal domains of the phased array system are under good control.

Comparison with a standard meander coil

Measurements were then undertaken to investigate the frequency/wavelength behaviour of the phased four-coil array EMAT compared to the conventional meander EMAT. The array EMAT shown in figure 6.8 was used with the phased pulser to output different narrowband Rayleigh signals. Several standard meander coils were made to perform the comparison. In summary, three types of EMATs were employed in this experiment:

1. conventional standard meander coils (SM). These coils consisted of a single piece of wire fabricated into the meander shape, and each coil giving a different value of d. The SM EMATs contained four turns with a coil width of 1.5 mm and length of 20 mm. The NdFeB magnet (size of $25 \times 15 \times 6$ mm^3) was used to introduce the static magnetic field. One of the channels of the four-channel pulser (CH0) was used to drive the standard meander EMATs.

2. Composite meanders (CM), which consisted of four individual linear coils, with the physical coil spacing d varied to match the spacing of the above SM meander coils. The CM EMATs also had a 1.5 mm width for each coil element.

They were made by wrapping the coil wire directly onto the same NdFeB magnet, but the coil physical separation was varied to different d using spacers. Four coils were individually controlled by the pulser, but were activated at the same time (no phasing).

3. Phased four-coil array EMAT (PA) shown in figure 6.8, whose physical separation d was fixed at 6 mm but the phasing was used to give different d_{eff}. d_{eff} can be varied to the same d values used in the above two EMAT types.

The key parameters (d or d_{eff}) in the experiment were chosen to be 2.4, 3.6, 4.8 and 6.0 mm. The geometries of SM EMATs are given in figures 6.11(a) to (d) for different d. The four-coil phased array EMAT for different d_{eff} was electronically obtained through the use of phasing. Coil 0 was treated as the reference coil and the time delays for other coils were calculated using equation 6.6. During the experiment, the centre frequency of the driving signal f_0 was progressively increased from 200 kHz to 2.0 MHz, with a 100 kHz step, for each chosen d or d_{eff} for each EMAT type. 32 signals were averaged to eliminate the incoherent noise. The peak to peak amplitude of the detected Rayleigh signal was found and is plotted as a function of f_0, shown in figures 6.11(e) to (h) and maxima are expected at frequencies where equation 6.5 is satisfied.

Figure 6.11 shows that the frequency behaviours of the standard meander EMAT and the array EMATs at different d (or d_{eff}) match well, showing that the phased array is equivalent to a meander coil but offering advantage of tuneability. However, there is a trend that the second harmonic starts to dominate when the coil separation is increased. Two reasons can be suggested for this; firstly, the second harmonic ($m = 1$ in equation 6.4) was contained in the optimal range of operation of the pulser and coils when d_{eff} or d was large enough. For small separations, such as $d = d_{eff} = 2.4$ mm, the second harmonic was expected to be 1.8 MHz, which was beyond the testing frequency range. Secondly, the effect of the racetrack receiver means that an extra linear factor of the frequency will affect detection compared to the actual ultrasound value due to the EMAT being a velocity detector (see section 3.2.3). Despite this, the primary harmonic (m =0) was still efficient for the cases when d or d_{eff} were 2.4, 3.6 or 4.8 mm. For $d = 6.0$ mm in figure 6.11(h), the expected primary peak (0.24 MHz) did not appear but the second and third harmonics did. This is due to the poor time resolution when a low frequency was under test. The bandwidth of the EMAT detector could also contribute.

Table 6.1 summarises the experimental parameters used for the three EMAT types, including the time delay factor for the phased array EMAT, and the pre-

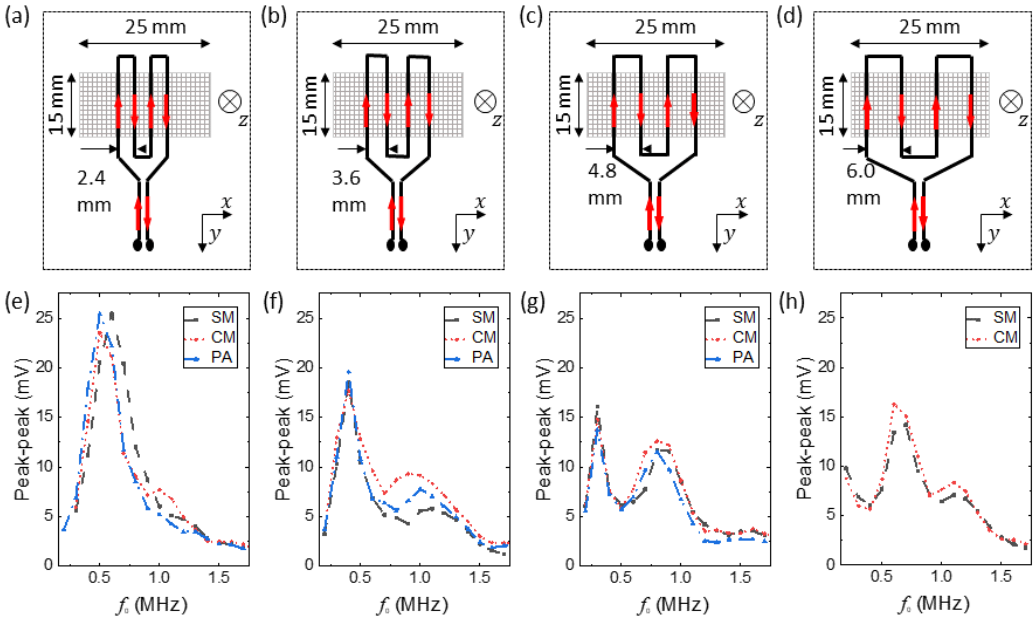

Figure 6.11: Comparisons of the frequency behaviour between a standard meander (SM), the four-coil composite meander (CM) and the four-coil phased array (PA) EMAT. The geometry of the standard meander EMAT is given from (a) to (d) for d of 2.4, 3.6, 4.8 and 6 mm. The external magnetic field is shown in gray blocks. The flowing current in the meander is indicated by red arrows. The experimental results of the EMAT frequency measurements are given in (e) to (h) for different d or d_{eff} for the same values of d (or d_{eff}).

Table 6.1: Experimental parameters of the standard meander (SM), composite meander (CM) and phased array (PA) EMATs for comparison. The Rayleigh wave was $c_R = 2906$ m/s. f_{fitted} represents the Gaussian fitted experimental result of the EMAT frequency output.

Coil separation			**Primary harmonic (m=0)**		
SM & CM	**PA** ($d = 6\ mm$)		**Wavelength**	**Frequency**	
d, mm	d_{eff}, mm	τ_j, ns	λ_p, mm	f_p, MHz	f_{fitted}, MHz
2.4	2.4	coil 0, 0	4.8	0.60	SM, 0.61±0.01
		coil 1, 1238.8			CM, 0.55±0.01
		coil 2, 2477.6			PA, 0.53±0.01
		coil 3, 3716.4			
3.6	3.6	coil 0, 0	7.2	0.40	SM, 0.41±0.01
		coil 1, 825.9			CM, 0.39±0.00
		coil 2, 1651.8			PA, 0.40±0.01
		coil 3, 2477.6			
4.8	4.8	coil 0, 0	9.6	0.30	SM, 0.30±0.01
		coil 1, 412.9			CM, 0.30±0.01
		coil 2, 825.9			PA, 0.30±0.01
		coil 0, 1238.8			
6.0	6.0	coil 0, 0	12.0	0.24	N/A
		coil 1, 0			
		coil 2, 0			
		coil 3, 0			

dicted wavelength/frequency from equation 6.3 when a certain d or d_{eff} was chosen. Since all chosen d or d_{eff} are larger than the coil width (1.5 mm), the predicted wavelengths are given by $\lambda_p = 2d$ (or d_{eff}). Additionally, the obtained frequency-amplitude curves were fitted using a Gaussian and the fitted peak frequencies, f_{fitted}, are given for comparison. A good agreement between the experimental primary peak frequency from d (column 6) and the prediction (column 5) can be observed.

Selectivity of wavelength

The ability of the phased pulser to tune the coil array in both the spatial and temporal domains allows one to generate multiple wavelengths of Rayleigh wave with a single EMAT configuration. This has been verified (see figure 6.10) for wavelengths 3.06 and 4.84 mm. The comparison between the meander coils and the phased array system confirmed the capability of the latter to be a narrowband generator. This can be used to replace multiple standard meander coils which may be required during practical NDT.

In this section, a measurement was undertaken to investigate the full perfor-

mance of the phased four-coil EMAT system. The aim was to show that an arbitrary wavelength can be obtained via electronic changing of the effective coil separation d_{eff} and the centre frequency of the driving signal f_0 of the four-coil phased design.

During the experiment, d_{eff} for the four-coil array transducer was continuously decreased from 6.0 mm (the fixed original separation) to 1.0 mm, with a 0.25 mm step. The driving signal was in three-cycle duration and its centre frequency f_0 at each d_{eff} was progressively increased from 200 kHz to 1.2 MHz, with a 25 kHz step. The detected A-scan signal was recorded, and the peak-peak amplitude was measured to represent the efficiency when the phased array was in the corresponding (d_{eff}, f_0) setting. Full results are given in figure 6.12. Activation of a single ($N_{di} = 1$) or two ($N_{di} = 2$) coil pairs were implemented separately for comparison.

Figures 6.12(a) and (b) show the phased array efficiency on the spatial (d_{eff}) - temporal (f_0) map when $N_{di} = 1$ and $N_{di} = 2$ were applied, respectively. The primary harmonic ($m = 0$) and second harmonic ($m = 1$) predictions are given by dotted red and black lines, respectively, for comparison, calculated using equation 6.4. The experimental results show good agreement with the prediction. However, the experimental fringes show a finite width for both modes, especially in the case when $N_{di} = 1$. This is attributable to the finite bandwidth of both the array spatial spectrum and the driving signal. The ideal situations represented by the dotted lines are not achievable via the phased four-coil array. This is because the number of applied coil pairs ($N_{di} = 1$ or 2) and the cycle number of the driving signal (three-cycle) were not sufficient to provide an infinitely narrow bandwidth centred at the desired wavelength or frequency. The bright fringe of $N_{di} = 2$ is narrower than that of $N_{di} = 1$, confirming that as N_{di} increases the measurement tends towards the ideal situation.

Both $N_{di} = 1$ and $N_{di} = 2$ show a tunable frequency range from about 900 kHz to 350 kHz when d_{eff} was increased from 1.5 to 4.5 mm. This proves the performance of the four-coil phased system to generate multiple wavelengths continuously. The second harmonic $m = 1$ (the second bright fringe) in $N_{di} = 1$ started to appear when d_{eff} was increased to 4 mm, but is less observable in $N_{di} = 2$ whose primary harmonic ($m = 0$) always dominated over this range. This can be understood from the theoretical analysis given in section 5.5 that shows, for a linear coil array with more elements ($N_{di} = 2$ in this experiment), the frequency/wavelength filtering performance will be better, compared to that with fewer elements ($N_{di} = 1$). The higher harmonics can be better suppressed by using more coil elements.

Figures 6.12(c) and (d) extract information from (a) and (b) to show the

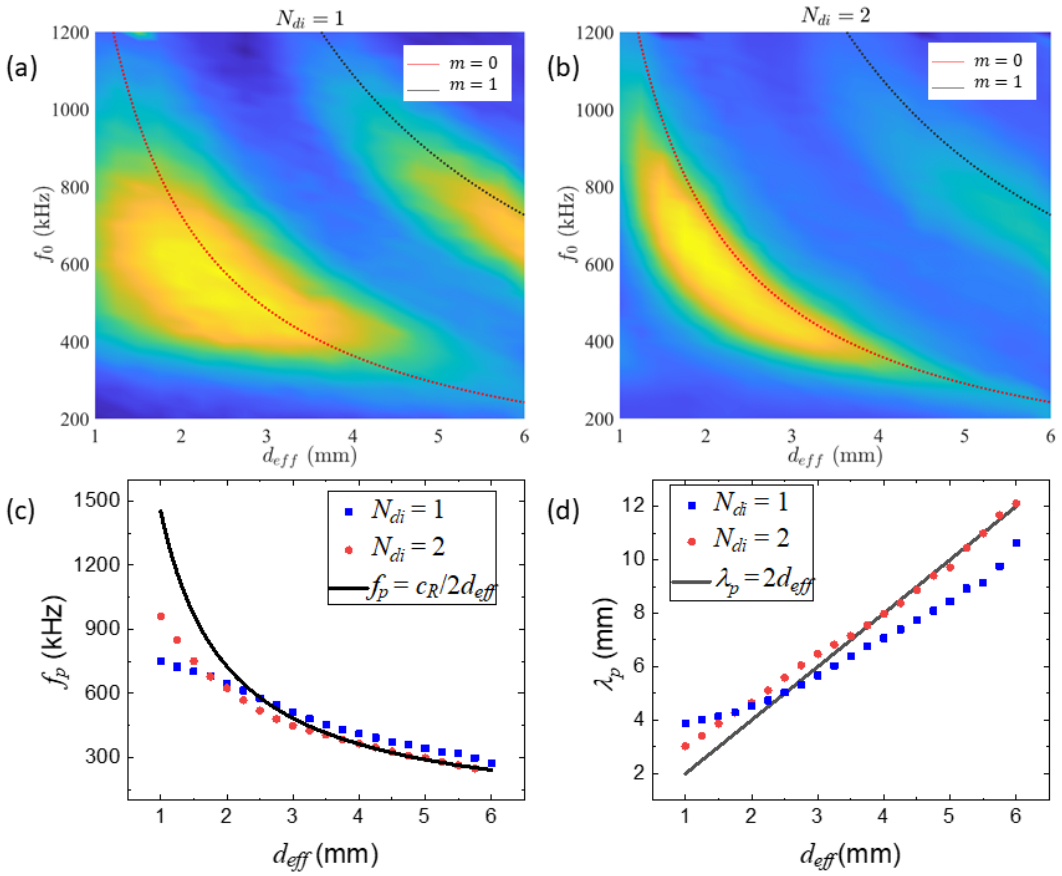

Figure 6.12: Full results of tuning the phased array EMAT for multiple-wavelength Rayleigh wave generation. (a) and (b) are the array efficiency results on the spatial-temporal map when $N_{di} = 1$ and $N_{di} = 2$ were used, respectively. (c) and (d) are the Gaussian fitted peak frequency and wavelength values respectively using the data given in (a) and (b). For a chosen d_{eff}, the phased array generated (c) frequency and (d) wavelength are illustrated, showing the capability of Rayleigh mode selectivity. The rule of thumb prediction is given by black solid lines for comparison.

Table 6.2: Technical data of the four-coil phased EMAT system generating different wavelengths. Suitable for aluminium material testpiece, $c_R = 2906$ m/s.

Array parameters $N_{di} = 2$; $a = 1.5$ mm; $d = 6$ mm, $1 \leq d_{eff} < 6$ mm					
Array wavelength setting λ_p (mm), (d_{eff}, f_p) (mm, kHz)					
λ_p	(d_{eff}, f_p)	λ_p	(d_{eff}, f_p)	λ_p	(d_{eff}, f_p)
3.02	(1.00, 959.81)	6.05	(2.75, 480.23)	8.87	(4.50, 327.57)
3.42	(1.25, 850.69)	6.48	(3.00, 448.70)	9.40	(4.75, 309.00)
3.87	(1.50, 750.48)	6.83	(3.25, 425.39)	9.72	(5.00, 298.97)
4.28	(1.75, 678.65)	7.15	(3.50, 406.65)	10.44	(5.25, 278.44)
4.65	(2.00, 624.79)	7.54	(3.75, 385.23)	10.99	(5.50, 264.39)
5.11	(2.25, 568.61)	7.97	(4.00, 364.43)	11.67	(5.74, 248.93)
5.59	(2.50, 519.96)	8.38	(4.25, 346.94)		

primary frequency (f_p) achieved and the wavelength (λ_p) at various d_{eff}. This was obtained by Gaussian fitting the signal amplitude - driving frequency curve at each d_{eff}. The peaks were found and plotted as a function of d_{eff}, shown in figure 6.12(c). The primary wavelength in figure 6.12(d) was calculated from the data in figure 6.12(c) using the relation $\lambda_p = c_R/f_p$. The rule of thumb predictions, $f_p = c_R/2d_{eff}$ or $\lambda_p = 2d_{eff}$, are also given by solid black lines for comparison. The continuous trend of f_p or λ_p with a varied d_{eff} shows the Rayleigh wavelength selectivity using the phased system. The behaviour of $N_{di} = 2$ matches better to the prediction than that of $N_{di} = 1$, as expected. The upturns occurring in both f_p and λ_p at small d_{eff} ($d_{eff} < 2.5$ mm) indicate that the width effect of the coil source ($a = 1.5$ mm) began to affect the behaviour of the coil array for small d_{eff}, as expected in chapter 5.

Table 6.2 summarises the specifications of the phased four-coil EMAT system for multiple-wavelength Rayleigh wave generation during this test. A target wavelength λ_p can be easily obtained by setting the system d_{eff} and f_0 to the values listed in the table. The designed four-coil phased system was able to deliver Rayleigh wavelengths from about 3 mm to 12 mm on aluminium samples.

Compared to the conventional meander coil EMATs, a phased array system can not only provide an enhanced flexibility in wave generation, but also overcome the production difficulty when a small coil separation is required for a meander-coil for high frequency operation. However, the effect caused by the coil finite width cannot be avoided when using the phasing technique. The discrepancy between the rule of thumb prediction and the experiment when $d_{eff} \to a$ (see figure 6.12(c)) confirms this point.

Building a high frequency Rayleigh EMAT is challenging, but one can use

phasing to achieve a small coil separation electronically. Some future directions can be suggested for optimising the EMAT system, for example, making thinner coils to enhance the high frequency bandwidth; updating the coil material to reduce the electrical loss; updating the EMAT driving electronics, such as building a more powerful current source or combining it with a digital method such as pulse compression, and so on [214].

6.4.3 Characterisation of surface breaking defects

Previous sections demonstrated the performance of a single phased array EMAT delivering different wavelengths. One can characterise a surface crack by selecting an appropriate wavelength and measuring transmission. An enhanced wavelength range hence means a wider detection range for the crack depths, as introduced in section 2.2.2. In this section, the four-coil phased EMAT system was used to measure several surface cracks. An aluminium bar sample was prepared, containing three machined surface slots. All slots were vertical and their opening width was 1.0 mm. The depths of the slots were A: 1.0, B: 2.5 and C: 5.0 mm, and they were across the full width of the bar. Figure 6.13 shows the sample geometry and the employed EMAT transmit-receive set-up. The inset shows a Rayleigh wave generated by the phased EMAT array system, transmitting underneath a surface crack. The transmission and reflection depend on the crack geometry and the Rayleigh wave frequency [82, 85, 86, 213]. The setting of (d_{eff}, f_0) of the array used the optimised results given in table 6.2. For example, to generate a Rayleigh wave with a wavelength of 5.59 mm, the (d_{eff}, f_0) for the four-coil array was (2.5 mm, 520 kHz) on an Aluminium testpiece.

Crack detection

Detection of cracks was done from the Rayleigh wave transmission. Figure 6.14 shows the behaviour for $\lambda_p = 5.59$ mm for a clean surface (black dashed lines) and for two different depth defects (red lines). For a shallow 1.0 mm depth crack, the Rayleigh wave amplitude dropped by only a small amount as most of the wave energy was transmitted underneath the crack. For the 5.0 mm deep crack, the majority of the energy was blocked by the crack and only a small amplitude signal was captured by the detector. This demonstrates that a higher sensitivity to small cracks can be obtained by generating a smaller wavelength, as expected.

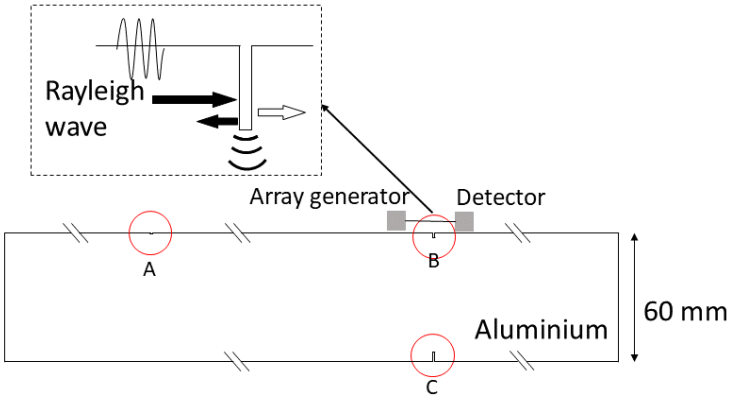

Figure 6.13: Diagram showing the crack characterisation set-up with an EMAT pair. A, B and C are the positions of the three machined surface slots. The Rayleigh wave is sent by the phased array EMAT generator and will be detected by the racetrack detector after transmitting around the crack.

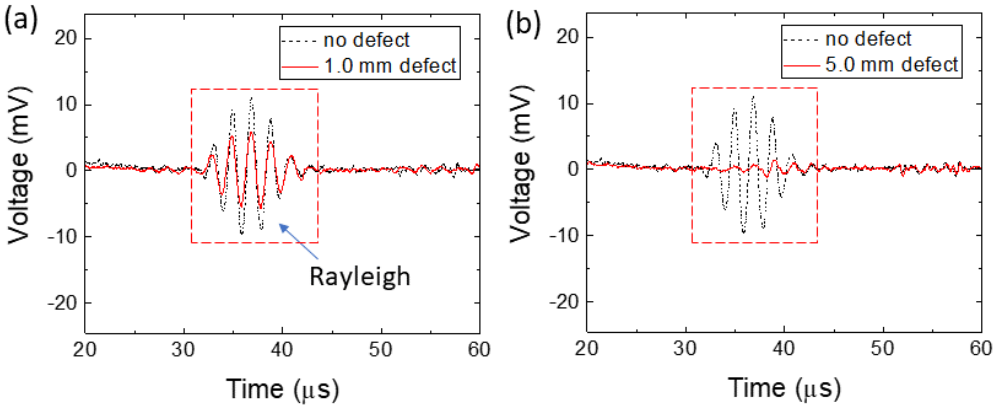

Figure 6.14: Crack sensing by the four-coil phased EMAT array for d_{eff}=2.5 mm, f_0=520 kHz and a generated wavelength of 5.59 mm. Two A-scans obtained for cracks A and C.

Depth gauging

The tuneability of the Rayleigh wavelength offers a unique ability to analyse the crack geometry. First, a small wavelength can be chosen to scan the sample. Since the Rayleigh wave propagates in the order of one-wavelength underneath the surface, any potential surface fatigue crack, or even surface roughness that is deep enough compared to the wavelength, could be identified. This is defined as the high sensitivity mode of the system and a *yes/no* answer would be immediately known as to whether a feature is present, without sizing information. This high sensitivity mode hence provides a means of fast localisation of the cracks. Once a crack was found, the crack depth could be gauged by varying the EMAT wavelength and identifying the cut-off frequency for the crack in order to gauge its depth [50].

Figure 6.15 shows the result of such a measurement for three different depth defects. For each defect, the setting of (d_{eff}, f_0) and hence wavelength λ_p were varied, with the generation and detection EMATs at fixed positions on either side of the defect. The peak-peak transmitted Rayleigh amplitude was measured and was plotted as a function of wavelength. Normalisation was undertaken using the no-defect reference amplitude measurement, indicating that some energy is still blocked even for larger wavelengths, as expected [92]. The experimental results for all slots are shown by the points. They were then fitted by a normal logistic function, so the trend can be better clarified. The corresponding frequency f_p is given in the upper x-axis.

For the 1.0 mm deep slot, the filtering behaviour can be clearly seen, with longer wavelengths mainly able to pass underneath the crack and short wavelengths mostly blocked. The 2.5 mm slot shows the start of the transition to waves being able to pass underneath the slot for higher wavelengths. The 5.0 mm deep slot predominantly blocked signals over all wavelengths investigated, as expected; even for a 10.0 mm wavelength, for example, the crack depth is still significant compared to the wavelength and blocked a significant amount of the wave energy. Some transmitted amplitude is measured even for small wavelengths, where Rayleigh waves should be blocked, due to a mode-converted longitudinal to shear (and vice-versa) wave from the back face of the sample which arrived close to the Rayleigh wave arrival time. The amplitude of this wave varied with d_{eff} due to interference effects, with the amplitude strongest for short wavelengths. Additionally, for the 1.0 and 2.5 slots, the scans were made close to the sample edge due to the presence of deep slots on the side face, adding the effect of edge reflections.

Figure 6.15 can be further used with the combination of a crack calibration curve, such as figure 2.11 in chapter 2 or figure 7.9(b) in chapter 7, for crack sizing.

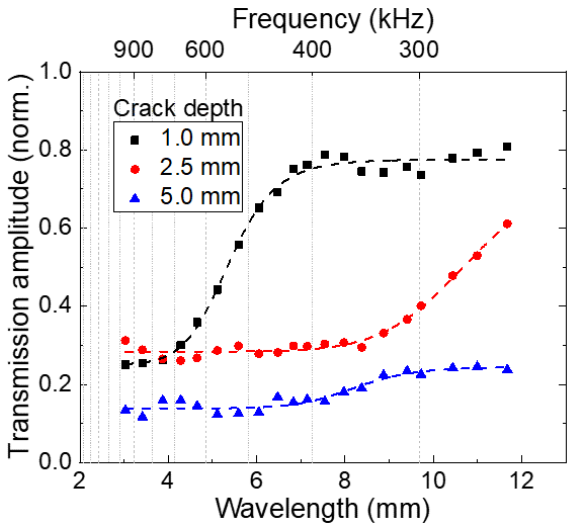

Figure 6.15: Results of characterising the surface defects by the four-coil phased EMAT. Different wavelenths were sent and the wave transmission coefficient was recorded.

Cut-off wavelengths that represent the waves which were mostly passed (transmission larger than 0.8) or blocked (transmission smaller than 0.25) can be defined. For the 1 mm slot, the measurable wavelength range during the cut-off behaviour is from 4 to 7 mm, and the corresponding frequency is from 400 to 700 kHz. Using the calibrated value of a 0.6 MHz Rayleigh wave given in figure 7.9(b), a 2.2 mm estimated crack depth is found. For the 2.5 mm slot, the measured transmission of 0.4 at frequency 300 kHz was chosen to compare with data in the work [57, 92], giving a 3.6 mm depth estimate. The results are not highly accurate, but provide a means of fast characterisation in the early cracking stage, and a full calibration for these EMATs would give a much improved estimate. Deeper cracks such as the 5 mm slot in the test are difficult to size in this experiment, but can be estimated by a broadband EMAT system with lower frequencies [92].

From the above work, two things are of note. Firstly, the in-house built phased EMAT system shows a good sensitivity for detecting surface cracks over a wide range of depths. For shallower cracks, waves will be transmitted, but the blocking of the wave becomes very clear when a smaller wavelength is used. Secondly, to widen the depth monitoring range, one can expand the range of λ_p. For example, to size the 5 mm deep crack, the testing wavelength should be increased until the upturn shape occurs. Sub-mm cracks offer uncertain hazards and challenges for detection, and for detection of these smaller wavelengths are needed. This can be optimised by changing the phased array parameters or producing narrower coils, as

suggested in section 6.4.2.

6.5 Lift-off comparison between phased arrays and physical arrays

The lift-off effect caused by the mirror current spreading has been discussed comprehensively in chapter 5 for EMATs consisting primarily of linear coils. For the phasing concept presented in this chapter, the parameter of coil separation (d for fixed physical arrays or d_{eff} for phased arrays) is the key factor to enhance the surface crack detection performance as it controls the optimal frequency. This section compares the lift-off performance between a phased EMAT array system and a normal EMAT array system to see if there are further benefits from phasing. The design of the phased EMAT array followed the conceptual design presented in this chapter, where linear coils with alternating current polarisation were applied. The fixed array system was the coil array with different fixed physical separations presented in section 5.4. The difference between the two systems was the use of phasing or not.

A quantitative study on the lift-off behaviour for each was undertaken through a two-coil system. Both theoretical and experimental analysis is presented here. The theory model with the distorted mirror current was based on $\tilde{J}_{e,y}^{tot-}$ from equation 5.25 in section 5.6.2, and the corresponding experimental configuration of the two-coils (phased and non-phased) has been introduced in section 6.2.1.

6.5.1 Influence of the coil separation

Apart from the issue caused by the coil finite width, the separation d between the coils can have a strong effect on the measured behaviour, as will the lift-off. Models were calculated using different values of d and h for $a = 1.5$ mm. The value of $\tilde{J}_{e,y}^{tot-}$ will always be zero at the centre of the two coils ($x = 0$) (see figures 5.17(a) to (e)). To quantify the distortion of the signals, the values of $\tilde{J}_{e,y}^{tot-}$ at each edge of the right hand coil were compared; at zero lift-off, these will be the same, but will change by different amounts as lift-off is increased if there is any spatial interaction between the generated currents from each coil. A factor R^- given by,

$$R^-(a,d,h) = \frac{\tilde{J}_{e,y}^{tot-}|_{x=d/2+a/2}}{\tilde{J}_{e,y}^{tot-}|_{x=d/2-a/2}}, \tag{6.8}$$

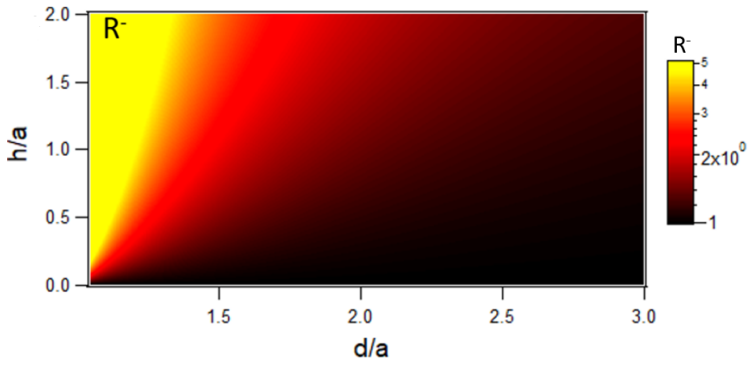

Figure 6.16: Colour scale plot showing the value of R^- as lift-off and coil separation is varied. The lift-off effect on the distortion of the signal is strongest for small coil separations.

was defined and is plotted in figure 6.16, where the lift-off and separation are normalised by the coil width a. A value of 1 (black on the colour scale) corresponds to no distortion, meaning the selected coil profile remains the same without influence from its neighbour. The R^- value drastically increases as d decreases and h increases, showing that the effect of lift-off on the generated ultrasound signals will be strongest for small coil separations.

For a meander-line coil, a small separation between each coil element allows for generation of surface waves with a high frequency, which is beneficial for detection of small cracks. However, the eddy-current cross-talk underneath the coils will lead to a decreased lift-off performance.

6.5.2 The equivalence of physical and phased separation of coils

Detection of the generated surface wave signal has been described by the convolution model $s(t)$ (equation 5.14) in chapter 5, which is determined by the driving signal y and the coil current distribution $\tilde{J}_{e,y}$. To compare the behaviour between a phased array and a normal array, the temporal term y needs to be further discussed. This is because the phasing allows the coils to be driven independently, thereby an extra phase lag can occur between coils in the phased arrays compared to the normal arrays, where all coil elements are driven simultaneously. A mathematical procedure is given in this section to prove that the operation of the two types of arrays are equivalent, and so the lift-off performance will be equivalent unless other factors are involved.

For a meander coil EMAT, or the arrays presented in chapters 5 and 6, the total ultrasound signal needs to consider the contribution from each turn in the

meander, or each coil in the array. Where there are N EMAT elements (turns or array coils), with coil j centred at a position x_j, the detected signal can be calculated by taking a sum over all the contributions. Assuming that each element is activated by a signal with the same properties (centre frequency, number of cycles) at the same time, $y(t)$, the total displacement at the detection point is given by,

$$S(t) \propto \left[\sum_{j=1}^{N} \tilde{J}_{e,y}(x + x_j) \right] \otimes y(t), \tag{6.9}$$

where $\tilde{J}_{e,y}$ is the current from each coil, as demonstrated in section 5.3. For a two-coil system with a separation of d, the sum part of this equation simplifies to the same form ($\tilde{J}_{e,y}^{tot-}$) as equation 5.25.

As demonstrated in section 6.3, multiple coils were driven at set times using a chosen delay sequence (i.e. were phased) to generate a Rayleigh wave. This allowed the coils to have one physical separation d, but behave as if they were at different locations. The effective coil separation d_{eff} in the array is governed by the physical separation and the delay on activation of each coil. The total signal generated by a phased linear array, when the jth coil is individually controlled by a temporal function $y(t - \tau_j)$, where τ_j is the fixed delay for the jth coil, is given by,

$$S_{ph}(t) \propto \sum_{j=1}^{N} \left[\tilde{J}_{e,y}(x + x_j^0) \otimes y(t - \tau_j) \right], \tag{6.10}$$

where x_j^0 denotes the physical location for the jth coil in the array. By using the properties of the convolution function, it can be shown that,

$$S_{ph}(t) \propto \left[\sum_{j=1}^{N} \tilde{J}_{e,y}(x + x_j^0 - \tau_j \times c_R) \right] \otimes y(t), \tag{6.11}$$

where the effective coil location is now given by $x_j^0 - \tau_j \times c_R$. If $x_j^0 - \tau_j \times c_R = x_j$ from equation 6.9, i.e. comparing the behaviour at a phased separation to the equivalent physical separation, the two equations (equations 6.9 and 6.11) would be equivalent mathematically, and the lift-off behaviour should be the same. Any difference in behaviour would be due to electrical differences between the two set-ups, which would be expected to dominate for whichever out of the phased and physical array had the smallest physical separation, and differences in magnetic field orientation at each coil.

Experimental validation

The lift-off performance of a meander coil (or well separated coil array) with large d is better than that of a tightly spaced array, due to the lower frequency of operation and the behaviour of the distortions shown in figure 6.16 for small values of d. This section compares the behaviour of the generated ultrasound with lift-off, for a set of physical separations, and for a pair of coils with 8 mm physical separation but phased to have smaller effective separations.

Coils spacings of d or d_{eff} of 2, 2.5, 3, 4 and 5 mm were tested. Each group was undertaken at lift-offs from 0.1 to 1.3 mm, where the lift-off of around 0.1 mm due to the tape protecting the coil has been included. The driving signal $y(t)$ was varied for each d or d_{eff}, but then remained the same for each value of d (d_{eff}) at all lift-offs. The choice of centre frequency was determined by the meander-coil rule, $\lambda = 2d$ or (d_{eff}), to ensure a good signal-to-noise ratio for each set-up. The corresponding frequencies were (d_{eff} : freq); 2 mm:725 kHz, 2.5 mm:580 kHz, 3 mm:465 kHz, 4 mm:350 kHz and 5 mm:285 kHz.

Results are shown in figure 6.17. Figure 6.17(a) shows the behaviour of the peak frequency with lift-off defined as the frequency at which the FFT is a maximum, normalised to the frequency for the smallest lift-off. The expected behaviour calculated using equations 5.8, 5.14 and 5.25 (theory) is also shown. Due to the small amplitude signals obtained experimentally, there is significant scatter in the results; however, good agreement between physical and phased separations and the theoretical predictions is observed. The overall trend shows that the change in frequency behaviour is dominated by the spatial behaviour of the coils, and electrical changes (see problem described in section 3.2.4) have limited effects. Better lift-off behaviour is observed for wider coil separations, with the frequency of the waves remaining closer to the chosen value for zero lift-off. The bandwidth of the detector and its frequency behaviour has not been considered in this work, and will give some extra frequency-dependence to the results [206].

Figure 6.17(b) shows the magnitude of the peak in the FFT with lift-off for each separation, for variable physical spacings (red points), phased two-coil with fixed spacing (black points), and the theoretical model. As with the single coil, the magnitude change has been calculated for a constant magnetic field (blue dashed lines) and for the measured field with lift-off combined with equation 5.10. Factors affecting the behaviour include the spatial spreading and lift-off dependence included in the theory, the reduction in the magnetic field strength with lift-off, changes in impedance, electrical interaction between the two coils, and the divergence of the magnetic field.

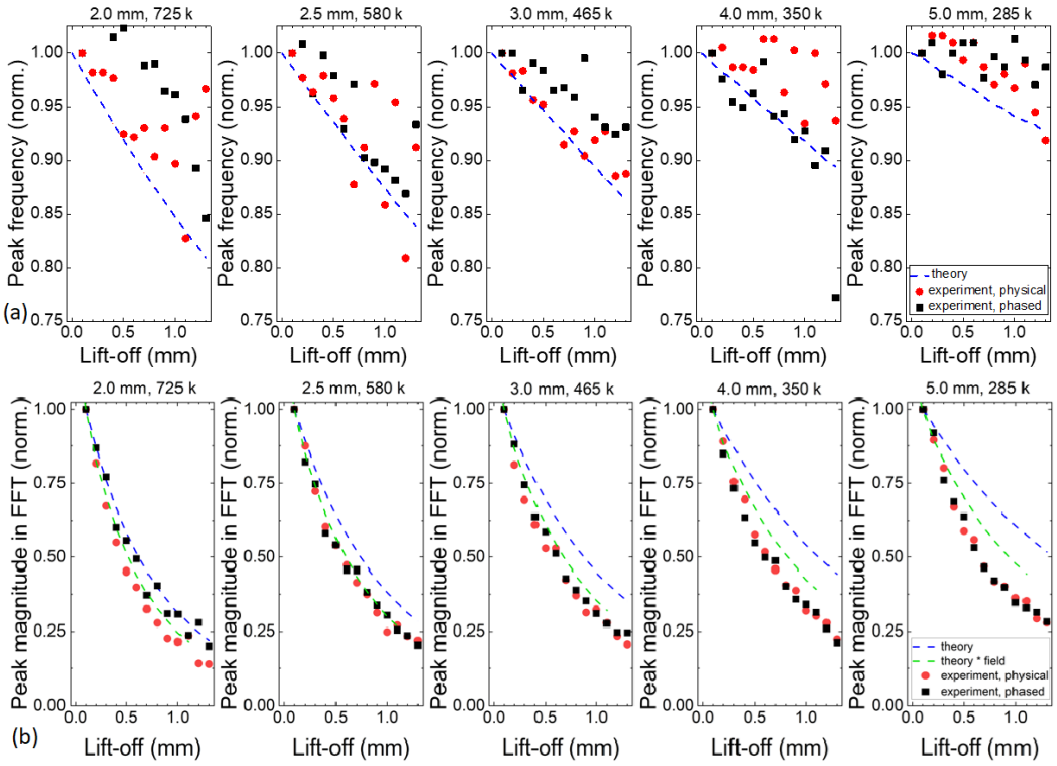

Figure 6.17: Two-coil measurements, for variable physical spacings (red points), phased two-coil with fixed spacing (black points), and theoretical model with constant field (blue dashed lines) or measured field (green dashed lines). (a) Peak frequency comparison. (b) Magnitude of the FFT peak comparison.

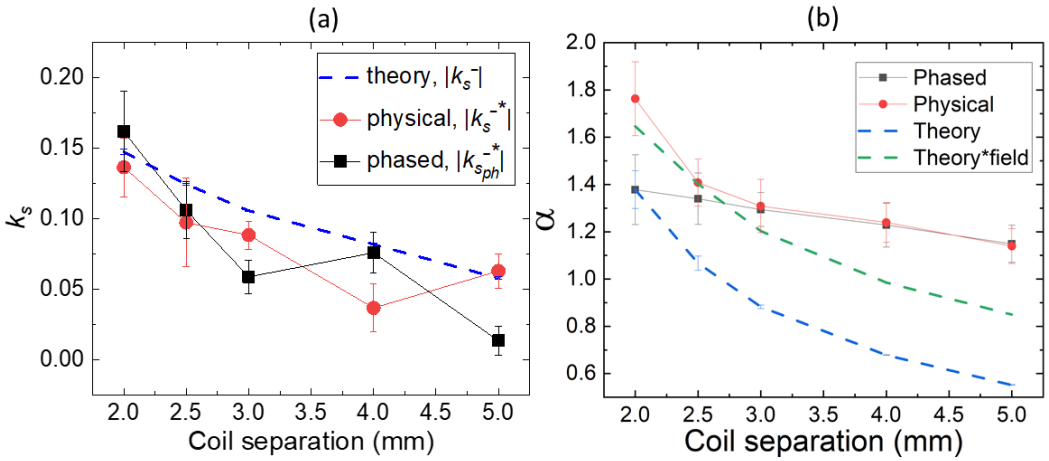

Figure 6.18: Experimental fits to the data in figure 6.17. (a) Frequency decrease slop, k_s. (b) Amplitude drop rate, α.

The experimental data for phased and physical spacings match well for the larger separations, with a clear disagreement only for the smallest spacing tested. Agreement in the data for larger values of d and d_{eff} show that there are minimal electrical interactions between the coils, and that the field divergence effect is small. For the smallest physical separations, the effect of coil interaction must also be considered, accounting for the disagreement between phased and physical results. Where very high frequency (small d) operation is required, using coils with a large physical separation and phasing them to give a small d_{eff} may be beneficial, but the benefits are limited. The model fits very well to the data for small separations, accurately predicting the lift-off behaviour when the magnetic field is taken into account. There are some disagreements at larger separations, where the model suggests that better lift-off performance is expected.

While peak frequency shift with lift-off is an intrinsic property of EMAT lift-off behaviour, as explained in chapter 5, the speed of the shift was found to further compare the performance between phased pair and non-phased pair and the theoretical predictions. Linear fitting was performed for each coil spacing in figure 6.17(a). The slope of the fit was denoted k_s^- for the theory, k_s^{-*} for the physical spacing, and $k_{s_{ph}}^{-*}$ for the phased spacing. Results are given in figure 6.18(a), showing good agreement between the physical and phased separations, and the theoretical predictions.

Another intrinsic property of lift-off to be considered is the amplitude drop. Figure 6.18(b) shows exponential fit values α, when $A\exp\alpha h$ is fit to the FFT magnitudes in figure 6.17(b), for all experimental data and calculations. As before

(section 5.3.3 for single coil), the prediction from the calculations underestimates the decay in all cases. Including the measurement of magnetic field agreement is improved, but the behaviour is not fully modelled using the very simple model presented in chapter 5. This may be due to conflict between the meander coil 'rule of thumb' and the coil width frequency influence used when choosing the frequency of operation, or potentially due to further influence from the coil electrical behaviour. This will be investigated in future work.

6.6 Summary

This chapter presents a four-coil phased EMAT system for enhanced Rayleigh wave surface crack characterisation. The four-coil design was based on the linear array formation demonstrated in section 5.4, and a pseudo meander-coil (4 turns) was constructed. With the use of phasing, the capability of variable working wavelengths was obtained. Comparison between the phased four-coil and meander-line coils was undertaken, showing good agreement of the EMAT ability for Rayleigh wavelength selectivity (designed narrowband performance).

The changeable wavelength of the prototype phased four-coil system was from 3 mm to 11 mm on aluminium samples, giving pronounced sensitivity to surface cracks that were deeper than 1 mm. To achieve higher sensitivity for demanding uses, one can use thinner coil elements or increase the number of applied coil elements.

The lift-off performance of the phased array was also discussed. This was undertaken through a two-coil model mimicking the meander shape in the simplest way. The phased two-coil EMAT was compared with the non-phased (physical) two-coil EMAT which was formed in section 5.6. The eddy current spatial changes with lift-off due to the coil finite width cannot be neglected, and the effect can significantly depend on the coil spacings, either d for physical coil arrays or d_{eff} for phased arrays. Experimental results and theoretical predictions for the frequency shift due to the lift-off effect agreed well, with the phased and physical separations shown to be equivalent within noise levels for all but the smallest physical coil separations. The benefits of using a phased array to achieve EMATs with good lift-off performance are limited, but may be clearer if very small separations/high frequencies are required.

Chapter 7

Multi-mode EMATs for detection of surface cracks on multiple sides of a sample

7.1 Introduction

The non-contact and flexible generation mechanism of EMATs brings many benefits to Rayleigh wave generation, as reviewed in chapters 2 and 3. Other wave modes may also be excited by the EMAT, depending on the design of the EMAT and the thickness of the testpiece sample [3, 11]. Studies using a pancake coil for bulk wave generation confirmed such a point [148, 174, 178], revealing the potential of EMATs for a more comprehensive scanning purpose by including both surface and bulk inspections in the same scan.

Given the advantage of adaptability in design of EMATs and the potential for a more detailed inspection process by using all the modes generated, the performance of an EMAT for generating multiple wavemodes is investigated in this chapter. The standard method of using EMATs in a single mode, such as just considering a Rayleigh wave for inspection, is expanded into the use of multiple wavemodes for multi-dimension inspection. The knowledge of the interaction between Rayleigh waves and surface cracks [57] is combined with the standard method of using bulk waves for far-side surface defect detection, where signal blocking or reflection of the shear wave reflected from the back wall is used for indicating a deep far-side surface defect [215, 216, 217]. The latter has been developed further into the technique of time-of-flight diffraction, introduced in chapter 1. The potential for multi-mode EMATs for enhanced NDT is then explored.

An EMAT pair in transmit-receive mode was developed for sample surface scanning. The design of the multi-wavemode EMAT considers a sample where defects may occur on both faces, but inspection access is limited to just a single side. The design of the EMAT coils are introduced here, including the geometry of the coil and the generated wave properties, such as the frequency and the beam directivity. The EMAT system was calibrated for crack characterisation on either the near-side surface (using the Rayleigh surface wave and the shear bulk wave) or far-side surface (using just the shear bulk wave). The use of the dual-mode to fully characterise the material front and back faces is demonstrated through several measurements, using manual scans and an automated B-scan on several bar samples. The benefits of using both wavemodes simultaneously is well-demonstrated.

7.2 Experimental apparatus

In this section, the experimental set-ups used in this chapter are introduced, including the instrumentation that was used for EMAT driving and data processing, and the sample geometries that were used for different experimental purposes. Details such as the driving signal properties (frequency etc.) and the scanning methods, i.e. manual or automated scan, are given in the relevant sections. The details of the EMAT designs for ultrasound generation and detection are given in section 7.3.

7.2.1 EMAT instrumentation

The experimental set-up used to scan the surface cracks is shown in figure 7.1. The generation EMAT was driven by a single channel of the four-channel high energy pulser introduced in chapter 4. The receiving EMAT was used to detect the ultrasound signal. The separation between transmitter and receiver was adjustable and was optimised as described in section 7.3. The captured ultrasound signal was amplified and passed through a 2.5 MHz low pass analogue filter. The signal was digitalised and saved by the digital oscilloscope with a 32 times averaging. The recorded signal was then processed by a desktop computer. A LabVIEW controlled xy stage system was used for some scans, which was able to provide an automated scan for high accuracy analysis by setting a small step size. The LabVIEW programme enables control of the xy platform and also synchronises both the xy stage and the digital oscilloscope so the data can be automatically saved.

For automated scans, the EMAT pair was connected onto the y-beam of the xy stage using a configurable connector. The scanning method can be switched from either manual or automated scan by using or removing this connector. The use of

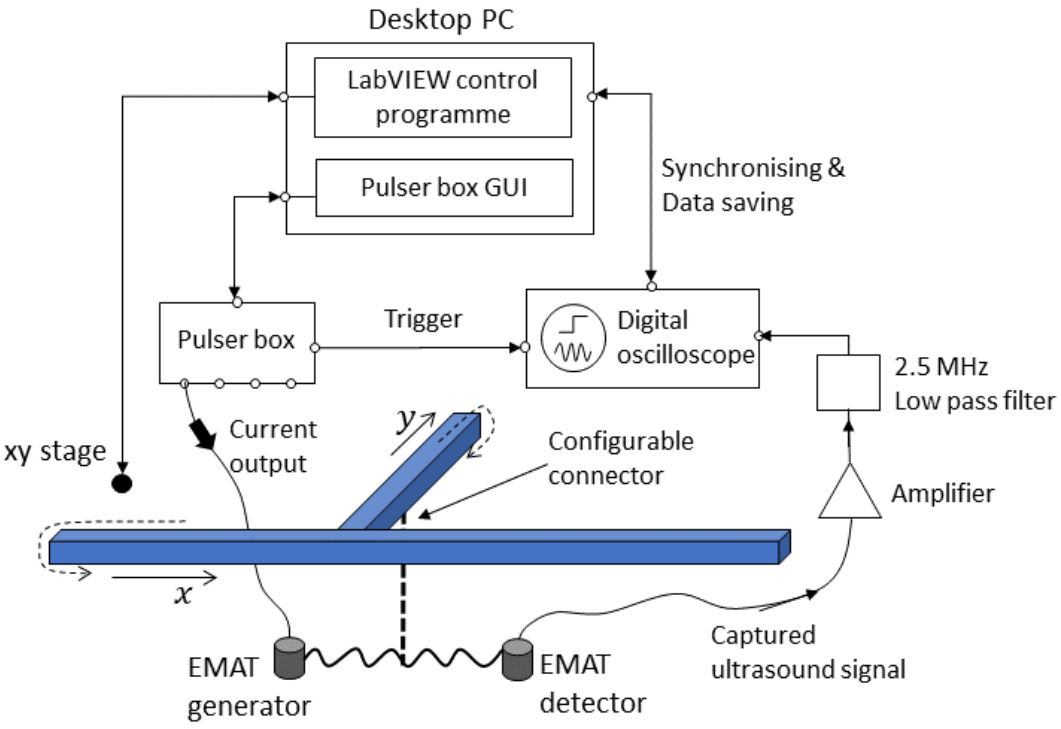

Figure 7.1: Schematic diagram showing the EMAT instrumentation for characterising material surface cracks. The designed EMAT transmit-receive pair was scanned using either a manual scan or an automated scan, depending on the scanning purposes, and will be introduced in section 7.3 and 7.4. The latter was implemented through a LabVIEW platform controlled xy stage.

the xy stage system or manual scanning depends on the scan purpose. For analysis of the EMAT designs and for wave calibrations (sections 7.3 and 7.4.1), the EMAT was not connected to the xy stage and the tests were manually performed. For a low resolution scan on a bar sample with double sided vertical cracks (section 7.4.2.1), the measurement was also done manually. A highly detailed scan for a sample with a complex near-side crack (section 7.4.2.2) was undertaken using the automated system, so more details could be recorded and analysed. The scan set-up, including the EMAT starting positions and sample material geometry, will be given in the relevant sections. For shear wave directivity measurements, an alternative set-up was used.

7.2.2 Preparation of samples

All samples tested in this chapter were aluminium. The prepared sample surface was smooth but not polished, with the top 3.0 mm machined off at the surface. This was to reduce the grain structure impact on Rayleigh wave propagation when the top layers show a different grain structure to the deeper layers with a mix of material properties in an extruded aluminium [55]. The Rayleigh wavelengths used in the work were significantly larger than any surface roughness.

Figure 7.2 shows the geometry of the EMAT transmit-receive system when applied to different sample materials. A 70 mm radius aluminium semi-cylindrical sample was used to study the EMAT shear wave directivity, given in figure 7.2(a). This experiment relates to section 7.3.2. For this sample the generator was fixed in place, and the detector was scanned by hand around the sample. Block samples with 60 mm thickness were used for scanning a bar, shown in figure 7.2(b). This geometry applies for all the rest of the experiments undertaken in sections 7.3 and 7.4. Both generator and detector EMAT were placed on the same side of the bar sample, mimicking the situation where the other side of the sample is not accessible in real-world NDT conditions.

7.3 EMATs in pitch-catch mode

7.3.1 EMAT configuration

The work reported in [174] investigated shear wave generation using an EMAT with a flat spiral (pancake) coil. The spatial distribution of the spiral coil is different from a typical piston force behaviour for a piezoelectric transducer. The ultrasound amplitude is zero on the axis through the centre of the coil due to antisymmetry of

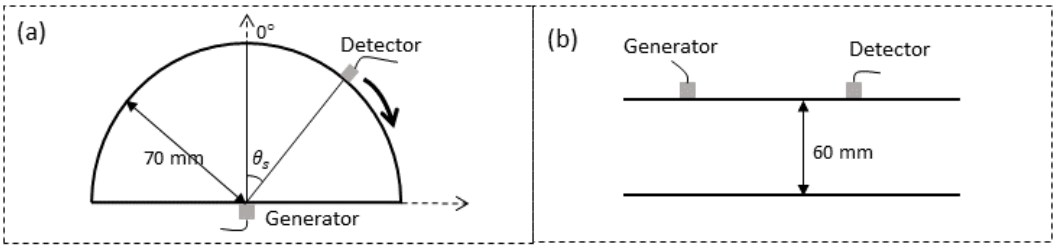

Figure 7.2: Schematic diagram showing the geometry using an EMAT transmit-receive pair for different purposes in this chapter (EMAT drivers and control modules are omitted in this graph).(a) is used for studying the directivity property of the EMAT generator. (b) is for using the EMAT pair to to scan a bar sample.

the signal generated by a spiral coil. The generated shear wave is hence not purely plane, but a combination of a plane and an edge or a head wave. A beam profile with an intrinsic angular behaviour was observed in reference [174], with the maximum at around 35° to the surface normal, due to constructive interference between the edge shear wave and the head wave. A good beam directivity of the shear bulk wave was shown and can potentially be applied to inspect samples.

The racetrack coil design was chosen as the generation EMAT coil for both bulk shear wave and Rayleigh wave in this work. Figures 7.3(a) and (b) show the geometry. The racetrack coil can be considered as two contacting line sources, but is antisymmetric around the coil centre, similar to a spiral coil in two-dimensions. Unlike a spiral coil, however, where the coil turns are radially polarised and the generated waves are omni-directional in the xy-plane, the racetrack provides a majority of the energy in the x-direction for Rayleigh waves and in the xz-plane for shear waves, which can better suit inspection of a bar sample. A single linear coil (figure 7.3(c) and (d)), which can be treated as a uniform line source, was also tested, to give a comparison with the racetrack coil for the study of the bulk shear wave directivity. For these generation EMATs, copper wire of diameter 0.1 mm was used to make the coil, and the effective widths and lengths of both coils were 1.5 mm and 15 mm, respectively, with the same block magnets used, as can be seen from figure 7.3(a) and (c). Figure 7.3(b) and (d) show the racetrack and linear coil induced Lorentz force in an aluminium material sample. Both coils show a reasonably good response for frequencies that are below 2.0 MHz [206].

Detection EMATs used one configurable design; a linear coil, that can be used with two polarisations of the external magnet for directivity measurements, shown in figure 7.4. The linear detector coil was hand-wound using 7 turns of 0.2 mm diameter wire, giving a total width of 1.5 mm including gaps. These de-

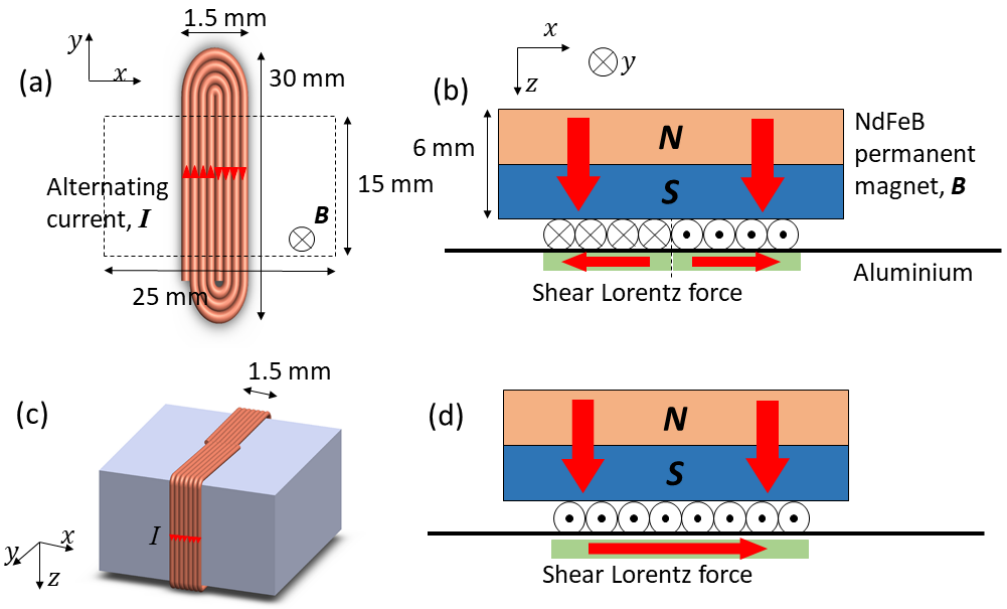

Figure 7.3: Schematic diagram of the generation EMATs. Racetrack generator is shown in (a) top view and (b) cut-through of EMAT-material. Linear generator is shown in (c) 3D sketch and (d) cut-through of the EMAT-material. The same magnet of dimensions 25 × 15 × 6 mm ($x \times y \times z$) was used for both coils.

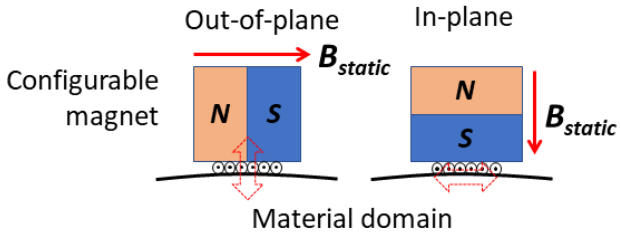

Figure 7.4: Schematic showing the linear coil EMAT detector for measuring the shear wave directivity of the EMAT generator. Both in-plane and out-of-plane velocity components can be detected.

signs of EMATs have been proven to be sensitive to primarily either the in-plane or out-of-plane velocity components by careful choice of the direction of the magnetic field from the permanent magnet [85, 139]. For a magnetic field directed into the sample (perpendicular to the surface), the in-plane particle motion will give a Lorentz force which is parallel to the EMAT coil, and hence will give a detectable current. Conversely, for a magnetic field directed parallel to the sample surface, a suitable current direction will be generated by particle motion which is out-of-plane (perpendicular to the sample surface). Figures 7.4(a) and (b) show schematics of the configuration of the linear in-plane and out-of-plane coil detectors, respectively. The orientation of the magnet is changeable and hence so is the sensing direction of the ultrasonic velocity signal.

7.3.2 Shear wave directivity

Using bulk waves for ultrasonic NDT has been widely applied in both industrial and fundamental research areas [53]. In this work, a shear wave was chosen as the mode for detecting a surface crack growing on the inaccessible (far) surface of the sample, while a Rayleigh wave was used as the primary mode for inspection of the near-side surface. Measurements use the blocking of the signal by a crack during scanning [217]. The sound velocity of a bulk shear wave (3040 m/s) is close to that of a Rayleigh wave (first mode, 2906 m/s) in aluminium, so in the chosen measurement geometry shown in figure 7.2, the detected shear wave can be well distinguished from the Rayleigh wave. Also, the transducer dead zone (electrical cross-talk when the coil is driven, showing as the noise from the starting time point) can be avoided, which can sometimes be an issue for the longitudinal mode due to its large speed. The EMAT generator is also more efficient for shear wave generation than for longitudinal waves [3, 143, 174].

To optimise the set-up of the EMAT transmit-receive pair (i.e. finding the ideal EMAT separation for a given bar thickness), the beam profile of the shear wave generated by the EMAT generator was first investigated. Earlier papers have studied the directivity of a range of EMAT coil designs, primarily considering spiral, linear, meander, or coils generating SH waves, but not for the racetrack coil for bulk shear wave generation [172, 173, 174, 178, 183]. A similar racetrack coil was used by [173], but they used a compound magnet such that their magnetic field switched direction on either side of the coil, resulting in a force similar to that generated by a linear coil.

Experimental measurements and numerical modelling were undertaken to study the directivity of the EMAT generation coils shown in figure 7.3. The driv-

ing signal was operated at 0.6, 1.0, 1.5 and 2.0 MHz for a three-cycle, relatively narrowband pulse. The generation EMAT was positioned at the centre of the semi-cylindrical sample's flat surface, and the linear coil detector was moved around the curved side of the sample, with the moving direction indicated in figure 7.2(a). The measurements were taken every 5°, and both in-plane and out-of-plane velocities were measured. The commercial FEM package PZFlex was also used to verify the beam profile. An identical two dimensional aluminium model was built to match the experiments, quadrilaterally meshed with an element size of 75 μm, which is approximately 21 elements per wavelength when the centre frequency is 2.0 MHz. The generation coil was modelled as an ideal pressure source, with the pressure applied uniformly to each element over a distance matching the width of the coil used in the experiments. Each source load was defined as a standard sinusoidal burst with three periods and a centre frequency of 0.5, 1.0, 1.5 or 2.0 MHz. The modelled x- and y- velocity data matrix was output from the numerical model, and the in-plane and out-of-plane velocities relative to the curved surface were calculated at each detection position from these two orthogonal components. The relations between two coordinate systems are given by

$$\begin{bmatrix} v_{IP} \\ v_{OP} \end{bmatrix} = \begin{bmatrix} -\cos\theta_s & \sin\theta_s \\ \sin\theta_s & \cos\theta_s \end{bmatrix} \begin{bmatrix} v_x \\ v_y \end{bmatrix}, \tag{7.1}$$

where θ_s is the incident angle of the shear wave. v_{IP} and v_{OP} refer to the desired in-plane and out-of-plane ultrasound velocities for comparison with experiments.

Figure 7.5 exemplifies the 2D numerical simulation of the racetrack generator at 1.0 MHz using PZFlex. Figures 7.5(a) and (b) are snapshots for the modelling of the x-velocity and y-velocity, respectively, at a time of 9.08 μs. Generally, four waves can be observed; the Rayleigh wave, shear bulk wave, longitudinal wave and head wave [1], as indicated by the arrows in figure 7.5(a). It can be roughly seen from the colour intensity that the amplitudes of the shear bulk wave and Rayleigh wave are greater than that of the longitudinal wave. Also, the longitudinal and shear waves are well-distinguished due to the large difference between their velocities. In the A-scan given in figure 7.5(c) for an angle of $\theta_s = 45°$ for the x-velocity (v_x), there are three waves visible; the incident longitudinal wave appearing at around 12 μs, the incident shear wave appearing at around 24 μs and a Rayleigh wave that

[1] A head wave is the wave associated with the surface skimming longitudinal wave. According to Huygen's theory of wavelets, the primary critically refracted wave (surface skimming wave) acts as a source for new secondary wavefronts and ray paths. The created head wave exhibits a normal wavefront due to the propagation of the surface skimming wave, with an angle that equal to that of the mode converted shear wave.

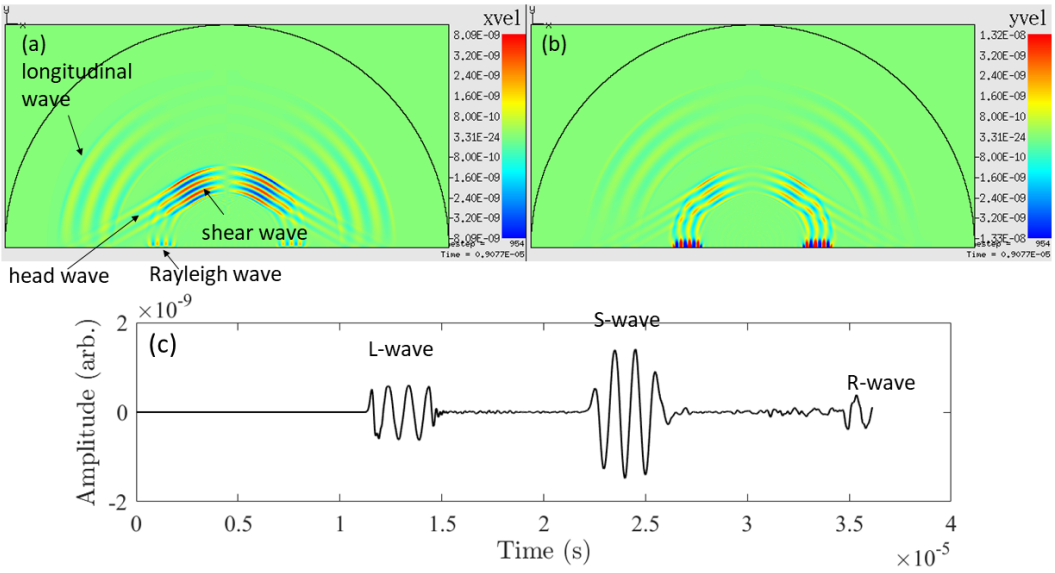

Figure 7.5: 2D simulation of racetrack generator. This is from 9.08 μs after the coil has been fired. (a) shows x-velocity. (b) shows y-velocity. (c) The A-scan of x-velocity, v_x at an incident angle, θ_s of 45°.

travelled around the sample surface at around 34 μs.

Full analysed amplitude results for both simulation and experimental measurement are shown in figure 7.6, giving the amplitude of the signal at each position on a polar plot. Points in the higher angle range, such as $\theta_s > 85°$, or lower angle range, $\theta_s < 5°$, were removed for clarity. This is due to the interference between the bulk waves and the Rayleigh wave, as the latter was travelling bidirectionally along the sample surface. The ultrasound near the sample surface is not a single wavemode but can be very complicated. The out-of-plane component for both linear and racetrack coils shows primarily noise, as expected for a shear wave, although some directivity is observed. For the in-plane, there is overall a good agreement between modelling and experimental results.

The shear waves generated by both racetrack and linear coils are directed to a certain region in the bulk. The racetrack coil was mostly radiating at an angle of 35°, whereas the linear coil was more scattered into the region of lower angles. This confirms the previous work [174] and can be explained by the source distribution of the coil. The racetrack is antisymmetric around the coil centre, so less wave appears along the axis of the coil due to the cancellation of shear waves. The linear coil, on the other hand, has a force that is uniformly distributed, so more wave energy travels straight down and the radiated wave can be described more as a plane wave. The geometrical spread of the shear beam radiated by EMATs cannot be avoided,

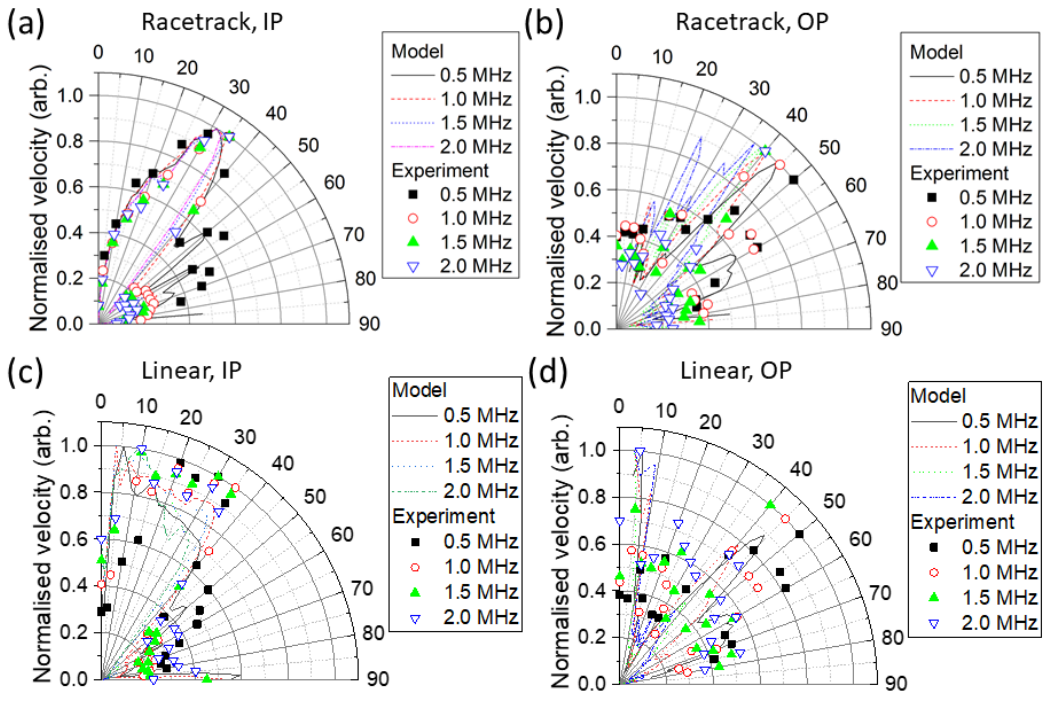

Figure 7.6: Normalised shear wave directivity pattern of the generation EMAT. Results of the racetrack generator are given in (a) and (b). Linear generator is in (c) and (d). IP refers to in-plane component and OP is out-of-plane.

but within a small chosen detection domain, it can be acceptable.

Since the racetrack is able to provide a better performance of shear wave directivity than that of a linear coil, it was used for scanning. The separation between the transmit-receive EMAT pair was optimised for a given sample thickness on a bar sample to ensure the largest signal is obtained, while still maintaining separation between the shear and Rayleigh wavemodes. The separation of transmit and receive EMATs was optimised such that they detected the beam travel at around 35°.

An experiment based on the schematic shown in figure 7.2(b) was used to confirm the transducer separation on a 60 mm thick aluminium bar sample. The racetrack generation EMAT was fixed and the detector was scanned along the sample length by hand to increase separation, with a spatial interval of 10 mm. The corresponding incident angle range for the shear wave that was reflected once from the back wall before returning to the detector, was from 19.7° to 60.8°. Multiple driving frequencies were tested, from 400 kHz to 2.0 MHz, with a 200 kHz step. The magnitude of the detected signal as a function of transducer separation at each generation frequency is shown in figure 7.7 for both in-plane and out-of-plane velocities. As the

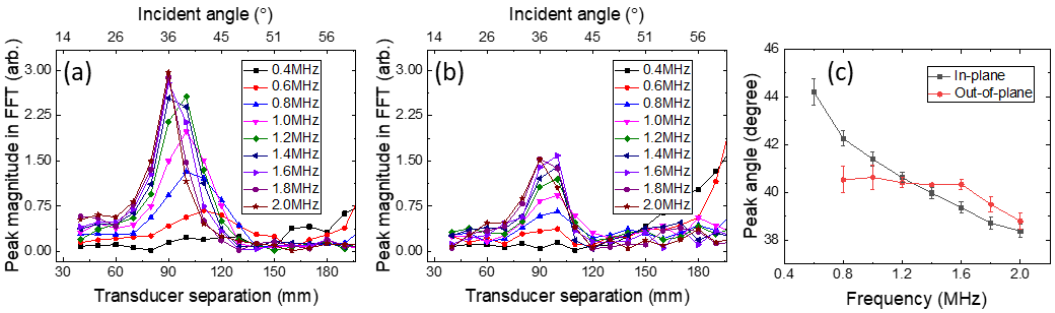

Figure 7.7: Experimental analysis for EMAT pair separtion. Magnitude of the shear wave for (a) in-plane velocity and (b) out-of-plane velocity. (c) Peak incident angle from a Gaussian fit to the data.

shear wave approaches the top sample surface at an angle, it has motion which is partially in-plane and partially out-of-plane relative to the top surface of the sample. The angle at which the amplitude was at the maximum (peak angle) for each frequency was found by Gaussian fitting to the data and is plotted in figure 7.7(c). The amplitudes are shown to scale, and the in-plane signals are stronger than the out-of-plane. Both signals are strongest in the region of 90-110 mm, which corresponds to an angle region of 36° to 43°, in agreement with the directivity measured before. A strong frequency dependence was observed, as can be seen in figure 7.7(c). This is due to the shear wave interference when some phase lag exists across the coil source due to its finite width, i.e. at a position where the constructive interference is satisfied for a certain wavelength (frequency) [183]. However, this was not fully observed in the out-of-plane data. This is because the wave energy in this direction was insufficient, and there were issues with beam spread.

The EMAT transmit-receive pair used for the rest of the work in this chapter was a racetrack generator and in-plane detector. This combination gave a good beam directivity and good signal to noise ratio for the shear wave, and hence was chosen as the optimised set-up.

7.3.3 Multi-wavemodes detected at the bar sample surface

The measurement of waves on the surface of a bar sample can be rather complicated for an EMAT system. Many modes, other than the surface wave, could be sensed by an EMAT receiver, especially when waves have travelled through multiple reflections between the front face and back wall of the sample. Mode conversion between various ultrasound modes can also occur [81]. Before testing the sample for crack detection, identifying different wavemodes is therefore of necessity. The directivity

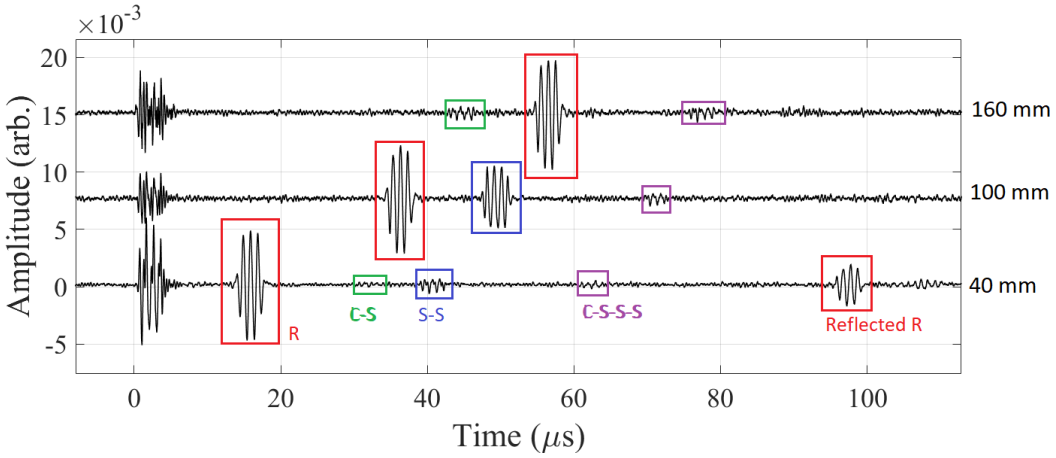

Figure 7.8: Three experimental A-scans obtained by the EMAT transmit-receive pair on an aluminium sample surface are shown. They were obtained at different transducer separations, 40, 100 and 160 mm, labelled on the right. R refers to Rayleigh wave, C is longitudinal wave and S means shear wave.

measurements above allow a prediction of the behaviour.

Figure 7.8 shows a few A-scans taken on a 60 mm thick aluminium bar. The generation EMAT was fixed and the detection EMAT was placed at 40 mm, 100 mm and 160 mm away from the generator. The system frequency was 1.0 MHz, with a three-cycle driving signal. Apart from the electrical cross-talk around 0 s, there are four modes that can be clearly observed: Rayleigh waves, including both the incident (R) and the reflected waves (reflected R) from the sample edge, are windowed by the red boxes; a shear wave arising from the mode conversion of a longitudinal wave at the back wall (CS), is highlighted in the green boxes; a shear wave reflected from the back wall (SS), in the blue boxes, and another shear wave which is reflected twice at the back wall, mode converted from the incident longitudinal wave ($CSSS$), is in the purple boxes. $SSSS$ is not visible.

With an increase or decrease of the transducer separation, different wave modes arrived at various times, as expected and shown clearly by the trend in the time domain in figure 7.8. The amplitudes of the bulk waves vary with separation/incident angle, and at certain separations, different wavemodes can overlap. The effect of Rayleigh wave attenuation for different transducer separations is not observed for these small variations in separations, hence all three Rayleigh signals are of the same amplitude level. The undesired modes, such as the longitudinal to shear wave, are not the major modes that dominate the signal trace, but the situation could be worse if the sample properties are changed, for example using a thinner sample or having a different type of material. Using the EMAT pair for bar

sample scanning thus should have a specific set-up, depending on multiple aspects, from the design of the transducer system to the physical environment and sample geometry. The key thing is to ensure that the ultrasonic waves can propagate in the testpiece and can be interpreted correctly. There are a few conditions outlined as follows for devising a proper separation of the EMAT pair:

1. The separation is sufficient so that the wave arrival times are outside the electrical dead-time following the generation pulse.

2. Within the propagation distance, the issue of wave attenuation (not just Rayleigh wave but also the shear waves) is not significant, so that sufficient wave signal to noise ratio (SNR) can be guaranteed.

3. The chosen wave modes, Rayleigh wave and shear wave, are well separated in time. Interference with other modes is not obvious, so that the signal waveforms are not obviously distorted and the SNR is guaranteed.

According to the shear wave performance (figure 7.7(a)), the sample thickness, and the relative arrival times for the Rayleigh and shear waves, the transducer separation was set as 102 mm, corresponding to a 40.3° shear wave incident angle for a 60 mm thick bar. The ultrasound frequency was set to a value between 0.6 MHz and 1.5 MHz, normally using 1.0 MHz, as the shear wave generation was inefficient at lower frequencies, while the Rayleigh wave generation and detection was inefficient at higher frequencies using the present system.

7.4 Dual-wavemode surface scanning

In this section, the transmit-receive dual mode (Rayleigh and shear waves) EMAT pair was used to scan the material near- and far-side surfaces for surface crack characterisation. Measurements on near-side crack detection using just a Rayleigh wave, and far-side crack detection using a shear bulk wave, were first undertaken. This was to calibrate the EMAT performance for crack depth gauging purposes, so that depth information for cracks on both the near and far side can be obtained by a single scan using both waves. The second part was to use the calibrated EMAT system to scan a bar sample with prepared surface cracks on both faces, and use the waves in combination.

7.4.1 Transducer calibration

It is essential to calibrate the EMAT behaviour before crack detection is done [50, 218]. Two methods which are reported in the literature were used: the surface crack depth calibration curve was obtained for the EMATs for the specific Rayleigh wave frequency/wavelength and bandwidth of operation for the EMAT system used; and the threshold value to be used for shear wave analysis for crack depth was tested. Rayleigh calibration depends on the wave properties such as central frequency, bandwidth, etc., so needs to be tested for each EMAT design/sample material.

Near-side defects: Rayleigh transmission

A bar sample (sample A) shown in figure 7.9(a) was used; this contained two surface slots (cracks A and B, with depths of 2.5 and 1 mm) on the near side surface and three (cracks C, D and M, with depths of 5, 15 and 10 mm) on the back wall. Cracks A and C are vertically aligned, as are cracks B and D.

All cracks were characterised using the Rayleigh wave. Cracks on the far side were tested by simply flipping the sample, so that the EMATs were on the same side of the sample as the cracks. Figure 7.9(b) shows the Rayleigh wave calibration results using the EMAT pair, plotting the transmission coefficient as a function of crack depth. The driving signal was relatively narrowband compared to earlier work [80, 85] with a three-cycle duration. Two centre frequencies, 0.6 and 1.0 MHz, were chosen for producing the calibration curves. The peak to peak amplitude of the detected transmitted wave was recorded and normalised to the level of the 'no defect' signal. For a 0.6 MHz Rayleigh wave, cracks deeper than 9 mm mostly block the wave energy, whereas the blocking depth is about 6 mm for the 1 MHz Rayleigh wave, showing that the range of depth sensitivity depends on the frequency chosen, due to the different Rayleigh wavelengths [57].

Far-side defects: Blocking of the shear wave

The ray path of the shear wave generation and detection using the EMAT pair is illustrated in figure 7.10 for an idealised system (no beam spread). The shadow region is where direct reflections cannot reach the detection EMAT due to the existence of the surface crack on the sample far side, thus no signal is received at the expected arrival time. The crack depth affects the duration of the shadow region, with the depth t_F related to the length of the region x by

$$t_F = \frac{x}{2 \tan \theta_s} \tag{7.2}$$

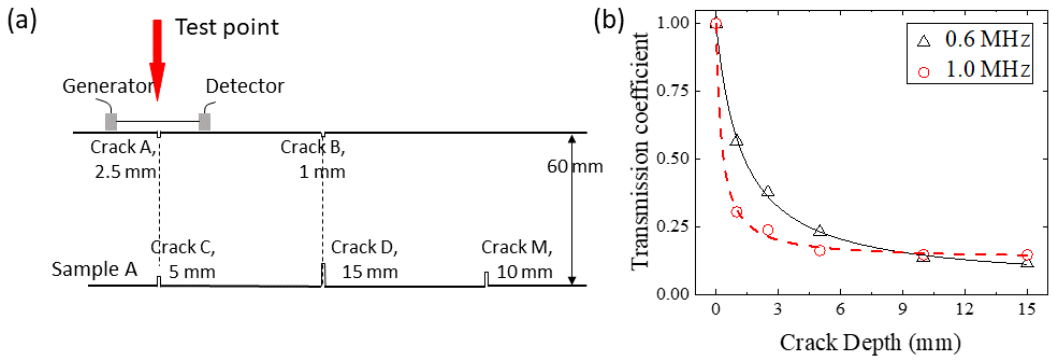

Figure 7.9: Depth gauging using Rayleigh wave mode. (a) The geometry of the testpiece (sample A). (b) Normalised peak-peak of the transmitted Rayleigh wave for different crack depths.

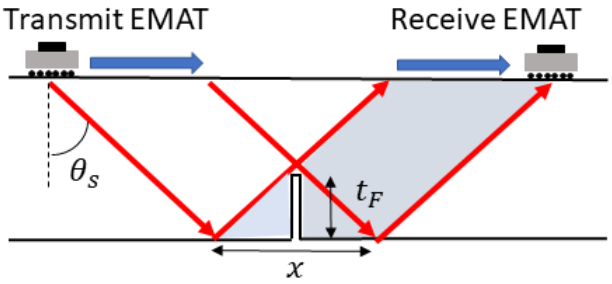

Figure 7.10: Blocked region of the shear wave when the EMAT pair is scanned on the opposite side of the sample to the surface crack.

for a crack propagating normal to the sample surface and a sharp beam profile, where $\theta_s = 40.3°$ is the chosen incident angle of the shear wave in the EMAT system used.

The transducer calibration was undertaken using two steps: 1. investigate the frequency behaviour when the blocking was used to detect a crack. This is to compensate for the effect of the minor frequency dependence shown in figure 7.7(c); 2. find the threshold for crack depth gauging, given the finite beam width of the EMAT. Criteria 1 was fulfilled by applying a three-cycle signal at a range of frequencies (from 0.4 to 2.0 MHz with a 0.2 MHz step) for inspection of a 15.0 mm deep crack. The EMAT system was moved along the bar surface, from the far left end to the right end, with 160 mm total scan length and a fixed EMAT separation. The spatial interval of the scanning was 5.0 mm and the detected shear wave was recorded at each position. The peak to peak amplitude of the received signal was found and normalised to the average value where no defect was present. Criteria 2 was investigated by scanning two cracks, with depths of 4.0 mm (shallow) and

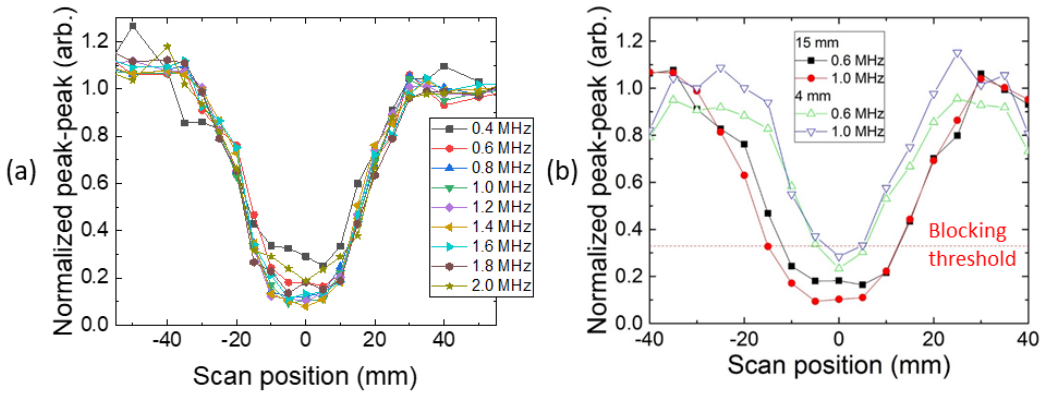

Figure 7.11: Calibration of the EMAT shear wave mode for far side surface scan. (a) Frequency characteristics. (b) Shear bulk wave for defects of depths $d = 15$ mm and $d = 4$ mm for two frequencies. The $x-$axis corresponds to position relative to the crack centre.

15.0 mm (deep). Two frequencies, 0.6 MHz and 1.0 MHz, were used on both cracks for clarity. Figure 7.11 shows the results.

It can be seen that the edge of the wave blocked region is not sharp. This is due to the width of the beam; the EMAT coils contain multiple wires and have a finite width, with generation and detection stronger towards the centre. The geometric spread of the beam within the sample bulk needs also to be considered. Therefore some width to both the generated and detected ultrasound beam is expected, which provides the sloping edges to the graphs shown in figure 7.11 rather than a sharp cut-off of the signal. The width of the blocking shows generally the same profile for different applied frequencies, as expected and shown in figure 7.11(a), meaning that the frequency dependence of the shear directivity is suppressed by the constant, chosen transducer separation. Lower frequencies, such as 0.4 or 0.6 MHz show a shallower drop than those of the higher frequencies. This is because of the small SNR obtained for the lower frequencies, so the normalised noise level is higher and measured values are less accurate.

Based on figure 7.11(b), a suitable threshold was chosen to obtained defect depth; here a threshold of 0.33 returns $x = 25.4$ mm for the deeper defect corresponding to a depth of exactly 15 mm. As the threshold is primarily related to the beamwidth, the same value can be used for all defect depths, and will give a reliable measurement where the depth is of the order of the beamwidth and higher. Applying a threshold of 0.33 to the crack with depth 4.0 mm, gives an estimate of 5.17 mm for the crack depth, with some errors due to the limited resolution of the scan.

7.4.2 Inspection of sample near & far side surface cracks

The two techniques described above could be applied separately for analysis of the front and back faces of the sample. However, near-side defects will also affect propagation of the shear wave, hence the strength of the technique comes from combining results from both wavemodes in order to obtain more information than when using just a single mode, or each mode individually, allowing identification of defect position relative to the EMATs.

To demonstrate this, two samples with machined defects on both sides were used. First, sample A was scanned; cracks A and B on the near side surface were scanned using the Rayleigh wave and cracks C and D on the back wall were detected by the shear wave in a single scan, illustrated in figure 7.12(a). A three-cycle driving signal with a centre frequency of 0.6 or 1.0 MHz was chosen. The sample was manually scanned with a spatial interval of 10 mm in the moving direction. For the test demonstrated in figure 7.12(b), sample B was scanned to understand the EMAT pair performance for the situation of a more complex near side defect (crack E) when also investigating a simple vertical far side surface crack (crack F). The feasibility of using the dual-wave for a more accurate surface scan was investigated in this experiment via implementing the LabView controlled xy stage. A 1.0 MHz single cycle pulse was used to drive the generator, chosen to give good time resolution for the waves. The full geometry of cracks E and F is shown on the right in figure 7.12(b). Here crack E exhibited a 20° angle to the surface and a 15 mm length, and crack F exhibited a 15 mm vertical depth. Automated scanning was undertaken using the xy stage with a step size of 0.5 mm. This was to not only provide a more detailed result, but also simulate the practical use in an environment or when using a unmanned vehicle for scanning [48, 219].

Depth gauging for surface cracks on both faces

The EMAT system was scanned over the near side surface of sample A. The received ultrasound signal was recorded at each scan position and the peak to peak amplitude of both waves (Rayleigh and shear-to-shear) were recorded, normalised and plotted, shown in figure 7.13.

Two notches can be clearly seen from the behaviour of the Rayleigh wave (figure 7.13(a)) by the two regions of reduced amplitude, indicating two surface cracks (cracks A and B) growing on the near side surface. At a frequency of 0.6 MHz, the notch profile of crack B is shallower, indicating its smaller depth compared to that of crack A. Using the calibration curve for 0.6 MHz, given in figure 7.9, the

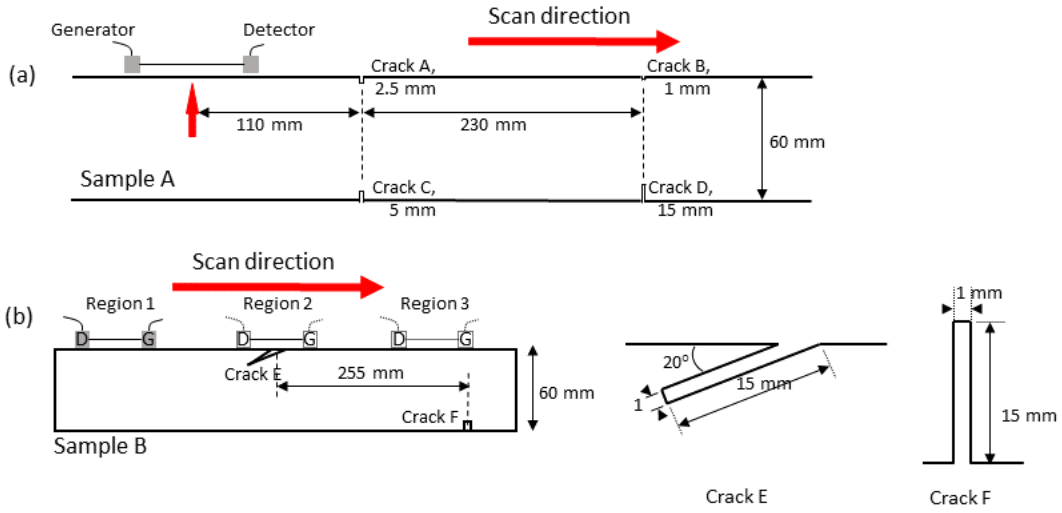

Figure 7.12: EMAT scanning path in dual-wave mode, and defect geometry. Two aluminium bar sample were prepared, for (a) manual test and (b) automated scanning respectively.

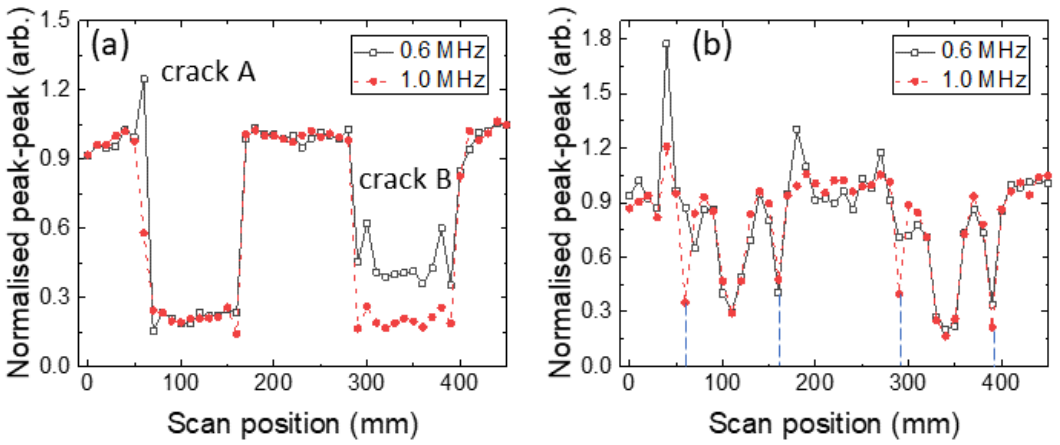

Figure 7.13: Measurement results on sample A. Implementing dual waves for inspecting both faces of an aluminium block. Normalised transmission of (a) Rayleigh wave and (b) shear wave.

depth of crack B can be estimated as 1.77±1 mm. Since the transmitted waves for crack A have a small amplitude, the wave energy at each wavelength was mostly blocked by crack A. Crack A is therefore measured to be deeper than crack B, as expected. For crack A, both 0.6 and 1.0 MHz show a signal amplitude that is very close to the noise level, hence only a rough estimation of crack A depth can be obtained with an estimate that it is of the order of or deeper than 3 mm. A lower frequency (larger wavelength) Rayleigh wave would need to be used for accurate depth gauging of crack A, with the frequency range chosen such that all depth defects greater than a chosen value will be clearly detected.

In figure 7.13(b) for results of the shear wave, a number of dips were observed. Comparing all these dips with the positions of the near-side defects obtained by the dips in the Rayleigh wave amplitude, four of the dips, which occur at 60, 160, 290 and 390 mm, are attributed to signal blocking due to the presence of the near side cracks. These dips in the shear wave amplitude are generally very narrow dips because the defects are relatively shallow. The four dips which are due to the near-side defects appear to be symmetric in pairs, indicating that the near-side surface defects are close to propagating normal to the surface. The dips located at 110 and 340 mm are wider and do not align with the start and end of the defects found using Rayleigh waves, and are therefore identified as the surface cracks on the far side surface. Applying a shear wave threshold of 0.33 gives depth estimations of 5.8±1 and 12.5±1 mm for cracks C and D respectively, in generally good agreement with the true depths of 5.0 and 15.0 mm shown in the sample schematic.

There are a few signal enhancements observed on the edges of the notches. This is mainly caused by the constructive interference between the incident wave and the reflected wave from the crack [5]. It is not always observed due to the large step size used.

Characterisation for complex near side cracks

In this section, sample B with an angled near side surface crack and a vertical far side surface crack, shown in figure 7.12(b), was scanned comprehensively to further study the performance of dual-wavemode scanning. The scan was performed automatically using the xy stage with a 0.25 mm spatial step using the calibrated EMAT pair (Rayleigh wave for looking at the near-side surface, and shear bulk wave for the far-side surface). The detected data is presented in two ways; B-scan imaging and peak to peak analysis. Details are given below.

Before studying the full B-scan result, ultrasound ray path analysis for the key wavemodes presented on B-scan is given. This is because a single Rayleigh wave

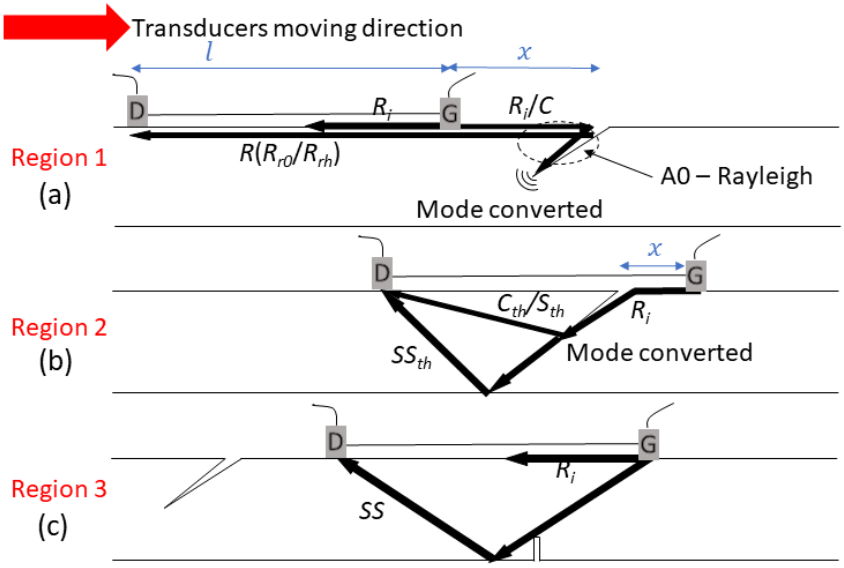

Figure 7.14: Ray path analysis of B-scan for scanning sample B using the EMAT transmit-receive pair.

encountering an angled crack can lead to multiple wave reflections/transmissions and mode conversions, as introduced in section 2.2.2. Identifying the key features in the B-scan is therefore necessary to ensure the results are properly analysed. Figure 7.14 shows the schematic diagram for several possible wavemodes travelling along the near-side surface when the EMAT pair is scanned along the surface. Three spatial regions, according to the relative position of crack and EMAT generator, are identified. In region 1, demonstrated in figure 7.14(a), both EMATs are on the same side of the near-side defect prior to interaction. In region 2 (figure 7.14(b)), the EMATs are on opposite sides of the near-side defect. The region 3 shown in figure 7.14(c) indicates when the EMATs have both passed over the near-side defect (this includes when they encounter the far-side defect). The wavemodes of interest are; the Rayleigh waves, the shear wave reflected from the back wall, and the bulk wave converted from the incident Rayleigh wave due to the presence of the crack. The above wavemodes are labelled as; Rayleigh (R), longitudinal (C) and shear (S), with several subscripts; r corresponds to a reflected wave, i to an incident wave, t to a transmitted wave and h to a mode converted wave. Explanation of each expected wavemode in each region is given below, which is mostly based on the previous studies presented in [80, 82, 85].

1. Region 1. Three significant waves are expected to be detected; the direct incident Rayleigh, R_i, the Rayleigh wave reflected by the crack, R_{r0} and the

reflected Rayleigh that is mode converted from the incident Longitudinal generated by the EMAT generator, R_{rh}. The time of flight for each wavemode is given by,

$$t_{R_i} = l/c_R, \tag{7.3}$$

$$t_{R_{r0}} = (l+2x)/c_R, \tag{7.4}$$

$$t_{R_{rh}} = x/c_L + (l+x)/c_R, \tag{7.5}$$

where l is the separation between the generator and detector and x indicates the separation between crack E and the generator, as marked on the figure.

2. Region 2. Three mode converted waves are expected, two shear wave arrivals and one longitudinal, as well as the transmitted Rayleigh wave. All of these waves were mode-converted at the angled crack bottom when the incident Rayleigh wave reached this point. One of the mode-converted shear waves, S_{th}, and the longitudinal wave, C_{th}, directly propagate to the detector, whereas the other mode-converted shear SS_{th} was detected after it has been reflected by the back wall. The time of flight of these waves are given by [82],

$$t_{C_{th}} = (x+d)/c_R + M/c_L, \tag{7.6}$$

$$t_{S_{th}} = (x+d)/c_R + M/c_T, \tag{7.7}$$

$$t_{SS_{th}} = (x+d)/c_R + (2t_{Al} - d\sin\theta_E)/\cos\alpha, \tag{7.8}$$

where $M = \sqrt{d^2 + (l-x)^2 - 2d(l-x)\cos\theta_E}$ and $\alpha = \arctan\dfrac{l - x - d\cos\theta_E}{2t_{Al} - d\sin\theta_E}$. $\theta_E = 20°$ is the angle of crack E, $t_{Al} = 60$ mm is the sample thickness. $d = 15$ mm here indicates the length of the near-side surface crack. The amplitude of the CC wave was too small to be measured.

3. Region 3. Since both generator and detector have passed over the near-side crack, only the generated shear bulk wave that was reflected from the back wall, SS is considered. The time of flight of this wave is straightforward,

$$t_{SS} = 2\sqrt{[(l/2)^2 + t_{Al}^2]}/c_T. \tag{7.9}$$

It can be seen from the above expressions that only the arrival times of R_i and SS are independent of the transducer location, x.

The full results of B-scan imaging are given in figure 7.15. The B-scan in this work is the 3D picture that consists of multiple A-scans obtained at multiple EMAT

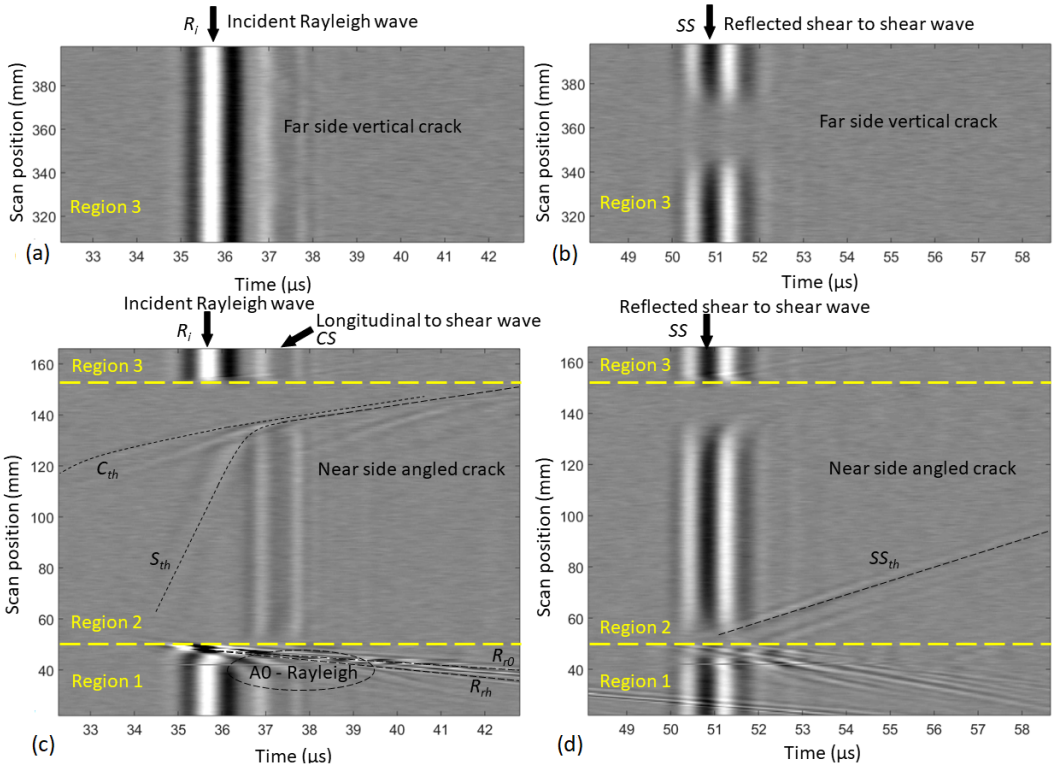

Figure 7.15: Measurement results on sample B. EMAT B-scans for the sample near- and far-side surfaces. (a) and (c) show the time period between 32.27 and 42.8 μs, containing the Rayleigh wave, while (b) and (d) show the time period between 48.12 and 58.65 μs, containing the shear wave. The scanning position of EMATs are increased from lower plots to higher plots. Different regions are indicated based on the ray path analysis (figure 7.14).

pair scanning locations. The x-axis of the B-scan maps to the time of flight from generator to detector, t, and the y-axis to the scanning position, x, and the colour scale corresponds to the signal amplitude at each chosen (t, x) [81]. The results are separated into four sections for better illustration; two time regions, from 32.3 μs to 42.7 μs to show in detail the arrival times of the Rayleigh wave ((a) and (c)) and from 48.1 μs to 58.7 μs to show that of the shear-to-shear ((b) and (d)) wave, and two spatial regions, from 22 to 164 mm, to show the interaction with the near-side defect ((a) and (b)), and from 312 to 412 mm to show that of the far-side defect ((c) and (d)).

Many wavemodes can be seen on the B-scan, shown by the light or dark lines. Waves which always have the same path length, i.e. signals passing directly from generator to detector, and with no x-dependence in the calculation above, are shown by vertical lines (independent of the relative position of transducer and crack).

Reflections and mode converted waves are indicated by angled lines. R_i and SS are clearly identified by the vertical lines appearing at $t = 35$ μs and $t = 50$ μs in all graphs in figure 7.15. In addition, a shear bulk wave, CS that was mode-converted from the incident longitudinal generated by the EMAT generator is also observed at $t = 36.5$ μs. CS is much weaker than R_i or SS, shown by its lighter colour. The effects of the near- and far-side surface cracks are identified by the signal blocking of R_i and SS shown in figures 7.15(c) and (b) when the EMATs were moved from 52 to 155 mm and from 347 to 370 mm, respectively. Other reflected and mode-converted modes that have been predicted in the ray path analysis (i.e. R_{r0}, R_{rh}, C_{th}, S_{th} and SS_{th}) are also given in the corresponding graphs by angled dashed lines, for example, the Rayleigh wave that was reflected by the angled crack, R_{r0} is indicated in figure 7.15(c). Its time-location trajectory is given by the black dashed line which was calculated from equation 7.4.

Some other features are worth noting. A dispersive feature (highlighted by the dashed circle in figure 7.15(c)) can be observed in region 1 when the generator was approaching the angled crack (crack E); these are due to the mode conversion between the Rayleigh and a Lamb-like mode within the wedge geometry created by the angled defect [220]. Similarly, some dispersive/non-dispersive features are also observed near the arrival times of SS shown in region 1 in figure 7.15(d). This could be due to multiple reflections/mode conversions among the bulk waves or bulk waves and surface wave when the EMAT was approaching crack E. The behaviour of waves at the far-side defect is very clear (figure 7.15(a) and (b)), shown by a blocking of the shear bulk wave without interruptions of any other wavemodes.

A more detailed study of the Rayleigh wave and shear-to-shear wave behaviours was undertaken by measuring the peak to peak amplitude of each wave (R_i, SS) at each position during the scan. The signal has been normalised to the average of the 'no defect' signal, with data shown in figure 7.16. Several features are of note;

1. The normalised signal where there are no defect indications behaves similarly for both shear and Rayleigh waves, and can be used to check whether changes in the measured amplitude are due to changes in EMAT lift-off or sample composition, which should affect both wave-modes similarly, rather than being due to defects.

2. The shear wave shows a feature at around 25 mm, which corresponds to interference with a reflected Rayleigh wave.

3. The Rayleigh wave shows a single dip.

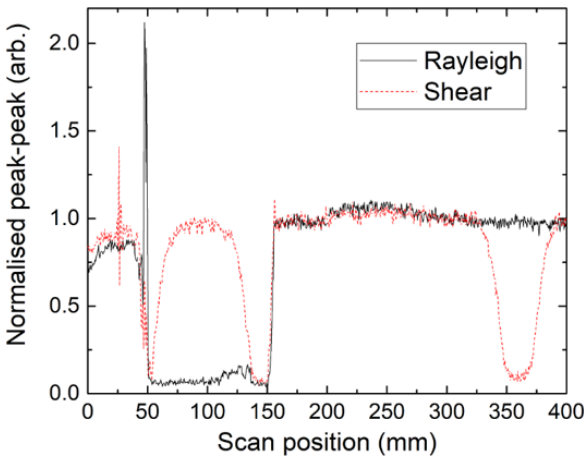

Figure 7.16: Normalised amplitudes of the Rayleigh R_i and shear SS waves at each point in the scan shown in figure 7.15.

4. Additionally, the shear wave shows three dips.

Crack characterisation is then performed from the above peak-peak analysis. First, considering the results from the Rayleigh wave (noting point 3 from above) with a single dip, clearly implying that a single surface-breaking defect is on the near-side surface. The transmitted signal is small, meaning that the defect is deep compared to the wavelength used for the inspection [92]. Additionally, a large signal enhancement occurring at around 50 mm is observed when the first transducer (EMAT generator) was passing over the defect, but not when the detector passed over. This can be used to deduce that the target crack is angled and that the crack orientation is facing the incident Rayleigh wave [85]. The measured signal enhancement factor, $F_{E_{IP}}$ for the Rayleigh wave (the normalised amplitude) in figure 7.16 is around 2.2, predicting a 21° incline angle of the crack according to the work presented by Rosli et al. [85]. The transmission coefficient in this measurement (less than 0.2), however, is too low and beyond the reliable region of the Rayleigh characterisation curve given in figure 7.9 and that given by [85]. An estimated crack depth of the order of or greater than 15 mm is obtained.

Using the results of a single shear-to-shear wave measurement (note 4) with three dips, without considering the Rayleigh wave results, can lead to an indication of three surface cracks on the far-side face. Applying a threshold of 0.33 (shear wave calibration given in section 7.4.1.2) to all the dips gives the predication of the crack depths as 5, 11 and 16.8 mm respectively for the dips at positions 50, 140 and 360 mm (the one with 16.8 mm is close to the actual depth of 15 mm).

The above prediction based on using a single wavemode only shows incom-

plete or incorrect information about the bar sample surfaces; the complex geometry of the near-side crack makes the Rayleigh depth measurement overestimated due to the small incline angle, and the spurious dip features in the shear-to-shear wave leads to the prediction of two cracks which are not present on the far side of the sample. By taking account of the results from the two wavemodes, the prediction can be modified to be more correct. The shear wave is first blocked at around 50 mm and 140 mm; it is clear from figure 7.16 that this is due to blocking of the signal by the near-side defect when the generator or detector passes over it, as the reduction in the signal occurs at the start and end points of the defect measured by the Rayleigh wave. The signal enhancement in the shear-to-shear wave near the first dip (note 2) also confirms this, as such a phenomenon can be only be formed when a Rayleigh wave was reflected by a near-side crack. In contrast, the dip in the shear wave amplitude at around 350 mm occurs where the Rayleigh wave shows no disruption, indicating that there is no near-surface defect. It is now clear that only one near-side surface crack and one far-side surface crack exist.

Further information can be obtained from the non-symmetric response of both waves at the start and end of the near-side defect. As discussed above, the measured Rayleigh wave enhancement feature implies an angled near-side surface crack. The asymmetry in the shear wave blocked region widths at 50 and 140 mm confirms this assumption. Figure 7.17 explains the origin of this asymmetry in the shear wave behaviour in the region of an angled surface-breaking defect on the near-side of the sample. For a surface crack propagating at an angle θ_E to the surface, with a vertical depth t_E, the length of the blocked region shown in figure 7.17(a) is given by

$$x_1 = t_E \left(\frac{1}{\tan \theta_E} - \tan \theta_s \right) \tag{7.10}$$

where the dimensions are shown in the graph. Similarly, in figure 7.17(b), the length of the blocked region is

$$x_2 = t_E \left(\frac{1}{\tan \theta_E} + \tan \theta_s \right) \tag{7.11}$$

In figure 7.16, the shear wave dips have $x_1 = 8.5$, and $x_2 = 18.5$, after applying the 0.33 threshold. As $\theta_s = 40.3°$, taking the ratio of x_1 to x_2 gives a measurement of $\tan \theta_E = 0.437$, corresponding to an angle of 23.6°. Substituting that into equation 7.10 and 7.11 gives a crack vertical depth (t_E) of 5.9 mm and a crack length (d) of 14.7 mm. These agree very well with the angle and length measured from the side of the sample, which are 20° and 15 mm respectively.

Table 7.1 summaries the crack characterisation results from using each wave-

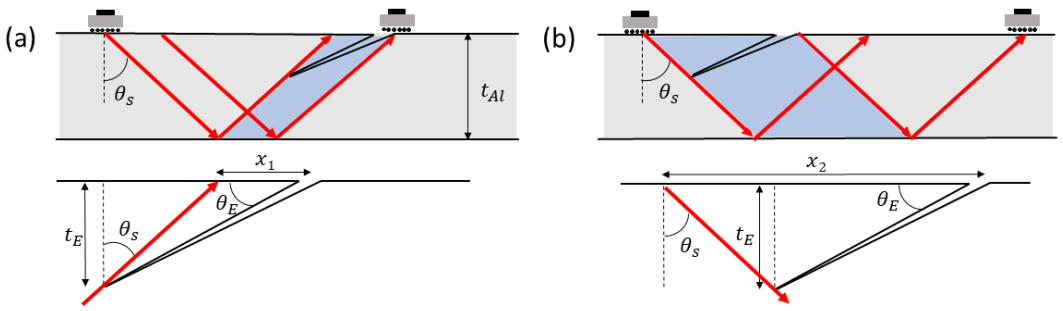

Figure 7.17: Origin of the asymmetry in the shear wave blocking for an angled surface-breaking defect.

Table 7.1: Summary of defect detection results of sample B using either a single wavemode or dual wavemodes. θ_E refers to the crack incline angle, t_E and d are crack vertical depth and length, respectively. The units of t_E and d are mm.

	near-side, crack E				far-side, crack F			
	θ_E	t_E	d	Qty.	θ_E	t_E	d	Qty.
R wave only	21°	>15	>15	1		\		\
SS wave only		\		\	90°	5	5	3
					90°	11	11	
					90°	16.8	16.8	
R, SS waves	23.6°	5.9	14.7	1	90°	16.8	16.8	1

mode (R_i or SS) or dual-wavemodes on sample B from the peak to peak analysis. Both cracks E and F are considered as unknown cracks to be detected. It shows that dual-wavemodes scans offer many benefits, not just for widening the scanning ability from probing a single surface to analysing both surfaces of a bar sample, but also because it offers more accurate information for the crack geometry in the near side. The overestimated crack E depth obtained by the single Rayleigh wave (more than 15 mm) is corrected by the dual waves when there is a near-side defect affecting the shear wave and causing the asymmetric dip feature. The number of far-side cracks estimated by a single shear-to-shear wave analysis is three, and is corrected to only one when comparing both Rayleigh and shear wave behaviours.

It can be seen that the situation for just far-side surface cracks is rather simple without any interaction with the Rayleigh signal in the near-side (see the calibration process of shear-to-shear in section 7). However, it can be complicated when cracks are growing on both sides. Performing analysis on both Rayleigh and shear-to-shear provides an efficient way of improving the accuracy of the sample surface scanning.

7.5 Summary

This chapter has presented an EMAT based method to simultaneously monitor both faces of a bar sample. By taking advantage of multi-mode generation from a single EMAT, a metallic sample with limited access to the back face can be inspected thoroughly from a fast near-side B-scan by using both Rayleigh and shear wavemodes.

The directivity patterns of the shear wave generated by the generation EMATs for linear and straight racetrack designs have been investigated. There is a good agreement between experimental and modelling results. The radiated wavefront for the linear coil is dominated by plane waves, showing less directivity of the desired shear wave. The racetrack coil, which provides asymmetry of the source Lorentz force, confirms steering of the beam primarily over a region of around 30° to 40°, enabling a suitable EMAT separation to be chosen. It should be noted that the above directivity exhibits bi-directional performance, i.e. waves are travelling in both the positive xz-plane ($x > 0$) and negative xz-plane ($x < 0$). The analysis given in this chapter only considers a single direction, but both could be used if two detectors were present.

The scans show a pronounced sensitivity for detecting surface defects using the Rayleigh wave, with the shear wave also being affected when the generation or detection EMAT is directly over the defect. For far-side defects, locating a flaw is straightforward, but the conclusion can sometimes be misguided by disturbances due to the presence of a near-side crack.

The combination of inspection using a Rayleigh wave and a shear wave gives several advantages. Firstly, it gives a higher accuracy to identification of the location of defects, enabling confirmation of whether defects are present on the near-side or far-side of the sample. Additionally, any asymmetry in the shear wave blocking can be used to identify the angle of propagation of the near-side defect, as well as its depth, and this can be used in combination with the Rayleigh waves for high accuracy characterisation of near-side defects when only a single side of the sample is accessible.

It should be noted that with this technique there exists a shadow zone for the shear wave when there is a surface crack, as indicated in figure 7.17, where a far-side defect may not be detected, or may be mis-sized. This can be overcome by taking advantage of the fact that the shear wave directivity is not a tight beam, but that different propagation angles could be chosen if signal to noise ratio was sufficient. Using two or more detectors at different positions (giving different angles of propagation of shear wave) would overcome this issue, by giving different shadow

zones. Full analysis would use the position with the highest signal to noise ratio for the shear wave, while the other position(s) could be used as a check against missing features.

The inspections thus far have used calibration defects and samples with smooth faces. For real-life applications, the next steps must consider the scattering effect of a rough far-side surface, and more realistic defects, including branched or angled defects on the far-side.

Chapter 8

Conclusions

8.1 Conclusions

This work mainly focused on developing an enhanced EMAT ability for characterising surface-breaking defects on metal samples. Surface cracks such as rolling contact fatigue (RCF) on railway tracks or stress corrosion cracking (SCC) (see section 1.1) need to be identified in their early stages before hazardous failures occur. EMATs have been proven to be a promising technique to tackle the surface crack challenge, with ability to work on a large scale or under high temperature conditions [46, 49], due to their natural advantages of being couplant-free and offering great flexibility in generating multiple ultrasonic wavemodes (including surface guided waves) [11, 122]. The main contribution of this work can be summarised into two aspects. The first is the design and understanding of a tunable surface wave phased EMAT array system (chapters 5 and 6). Enhanced surface crack characterisation performance was obtained, giving a larger detection size range with a good sizing accuracy by using multiple frequencies. The second is the surface and bulk wave combined pitch-catch EMAT system for faster inspection for defects on both the front and opposite faces of a billet sample (chapter 7).

Chapter 4 detailed the methodologies used in this work, including the EMAT production method, the multi-channel EMAT driver and the method of finite element modelling to study the EMAT performance for the experimental chapters (chapters 5 to 7). The multi-channel driver is an in-house built four-channel high current phased EMAT driver, which provides the core part of the electronics that makes the experimental development in chapters 5 and 6 possible. The block diagram of the pulser has been introduced. Special care was given to the pulser frequency characteristics study, showing a tread of decreasing output amplitude

with the increase of input frequency due to the complexity of internal network. This study is necessary as the multi-frequency operation was the central principle in chapter 6.

Chapter 5 was concerned with the analytical formation of the linear array EMAT for this work. Linear coils with a finite width (of the order of millimeters) were chosen as the ultrasonic element to generate the surface (Rayleigh) wave via the Lorentz force mechanism. The electromagnetic field distribution radiated by a single coil element was derived and studied in detail, including understanding the distortion effect caused by the coil lift-off variation (of the order of sub-millimetres). It was shown that the desired eddy-current field will decay and the spatial extent of the generated currents will be broadened with the increasing lift-off. The subsequent ultrasonic behaviour includes a significant signal reduction and a frequency shift. This explains the frequency shift with lift-off determined experimentally [155].

An analytical formation of the coil array was then given. A one-dimensional linear array was proposed, consisting of multiple identical linear coils. The spatial behaviour of the array model was studied to give precise prediction of the narrow-band Rayleigh generation when an array with arbitrary coil width (a), coil spacing (d) and number of coils (N) is applied. The theoretical analysis shows clearly that the frequency at which the fast Fourier Transform (FFT) of the Rayleigh wave shows a maximum, f_p^T, is closely related to the applied coil spacing, via $f_p^T \approx c_R/2d$, where c_R is the Rayleigh speed, when the coil width is much smaller than the wavelength. The frequency can be increased by decreasing the coil spacing, but will encounter a bottleneck when the desired wavelength becomes comparable to the coil width. Increasing the number of applied coils gives a frequency closer to that designed, but one can never reach an infinitely high frequency (see figure 5.14).

The lift-off behaviour of the coil array was studied through a two-coil model. The eddy-current cross-talk from the neighbouring coils was demonstrated analytically and was validated experimentally. It was found that when two coils are placed nearby to each other with their currents out-of-phase (meander-coil), the ultrasound frequency will shift as lift-off is increased, similar to that of a single coil. When two coils have currents which are in-phase (normal array configurations), the narrowband feature of the array can vanish with increasing lift-off. This is understandable, as the multi-coil profile can merge into behaving like a wider single coil with increasing lift-off (see figure 5.17(b)).

Chapter 6 implemented the phasing concept onto the linear array described above. The ultrasonic constructive interference phenomenon is the central idea to form the phasing modality. For surface waves, there are three interesting phasing

phenomena and benefits that can be expected; the generated surface wave signal can be enhanced to give a larger signal amplitude (1), there is the ability to generate multiple wavelengths electronically (2). There is also potential for controlling the bidirectional generation which is obtained from a single linear coil. This is promising for improving the detection efficiency when multiple wavemodes and reflections are present and is suggested as one area of future work (3).

The rest of chapter 6 focused on developing a four-coil phased EMAT system with enhanced Rayleigh generation performance, giving benefits 1 and 2. The four-coil prototype had $a = 1.5$ mm and $d = 6.0$ mm, providing a much better signal-to-noise ratio (SNR) compared to a single coil (see figures 6.9 and 6.10), equivalent performance to standard meander-coil EMATs (see figure 6.11) and multiple wavelength generation from 3 to 11.67 mm by using phasing (see table 6.2). The ability of surface crack characterisation was validated on an aluminium sample, and the results (figures 6.14 and 6.15) show that the above four-coil system was sensitive to cracks that were deeper than 1 mm. Better sensitivity to small defects could be obtained by using thinner coils and higher frequencies.

The lift-off performance comparison between the normal array (without phasing) and the phased array of EMATs was given. This showed that the frequency shift phenomenon with lift-off cannot be avoided by using phasing, but the signal amplitude decrease was reduced for very high frequencies, when coils in normal arrays were required to be physically close to each other. This is attributable to the dipole effect contributed from a close neighbouring coil (2 mm in this work), but can be minimised by using the phasing technique with a large physical spacing between the coils (8 mm in this work).

Chapter 7 detailed the design of the multi-mode pitch-catch EMAT system for improved high speed surface inspection. A pair of racetrack coils was used as the transmitter and the receiver. There were four generated/mode-converted wavemodes available, and the Rayleigh wave and bulk shear wave were chosen for defect analysis. The Rayleigh wave was used to inspect the near-side surface. The shear wave generated by a racetrack coil showed good directivity characteristics (main energy directed at between 30° to 40° to the sample surface) and was used to inspect surface cracks on the far-side (opposite) surface.

Experimental validation was undertaken. The combination of measurements using both of these waves provided several advantages; firstly, simultaneous double-side surface inspection was shown to be possible. Secondly, self-contained crack location correction was possible. For example, spurious crack signals can be obtained when using a shear wave, but the true position can be identified by using

the Rayleigh surface wave. The accuracy of sizing the near-side surface crack can also be improved by using two waves instead of a single Rayleigh wave and this also enables accurate characterisation of the angle of propagation of only near-side defects. This does require parallel sample faces (see summary in table 7.1).

8.2 Suggestion for future work

The main focus of this work was to develop advanced EMAT techniques to characterise surface breaking defects. The Rayleigh surface wave was chosen as the major tool to inspect the metal surface. Ultrasound is recognised as a versatile tool, where different wavemodes can be generated in various industrial structures, such as shear-horizontal (SH) guided waves and Lamb waves in plate structures, longitudinal and torsional waves in cylindrical structures (pipelines, tubes, etc.) [3]. Despite the natural complexity of ultrasound guided waves, there are more attempts nowadays to use these waves to inspect complex geometries in industry (see introduction in chapter 1). The critical requirement is a deep understanding of wave propagation in different media, in order to solve practical problems. The techniques developed and described in this thesis could bring multiple advantages to guided wave inspection.

Mode selectivity of ultrasonic guided waves

For EMAT phasing applications, the first suggested direction is to extend the Rayleigh wave method (see section 6.3) onto using plate guided waves. The ability of Rayleigh wavelength selection using the phased EMAT array proposed in chapter 6 is transferable to other wavemodes. A similar array pattern (comb or meander-line shaped) has been used for mode tuning of Lamb waves [182], but using different transducer types [35, 221, 222], including laser ultrasound or piezoelectric transducers. One of the benefits of enhanced mode control of Lamb waves is the potential to reduce the complexity of post data interpretation [36]. Since Lamb waves are dispersive, careful choice of delays can give a chosen enhanced mode.

Control of surface wave bi-directivity

The second suggested direction is the extended use of wave directivity control using phasing. The surface wave emission from an EMAT transmitter is typically bi-directional, but is tunable such that it is uni-directional with the combination of phasing. Section 6.3.1 presents two possible approaches of uni-directional signal enhancement, but the coil bi-directional behaviour, i.e. both waves emitted in the $+x$-direction and $-x$-direction, is not fully studied yet (see introduction in section 6.3.2).

The phasing technique allows one to change the array layout electronically, and this will have different effects on waves propagating in different directions. One feasible strategy is to present an EMAT phasing design that can send surface waves in a chosen direction with a cancelled direction. This idea has been proven useful to improve the longitudinal wave detection accuracy in the pipeline industry [223]. The received signals from bi-directional generation were over-complicated, so the cracks/corrosion were hard to localise. Uni-directional control reduced significantly the crack misidentification, because the inspection direction was pre-determined. The idea can be extended to Rayleigh waves for rail inspection [50], SH guided wave for plate inspection [34] or flexural waves for pipe inspection [32], using the proposed phased EMAT system.

To generalise the bi-directivity problem, the conceptual study in section 6.3.1 for coil uni-directional enhancement is extended here. A schematic is given in figure 8.1(a), where four coils are well spaced in the horizontal (x), and the vertical layers are used to understand the effective position of each coil after delays have been applied. Note, all coils are located above the sample surface with the same lift-off. The coil (horizontal) physical separation is d. A dashed line is drawn through the positions of four coils to separate the waves propagating in the positive x-direction (right hand side) and negative x-direction (left hand side). When coils are driven with zero time delay (no phasing, $\Delta\tau = 0$, where $\Delta\tau$ is the time delay unit), the relative positions of the waves in both directions are fixed, and the coil separation is defined by d for both directions of propagation.

However, the coil effective separation (d_{eff}, see section 6.3.1) will be changed when phasing is applied ($\Delta\tau \neq 0$), and so will the generated ultrasound. $d^{\pm}_{eff}$ are used to describe the coil effective separation when the array output is measured from the positive x- and negative x-directions, respectively. The relationships $d^{-}_{eff} = d - \Delta\tau \times c_R$, $d^{+}_{eff} = d + \Delta\tau \times c_R$ and $d^{-}_{eff} + d^{+}_{eff} = 2d$ explain the behaviour (see equations 6.3 and 6.4). A time period $\Delta\tau^{'} = d/c_R$, where c_R is the Rayleigh speed can be defined. Figure 8.1(b) demonstrates the array scenario when phasing is varied within the first period, $\Delta\tau \leq \Delta\tau^{'}$. The black dashed line is given to indicate the coil physical positions, whereas red dashed lines and green dashed lines are used to indicated the coil effective positions during the changing of phasing ($0 < \Delta\tau \leq \Delta\tau^{'}$) and the limits when $\Delta\tau = d/c_R$, respectively. It is clear that, with the increasing of $\Delta\tau$, the coil array is 'expanded' in the positive direction (d^{+}_{eff} is increased), and is 'tightened' in the negative direction (d^{-}_{eff} is decreased), as expected in chapter 6. The red lines will hit the limits (green lines) at $\Delta\tau = d/c_R$, giving the special case where $d^{-}_{eff} = 0$ and $d^{+}_{eff} = 2d$.

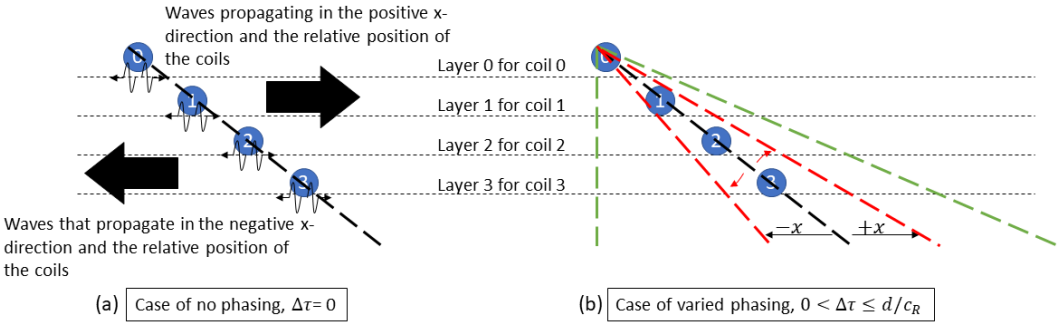

Figure 8.1: Bi-directivity study of EMAT coil generating Rayleigh surface wave. EMAT array with four-coils is used. Coil wave emission is given on different vertical layers to distinguish the horizontal bi-directional behaviour. Black line indicates the coil physical positions. (a) Coil normal generation without phasing. (b) Coil effective generation with changing phasing. Red lines indicate the coil effective locations in both directions as $\Delta\tau$ is varied , where $\Delta\tau$ is the time delay factor. Green lines are the special case when $\Delta\tau = d/c_R$, where d is the coil physical horizontal separation and c_R is the Rayleigh speed.

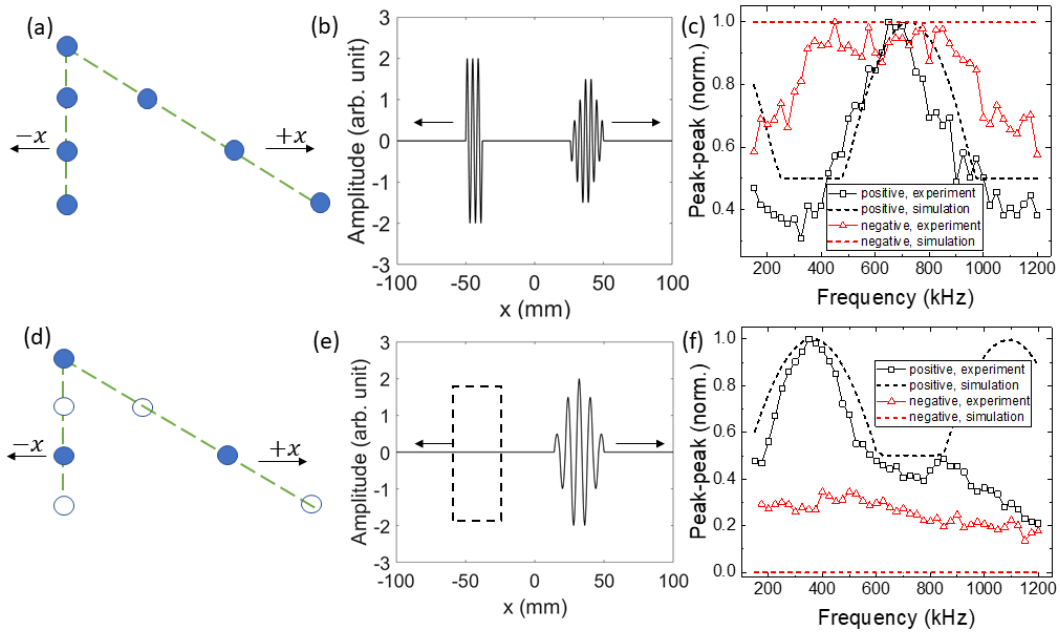

Figure 8.2: Coil array Rayleigh wave bi-directivity study when $\Delta\tau = d/c_R$. Two array configurations are studied; (a) all coil currents in the same current direction. (d) Neighbouring coil is in alternating current direction. (b) and (e) are the wave simulations in the x-domain for both configurations (four-coil), and (c) and (f) are the array (only two-coil here for preliminary study) frequency behaviour in both the negative and positive x-directions for two configurations.

A preliminary study of the special case has been undertaken using the phased EMAT system, and the results are given in figure 8.2. The coil layout was classified by the polarisation directions of the driving currents, i.e. if all coils are polarised in the same current direction (in-phase, figures 8.2(a)-(c)) or the neighbouring coil currents are in alternating directions (out-of-phase, figures 8.2(d)-(f)). The array generation was firstly modelled in the x-domain in MATLAB using Huygens principle[1]. The coil separation (d) was 2 mm, the Rayleigh speed (c_R) was 2906 m/s and the number of coils was 4. The coil was considered as a point source without the effect of finite width for simplicity. The driving pulse was three-cycle and was 726 kHz ($\lambda = 2d$) for the in-phase group, and 363 kHz ($\lambda = 4d$) for the out-of-phase group. The delay unit was $\Delta\tau = d/c_R = 0.69$ μs. The simulation results are given in figures 8.1(b) and (e), showing the emitted wave in the x-domain at 17.2 μs after the first coil has been fired. For in-phase configuration, the negative direction gave an improved SNR three-cycle signal as $d^{-}_{eff} = 0$ and all coils were in phase. The positive direction showed a partially enhanced toneburst signal, as expected (see figure 6.4). For the out-of-phase configuration, the negative direction was cancelled, as $d^{-}_{eff} = 0$ and the signals destructively interfered. The positive direction gave a well-shaped toneburst output.

Figures 8.2(c) and (f) show the calculated and experimental results of the array bandwidth study when $\Delta\tau = d/c_R$ for in-phase and out-of-phase configurations, respectively. Only two coils were used for this preliminary study. The driving frequency was not fixed at the designed value but varied from 150 to 1200 kHz with a 25 kHz step. The peak-to-peak value of the output signal was found and plotted as a function of driving frequency. Both experimental and modelling data is given and the result has been normalised for better comparison. Data in the positive x-direction is shown by a black dashed line (simulation) or square symbols and line (experiment), while that is the negative x-direction is shown in red. In figure 8.1(c), good agreements are obtained between the simulation and the experiment; the positive direction shows a peak frequency (frequency that gives maximum amplitude) at around 700 kHz. The minimum amplitude of the simulated positive direction is 0.5, which is the value of a single coil without phased operation under an ideal modelling. The sound behaviour in the negative direction shows some discrepancy between model and experiment; the signals are improved by a factor of 2 (1/0.5) in the simulation throughout the testing frequency range. This was not achieved in the experiment, where a bandwidth is shown, because of the finite bandwidth of the

[1] $\mathbf{P}(\mathbf{r}) = A\mathbf{r}^{-1}e^{i(k\mathbf{r}-\omega t)}$, where $\mathbf{P}$ indicates the wave field at a distance $\mathbf{r}$ from a point source. A is a complex number representing the size and phase of the source. k, ω and t indicate wavenumber, frequency and time, respectively [224].

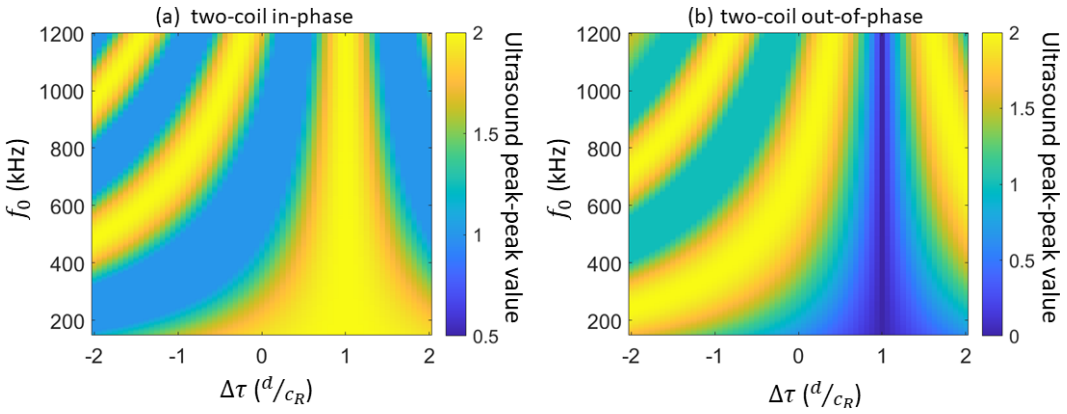

Figure 8.3: Simulation of the array bi-directivity behaviour for different time delays. Two coils were used. d = 2 mm and c_R=2906 m/s. Simulation was performed through Huygens principle without considering the coil finite width. The driving signal was three-cycle. For a pixel located at coordinate ($\Delta\tau$, f_0), its value is the peak-peak amplitude of the output signal. Two coils are in (a) in-phase or (b) out-of-phase configurations.

ultrasonic detector (racetrack coil, see figure 6.1).

In figure 8.1(f) for the out-of-phase configuration and the positive x-direction, a peak frequency occurring at 360 kHz is obtained in both the simulation and the experiment, as expected, but a harmonic at around 1100 kHz is also shown in the simulation. Multiple factors can contribute to this phenomenon. More details are given in section 6.4.2. For the negative direction, the simulation shows a consistent zero throughout the testing frequency range, while the experiment shows a noise level with an amplitude of around 0.2 to 0.3.

The above study considers the special case of $d_{eff}^{-} = 0$, $d_{eff}^{+} = 2d$ when $\Delta\tau = d/c_R$. To fully verify the bi-directivity behaviour, $\Delta\tau$ needs to be discussed in more detail. Simulation of the array bandwidth prediction when $\Delta\tau$ is varied within two time periods ($\pm 2d/c_R$) is shown in figure 8.3, with negative values equivalent to switching x-direction. Interference fringes can be observed in both the in-phase (figure 8.3(a)) and the out-of-phase (figure 8.3(b)) configurations. This is understandable since $d_{eff}^{\pm}$ holds a linear relationship with $\Delta\tau$ which can provide constructive interference when it is equal to a certain amount of wavelengths (see equations 6.3 and 6.4). The bright band has finite width, and this is due to the limited number of coils applied (here only 2). To improve the system performance, more coils need to be used, such as 4 as the next step for both the simulated and experimental studies.

Extending this to use to other surface waves is also necessary. Rayleigh

waves, which are non-dispersive, can be used as the simplest form of guided wave travelling in the material surface. Many other industrial structures, however, can possess complicated wavemodes, such as Lamb waves or SH waves in plate structures, flexural waves in pipelines etc. (see chapter 1). Controlling such waves can be more difficult, for example, careful choice of frequency and digital filtering is needed to compensate the dispersion of lamb waves [225]. The array EMAT needs to be carefully designed beforehand, so only a single mode will be sent by a coil. The special case of $d_{eff}^{-} = 0$ is useful to further reduce the mode complexity, as has been explained before.

Rayleigh wave imaging in pseudo-pulse-echo EMAT configuration

Apart from the extensive phasing applications when using different wavemodes for different structures, one can make better use of the EMAT's potential for fast speed detection. A vision for future NDE [19] emphasises the role of integration of robots/manipulators and long-life reliable sensors adapted to the Fourth Industrial Revolution (4IR), where EMATs can be a good candidate for data sending/capturing under an intelligent inspection framework. Chapters 5 to 7 focused on crack detection in one-dimension (transducers moving only in the x-direction), another direction to be suggested is to expand the one-dimensional detection to two-dimensional detection by the use of 2-D dynamic beam forming. Previous work showed that EMAT systems can provide 2-D crack information of a sample surface when used in association with an automated device, for example, focused Rayleigh wave EMATs to scan sum-mm surface cracks with a xy stage [9] or a miniaturised SH guide wave EMAT to screen the wall thickness with a robot [219]. These EMAT systems, however, can only send ultrasound in one-dimension, and the imaging ability was achieved by a point-to-point scan through the mechanical moving of the external devices. Improvement of the EMAT ultrasound beam performance is therefore of interest, since a 2-D beam EMAT can provide richer information than a conventional 1-D EMAT under the same mechanical scan. A further improved inspection efficiency can be expected.

A preliminary study of a 2-D EMAT design used Rayleigh waves for sample surface inspection. This can continue the EMAT advantage of simpler generation of Rayleigh waves than with conventional pieozoelectric transducers (see section 2.3.1) and also fill in the gap of 2-D Rayleigh wave beam forming using EMAT technique. A Rayleigh wave phased array (PA) EMAT is presented here, following the concept of a classical 1-D linear ultrasonic PA system (see section 1.4.3). The schematic of the EMAT array is demonstrated in figure 8.4(a), where four EMAT coils are shown. A

coil with a single layer of wire (0.08 mm diameter) was used as the ultrasonic element to generate a Rayleigh wave for a simplified preliminary study. An inset is given on the right top to demonstrate the EMAT working principle; the coil was polarised in the x-direction (I_0) with a z-direction polarised static magnetic field ($B_{0,z}$) to produce a Lorentz force in the y-direction ($F_s^{(L)}$). The generated Rayleigh wave would propagate primarily in the y-direction, and the beam width was primarily determined by the coil width (a).

The work of PA EMAT has been reviewed in sections 3.4.4. The major drawback that hinders the development is the low ultrasonic transduction efficiency of EMATs. Conventional piezoelectric PA system can use small elements and also contain tens to hundreds of individual channels. However, this is not suitable for EMAT PA systems due to the current limit of the material and electronics techniques. The proposed EMAT phasing system in this work can only support four channels, and the EMAT elements cannot be too small to guarantee the SNR. Even though, preliminary design of a four-element PA EMAT was worth doing to investigate the proposal feasibility. The work mainly contained the following stages; 1. material preparation. 2. Conceptual design of the PA system using the available materials. 3. Experimental design and verification. 4. Data acquisition and discussion.

In stage 1, it was noticed that the core instruments needed for system design were the EMAT driving and receiving electronics. The lab has the four-channel real-time phased driving, as introduced in chapter 4. Although a multi-channel pulse-echo system is under development, a separate four-channel receiver was available. The receiving was not as fast as real-time, and used an amplifier to amplify the signal before an oscilloscope was used to save the data. The maximum number of receiving channels was four. For the testing sample, both steel and aluminium were options. Aluminium was chosen here to simply the EMAT generation mechanism.

The conceptual design in stage 2 was the central basis of the preliminary work. This was not easy as the PA performance can significantly depend on multiple aspects, including the electronics, EMAT configuration, data processing method, etc. The critical problem was to identify the PA EMAT modality which was achievable using the current hard/software and but which was also constructively meaningful to connect the future work. Since the detection EMAT was separated from the generator, there was flexibility to study the array generation field in detail. The four-coil linear array shown in figure 8.4(a) was used as the EMAT generation array, and the numerical modelling was undertaken via Huygen's principle. The coil width in the y-direction (w) was ignored for simplicity, and the coil number (N) was fixed at 4. Other array parameters, including the coil width (a), the coil spac-

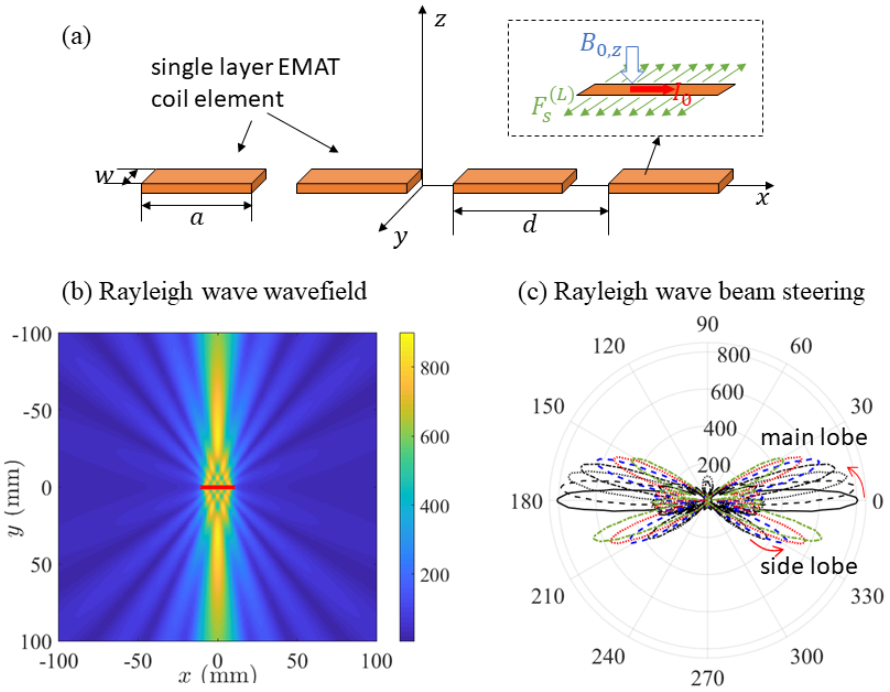

Figure 8.4: Four element linear array EMAT modelling. The array parameters are: element (coil) width (a) 4.8 mm, element spacing (d) 5 mm, frequency 700 kHz. (a) Schematic of the coil array generating Rayleigh wave in xy-plane. (b) EMAT wavefield modelling. The EMAT generation array is positioned at the place highlighted by the red line. (c) Beam steering study of the array presented in (b). Angles from 0 to 30° with a 5° step are chosen.

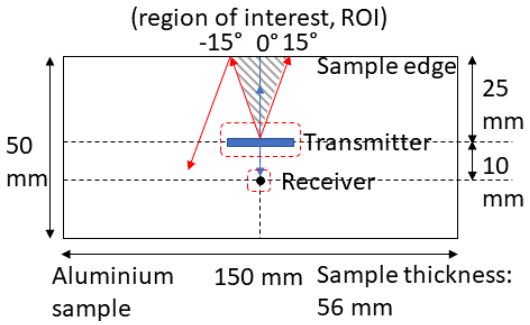

Figure 8.5: Preliminary set-up to evaluate the array beam-steering property. An omnidirectional spiral coil EMAT was chosen to receive the Rayleigh wave. Ray paths of the 0° and the -15° beams are given for clarity. Beams at higher angles were not expected to be received by the fixed single receiver.

ing (d), the Rayleigh wave frequency/wavelength (f/λ) were evaluated to optimise the array beam performance, either for beam steering or focusing. A normal beam (zero delay law) modelling is given in figure 8.4(b), showing the straight beams that were emitted bi-directionally from the coil array (red line) into the xy-plane. The array parameters were; $a = 4.8$ mm, $d = 5$ mm, $N = 4$ and $f = 700$ kHz ($\lambda = 4.15$ mm when $c_R = 2906$ m/s). Due to the limitation of the coil number and size, a beam-steering[2] array with a small steering region, -15° to 15°, was decided as the first model to be tested. Results of beam steering from 0° to 30° are given in figure 8.4(c). It is clear that, with the increasing of the steering angle, the side lobe dominates, and so the angle range over which the four coil prototype can be steered is very limited.

In stage 3, an initial experiment was designed to verify the above generation beam-steering model. The geometry of the system is demonstrated in figure 8.5. An aluminium sample with 150×50 mm^2 ($x \times y$) size was used. The sample thickness is 56 mm. The EMAT generation array was positioned close to the sample edge. A Rayleigh wave is a sensitive tool to inspect a surface discontinuity, and it will be partially reflected by the sample edge and then detected, using the sample edge as an ideal defect. A receiving coil (spiral, with a 3 mm diameter) was used to detect the reflected Rayleigh signal. The spiral shape allows one to capture the incoming waves from all directions. The generator was 25 mm away from the sample edge to avoid the EMAT dead zone, and the receiver was fixed behind the transmitter with a 10 mm distance. Ray paths of the straight beam (blue) and the steered beam (red) are shown. At higher steered angles, the aperture size of the receiver was too

[2] Time delay $\Delta\tau_j = jd\sin(\theta_{st})/c_R$ for jth coil, where θ_{st} is the steering angle. Phase delay is $\beta_j = \exp(i\omega\Delta\tau_j)$ to Huygen's principle, where ω is the angular frequency.

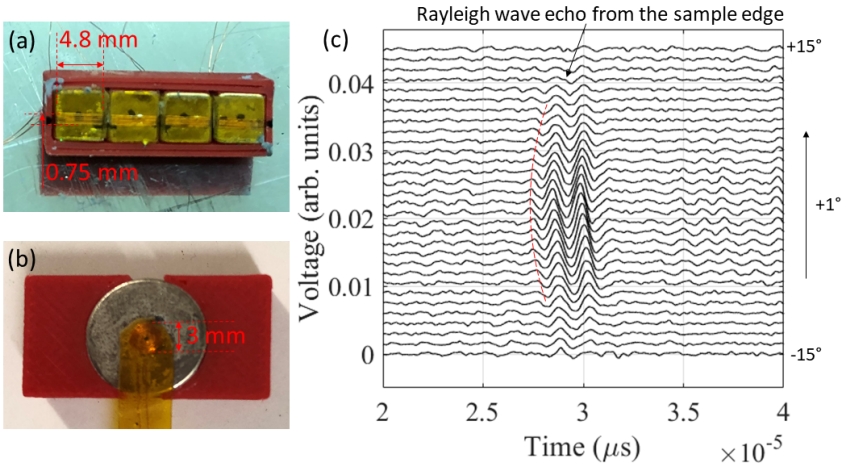

Figure 8.6: (a) Appearance of the EMAT array generator. Cubic magnets with a 4.7 mm length were used to produce the coil elements. (b) Appearance of the omnidirectional (spiral) receiver. The diameter of the receiving coil was 3 mm and the cubic magnet was 10 mm. (c) Beam steering testing results. The received A-scans are shown sequentially from -15° to 15°, with a 1° step.

small to capture the signal, thereby zero Rayleigh would be expected.

Experimental development of EMATs were then performed. The EMAT production was through the method described in section 4.1. The photo of the hand-made transmitter and receiver is shown in figures 8.6(a) and (b), respectively. The driving and receiving electronics were the same as those used in figure 6.1(a). The experiment was conducted based on the plan illustrated in figure 8.5. The driving signal was set to two-cycle to increase the time resolution. The array beam angle was varied from -15° to 15° with a 1° angular step. There were 31 A-scans in total captured by the fixed spiral receiver.

In stage 4, the data interpretation was performed. The testing results are given in figure 8.6(c). The Rayleigh reflection from the sample edge occurs at around 27 μs for small angles (-8° to 8°), as expected. Due to the beam steering, no Rayleigh signal at the corresponding time point was received by the fixed receiver, at angles higher than 10° (or -10°).

The above study confirms the feasibility of using a Rayleigh wave PA EMAT to perform a 2-D surface crack detection. However, the construction of the system is not yet completed, since only the generation field has been studied and verified. A classical ultrasonic PA system (like those used in medical applications) can contain a comprehensive system from ultrasonic generation, detection to data processing and imaging. The next step to improve the performance of the PA EMAT presented here

is therefore to design the detection array, and the novel post-processing algorithm, such as full matrix capture (FMC) and total focusing method (TFM) introduced in chapter 1. Since the four-channel receiving is achievable in the lab, the next step of designing the detection half of the PA EMAT is suggested as;

1. build four-coil detection array. The receiving coil can be spiral to capture signal omni-directionally, and the size can be slightly smaller ($\sim$ 2 mm diameter) than the previous one.

2. Implement different detection strategies to evaluate the performance of the whole system. These strategies could be 1. beam steering (generation) - delay and sum (detection) to produce a traditional sectorial B-scan. 2. FMC (generation - detection) to TFM to construct an image with a higher resolution.

3. Implement the above system for surface crack detection.

Steps 2 and 3 can also work with the synthetic aperture method (SAM) [224] to increase the aperture size of the receiver.

After the above procedures, the PA EMAT capability for 2-D surface crack imaging can be understood. It is expected that the resolution of the crack imaging will not be satisfactory nor will the effective region of interest (ROI), due to the limited channel number of the transmitter/receiver. To optimise the system, long-term systematic efforts need to be planned, including the application/development of new electronics techniques onto the EMAT PA array, so more elements/channels or larger aperture size can be applied. Also, a study on new materials, such as low impedance coils or high flux density magnets, can be very useful. This can solve the drawback of EMATs' low SNR, hence the electrical consumption can be reduced, making it possible to use smaller EMAT elements.

EMATs have their unique advantages, and are gaining more attention in this changing world. Trending on the intelligent revolution, EMATs and other NDT methods, such as eddy-current testing (ECT), can be used together to give higher probability of detection [226]; data fusion can be performed to increase the reliability of crack identification on steel and aluminium samples. A safer world can be expected.

Bibliography

[1] J. E. Garnham, F. J. Franklin, D. I. Fletcher, A. Kapoor, and C. L. Davis. Predicting the life of steel rails. Proceedings of the Institution of Mechanical Engineers, 221(1):45–58, 2007.

[2] H. Czichos. Handbook of Technical Diagnostics. Springer, Berlin, Heidelberg, 2013.

[3] J. L. Rose. Ultrasonic Guided Waves in Solid Media. Cambridge University Press, 2014.

[4] M. Sofer, P. Ferfecki, and P. Sofer. Numerical solution of Rayleigh-Lamb frequency equation for real, imaginary and complex wavenumbers. In MATEC Web of Conferences, volume 157, 2018.

[5] R. S. Edwards, X. Jian, Y. Fan, and S. Dixon. Signal enhancement of the in-plane and out-of-plane Rayleigh wave components. Applied Physics Letters, 87:194104, 2005.

[6] B. Q. Vu and V. K. Kinra. Diffraction of Rayleigh waves in a half-space. I. Normal edge crack. The Journal of the Acoustical Society of America, 77(4):1425–1430, 1985.

[7] S. Zhang, X. Li, and H. Jeong. Measurement of Rayleigh wave beams using angle beam wedge transducers as the transmitter and receiver with consideration of beam spreading. Sensors, 17:1449, 2017.

[8] H. Ogi, M. Hirao, and T. Ohtani. Line-focusing of ultrasonic SV wave by electromagnetic acoustic transducer. The Journal of the Acoustical Society of America, 103:2411, 1998.

[9] C. B. Thring, Y. Fan, and R. S. Edwards. Multi-coil focused EMAT for characterisation of surface-breaking defects of arbitrary orientation. NDT & E International, 88:1–7, 2017.

[10] J. Tkocz and S. Dixon. Electromagnetic acoustic transducer optimisation for surface wave applications. NDT & E International, 107:102142, 2019.

[11] M. Hirao and H. Ogi. Electromagnetic Acoustic Transducers: Noncontacting Ultrasonic Measurements using EMATs. Springer, 2017.

[12] M. F. Ashby, Y. Bréchet, and D. Cebon. Selection strategies for materials and processes. Advanced Engineering Materials, 4(6):327–334.

[13] H. A. Richard and M. Sander. Fatigue Crack Growth. Springer International Publishing, 2016.

[14] A. Kapoor, I. Salehi, and A. M. S. Asih. Rolling contact fatigue (RCF). In Encyclopedia of Tribology, pages 2904–2910. Springer US, 2013.

[15] C. Vargel. Stress corrosion cracking. In Corrosion of Aluminium, pages 209 – 235. Academic Press, 2020.

[16] L. Cartz. Nondestructive Testing. A S M International, 1995.

[17] R. Halmshaw. Non-destructive testing. London : Edward Arnold, 1991.

[18] R. Prakash. Non-Destructive Testing Techniques. New Academic Science, 2009.

[19] P. Thayer. Enabling the fourth industrial revolution (4IR) and the role of NDE and monitoring. Insight, 59:469–472, 2017.

[20] P. E. Mix. Visual and optical testing. In Introduction to Nondestructive Testing, pages 575–638. John Wiley & Sons, 2004.

[21] L. B. Pedersen, K.-Å. Magnusson, and Y. Zhengsheng. Eddy current testing of thin layers using co-planar coils. Research in Nondestructive Evaluation, 12(1):53–64, 2000.

[22] D. Mercier, J. Lesage, X. Decoopman, and D. Chicot. Eddy currents and hardness testing for evaluation of steel decarburizing. NDT & E International, 39(8):652–660, 2006.

[23] H. J. Pain. The physics of vibrations and waves. John Wiley & Sons, 1999.

[24] N.-B. Luciano, S. J. Alberto, P. J. Carlos, and R. J. Manuel. Development of an ultrasonic thickness measurement equipment prototype. In International Conference on Electronics Communications and Computers, pages 124–129, 2010.

[25] Olympus. Advanced ultrasonic with phased array imaging, 2021. https://www.olympus-ims.com/en/ut-flaw/epoch1000/, Last accessed on 19-07-2021.

[26] J. P. Charlesworth and J. A. G. Temple. Engineering Applications of Ultrasonic Time-of-Flight Diffraction. Research Studies Press, 2001.

[27] A. Erhard and U. Ewert. The TOFD method - between radiography and ultrasonic in weld testing, 1999. https://www.ndt.net/article/v04n09/erhard/erhard.htm, Last accessed on 19-07-2021.

[28] P. Petcher and S. Dixon. A modified hough transform for removal of direct and reflected surface waves from B-scans. NDT& E International, 44:139–144, 2011.

[29] R. Subbaratnam, S. T. Abraham, B. Venkatraman, and B. Raj. Immersion and TOFD (I-TOFD): A novel combination for examination of lower thicknesses. Journal of Nondestructive Evaluation, 30(137):45–58, 2011.

[30] Z. Su and L. Ye. Identification of Damage Using Lamb Waves. Springer, London, 2009.

[31] J. L. Rose. A baseline and vision of ultrasonic guided wave inspection potential. ASME. J. Pressure Vessel Technol, 124(3):273–282, 2002.

[32] M. J. S. Lowe, D. N. Alleyne, and P. Cawley. Defect detection in pipes using guided waves. Ultrasonics, 36(1):147–154, 1998.

[33] H. Al-Rizzo W. Alobaidi, E. Alkuam and E. Sandgren. Applications of ultrasonic techniques in oil and gas pipeline industries: A review. American Journal of Operations Research, 5:274–287, 2015.

[34] P. A. Petcher, S. E. Burrows, and S. Dixon. Shear horizontal (SH) ultrasound wave propagation around smooth corners. Ultrasonics, 54(4):997–1004, 2014.

[35] J. L. Rose, S. P. Pelts, and M. J. Quarry. A comb transducer model for guided wave NDE. Ultrasonics, 36:163–169, 1998.

[36] J. Li and J. L. Rose. Implementing guided wave mode control by use of a phased transducer array. IEEE transactions on ultrasonics, ferroelectrics, and frequency control.

[37] B. Munk, R. Taylor, T. Durharn, W. Croswell, B. Pigon, R. Boozer, S. Brown, M. Jones, J. Pryor, S. Ortiz, J. Rawnick, K. Krebs, M. Vanstrum, G. Gothard, and D. Wiebelt. A low-profile broadband phased array antenna. In IEEE Antennas and Propagation Society International Symposium, volume 2, pages 448–451, 2003.

[38] S. Harput and A. Bozkurt. Ultrasonic phased array device for acoustic imaging in air. IEEE Sensors Journal, 8(11):1755–1762, 2008.

[39] D. R. Daum and K. Hynynen. A 256-element ultrasonic phased array system for the treatment of large volumes of deep seated tissue. IEEE Transactions on Ultrasonics, Ferroelectrics, and Frequency Control, 46(5):1254–1268, 1999.

[40] Olympus. Introduction to Phased Array Ultrasonic Technology Applications. R&D Tech, 2004.

[41] M. Moles, N. Dube, and E. Ginzel. Pipeline girth weld inspections using ultrasonic phased arrays. In Proceedings of the ASME Pressure Vessel and Piping Conference., pages 19–27, 2003.

[42] B. W. Drinkwater and P. D. Wilcox. Ultrasonic arrays for non-destructive evaluation: A review. NDT & E International, 39(7):525–541, 2006.

[43] M. Gori, S. Giamboni, E. D'Alessio, S. Ghia, and F. Cernuschi. EMAT transducers and thickness characterization on aged boiler tubes. Ultrasonics, 34(2):339–342, 1996.

[44] M. Hirao and H. Ogi. An SH-wave EMAT technique for gas pipeline inspection. NDT & E International, 32:127–132, 1999.

[45] X. Huang, J. Saniie, S. Bakhtiari, and A. Heifetz. Ultrasonic communication system design using electromagnetic acoustic transducer. In IEEE International Ultrasonics Symposium Proceedings, 2018.

[46] F. Hernandez-Valle and S. Dixon. Pulsed electromagnet EMAT for ultrasonic measurement at elevated temperatures. Insight, 53:96–99, 2011.

[47] N. Lunn, S. Dixon, and M. D. G. Potter. High temperature EMAT design for scanning or fixed point operation on magnetite coated steel. NDT & E International, 89:74–80, 2017.

[48] F. Hernandez-Valle, A. R. Clough, and R. S. Edwards. Stress corrosion cracking detection using non-contact ultrasonic techniques. Corrosion Science, 78:335–342, 2014.

[49] I. Baillie, P. Griffith, X. Jian, and S. Dixon. Implementing an ultrasonic inspection system to find surface and internal defects in hot, moving steel using EMATs. AIP Conference Proceedings, 1096(1):1711–1718, 2009.

[50] R. S. Edwards, S. Dixon, and X. Jian. Characterisation of defects in the railhead using ultrasonic surface waves. NDT & E International, 39:468–475, 2006.

[51] P. L. Gould and Y. Feng. Introduction to Linear Elasticity. Springer, Cham, 2018.

[52] A. Maceri. Theory of Elasticity. Springer-Verlag Berlin Heidelberg, 2010.

[53] J. David N. Cheeke. Fundamentals and Applications of Ultrasonic Waves. Boca Raton: CRC Press, 2012.

[54] B. A. Auld. Acoustic fields and waves in solids. Malabar, Fla. : R.E. Krieger, 1990.

[55] S. Dixon, C. Edwards, and S. B. Palmer. Rayleigh wave dispersion on extruded aluminium. Insight, 40(9):632–634, 1998.

[56] J. D. Achenbach. Wave propagation in elastic solids. North-Holland, 1973.

[57] I. A. Viktorov. Rayleigh and Lamb Waves: Physical Theory and Applications. Springer US, 1967.

[58] G. W. C. Kaye and T. H. Laby. Tables of physical and chemical constants. Harlow:Longman, 1995.

[59] N. Ida and N. Meyendorf. Handbook of advanced nondestructive evaluation. Springer, Cham, 2019.

[60] R. L. Wegel and H. Walther. Internal dissipation in solids for small cyclic strains. Physics, 6(4):141–157, 1935.

[61] K. Lücke. Ultrasonic attenuation caused by thermoelastic heat flow. Journal of Applied Physics, 27(12):1433–1438, 1956.

[62] E. P. Papadakis. Scattering in polycrystalline media. In Ultrasonics, volume 19, pages 237 – 298. Academic Press, 1981.

[63] T. L. Szabo and J. Wu. A model for longitudinal and shear wave propagation in viscoelastic media. The Journal of the Acoustical Society of America, 107(5):2437–2446, 2000.

[64] L. Mordfin. Handbook of Reference Data for Nondestructive Testing. Astm Intl, 2001.

[65] P. N. T. Wells. Absorption and dispersion of ultrasound in biological tissue. Ultrasound in Medicine & Biology, 1(4):369 – 376, 1975.

[66] W. P. Mason and H. J. McSkimin. Attenuation and scattering of high frequency sound waves in metals and glasses. The Journal of the Acoustical Society of America, 19(3):464–473, 1947.

[67] W. P. Mason and H. J. McSkimin. Energy losses of sound waves in metals due to scattering and diffusion. Journal of Applied Physics, 19(10):940–946, 1948.

[68] L. M. Brekhovskikh and O. A. Godin. Acoustics of Layered Media I. Springer, Berlin, Heidelberg, 1990.

[69] J. Zhang, B. W. Drinkwater, and P. D. Wilcox. Defect characterization using an ultrasonic array to measure the scattering coefficient matrix. IEEE Transactions on Ultrasonics, Ferroelectrics, and Frequency Control, 55(10):2254–2265, 2008.

[70] L. Bai, A. Velichko, and B. W. Drinkwater. Ultrasonic characterization of crack-like defects using scattering matrix similarity metrics. IEEE Transactions on Ultrasonics, Ferroelectrics, and Frequency Control, 62(3):545–559, 2015.

[71] M. Hirao, K. Tojo, and H. Fukuoka. Small fatigue crack behavior in 7075-T651. Metall Mater Trans A, 24:1773 – 1783, 1993.

[72] D. A. Cook and Y. H. Berthelot. Detection of small surface-breaking fatigue cracks in steel using scattering of Rayleigh waves. NDT & E International, 34(7):483 – 492, 2001.

[73] B. Masserey and E. Mazza. Ultrasonic sizing of short surface cracks. Ultrasonics, 46(3):195 – 204, 2007.

[74] K. G. Hall. Crack depth measurement in rail steel by Rayleigh waves aided by photoelastic visualization. Non-Destructive Testing, 9(3):121 – 126, 1976.

[75] G. Hévin, O. Abraham, H. A. Pedersen, and M. Campillo. Characterization of surface cracks with Rayleigh waves: a numerical model. NDT & E International, 31(4):289 – 297, 1998.

[76] W. Song, J. S. Popovics, J. C. Aldrin, and S. P. Shah. Measurement of surface wave transmission coefficient across surface-breaking cracks and notches in concrete. The Journal of the Acoustical Society of America, 113(2):717–725, 2003.

[77] L. J. Bond. A computer model of the interaction of acoustic surface waves with discontinuities. Ultrasonics, 17(2):71 – 77, 1979.

[78] J. A. Cooper, R. A. Crosbie, R. J. Dewhurst, A. D. McKie, and S. B. Palmer. Surface acoustic wave interations with cracks and slots: A non-contacting study using lasers. IEEE Transducers on Ultrasonics, Ferroelectrics, and Frequency Control, 33:462–470, 1986.

[79] Q. Shan and R. J. Dewhurst. Surface-breaking fatigue crack detection using laser ultrasound. Applied Phyiscs Letter, 62:2649, 1993.

[80] X. Jian, S. Dixon, N. Guo, and R. Edwards. Rayleigh wave interaction with surface-breaking cracks. Journal of Applied Physics, 101:064906, 2007.

[81] X. Jian, S. Dixon, N. Guo, R. Edwards, and M. Potter. Pulsed Rayleigh wave scattered at a surface crack. Ultrasonics, 44:1131–1134, 2006.

[82] B. Dutton, A. R. Clough, M. H. Rosli, and R. S. Edwards. Non-contact ultrasonic detection of angled surface defects. NDT & E International, 44:353–360, 2011.

[83] J. L. Blackshire and S. Sathish. Near-field ultrasonic scattering from surface-breaking cracks. Applied Physics Letters, 80(18):3442–3444, 2002.

[84] B. Masserey and E. Mazza. Characterization of surface cracks using Rayleigh waves. AIP Conference Proceedings, 760(1):805–812, 2005.

[85] M. H. Rosli, R. S. Edwards, and Y. Fan. In-plane and out-of-plane measurements of Rayleigh waves using EMATs for characterising surface cracks. NDT & E International, 49:1–9, 2012.

[86] F. Hernandez-Valle, B. Dutton, and R. S. Edwards. Laser ultrasonic characterisation of branched surface-breaking defects. NDT & E International, 68:113–119, 2014.

[87] P. A. Doyle and C. M. Scala. Crack depth measurement by ultrasonics: a review. Ultrasonics, 16(4):164 – 170, 1978.

[88] J. D. Achenbach, A. K. Gautesen, and D. A. Mendelsohn. Ray analysis of surface-wave interaction with an edge crack. IEEE Transactions on Sonics and Ultrasonics, 27(3):124–129, 1980.

[89] M. Hirao, H. Fukuoka, and Y. Miura. Scattering of Rayleigh surface waves by edge cracks: Numerical simulation and experiment. The Journal of the Acoustical Society of America, 72(2):602–606, 1982.

[90] G. A. Georgious and L. J. Bond. Quantitative studies in ultrasonic wave-defect interaction. Ultrasonics, 25:328–334, 1987.

[91] R. Longo, S. Vanlanduit, J. Vanherzeele, and P. Guillaume. A method for crack sizing using Laser Doppler Vibrometer measurements of Surface Acoustic Waves. Ultrasonics, 50(1):76 – 80, 2010.

[92] R. S. Edwards, S. Dixon, and X. Jian. Depth gauging of defects using low frequency wideband Rayleigh waves. Ultrasonics, 44:93–98, 2006.

[93] Y. Poplavko and Y. Yakymenko. Piezoelectricity. In Functional Dielectrics for Electronics, pages 161 – 216. Woodhead Publishing, 2020.

[94] H. Kim, W. Kang, Ch. Hong, G. Lee, G. Choi, J. Ryu, and W. Jo. Piezoelectrics. In Advanced Ceramics for Energy Conversion and Storage, pages 157 – 206. Academic Press, 2020.

[95] M. G. Silk. Ultrasonic transducers for nondestructive testing. Adam Hilger, 1984.

[96] S. Rhee, T. A. Ritter, K. K. Shung, H. Wang, and W. Cao. Materials for acoustic matching in ultrasound transducers. In IEEE Ultrasonics Symposium Proceedings, volume 2, pages 1051–1055, 2001.

[97] T. Inoue, M. Ohta, and S. Takahashi. Design of ultrasonic transducers with multiple acoustic matching layers for medical application. IEEE Transactions on Ultrasonics, Ferroelectrics, and Frequency Control, 34(1):8–16, 1987.

[98] K. Ries, K. Hannoschock, and G. Simoneit. Ultrasonic immersion type testing, 1977. US4058000A.

[99] T. J. Batzinger and F. Alexander. System and method for ultrasonic immersion inspection for components, 2003. US6591680A.

[100] A. Castellano, P. Foti, A. Fraddosio, U. Galietti, S. Marzano, and M. D. Piccioni. Characterization of material damage by ultrasonic immersion test. Procedia Engineering, 109:395 – 402, 2015.

[101] S. Zhang, X. Li, H. Jeong, and H. Hu. Modeling linear Rayleigh wave sound fields generated by angle beam wedge transducers. AIP Advances, 7(1):015005, 2017.

[102] S. Shevtsov, V. Chebanenko, M. Shevtsova, E. Kirillova, and E. Rozhkov. On the directivity of acoustic waves generated by the angle beam wedge actuator in thin-walled structures. Actuators, 8:64, 2019.

[103] D. E. Chimenti. Review of air-coupled ultrasonic materials characterization. Ultrasonics, 54(7):1804 – 1816, 2014.

[104] M. S. Salim, M. F. Abd Malek, R. B. W. Heng, K. M. Juni, and N. Sabri. Capacitive micromachined ultrasonic transducers: Technology and application. Journal of Medical Ultrasound, 20(1):8 – 31, 2012.

[105] Y. Qiu, J. V. Gigliotti, M. Wallace, F. Griggio, C. E. M. Demore, S. Cochran, and S. Trolier-Mckinstry. Piezoelectric micromachined ultrasound transducer (PMUT) arrays for integrated sensing. Sensors, 15:8020–8041, 2015.

[106] M. Kobayashi, Y. Ono, C. Jen, and C. Cheng. High-temperature piezoelectric film ultrasonic transducers by a sol-gel spray technique and their application to process monitoring of polymer injection molding. IEEE Sensors Journal, 6(1):55–62, 2006.

[107] D. W. Schindel, D. A. Hutchins, L. Zou, and M. Sayer. The design and characterization of micromachined air-coupled capacitance transducers. IEEE Transactions on Ultrasonics, Ferroelectrics, and Frequency Control, 42(1):42–50, 1995.

[108] S. T. Hansen, B. J. Mossawir, A. S. Ergun, F. L. Degertekin, and B. T. Khuri-Yakub. Air-coupled nondestructive evaluation using micromachined ultrasonic transducers. In IEEE Ultrasonics Symposium Proceedings, volume 2, pages 1037–1040, 1999.

[109] F. Akasheh, T. Myers, J. D. Fraser, S. Bose, and A. Bandyopadhyay. Development of piezoelectric micromachined ultrasonic transducers. Sensors and Actuators A: Physical, 111(2):275 – 287, 2004.

[110] S. Trolier-McKinstry and S. Muralt. Thin film piezoelectrics for MEMS. Journal of Electroceramics, 12:7–17, 1995.

[111] A. S. Savoia, G. Caliano, and M. Pappalardo. A CMUT probe for medical ultrasonography: from microfabrication to system integration. IEEE Transactions on Ultrasonics, Ferroelectrics, and Frequency Control, 59(6):1127–1138, 2012.

[112] W. J. Denkmann, R. E Nickell, and D. C Stickler. Analysis of structural-acoustic interactions in metal-ceramic transducers. IEEE Transactions on Audio and Electroacoustics, 21(4):317–323, 1973.

[113] A. Feeney, L. Kang, W. E. Somerset, and S. Dixon. The influence of air pressure on the dynamics of flexural ultrasonic transducers. Sensors, 19:4710, 2019.

[114] A. Feeney, L. Kang, W. E. Somerset, and S. Dixon. Venting in the comparative study of flexural ultrasonic transducers to improve resilience at elevated environmental pressure levels. IEEE Sensors Journal, 20(11):5776–5784, 2020.

[115] S. Zhang, F. Li, and F. Yu. Piezoelectric materials for cryogenic and high-temperature applications. In Structural Health Monitoring (SHM) in Aerospace Structures, pages 59 – 93. Woodhead Publishing, 2016.

[116] B. R. Tittmann, C. F. Batista, Y. P. Trivedi, and C. J. Lissenden III. State-of-the-art and practical guide to ultrasonic transducers for harsh environments including temperatures above 2120°F (1000°C) and neutron flux above 1013 n/cm2. Sensors, 19:4755, 2019.

[117] D. A. Hutchins. Ultrasonic generation by pulsed lasers. In Physical Acoustics, volume 18, pages 21–123. Academic Press, 1988.

[118] J.-P. Monchalin. Optical detection of ultrasound. IEEE Transactions on Ultrasonics, Ferroelectrics and Frequency Control, 33:485–499, 1986.

[119] R. K. Ing and J.-P. Monchalin. Broadband optical detection of ultrasound by two-wave mixing in a photorefractive crystal. Applied Physics Letters, 59(25):3233–3235, 1991.

[120] M. B. Klein, G. D. Bacher, A. G-. Jepsen, D. Wright, and W.E Moerner. Homodyne detection of ultrasonic surface displacements using two-wave mixing in photorefractive polymers. Optics Communications, 162(1):79 – 84, 1999.

[121] C. Ho, J. Lee, H. Shih, J. Shaw, and Y. Liu. Two-wave mixing interferometer for ultrasonic NDT in defect detection. In Advances in Nondestructive Evaluation, volume 270, pages 359–363, 8 2004.

[122] R. B. Thompson. Physical principles of measurement with EMAT transducers. In Physical Acoustics, volume 19, pages 157–200. Academic Press, 1990.

[123] I. S. Grant and W.R.Phillips. Electromagnetism. John Wiley & Sons, 1991.

[124] J. K. Stanley. Electric and magnetic properties of metals. Metals Park, Ohio: American Society of Metals, 1963.

[125] K. W. Whites. Magnetostatics. In The Electrical Engineering Handbook, pages 479 – 497. Academic Press, 2005.

[126] R. B. Thompson. Mechanisms of electromagnetic generation and detection of ultrasonic Lamb waves in iron-nickel alloy polycrystals. Journal of Applied Physics, 48(12):4942–4950, 1977.

[127] R. R. Hughes. High-sensitivity Eddy-Current Testing Technology for Defect Detection in Aerospace Superalloys. PhD thesis, University of Warwick, 2015.

[128] D. Rueter. Induction coil as a non-contacting ultrasound transmitter and detector: Modeling of magnetic fields for improving the performance. Ultrasonics, 65:200 – 210, 2016.

[129] J. Tkocz, D. Greenshields, and S. Dixon. High power phased EMAT arrays for nondestructive testing of as-cast steel. NDT & E International, 102:47 – 55, 2019.

[130] X. Jian, S. Dixon, K. T. V. Grattan, and R. S. Edwards. A model for pulsed Rayleigh wave and optimal EMAT design. Sensors & Actuators A, 128:296–304, 2006.

[131] W. F. Jr. Brown. Magnetoelastic Interactions. Springer-Verlag Berlin Heidelberg, 1966.

[132] M. Seher and P. B. Nagy. On the separation of Lorentz and magnetization forces in the transduction mechanism of electromagnetic acoustic transducers (EMATs). NDT & E International, 84:1 – 10, 2016.

[133] Y. L. Bras and J. Greneche. Magneto-elastic resonance: Principles, modeling and applications. In Resonance. IntechOpen, 2017.

[134] H. Ogi, M. Hirao, and T. Ohtani. Flaw detection by line-focusing electromagnetic acoustic transducers. In IEEE Ultrasonic Symposium Proceedings, 1997.

[135] R. Ribichini, F. Cegla, P.B. Nagy, and P. Cawley. Experimental and numerical evaluation of electromagnetic acoustic transducer performance on steel materials. NDT & E International, 45(1):32 – 38, 2012.

[136] S. B. Palmer and S. Dixon. Industrially viable non-contact ultrasound. Insight, 45(3):211–217, 2003.

[137] K. Kawashima. Quantitative calculation and measurement of longitudinal and transverse ultrasonic wave pulses in solid. IEEE Transactions on Sonics and Ultrasonics, SU-31(2):83–94, 1984.

[138] X. Jian, S. Dixon, and S. B. Palmer. In-plane and out-of-plane particle velocity measurement using electromagnetic acoustical transducers. In IEEE Ultrasonics Symposium Proceedings, volume 2, pages 1276–1279, 2005.

[139] X. Jian, S. Dixon, K. Quirk, and K. T. V. Grattan. Electromagnetic acoustic transducers for in- and out-of plane ultrasonic wave detection. Sensors and Actuators A: Physical, 148(1):51 – 56, 2008.

[140] S. Dixon, C. Edwards, and S.B. Palmer. High accuracy non-contact ultrasonic thickness gauging of aluminium sheet using electromagnetic acoustic transducers. Ultrasonics, 39(6):445 – 453, 2001.

[141] P. Hariharan and P. Hariharan. Two-beam interferometers. In Basics of Interferometry, pages 13 – 22. Academic Press, 2007.

[142] A. Wilbrand. EMUS-probes for bulk waves and Rayleigh waves. model for sound field and efficiency calculations. In New Procedures in Nondestructive Testing. Springer Berlin Heidelberg, 1983.

[143] H. Ogi. Field dependence of coupling efficiency between electromagnetic field and ultrasonic bulk waves. Journal of Applied Physics, 82(8):3940–3949, 1997.

[144] M. Hirao, H. Ogi, and H. Fukuoka. Resonance EMAT system for acoustoelastic stress measurement in sheet metals. Review of Scientific Instruments, 64(11):3198–3205, 1993.

[145] S. Huang, W. Zhao, Y. Zhang, and S. Wang. Study on the lift-off effect of EMAT. Sensors and Actuators A: Physical, 153:218–221, 2009.

[146] Y. Fan, S. Dixon, and X. Jian. Lift-off performance of ferrite enhanced generation EMATs. AIP Conference Proceedings, 975(1):835–840, 2008.

[147] C. V. Dodd and W. E. Deeds. Analytical solutions to eddy-current probe-coil problems. Journal of Applied Physics, 39(6):2829, 1968.

[148] K. Kawashima. Theory and numerical calculation of the acoustic field produced in metal by an electromagnetic ultrasonic transducer. The Journal of the Acoustical Society of America, 60(5):1089–1099, 1976.

[149] H. J. Tsaknakis and E. E. Kriezis. Field distribution due to a circular current loop placed in an arbitrary position above a conducting plate. IEEE Transactions on Geoscience and Remote Sensing, GE-23(6):834–840, 1985.

[150] S. H. H. Sadeghi and A. H. Salemi. Electromagnetic field distributions around conducting slabs, produced by eddy-current probes with arbitrary shape current-carrying excitation loops. IEE Proceedings - Science, Measurement and Technology, 148(4):187–192, 2001.

[151] A. V. Clark and Y. Berlinsky. Effect of liftoff on accuracy of phase velocity measurements made with electromagnetic-acoustic transducers. Journal of Research in Nondestructive Evaluation, 4:2:79–96, 1992.

[152] J. P. Morrison, S. Dixon, M. D. G Potter, and X. Jian. Lift-off compensation for improved accuracy in ultrasonic Lamb wave velocity measurements using electromagnetic acoustic transducers (EMATs). Ultrasonics, 44:1401–1404, 2006.

[153] P. Yi, K. Zhang, Y. Li, and X. Zhang. Influence of the lift-off effect on the cut-off frequency of the EMAT-generated Rayleigh wave signal. Sensors, 14(10):19686–19699, 2014.

[154] X. Jian, S. Dixon, R. S. Edwards, and J. Reed. Coupling mechanism of electromagnetic acoustical transducers for ultrasonic generation. The Journal of the Acoustical Society of America, 119:2693, 2006.

[155] X. Jian, S. Dixon, R. S. Edwards, and J. Morrison. Coupling mechanism of an EMAT. Ultrasonics, 44:653–656, 2006.

[156] H. A. Wheeler. Formulas for the skin effect. Proceedings of the IRE, 30(9):412–424, 1942.

[157] J. F. Hernandez-Valle. Pulsed-electromagnet EMAT for high temperature applications. PhD thesis, University of Warwick, 2011.

[158] S. Dixon and X. Jian. Eddy current generation enhancement using ferrite for electromagnetic acoustic transduction. Applied Physics Letters, 89:193503, 2006.

[159] X. Jian and S. Dixon. Enhancement of EMAT and eddy current using a ferrite back-plate. Sensors and Actuator A: Physical, 136(0):132–136, 2007.

[160] R. Hughes, Y. Fan, and S. Dixon. Near electrical resonance signal enhancement (NERSE) in eddy-current crack detection. NDT & E International, 66:82 – 89, 2014.

[161] P. Horowitz and W. Hill. The art of electronics. Cambridge University Press, 2015.

[162] X. Ding, H. Ba, X. Wu, and L. He. Lift-off performance of receiving EMAT transducer enhanced by voltage resonance. In World Conference on Nondestructive Testing, 2012.

[163] C. B. Thring. Enhanced EMAT Techniques for the Characterisation of Hidden Defects. PhD thesis, University of Warwick, 2019.

[164] L. Kang, W. Mi, C. Lv, and S. Wang. Research on weak signal detection technique for electromagnetic ultrasonic inspection system. In IEEE Conference on Industrial Electronics and Applications, pages 2394–2399, 2008.

[165] H. Ogi, H. Ledbetter, S. Kim, and M. Hirao. Contactless mode-selective resonance ultrasound spectroscopy: Electromagnetic acoustic resonance. The Journal of the Acoustical Society of America, 106(2):660–665, 1999.

[166] D. MacLauchlan, S. Clark, B. Cox, T. Doyle, B. Grimmett, J. Hancock, and K. Hour. Recent advancements in the application of EMATs to NDE. In World Conference on Nondestructive Testing, 2004.

[167] B. Mi and C. Ume. Real-time weld penetration depth monitoring with laser ultrasonic sensing system. Journal of Manufacturing Science and Engineering, 128:280–286, 2006.

[168] Nurmalia, N. Nakamura, H. Ogi, M. Hirao, and K. Nakahata. Mode conversion behavior of SH guided wave in a tapered plate. NDT & E International, 45(1):156 – 161, 2012.

[169] K. S. Ho, T. H. Gan, D. R. Billson, and D. A. Hutchins. Application of pulse compression signal processing techniques to electromagnetic acoustic transducers for noncontact thickness measurements and imaging. Review of Scientific Instruments, 76(5):054902, 2005.

[170] Y. Iizuka and Y. Awajiya. High sensitivity EMAT system using chirp pulse compression and its application to crater end detection in continuous casting. Journal of Physics: Conference Series, 520:012011, 2014.

[171] F. Hernandez-Valle and S. Dixon. Initial tests for designing a high temperature EMAT with pulsed electromagnet. NDT & E International, 43:171–175, 2010.

[172] J. K. Hu, Q. L. Zhang, and D. A. Hutchins. Directional characterisitcs of electromagnetic acoustic transducers. Ultrasonics, 26:5–13, 1988.

[173] D. Wu, M. Li, and X. Wang. Shear wave field radiated by an electromagnetic acoustic transducer. Chinese Physics Letter, 23:3294, 2006.

[174] X. Jian, S. Dixon, I. Baillie, R. S. Edwards, J. Morrison, and Y. Fan. Shear wave generation using a spiral electromagnetic acoustic transducer. Applied Physics Letters, 89:244106, 2006.

[175] S. Wang, Z. Li, L. Kang, X. Hu, and X. Zhang. Modeling and comparison of three bulk wave EMATs. In Annual Conference of the IEEE Industrial Electronics Society, pages 2645–2650, 2011.

[176] J. Isla and F. Cegla. Optimization of the bias magnetic field of shear wave EMATs. IEEE Transactions on Ultrasonics, Ferroelectrics, and Frequency Control, 63(8):1148–1160, 2016.

[177] B. Dutton, S. Boonsang, and R. J. Dewhurst. A new magnetic configuration for a small in-plane electromagnetic acoustic transducer applied to laser ultrasound measurements: Modelling and validation. Sensors and Actuators A: Physical, 125:249–259, 2006.

[178] W. J. Pardee and R. B. Thompson. Half-space radiation by EMATs. Journal of Nondestructive Evaluation, 1:157–181, 1980.

[179] S. Wang, R.iliang Su, X. Chen, L. Kang, and G. Zhai. Numerical and experimental analysis of unidirectional meander-line coil electromagnetic acoustic transducers. IEEE Transducers on Ultrasonics, Ferroelectrics, and Frequency Control, 60:2657, 2013.

[180] T. J. Moran and R. M. Panos. Electromagnetic generation of electronically steered ultrasonic bulk waves. Jounal of Applied Physics, 47:2225, 1976.

[181] H. Talaat and E. Burstein. Phase-matched electromagnetic generation and detection of surface elastic waves on nonconducting solids. Jounal of Applied Physics, 45:4360, 1974.

[182] P. Khalili and P. Cawley. Relative ability of wedge-coupled piezoelectric and meander coil EMAT probes to generate single-mode Lamb waves. IEEE Transactions on Ultrasonics, Ferroelectrics, and Frequency Control, 65(4):648–656, 2018.

[183] S. Hill and S. Dixon. Frequency dependent directivity of periodic permanent magnet electromagnetic acoustic transducers. NDT & E International, 62:137–143, 2014.

[184] S. Dixon, S. Hill, Y. Fan, and G. Rowlands. The wave-field from an array of periodic emitters driven simultaneously by a broadband pulse. The Journal of the Acoustical Society of America, 133:3692, 2013.

[185] H. Gao and B. Lopez. Development of single-channel and phased array electromagnetic acoustic transducers for austenitic weld testing. Materials Evaluation, 68(7):821–827, 2010.

[186] P. A. Petcher and S. Dixon. Weld defect detection using PPM EMAT generated shear horizontal ultrasound. NDT & E International, 74:58–65, 2015.

[187] A. C. Cobb, J. L. Fisher, N. Shiokawa, T. Hamano, R. Horikoshi, and N. Ido. Development of a pseudo phased array technique using EMATs for DM weld testing. AIP Conference Proceedings, 1650(1):1015–1022, 2015.

[188] M. Clough, M. Fleming, and S. Dixon. Circumferential guided wave EMAT system for pipeline screening using shear horizontal ultrasound. NDT & E International, 86:20 – 27, 2017.

[189] N. Nakamura, H. Ogi, and M. Hirao. Mode conversion and total reflection of torsional waves for pipe inspection. Japanese Journal of Applied Physics, 52(7S):07HC14, 2013.

[190] A. Demma, P. Cawley, M. Lowe, and A. G. Roosenbrand. The reflection of the fundamental torsional mode from cracks and notches in pipes. The Journal of the Acoustical Society of America, 114(2):611–625, 2003.

[191] H. Ogi, M. Hirao, and T. Ohtani. Line-focusing electromagnetic acoustic transducers for the detection of slit defects. IEEE Transactions on Ultrasonics, Ferroelectrics, and Frequency Control, 46(2):341–346, 1999.

[192] C. B. Thring, Y. Fan, and R. S. Edwards. Focused Rayleigh wave EMAT for characterisation of surface-breaking defects. NDT& E International, 81:20–27, 2016.

[193] T. Takishita, K. Ashida, N. Nakamura, H. Ogi, and M. Hirao. Development of shear-vertical-wave point-focusing electromagnetic acoustic transducer. Japanese Journal of Applied Physics, 54(7S1):07HC04, 2015.

[194] H. Sun, S. Wang, S. Huang, Q. Wang, and W. Zhao. Point-focusing of shear-horizontal wave using fan-shaped periodic permanent magnet focusing coils EMAT for plate inspection. IEEE Sensors Journal, 19(12):4393–4404, 2019.

[195] J. Isla and F. Cegla. Coded excitation for pulse-echo systems. IEEE Transactions on Ultrasonics, Ferroelectrics, and Frequency Control, 64(4):736–748, 2017.

[196] J. Isla and F. Cegla. EMAT phased array: A feasibility study of surface crack detection. Ultrasonics, 78:1–9, 2017.

[197] K. Sawaragi, H. J. Salzburger, G. Hubschen, K. Enami, A. Kirihigashi, and N. Tachibana. Improvement of SH-wave EMAT phased array inspection by new eight segment probes. Nuclear Engineering and Design, 198:153–163, 2000.

[198] L. Pucci, R. Raillon, L. Taupin, and F. Baque. Design of a phased array EMAT for inpsection applications in liquid sodium. Sensors, 19(20):4460, 2019.

[199] F. Le Bourdais and B. Marchand. Development of electromagnetic acoustic transducer (EMAT) phased arrays for SFR inspection. AIP Conference Proceedings, 1581(1):1022–1029, 2014.

[200] F. Le Bourdais and B. Marchand. Experimental validation of an 8 element EMAT phased array probe for longitudinal wave generation. AIP Conference Proceedings, 1650(1):1496–1505, 2015.

[201] F. Le Bourdais, T. Le Pollès, and F. Baqué. Liquid sodium testing of in-house phased array emat transducer for l-wave applications. In International Conference on Advancements in Nuclear Instrumentation Measurement Methods and their Applications (ANIMMA), pages 1–5, 2015.

[202] J. A. F. Tkocz. High Power Phased EMAT Arrays for Non-destructive Testing of As-Cast Steel. PhD thesis, University of Warwick, 2019.

[203] G. Li. Introduction to the Finite Element Method and Implementation with MATLAB®. Cambridge University Press, 2020.

[204] C. Liu. Introduction to weak form, 2014. `https://www.comsol.com/blogs/brief-introduction-weak-form/?setlang=1`, Last accessed on 19-07-2021.

[205] C. Allison. The basics of OnScale, 2019. `https://support.onscale.com/hc/en-us/articles/360015653612-The-Basics`, Last accessed on 19-07-2021.

[206] C. B. Thring, S. J. Hill, S. Dixon, and R. S. Edwards. The effect of EMAT coil geometry on the Rayleigh wave frequency behaviour. Ultrasonics, 99:105945, 2019.

[207] S. Dixon and S.B. Palmer. Wideband low frequency generation and detection of Lamb and Rayleigh waves using electromagnetic acoustic transducers (EMATs). Ultrasonics, 42(10):1129 – 1136, 2004.

[208] S. Dixon, S. E. Burrows, B. Dutton, and Y. Fan. Detection of cracks in metal sheets using pulsed laser generated ultrasound and EMAT detection. Ultrasonics, 51:7–16, 2011.

[209] M. Duquennoy, M. Ouaftouh, and M. Ourak. Ultrasonic evaluation of stressed in orthotropic materials using Rayleigh waves. NDT & E International, 32:189–199, 1999.

[210] D. G. Aggelis, T. Shiotani, and D. Polyzos. Characterization of surface crack depth and repair evaluation using Rayleigh waves. Cemant&Concret Composites, 31:77–83, 2009.

[211] R. J. Blake and L. J. Bond. Rayleigh wave scattering from surface features: up-steps and troughs. Ultrasonics, 30:255–265, 1992.

[212] R. J. Blake and L. J. Bond. Rayleigh wave scattering from surface features: wedges and down-steps. Ultrasonics, 28:214–228, 1990.

[213] X. Jian, Y. Fan, R. S. Edwards, and S. Dixon. Surface-breaking crack gauging with the use of laser-generated Rayleigh waves. Journal of Applied Physics, 100:064907, 2006.

[214] D. Hutchins, P. Burrascano, L. Davis, S. Laureti, and M. Ricci. Coded waveforms for optimised air-coupled ultrasonic nondestructive evaluation. Ultrasonics, 54:1745–1759, 2014.

[215] S. K. Datta, A. H. Shah, and C. M. Fortunko. Diffraction of medium and long wavelength horizontally polarized shear waves by edge cracks. Journal of Applied Physics, 53(4):2895–2903, 1982.

[216] D. K. Mak. Ultrasonic methods for measuring crack location, crack height and crack angle. Ultrasonics, 23(5):223 – 226, 1985.

[217] J. Parra-Raad, P. Khalili, and F. Cegla. Shear waves with orthogonal polarisations for thickness measurement and crack detection using EMATs. NDT & E International, 111:102212, 2020.

[218] M. H. Rosli, R. S. Edwards, B. Dutton, C. G. Johnson, and P. T. Cattani. Identifying surface angled cracks on aluminium bar using EMATs and automated computer system. AIP Conference Proceedings, 1211(1):1593–1600, 2010.

[219] O. Trushkevych, S. Dixon, M. Tabatabaeipour, G. Dobie, M. D. G. Potter, C. MacLeod, A. Gachagan, S. G. Pierce, and R. S. Edwards. Towards guided wave robotic NDT inspection: EMAT size matters. In IEEE International Ultrasonics Symposium Proceedings, pages 104–107, 2019.

[220] R. S. Edwards, B. Dutton, A. R. Clough, and M. H. Rosli. Enhancement of ultrasonic surface waves at wedge tips and angled defects. Applied Physics Letter, 99:094104, 2011.

[221] R. S. C. Monkhouse, P. D. Wilcox, and P. Cawley. Flexible interdigital PVDF transducers for the generation of Lamb waves in structures. Ultrasonics, 35:489–498, 1997.

[222] R. C. Addison and A. D. McKie. Generation and detection of single mode Lamb waves using laser-based ultrasound. Review of Progress in Quantitative Nondestructive Evaluation, 14:521–528, 1995.

[223] T. Yamasaki, S. Tamai, and M. Hirao. Arrayed-coil EMAT for longitudinal wave in steel wires. In IEEE Ultrasonics Symposium Prceedings, pages 789–792, 1998.

[224] L. W. Schmerr Jr. Fundamentals of Ultrasonic Phased Arrays. Springer, Cham, 2015.

[225] P. D. Wilcox. A rapid signal processing technique to remove the effect of dispersion from guided wave signals. IEEE Transactions on Ultrasonics, Ferroelectrics, and Frequency Control, 50(4):419–427, 2003.

[226] R. S. Edwards, A. Sophian, S. Dixon, and G. Tian. Data fusion for defect characterisation using a dual probe system. Sensors and Actuators A: Physical, 144:222–228, 2008.